Numerical methods applied to the computation of electromagnetic vibrations : magnetic force projection and model reduction

Raphaël Pile

UNIVERSITE DE LILLE

THESE

Présentée en vue
d'obtenir le grade de

DOCTEUR

Spécialité : Génie Electrique

Par **Raphaël Pile**

DOCTORAT DELIVRE PAR L'UNIVERSITE DE LILLE
Ecole Doctorale Sciences Pour l'Ingénieur (SPI) 072

Titre de la thèse :

Méthodes Numériques Appliquées au Calcul des Vibrations d'Origine Electromagnétique : Schémas de Projection des Efforts Magnétiques et Développement de Modèles Réduits

(EN) Numerical Methods Applied to the Computation of Electromagnetic Vibrations: Magnetic Force Projection and Model Reduction

Soutenue le 20 Janvier 2021 devant le jury d'examen :

Président, Rapporteur	Georges BARAKAT	Pr, Université du Havre, France.
Rapporteur	Anouar BELAHCEN	Pr, Aalto University, Finland.
Examinatrice	Emeline SADOULET-REBOUL	MCF-HDR, Université de Franche-Comté, France.
Examinateur	François HENROTTE	Dr, Université Catholique de Louvain, Belgique.
Directeur de thèse	Yvonnick LE MENACH	Pr, Université de Lille, France.
Directeur de thèse	Guillaume PARENT	Pr, Université d'Artois, France.
Invité	Jean-Philippe LECOINTE	Pr, Université d'Artois, France.
Invité	Thomas HENNERON	MCF, Université de Lille, France.
Invité	Jean LE BESNERAIS	Dr Ing., EOMYS ENGINEERING, France.

Thèse préparée dans le laboratoire L2EP - Equipe OMN (Université de Lille), dans le laboratoire LSEE (Université d'Artois), et dans l'entreprise EOMYS ENGINEERING.

L2EP Laboratoire d'électrotechnique et d'électronique de puissance de Lille

LSEE

EOMYS

Contents

Remerciements

Un mois après la soutenance, il est largement temps de rédiger ces lignes pour les incontournables remerciements. Je fais le choix de remercier dans un ordre qui ne saurait représenter l'importance de chacun au bon déroulement de cette thèse. Parfois, l'essentiel nécessite peu de mots.

Je peux désormais user de mon grade de docteur. Vous vous en doutez, cela n'a pas changé la façon dont j'achète mon pain. En revanche, mon quotidien est devenu, grâce à cette thèse CIFRE, rythmé par la vie de la petite entreprise EOMYS. Je dois admettre y avoir passé beaucoup plus de temps que prévu dans le programme, mais pour les bonnes raisons. J'y avais trouvé une place, avec des valeurs qui me corrrespondent, et une dynamique joyeuse quelques soient les conditions. Même confinés, cet esprit d'équipe solidaire et déterminé m'a accompagné.

Si chaque membre de l'équipe a son rôle essentiel dans cet orchestre, c'est d'abord Jean qui m'a laissé ma chance quand j'ai postulé en candidature spontanée pour un stage de fin d'étude. Présents dès le départ, Emile et Pierre ont toujours été des soutiens indéfectibles, que ce soit en discussion technique ou pour remonter le moral. Margaux et Pierre-Olivier ne sont pas restés assez longtemps pour suivre mon travail, mais je leur adresse mes sympathiques pensées. Puis il y a eu de nouvelles entrées : Karine et Paul sont désormais des consultants incontournables et des habitués des débats de la pause déjeuner, Franco m'a appris l'importance d'être bien habillé à un mariage en plus d'être devenu notre référent IT, Cédric m'a aidé à corriger mes calculs et à relacher la pression au baby-foot, Anne ne lâche jamais une affaire sûrement grâce à son appétit imbattable. Je n'oublie pas les arrivants de la dernière année, Hélène, Benjamin, Sijie, et en particulier Martin qui m'a sauvé la vie sur les derniers résultats expérimentaux.

Du côté des laboratoires, je vais commencer par remercier Guillaume. Comme tu l'as souvent répété, cette thèse fût une "récréation", et te connaissant je suis assez fier de ce que cela signifie. Je retiendrai de ces 3 ans avec toi des méthodes et de la rigueur scientifique, ton franc-parler, des moments bon-vivants, et le baseball.

Je remercie également Jean-Philippe, qui a apporté une expertise experimentale précieuse même si l'on a manqué de temps sur ce point. Je retiens également ton esprit de synthèse et ta recherche de la conciliation lors de nos discussions plénières. J'espère sincèrement continuer à collaborer avec toi et le LSEE sur les perspectives de ma thèse.

Ensuite je tiens à remercier la bienveillance et la disponibilité d'Yvonnick. Tu avais toujours une question pertinente sous le coude lors de nos réunions, et de très bonnes idées lorsque j'étais dans l'impasse.

Et pour finir avec l'équipe d'encadrants, je remercie Thomas pour son aide sur les thématiques numériques et la projection. J'espère pouvoir continuer à collaborer avec toi sur la réduction de modèle au sens large.

Je remercie ensuite tous les membres du jury de thèse, qui ont répondu virtuellement présent. J'ai eu la chance de réunir un panel d'expertise adapté à l'étendu du sujet en regroupant le génie électrique, la modélisation des forces magnétiques, et la mécanique des milieux continus. J'espère avoir l'occasion de vous remercier en personne, lorsque nous pourrons retourner en congrès par exemple. En particulier, merci au Pr. Barakat et au Pr. Behlacen d'avoir accepté de rapporter mon manuscrit. J'ai particulièrement apprécié les critiques justes et constructives qui m'ont permis d'améliorer la qualité du manuscrit. Je remercie à nouveau Pr. Barakat d'avoir présidé, merci à Dr. Sadoulet-Reboul et Dr. Henrotte d'avoir examiné la soutenance.

J'ai également une pensée pour tous les collègues du LSEE et du L2EP que j'ai croisé au cours de ma thèse. En espérant que les parties de tarot reprennent bientôt!

Et pour finir mes proches, et en particulier ceux qui ont fait le déplacement pour la soutenance : mes parents, Thibaut, Lucas et Ambre, dont le soutien affectif fût précieux. Et enfin Anne, ma compagne, qui me supporte dans mes aventures depuis tout ce temps. Sa relecture précieuse du manuscrit mérite quelques applaudissements supplémentaires.

Introduction

Electromagnetic Noise & Vibration

Today, the ongoing electrification of society enables to put a distance between the energy source (power plant) and the consumer. In particular all the means of transport are being converted to electric power at the expense of oil, whether it is through the traction system or for all the auxiliaries (pumps, fans, actuators...). As a consequence, the field of energy conversion requires to increase performances on electrical machines to sustain the exponential growth in automotive, transport and renewable energies. These performances are evaluated according to criteria specific to each physical fields involved in the design of electrical machines: thermal management, control, power converters, losses in electromagnetic materials... and acoustic.

Noise and vibration are linked to various issues such as safety and health problems (in industrial environments), vibro-acoustic comfort (rail, automotive or domestic applications), security (in military applications), or mechanical fatigue (in the energy sector, such as hydroelectric generators). Noise and vibration can deteriorate working conditions, reducing the life span of the machines and increase their maintenance operations. The effect on the environment is mainly considered through standards, but the subjective feelings of individuals depend on each situation. In particular, the Covid-19 health crisis and containment measures have highlighted the omnipresence of noise pollution in our cities.

The automotive industry is deeply transformed by the electrification of society and by the new requirements on noise levels. Noise from motorized vehicle comes from three main sources: rolling, motoring and high-speed aerodynamic sources (interaction of solid surfaces with airflow) [Wang et al., 2017]. Motorisation is a major source when vehicles are travelling at low to medium speeds: the operation of the engine generates vibrations which are transmitted to the ambient air and generate noise in the audible frequencies.

An internal combustion engine has more sound sources than an electrical motor because the physical phenomena are significantly different (in particular air intake noise, combustion noise, and turbocharger noise). The vibrations of an internal combustion engine act mainly at low and medium frequencies (20 to 800 Hz) and their amplitudes depend mainly on the basic structure of the engine. The noise of an electric motor is more tonal, and extends at higher frequencies, especially due to pulse width modulation. In any case, an engine that vibrates is automatically a noisy engine. The fact that electrical machines are reversible (motor or generator) is another advantage over combustion engines. This also means that several types of working conditions are to be expected for the evaluation of vibration.

This work focuses on the vibration and noise from electromagnetic sources in electrical machines, also called Electromagnetic Noise, Vibrations and Harshness (e-NVH) in automotive. These specific vibrations are linked to the presence of electromagnetic

fields which generate parasitic forces in active structures. These magnetic forces interact with the mechanics of the structures that generates vibration and noise. Economic constraints are pushing electrical machine manufacturers to reduce the quantities of material, which makes machine structures more deformable and increases e-NVH level. In addition, changes in topology can have a significant effect on electromagnetic behaviour and ultimately magnetic forces. These issues have been concretely observed by the EOMYS ENGINEERING company in the context of its studies in the sectors of automotive, energy, domestic applications and naval propulsion. The main difficulty consists in reducing vibrations without degrading the electromechanical performances.

Experimental illustration of magneto-mechanical coupling

The elements that are systematically found in a radial flux electrical machine are a rotating magnetic field and a cylindrical yoke made of ferromagnetic material. Thus, a simplified experimental set-up can be built as illustrated in Fig. 1 to experience a magneto-mechanical coupling: a flexible steel tube in the middle of which two permanent magnets are placed. The shaft is rotating at rotation speed Ω. The permanent magnets create a magnetic dipole which interacts dynamically with the steel tube. The tube is flexible enough to have a visible deflection.

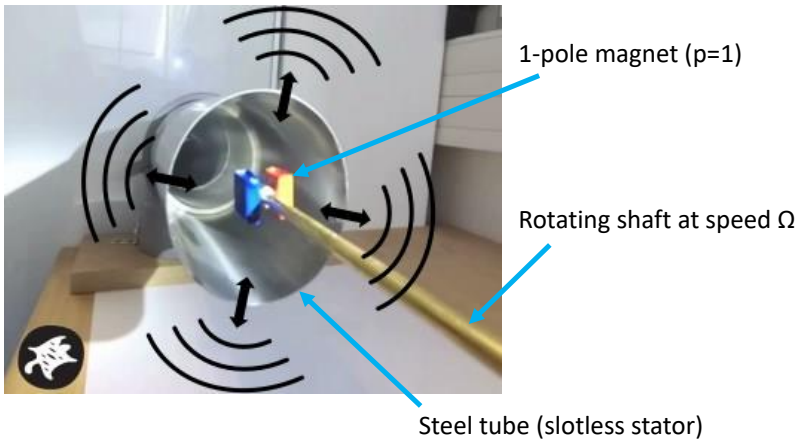

Figure 1 – Experimental setup to illustrate the deflection of a steel tube under magnetic forces [Eomys Engineering, 2017].

A simplified model is proposed to understand the observed magneto-mechanical coupling: if the equivalent pole pair number is p (here $p = 1$), then a first approximation of the magnetic flux density at the interface between the air and the steel as function of time t and angular position θ is a rotating magnetic wave of spatial frequency p such as

$$B(\theta, t) = B_0 \cos\left(\Omega t - p\theta\right). \tag{1}$$

As further discussed in Section 1.3, the magnetic surface force density applying at the air-steel interface is proportional to the square of the magnetic flux density such that

$$F(\theta, t) \propto B_0^2 \left[1 + \cos\left(2\Omega t - 2p\theta\right)\right]. \tag{2}$$

Therefore, a rotating magnetic wave is also responsible for a rotating force wave with a spatial frequency $2p$. This rotating force wave generates a displacement of the same spatial frequency. Indeed, two maxima and two minima are observed for the displacement in Fig. 1.

In industrial electrical machines, the displacement is not visible to the naked eye. Instead, experimental measurements (such as acceleration) are performed in order to understand the different physical interaction. However, some quantities such as magnetic forces are not directly measurable. Thus, it motivates the use of numerical methods.

Numerical Modelling

In a simplified vision of the scientific method, the establishment of scientific theory must enable to explain observed phenomena, but it must also enable to make predictions that will in turn be verified experimentally. Unfortunately, not all physical variables are directly observable and this is particularly true for e-NVH and magneto-mechanical coupling. If the global torque and global forces acting on the machine can be measured, it is not possible for the local distribution of magnetic forces. However, the distribution of forces largely determines the risk of nuisance. At this point, modelling is involved: on the basis of electromagnetic and mechanical theories, a number of assumptions are made to understand the coupling between both systems. Throughout this thesis, the aim is to evaluate the relevance of some of the hypotheses in the prediction of e-NVH.

The modelling of these multi-physics couplings consists in building mathematical environments which enable to predict the physical interactions. These mathematical environments are composed of physical laws, material properties and the geometry of the problem. Under certain assumptions, analytical solutions can be found. Another possibility is to use applied mathematics and numerical simulations to solve a range of physical problems, described by partial differential equations such as:

— electromagnetism,

— continuum mechanics,

— thermodynamical diffusion, and

— fluid dynamics.

The finite element analysis is a popular numerical method: the principle is to solve an equivalent weak formulation associated with the differential problem. The name "finite element" comes from the decomposition of the studied domain into small parts which constitute a mesh. Then, the approximation is performed on a finite dimension discrete space. Thereby, a linear matrix system is to solve by numerical means. Historically, J. H. Argyris, R. W. Clough, H. C. Martin, and O. C. Zienkiewicz are the four academicians who popularized the finite element method from the aerospace industry to a wider range of engineering applications during the 1950s and 1960s. Application to electrical machines started with thermal problems [Armor and Chari, 1976] before its diffusion for electromagnetic modelling as explained in [Bossavit, 1993]. Its success is largely linked to the powerful computing technology and its fast growing over the last decades. It is now a major technique in many industrial problem solving.

In practice, the finite element method requires to simplify the physical problem in order to find a compromise between calculation time and the obtained quality of the solution. Hence, the vast majority of work on magneto-mechanical coupling assumes a weak-coupling [Delaere et al., 1999]: the displacement induced by magnetic forces is considered to have a negligible effect on the electromagnetic solution. Under this assumption, electromagnetic and mechanical resolutions are achieved separately.

In the course of his work, engineers can also use the analytical methods in a complementary way to the finite elements. Indeed, analytical methods give a causal link between a part of the machine and a phenomenon (e.g. the magnetic field) [Virtic et al., 2009; Lubin et al., 2010; Tiegna et al., 2013]. Moreover, the economic competition between manufacturers makes the optimization of electrical machines unmissable. These calculations must be performed at variable speed, for several working conditions. While analytical calculation at variable speed takes few seconds to run on a laptop, it can take a considerable amount of time with purely numerical methods (typically 24 hours for a 3D electrical machine on a high-performance computer). From such a perspective, launching optimization algorithms that rely solely on finite element method can have an exorbitant cost in computing time. It is therefore natural to look for methods that keep only relevant information without redundant calculations. Thus, a judicious combination of analytical and numerical methods can save valuable time and give more physical insight.

Industrial Background

The e-NVH issues are more and more taken into account at early stage of conception [Meek et al., 2013] as sound quality of vehicles is a very important criteria for car manufacturers. It is interpreted as among the most relevant factors regarding perceived product quality, and is important in gaining market advantage. The general sound quality of the urban and professional environments was gradually improved over the years, especially after demonstrating adverse health effects [Passchier-Vermeer and Passchier, 2000; Niemann et al., 2006].

Today the development cycles in the automotive industry are constantly reduced to meet the customers' demands and to react quickly to market needs. In addition, new electrical drive concepts challenge the acoustic engineers to develop a low, pleasant, adequate, and informative sound for passengers as well as for the surroundings. This adds up to all the pre-existing constraints: cost, ecological specifications, increase of vehicle classes and diversifications, energy efficiency, life-cycle assessment ... It partly explains the need in fast design and optimization for e-NVH analysis.

EOMYS ENGINEERING is a company providing engineering consultancy and applied research services for the vibro-acoustics of electrical machines. The capitalization of knowledge and techniques developed within EOMYS ENGINEERING is mainly accomplished through the development of MANATEE (Magnetic Acoustic Noise Analysis Tool for Electrical Engineering) software. MANATEE is a simulation software for the fast design and optimization of electrical machines which includes, besides its electromagnetic model, some mechanical and acoustic models for the calculation of noise and vibrations due to electromagnetic forces. Thus, MANATEE enables the analysis of acoustic noise and vibrations due to electromagnetic forces. EOMYS ENGINEERING supports research effort in this field through Ph.D. thesis works carried out in partnership with research laboratories experienced in the field of e-NVH. In addition, the company wishes to capitalize on the development of new models in its MANATEE software tool. In order to calculate the level of original magnetic noise in a virtual environment, and be able to design a silent machine, electromagnetic and vibration modelling and acoustics must be established. The goal is to get different levels of trade-off between accuracy and speed of calculation through different modelling techniques: analytical, semi-analytical or numerical. That is why this Ph.D work focuses mainly on the development of numerical methods.

This Ph.D work has also been the occasion to significantly contribute to the recent open-source project PYLEECAN (Python Library for Electrical Engineering Computational Analysis) initiated by EOMYS ENGINEERING in 2018. PYLEECAN's objective is to provide a user-friendly, unified, flexible simulation framework for the multiphysic design and optimization of electrical machines. It is meant to be used by researchers, R&D engineers, students and teachers in electrical engineering, on both standard and novel topologies of electrical machines (e.g. during a PhD work). An objective of PYLEECAN is that every Ph.D student should start with PYLEECAN instead of implementing his own scripts. It is also a step towards improving reproducible science for the numerical simulation of electric machines.

Thesis Objectives and Outlines

The work presented in this thesis manuscript focuses on the weak coupling between magnetism and structural mechanics. Thus, it concerns the calculation of magnetic forces and its application on the mechanical model. The main models used in e-NVH simulations are considered for both electromagnetic and mechanical problems. The notion of model reduction is approached from the mechanical point of view: the objective is to reduce simulations to a minimum number of normalized cases.

The main methods used in the weak magneto-mechanical modelling of electrical machines are the air-gap surface force based on Maxwell stress tensor and the virtual work principle. The Maxwell stress tensor gives an approximation of the magnetic force while the virtual work principle is often taken as the reference method for accurate force calculation. Still, the Maxwell stress tensor method is much more popular in e-NVH related scientific publications. In both cases, the main magneto-mechanical coupling method relies on the lumped tooth force model: one resultant vector is applied on each tooth of the vibrating structure (stator or sometimes rotor) in order to compute the corresponding vibration response.

Thus, the main objectives of this thesis are to understand the advantages and disadvantages of each method, and then to look for ways to improve the vibro-acoustics simulation of electrical machines. For this purpose, the manuscript is divided into 3 chapters:

— Chapter 1 presents the state of the art for e-NVH simulations from electromagnetic to mechanical modelling. Special attention is paid to the different methods for calculating forces and their compatibility with the mechanical model.

— Chapter 2 focuses on the study of the calculation of forces using the Maxwell stress tensor method applied in the air-gap for e-NVH simulations. The main contributions presented in this Chapter proposes an analytical analysis of this Maxwell stress tensor method, in particular the dependency on the radius of application.

— Chapter 3 presents the contribution to magnetic forces projection on the mechanical model using lumped tooth force. In particular, the numerical analysis of the modulation effect is presented and discussed. Finally, the different contributions are applied to analyse an electrical machine, and compared to experimental measurements.

Chapter 1

State of the Art of Magneto-Mechanical Coupling for Vibroacoustic Study in Electrical Machines

Contents

1.1 Introduction

1.1.1 Outlines

The e-NVH study of electrical machines relies on the accurate modelling and coupling of involved area of physics: electricity, magnetism, mechanics and acoustics. The notion of coupling implies exchanges between at least two models. These exchanges are represented by transfer of energy between the different physics: electrical energy is converted into magnetic energy and then into mechanical energy. This is the purpose of an electric motor. These exchanges of energy are concretely carried out by means of physical quantities: electric current, electric field, magnetic field, magnetic flux density, magnetic force, stress, etc... One would like to be able to stop at the generation of the mechanical torque, but mechanical stress inevitably leads to unwanted vibrations. These vibrations propagate to a surface in contact with the air, and create small pressure variations which in turn propagate to our ears as sound waves. This is illustrated with solid line arrows in Fig. 1.1. A back effect exists in every coupling as illustrated by dotted arrows in Fig. 1.1:

— The strong circuit coupling might have a real impact on the e-NVH behaviour;

— It is commonly accepted that vibration has a negligible impact on the magnetic problem;

— Sound waves can have an impact on the mechanical behaviour, for example after reflection in the close machine's environment.

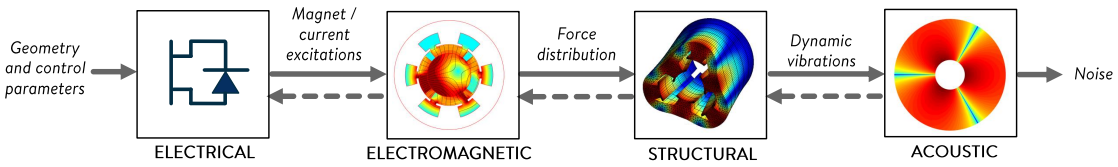

Figure 1.1 – Noise generation workflow from parameters to noise results.

This thesis focuses on the coupling between electromagnetic and structural physics. Different magnetic models are presented in Section 1.2 as the method for calculating the magnetic field determines the calculation of magnetic force. Of course, the accuracy of the coupling is important to correctly simulate the vibration behaviour of an electrical machine.

As a consequence, this chapter is organized as following: the existing magnetic force computation methods for e-NVH simulations are presented in Section 1.3. This thesis also focuses on the interpretability of the results to solve e-NVH issues and the efficiency of the models. Thus, it is necessary to understand the force-structure interactions presented in Section 1.4 and the common troubleshooting methods in Section 1.4.8. Finally, Section 1.5 concludes on the uncertainties that will be addressed in this thesis.

1.1.2 Studied Electrical Machines

The development of electromechanical converters has led to many different topologies depending on applications and requirements. This thesis work focuses on radial flux electrical machines because recent developments have raised new issues related to e-NVH prediction. In particular, the slotted electrical machines have different windings

strategy: distributed or concentrated. The latter type of winding has interesting properties for the automotive industry due to its capability in winding automation and less end turn length [Hasan et al., 2017b,a]. The winding factor and hence the torque density vary among these motor topologies, but in general it reduces losses and improves compactness. However, concentrated windings generate much denser harmonic content and therefore e-NVH issues.

In this thesis, specific analysis and applications are made on a 12 slot 10 poles Surface Permanent Magnet Synchronous Machine (SPMSM) because this topology type has been particularly studied in literature related to e-NVH. The 12s10p topology has a particularly high winding factor. Thus, it has the following advantages: high torque density, low cogging torque due to the large least common multiple of slots and poles number, and low torque ripple due to the absence of low order slot harmonics. However, radial electromagnetic force acting on the stator mainly excite mode order 2 and causes significant deformation. As a consequence, various strategies have been proposed to reduce the vibration for this kind of topology [Das et al., 2018, 2019; Chen et al., 2018; Fakam et al., 2015; Verez et al., 2014]. Lately, a recent phenomenon called the modulation effect has been highlighted in the literature, and 12s10p topologies could be subject to this effect [Fang et al., 2019].

Thus, many numerical applications and all experimental measurements in this thesis are performed on a dedicated benchmark based on a 12s10p machine. This machine is presented in Annex A.1. It was designed to study e-NVH issues during a previous Ph.D. thesis [Devillers, 2018] .

1.1.3 Scope of the Problem

A first issue is the dimensions of the problem with 2D or 3D modelling. As explained in [Gysen, 2011], it is often a valid assumption to consider 2D electromagnetic model since the 3D effects due to the finite axial length are often negligible. In the case of electrical machines which are not uniform in the axial length (for example skewed machine), it is possible to get an accurate approximation of longitudinal excitations with a 2D multi-slice model [Piriou and Razek, 1990; Weilharter et al., 2011]. Moreover, temperature variation has mainly an effect on mechanical natural frequencies [Tan-Kim et al., 2014; Millithaler, 2015]. Therefore, when taking the mechanical natural frequencies as inputs, the electromagnetic simulations can be reduced to 2D.

The issue of magnetostriction contribution to e-NVH is still the matter of recent research work [Belahcen, 2004; Fang et al., 2019]. So far, the results shows that magnetostriction is acting along stator teeth and along back-of-core but without creating new harmonic and with limited contribution to the noise for electrical rotating machines [Garvey, 1997; Fang et al., 2019]. As explained in [Belahcen, 2004], although the magnetostriction force is many times larger than the Maxwell magnetic force, the effect on the vibrations of the structures is less significant for most frequencies. In strong magneto-mechanical coupling, the Villari effect could also play a role on the magnetic properties [Belahcen, 2004]. These effects are assumed to have negligible impact on the studied electrical machines.

In summary, this thesis work focuses on weak magneto-mechanical coupling without magnetostriction. The thermal effects and induced currents are neglected as well. Thus, the electromagnetic models are studied in 2D.

1.2 Electromagnetic Models in Electrical Machines

In the e-NVH simulation process, the magnetic force is computed and applied on a mechanical model. However, the magnetic force calculation method directly depends on the choice of the electromagnetic model. Thus, it is necessary to discuss the granularity of electromagnetic models and the available outputs before looking at magnetic force models. This section focuses on the solutions in parts of the machine where magnetic force occurs, which means on the tip of the stator teeth of the electrical machines.

Moreover, the e-NVH simulations often evaluate the vibrations on the whole speed range. Without an extrapolation method, this can easily require thousands of magnetostatic simulations. Thus, the trade-off between accuracy and computation time is an important criterion. It is also a motivation to reduce the electromagnetic simulation to 2D.

In light of this background, this section proposes to introduce and discuss the main analytical and numerical methods to solve Maxwell's equations in e-NVH simulations. At first, the suitability of magnetostatic model for electrical machines is highlighted when neglecting thermal and induced current effects. Then, several available methods to solve the magnetostatic problem are presented: analytical, semi-analytical and Finite-Element (FE) methods.

1.2.1 Maxwell's Equations in Electrical Machines

A domain D is considered with its boundary Γ as illustrated in Fig. 1.2. Inside this domain, all electromagnetically active parts are modelled according to Maxwell's equations:

$$\nabla \times \mathbf{E} \overset{\text{law}}{=} -\frac{\partial \mathbf{B}}{\partial t}, \tag{1.1}$$

$$\nabla \times \mathbf{H} \overset{\text{law}}{=} \frac{\partial \mathbf{D}}{\partial t} + \mathbf{J}, \tag{1.2}$$

$$\nabla \cdot \mathbf{B} \overset{\text{law}}{=} 0, \tag{1.3}$$

$$\nabla \cdot \mathbf{D} \overset{\text{law}}{=} \rho, \tag{1.4}$$

where **E** is the electrical field, **D** the electrical flux density, **B** the magnetic flux density, **H** the magnetic field, **J** the electrical current density, ρ the electrical charge density, and t the time.

The order of magnitude for electric motor length is L = 1 [m], whereas the electromagnetic wavelengths will always be higher than

$$\lambda_{\min} \overset{\text{def}}{=} \frac{c}{f_{\max}} \approx 1.5 \times 10^4 \,\text{m}, \tag{1.5}$$

with $f_{\max}$ = 20kHz the maximum audible frequency, and $c \approx 3 \times 10^8 \,\text{m}\cdot\text{s}^{-2}$ the light velocity. As a consequence, it can be considered that the electromagnetic field is instantly established. Then, the electrodynamic aspect can be neglected in electrical machines:

$$\frac{\partial \mathbf{D}}{\partial t} \approx 0. \tag{1.6}$$

The thermal aspects with induced currents are neglected as well:

$$\frac{\partial \mathbf{B}}{\partial t} \approx 0. \tag{1.7}$$

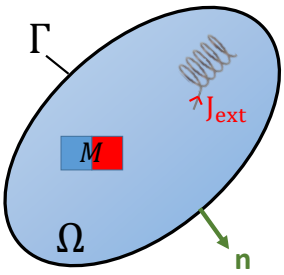

Figure 1.2 – Illustration of the electromagnetic domain of definition

The classical closure relations related to materials can be used:

$$\mathbf{D} \overset{\text{mat}}{=} \epsilon \mathbf{E}, \tag{1.8}$$

$$\mathbf{J} \overset{\text{mat}}{=} \sigma \mathbf{E}, \tag{1.9}$$

with ϵ the electric permittivity, and σ the conductivity. The last one is the relation between $\mathbf{B}$ and $\mathbf{H}$. However, this relation can be rather complex as it implies an hysteresis loop in the general case [Jiles, 2015]. Fortunately, it can be approximated by an anhysteretic relation for ferromagnetic media in electrical machines:

$$\mathbf{B} \overset{\text{mat}}{=} \mu(\mathbf{H})\,(\mathbf{H})\,, \tag{1.10}$$

with μ the magnetic permeability. Then, Maxwell's equations in electrical machines are simplified as:

$$\nabla \times \mathbf{H} = \mathbf{J}_{\text{ext}}\,, \tag{1.11}$$

$$\nabla \cdot \mathbf{B} = 0\,, \tag{1.12}$$

where $\mathbf{J}_{\text{ext}}$ only includes external source of currents (while induced currents are neglected). Applying Stoke's theorem on (1.12) leads to the boundary condition

$$\mathbf{B} \cdot \mathbf{n} \equiv 0 \quad \text{on } \Gamma\,, \tag{1.13}$$

where $\mathbf{n}$ is the outer normal to the boundary Γ. In numerical applications for electrical machine, this boundary condition is enclosing the active electromagnetic parts. For example, the stator yoke outer boundary can be taken as the external boundary condition.

Different ways exist to solve these equations. When using numerical or semi-analytical methods, a magnetic potential is introduced to solve this magnetic problem. Due to the duality that exists between $\mathbf{B}$ and $\mathbf{H}$, there is also a duality in the potentials: one can use a vector potential from which $\mathbf{B}$ is derived, or a scalar potential from which $\mathbf{H}$ is derived. The magnetic potential vector $\mathbf{A}$ can be introduced as

$$\nabla \times \mathbf{A} \overset{\text{def}}{=} \mathbf{B}, \tag{1.14}$$

such that

$$\nabla \cdot \mathbf{B} = \nabla \cdot (\nabla \times (\mathbf{A})) \equiv 0 \tag{1.15}$$

by construction. One can observed that $\mathbf{A} + \mathbf{A_0}$ with $\mathbf{A_0}$ a constant is also a solution since $\nabla \times (\mathbf{A} + \mathbf{A_0}) = \nabla \times \mathbf{A} = \mathbf{B}$. To ensure the uniqueness of solution $\mathbf{A}$, several gauge conditions are available. The Coulomb's gauge is the most used for magnetostatic [Biro and Preis, 1989]. The boundary conditions (1.13) can be expressed with the potential as:

$$\mathbf{A}(x) \times \mathbf{n}(x) = 0\,, \quad \forall x \in \Gamma\,. \tag{1.16}$$

Introducing this potential in (1.11) leads to the magneto-static equation [Jackson, 1999]:

$$\boldsymbol{\nabla} \times \left(\frac{1}{\mu} \boldsymbol{\nabla} \times (\mathbf{A}) \right) = \mathbf{J}, \tag{1.17}$$

where $\mathbf{J}$ is the equivalent current density (including magnetization for permanent magnet). If μ is constant over a finite region of space, then in that region (1.17) can be written as:

$$\boldsymbol{\nabla} (\boldsymbol{\nabla} \cdot \mathbf{A}) - \boldsymbol{\nabla} \mathbf{A}^2 = \mu \mathbf{J}, \tag{1.18}$$

where $\mathbf{J}$ is the excitation vector (it can be actual current density, or equivalent to magnetization). This thesis focuses on 2D electromagnetic computation, such that only one component of the magnetic potential vector can be considered. Then, the problem can be written under the form of Poisson's equation [Green, 1828; Landau and Lifshitz, 1975]:

$$-\Delta(A_z) = \mu_0 J_z . \tag{1.19}$$

Finally, for the air-gap or ferromagnetic without saturation (μ is a constant), (1.17) becomes a Laplace's equation [Green, 1828; Landau and Lifshitz, 1975]

$$\Delta(A_z) = 0 . \tag{1.20}$$

This last equation is used in FE method or semi-analytical method to solve 2D electromagnetic field. In e-NVH context, most of the electromagnetic simulations are performed in 2D with vector potential formulation. Indeed, the degrees of freedom are the same for both vector and scalar formulations in 2D. However, the source term J_z for potential vector in (1.19) has the advantage of being available without pre-calculation, while the potential scalar requires a two-step solving because of the source term pre-calculation [Bossavit, 1993]. Thus, the scalar potential is not used in this work.

1.2.2 Finite Element Method

The fundamental idea of the FE method is to reduce mathematical constraints on the solution of (1.19) by using the variational formulation Brezis [2010]; Larson and Bengzon [2010]; Thompson [2015]. This formulation enables to have some derivative of the solution which are continuous by pieces. Indeed, the electromagnetic model is decomposed into elementary volumes called elements (or cells). The assembly of the elements composes the mesh. Each degree of freedom is associated with its polynomial basis called shape functions. The magnetic potential is approximated by its projection on a finite dimension basis:

$$A_z(x, y) = \sum_{i=1}^{N} A_{z,i} \phi_i(x, y) , \tag{1.21}$$

where N is the total number of degrees of freedom. In 2D magnetostatic, these shape functions are associated with nodes (or 0-cells).

The error between the strong solution of (1.19) and the discrete interpolation (1.21) is linked to the thinness of the mesh [Bossavit, 1993]. Therefore, the numerical error can be controlled; so this numerical method is known to be the reference in term of accuracy. However, the high number of degrees of freedom naturally implies high computational cost.

In this thesis, all the magnetostatic FE simulations are performed using FEMM sowftare [Meeker, 2019] which generates an unstructured mesh only composed of triangular elements, and using a set of linear shape function (see C.1.2). In this particular case, the numerical magnetic field is constant in each cell, and therefore piecewise constant in the whole domain of definition.

1.2.3 Semi-analytical Models

The principle of semi-analytical methods is to rely on analytical solving for homogeneous part of the domain called subdomains. The coupling between equations of each subdomain requires to solve numerically a linear matrix system. Different types of semi-analytical methods are available in the litterature such as:

— Subdomain methods [Devillers et al., 2016],

— Magnetic equivalent circuit and reluctance networks [Ouagued et al., 2016],

— Complex permeance based on conformal transformation [Zarko et al., 2006].

A complete review of these methods is provided in [Devillers, 2018]. The principle of subdomain methods is detailed here because the mathematical developments in Chapter 2 are directly inspired by this formulation.

A typical sub-domain method problem is presented in Fig. 1.3. In 2D with a polar

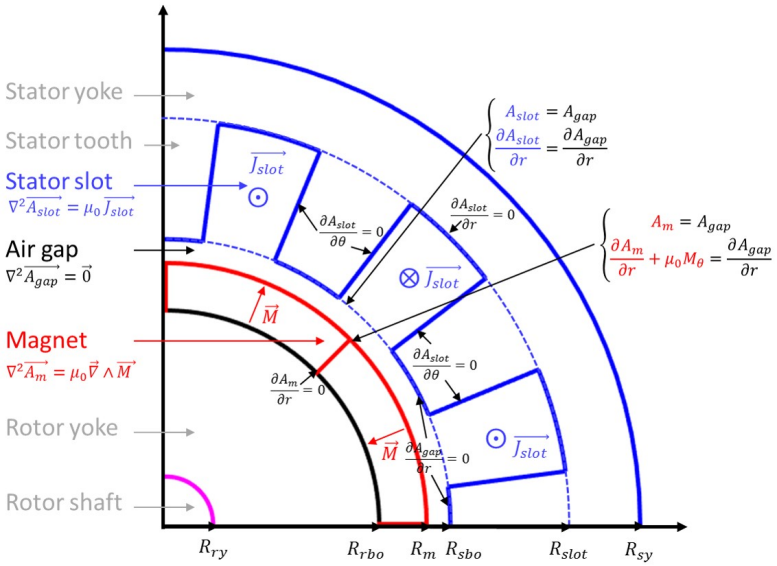

Figure 1.3 – Typical magnetic problem for semi-analytical solving [Devillers, 2018].

coordinate system, it leads to the following homogeneous equation:

$$\frac{1}{r}\frac{\partial}{\partial r}\left(\frac{1}{r}\frac{\partial A_z}{\partial r}\right) + \frac{\partial^2 A_z}{\partial \theta^2} = \mu_0 J_z(r,\theta)\,. \tag{1.22}$$

Then, the magnetic potential is solved based on Fourier decomposition. The degrees of freedom correspond to the total number of harmonics, without any meshing. Compared to FE analysis, the number of unknowns is considerably reduced [Lubin et al., 2012] but the problem is limited to simplified geometries (rectangular or polar subdomains). The semi-analytical model can take into account deteriorated conditions (eccentricities, broken-bars, etc.) [Boughrara et al., 2015; Devillers, 2018]. However, the issue of electromagnetic saturation is still the matter of research works. For example, recent works propose to approximate the saturation by taking into account subdomain in the ferromagnetic part with finite permeability [Roubache et al., 2019; Dubas and Boughrara, 2017].

1.2.4 Analytical Methods

Historically, the main output of interest is the torque of the electrical machine. Since this torque can be computed from the knowledge of the flux density in the air-gap, the

idea of analytical methods is to directly estimate the magnetic flux density only in the air-gap based on the geometrical and electrical properties of the machine (slot/pole combination, currents, etc.). As a consequence, analytical methods are computationally the lightest methods. This advantage is the main motivation to use analytical methods for magnetic force computation as well.

It would be ambitious to make an exhaustive list of all existing methods but the most representative and most used in e-NVH simulations is the permeance/magneto-motive force method: the principle is to compute the radial air-gap magnetic flux density B_r by multiplying a permeance function Λ with a magneto-motive force function [Doherty and Nickle, 1926; Brudny, 1997; Gaussens et al., 2012]:

$$B_r(\theta, t) = \Lambda(\theta, t)\mathrm{MMF}(\theta, t)\,. \tag{1.23}$$

where θ is the angular position, and t the time. The permeance function Λ characterizes the local air-gap length, and advanced methods use a relative complex permeance [Zarko et al., 2006] as illustrated in Figs. 1.4-1.5. It is generally assumed that the slot depth is infinite and that the iron is infinitely permeable. The magneto-motive force function characterizes the distribution of magnetic sources (magnets and windings).

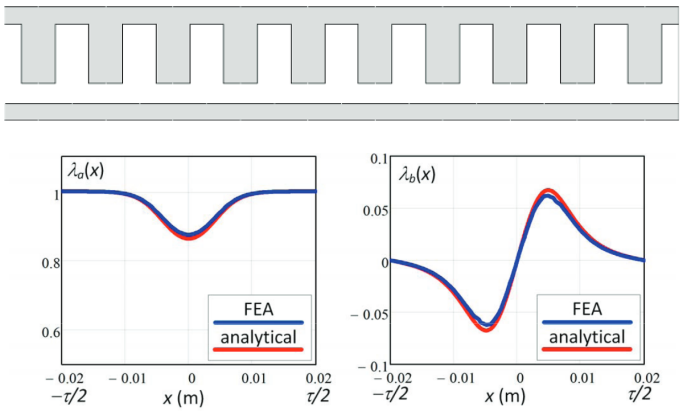

Figure 1.4 – Evaluation of the real part (left) and imaginary part (right) of the permeance function on a slot pitch for a design "A" (on top). [Tessarolo and Olivo, 2016].

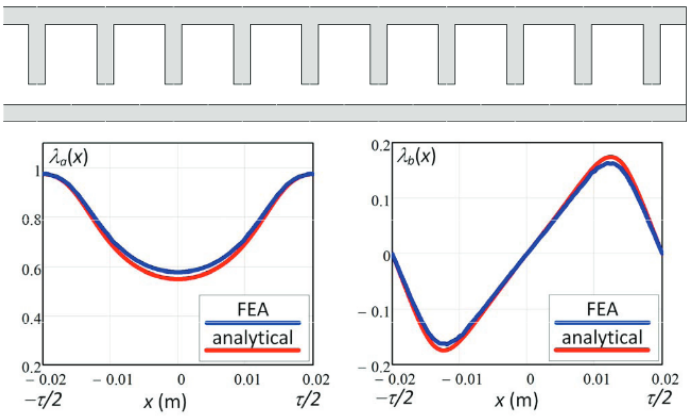

Figure 1.5 – Evaluation of the real part (left) and imaginary part (right) of the permeance function on a slot pitch for a design "B" (on top). [Tessarolo and Olivo, 2016].

1.2.5 Discussion

The three main methods used for electromagnetic simulations in e-NVH were presented and the trade-off between accuracy and speed was highlighted: FE model are more accurate, but the simulation of the full speed range can have a serious impact on the computation time. It is even worse when considering optimisation, because the process is repeated for each tested point in the optimisation loop. This motivates the use of analytical - or semi-analytical - models at early-design stage, prior to accurate FE model. Another advantage of the analytical models is the interpretability: there is an immediate relation of causality between a magnetic harmonic and its source (for example slot/pole combination). As a consequence, it is interesting to keep this interpretability through the magnetic force model. Moreover it allows us to provide spectrograms with little details on the machine parameters (see Section 1.4.8.1). Hence, the interaction between the main parameters (e.g. slot pole combination) and the e-NVH behaviour can be included in the early-design phase. The FE analysis is often saved for latter design phases, in order to carry out a finer electromagnetic optimisation of the machine (possibly in 3D).

The next section details the different methods for magnetic force calculation depending on the available electromagnetic model.

1.3 Electromagnetic excitations

In electrical machines, the magnetic excitations are divided into 3 different categories which are

— Maxwell force,

— magnetostriction, and

— Laplace force (or Lorentz force).

The Maxwell force corresponds to the reaction of the matter to its own magnetization by an external magnetic field. The magnetostriction appears when the mechanical properties of the material are locally modified because of the magnetic field. Finally, the Laplace force applies on electric conductors. A vast majority of the scientific literature focuses on the study of Maxwell force because it is the main electromagnetic excitation that generates vibrations. Indeed, the magnetostriction and Laplace force are expected to have little contribution to the vibration level. As a consequence, this thesis focuses only on the Maxwell force.

The notion of magnetic stress tensor provides a mathematical framework for the calculation of the magnetic volume force density, surface-force density and resultant force. The most common magnetic stress tensor is the so-called Maxwell Stress Tensor (MST) [Melcher, 1981]. The historic use of the MST is for the computation of electromagnetic torque and global force such as unbalanced magnetic pull [Melcher, 1981; Mizia et al., 1988]. The local force has been modelled from energy derivation and the link with the MST has been established [Henrotte and Hameyer, 2004].

Although there are methods to calculate magnetic force accurately [Rafinéjad, 1977; Coulomb and Meunier, 1984; Henrotte et al., 2004], a method to estimate magnetic force in the air-gap based on the MST is used in many works related to e-NVH [Gieras et al., 2005; Boesing et al., 2010; Saito et al., 2016].

The goal of this section is to explain the theoretic background of the main magnetic force computation methods to understand the advantages and disadvantages for e-NVH studies. First, the theoretic application of the magnetic stress tensor is detailed in order to compare with the common air-gap application of the MST. Second, a method based on the energy derivation called Virtual Work Principle (VWP) is presented, and the differences with the MST methods are highlighted.

1.3.1 Magnetic Stress Tensor

An elementary volume $d\Omega$ is considered to be immersed into a magneto-static field. The volume is small enough such that the magnetic field and mechanical properties are nearly uniform over the volume. Considering an isothermal deformation of a bounding surface of $d\Omega$, a second order stress tensor $\mathbf{T}'$ is sought such that [Rosensweig, 1985]:

$$\delta W \overset{\text{law}}{=} -\mathbf{n} \cdot \mathbf{T}' \cdot \mathbf{dx}, \tag{1.24}$$

with δW the mechanical work of the bounding surface, $\mathbf{n}$ the normal field to the bounding surface, and $\mathbf{dx}$ the infinitesimal displacement field. An illustration is provided in Fig. 1.6. Then, the stress tensor $\mathbf{T}'$ can be decomposed as:

$$\mathbf{T}' = \mathbf{T}_{\text{mech}} + \mathbf{T}_{\text{mag}}, \tag{1.25}$$

where $\mathbf{T}_{\text{mech}}$ is the stress tensor associated with the deformation, and $\mathbf{T}_{\text{mag}}$ the magnetic stress tensor. It is supposed that $\mathbf{T}_{\text{mag}}$ depends only on magnetic properties - while

$\mathbf{T}_{\text{mech}}$ depends on mechanical properties - by considering a weak magneto-mechanical coupling.

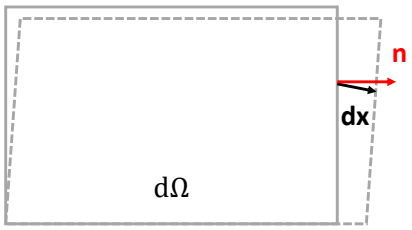

Figure 1.6 – Illustration of mechanical work by deformation of an elementary volume.

According to [Rosensweig, 1985; Henrotte and Hameyer, 2004], it is possible to determine a symmetric $\mathbf{T}_{\text{mag}}$ by expressing δW with the electromechanical energy density of the system. Considering independently an isothermal magnetization at constant volume, then an isothermal deformation, [Robinson, 1973; Rosensweig, 1985; Jackson, 1999] propose the magnetic stress tensor

$$\mathbf{T}_{\text{mag}} = -\left(\int_0^{\text{H}} \mu_0 \left[\frac{\partial(\nu \text{M})}{\partial \nu}\right]_{\text{H,T}} \text{dH} + \frac{1}{2}\mu_0 \text{H}^2\right)\mathbf{I} + \mathbf{BH}, \tag{1.26}$$

with M the magnetization, $\nu = 1/\mu$, μ the permeability, μ_0 the void permeability, $\mathbf{I}$ the identity tensor of order 2, T the temperature, and using a tensor product between $\mathbf{B}$ and $\mathbf{H}$. This expression is valid for an isotropic, magnetostrictive, compressible magnetic body. Unfortunately, it is not easily applicable under this form . Then, some hypotheses adapted to electrical machines can be formulated in order to reduce the complexity.

A non-linear magnetized media is considered in an isotropic or orthotropic material. The hypothesis of an incompressible material (i.e no magnetostriction) leads to the proposal of [Chu, 1959; Zelazo and Melcher, 1969] for the magnetic stress tensor based on the co-energy:

$$\mathbf{T}_{\text{mag}} = -\left(\int_0^{\text{H}} \text{B}\, \text{dH}\right)\mathbf{I} + \mathbf{BH}. \tag{1.27}$$

This is the magnetic stress tensor on which the VWP nodal force method [Coulomb, 1983; Coulomb and Meunier, 1984] is based as discussed in [Henrotte and Hameyer, 2004] and in Section 1.3.4.

Combining both simplifications for an incompressible linearly magnetized media ($\mathbf{B} = \mu\mathbf{H}$), the magnetic stress tensor reduces to the following MST form:

$$\mathbf{T}_{\text{mag}} = -\mu\frac{\text{H}^2}{2}\mathbf{I} + \mathbf{BH}. \tag{1.28}$$

This form is usually called the MST. Another method to obtain (1.28) is to look for a $\mathbf{T}_m$ expression which is compatible with the Lorentz force [Robinson, 1973; Melcher, 1981]. The particular case of the vacuum is obtained for $\mu = \mu_0$. Finally, the MST can be expressed in a more practical way using the radial and tangential magnetic flux density B_r and B_θ in a 2D cylindrical coordinate system [Meessen et al., 2013]:

$$\mathbf{T}_\text{m} = \frac{1}{2\mu}\begin{pmatrix} \text{B}_r^2 - \text{B}_\theta^2 & 2\text{B}_r\text{B}_\theta \\ 2\text{B}_\theta\text{B}_r & \text{B}_\theta^2 - \text{B}_r^2 \end{pmatrix}. \tag{1.29}$$

This magnetic stress tensor only account for the so-called Maxwell's forces. Some other research works propose to model the magnetostriction effect by using another magnetic stress tensor. For example, [Vandevelde et al., 2004]:

$$\mathbf{T}_c = -\alpha_1 \mu_0 \mathbf{M}\mathbf{M} - \alpha_2 \mu_0 M^2 \mathbf{I}, \tag{1.30}$$

with $\mathbf{M}$ the magnetization, and α_1 α_2 magnetoelastic parameters often calculated as polynomials functions of M. The determination of the numerical values requires to measure magnetic properties under a varying stress applied on the ferromagnetic materiel [Belahcen, 2004; Vandevelde et al., 2004]. Moreover, these properties also depends on the assembly process [Helbling et al., 2020] such that it is difficult to accurately model magneto-strictive effect at early design stage. This is another reason to drop the study of magnetostrictive effects in this thesis, and thus to concentrate on the dominant effect of Maxwell's forces.

1.3.2 Magnetic Forces

1.3.2.1 Local Stress

As a consequence of the relation (1.24), a magnetic force per unit volume $\mathbf{f}_m$ exists inside a continuous magnetic body corresponding to a magnetic stress tensor $\mathbf{T}_{\text{mag}}$ such that

$$\mathbf{f}_m = \nabla \cdot \mathbf{T}_{\text{mag}}. \tag{1.31}$$

For instance, using MST (1.28) [Henrotte and Hameyer, 2004]:

$$\mathbf{f}_m = \left(\nabla \times \frac{\mathbf{B}}{\mu}\right) \times \mathbf{B}. \tag{1.32}$$

If there is no current density, then $\nabla \times \frac{\mathbf{B}}{\mu} = \nabla \times \mathbf{H} = 0$ such that $\mathbf{f}_m = 0$.

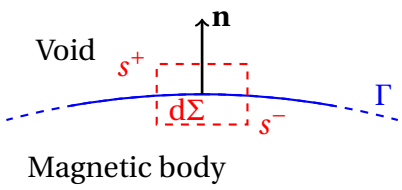

Figure 1.7 – Surface force density calculation

As a consequence, there is no volume force density inside a linearly magnetized media, but the magnetic force is concentrated at the interface with other media. The properties of a tensor enable to compute the surface magnetic force density $\mathbf{p}_m$ on a surface as the following stress vector [Rosensweig, 1985]:

$$\mathbf{p}_m = \mathbf{n} \cdot \mathbf{T}_{\text{mag}} \tag{1.33}$$

with $\mathbf{n}$ the outer normal to the surface. For example, using (1.28):

$$\mathbf{p}_m = -\frac{\mu}{2} H^2 \mathbf{n} + B_n \mathbf{H} \tag{1.34}$$

is the surface force density coming from the linearly magnetized incompressible body. Supposing this body is surrounded by the void, [Bossavit, 2016] proposes to use a "pill-box" method to compute the balance of forces between both sides of the interface as

presented in Fig.1.7: a volume of integration $d\Sigma$ includes a portion of the surface Γ, and to get the results the size of the volume tends to zero. It leads to the expression of the resultant magnetic surface force $\mathbf{p}_r(s)$, $\forall s \in \Gamma$ where Γ is the curvilinear abscissa of the interface:

$$\mathbf{p}_r(s) = \mathbf{p}_m(s^+) + \mathbf{p}_m(s^-), \tag{1.35}$$

where $\mathbf{p}_m(s^+)$ and $\mathbf{p}_m(s^-)$ correspond to (1.33) for each side of the interface. Considering the interface between a linearly magnetized media of permeability μ and the void, it leads to:

$$\mathbf{p}_m(s^+) = \frac{\mu_0}{2} H(s^+)^2 \mathbf{n} + B_n(s^+)\mathbf{H}(s^+), \tag{1.36}$$

$$\mathbf{p}_m(s^-) = -\frac{\mu}{2} H(s^-)^2 \mathbf{n} - B_n(s^-)\mathbf{H}(s^-). \tag{1.37}$$

Using the continuity of B_n and H_t, (1.35) is simplified:

$$\mathbf{p}_r = \frac{1}{2}\left(\left(\frac{1}{\mu_0} - \frac{1}{\mu}\right) B_n^2 - (\mu_0 - \mu) H_t^2\right)\mathbf{n}. \tag{1.38}$$

This result shows that there is no tangential surface force for ferromagnetic material. As a consequence, the torque in an electrical machine is linked to the geometry: the forces on the surfaces which are parallel to the radial direction such as the sides of teeth generate most of the torque thanks to the lever-arm. Volume force density also contribute in a lesser extent [Curti et al., 2017].

If the assumption of high relative permeability in iron is used, such that $\mu \to \infty$, then there are two different possibilities:

1. $\mu H_t^2 \to \infty$
2. $\mu H_t^2 \to 0$

If 1) is true, then it means that $\frac{1}{\mu} B_t^2 \to \infty$, implying $B_t \to \infty$, which is not physical. By elimination, only 2) can be true. As a consequence (1.38) becomes

$$\mathbf{p}_r = \left(\frac{1}{2\mu_0} B_n^2 - \frac{\mu_0}{2} H_t^2\right)\mathbf{n}. \tag{1.39}$$

This formula is only valid at the interface between void and a ferromagnetic media with very high permeability. Going back to (1.35) with two different linearly magnetized media, the contact surface force between both would be

$$\mathbf{p}_r = \frac{1}{2}\left[\left(\frac{1}{\mu_1} - \frac{1}{\mu_2}\right) B_n^2 - (\mu_1 - \mu_2) H_t^2\right]\mathbf{n}, \tag{1.40}$$

such that the surface force exists if, and only if, the materials have different permeabilities μ_1 and μ_2. The conclusion is that magnetic surface force is always oriented from the highest permeability material towards the lowest permeability material for linearly magnetized media. An illustration of the magnetic surface computed with this method on a stator tooth is shown in Fig. 1.8.

1.3.2.2 Integrated Force

The total magnetic force $\mathbf{F}_m$ applied to a body is calculated by integrating the body-force density on the whole volume V:

$$\mathbf{F}_m = \iiint_V \mathbf{f}_m \, dV = \iiint_V \nabla \cdot \mathbf{T}_{mag} \, dV. \tag{1.41}$$

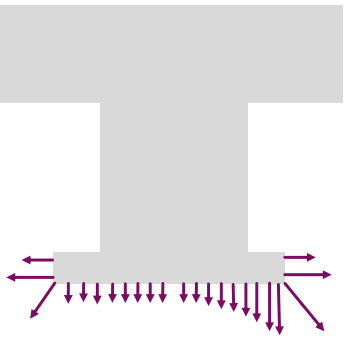

Figure 1.8 – Illustration of the magnetic surface force distribution.

Supposing V is a compact subset of $\mathbb{R}^3$ with a piece-wise smooth closed boundary Γ, and since $\mathbf{T}_{\text{mag}}$ is continuously differentiable on V and defined on a neighbourhood of V, then the Gauss's theorem [Green, 1828] can be applied on (1.41) leading to:

$$\mathbf{F}_{\text{m}} = \oint_{\Gamma} \mathbf{T}_{\text{mag}} \cdot \mathbf{n} \, \mathrm{d}\Gamma \,, \tag{1.42}$$

where $\mathbf{n}$ is the outward pointing unit normal field of the boundary Γ. If the body is surrounded by non-magnetic material (e.g. void) then the volume V can be extended to this non-magnetic domain without changing the total magnetic force acting on the body. Integrating (1.28) along a closed boundary Γ in the void surrounding the body Ω gives the total force acting on the body:

$$\mathbf{F}_{\text{m}} = \oint_{\Gamma} -\frac{\mu_0}{2}\mathrm{H}^2\mathbf{n} + \mathrm{B}_{\text{n}}\mathbf{H} \, \mathrm{d}\Gamma \,. \tag{1.43}$$

For example, the application of (1.43) in the air-gap of an electrical machine gives the resultant force applied to the rotor with outwards pointing normal, and on the stator with inwards pointing normal. Thus, the resultant force differs only by the sign between rotor and stator, which illustrates the principle of action-reaction.

An equivalent result for the magnetic torque M_m can be obtained with $\mathbf{r}$ the lever arm vector [Melcher, 1981; Marinescu and Marinescu, 1988]:

$$\mathrm{M}_{\text{m}} = \oint_{\Gamma} \mathbf{r} \times (\mathbf{n} \cdot \mathbf{T}_{\text{mag}}) \, \mathrm{d}\Gamma = \oint_{\Gamma} \mathrm{B}_{\text{n}}\mathrm{H}_{\text{t}}(\mathbf{r} \cdot \mathbf{n}) \, \mathrm{d}\Gamma \,. \tag{1.44}$$

In summary, the Gauss theorem associated with the physical absence of magnetic force in the void ensures that the total force/torque computed with these methods are the same for any closed surface Γ in the void, even one that wiggle and change radius. However, a circular path is often chosen in order to ease the physical interpretation of the magnetic force generation as discussed in Section 1.3.3.

1.3.3 Air-Gap Forces Based on Maxwell Tensor

The previous Section 1.3.2 presents the theoretic use of the magnetic stress tensor. In particular, the MST has been presented with its application for computing global magnetic torque & force with an integration on a closed surface. However it is common to find in the scientific literature the application of the MST in the air-gap in order to compute surface force density or integrated force per tooth for vibro-acoustic [Gieras et al., 2005; Boesing, 2013; Saito et al., 2016]. It is called the Air-Gap Surface Force (AGSF) model.

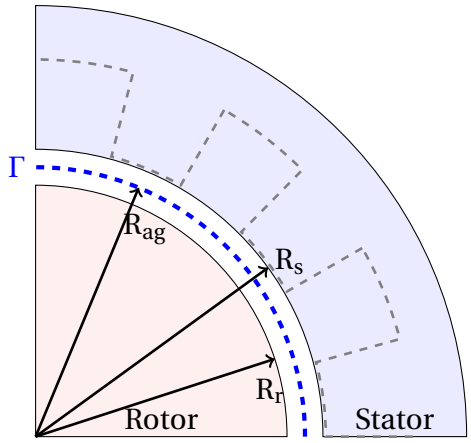

Figure 1.9 – Typical contour Γ for AGSF based on MST in electrical machines.

The AGSF model neglects the volume force contribution to vibrations. Coming back to the total magnetic force (1.43), the AGSF is identified as the term under the integral sign. Indeed, it has the dimension of a surface force density denoted $\mathbf{P}_{ag}$. It can be re-written as:

$$\mathbf{P}_{ag} = \left(\frac{1}{2\mu_0}B_n^2 - \frac{\mu_0}{2}H_t^2\right)\mathbf{n} + B_n H_t \mathbf{t}, \tag{1.45}$$

where $\mathbf{t}$ is the unit tangential field associated with $\mathbf{n}$. This approximation of the magnetic surface force density is called the AGSF based on MST. An illustration of the magnetic surface computed with this method in front of a stator tooth is shown in Fig. 1.10.

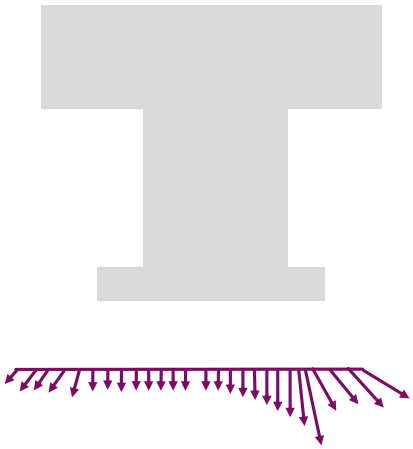

Figure 1.10 – Illustration of the AGSF distribution in front of a tooth.

The AGSF (1.45) is usually applied on a cylindrical surface Γ in the middle of the airgap. An illustration is provided in Fig. 1.9 with the blue dashed surface Γ. In fact, the choice of the surface location is arbitrary. In FE analysis, the middle of the air-gap is less prone to numerical errors which are concentrated near permeability jumps and geometrical angles (i.e. corners of teeth and slot-opening) [Ren, 1994; Li and Lowther, 2009]. Indeed, either B_n or H_t is numerically continuous with FE analysis - not both - depending on the formulation. Then (1.45) might give different results depending on the type of FE magnetostatic simulation (scalar potential or vector potential).

In the previous Section 1.3.2.1, the application of MST at ferromagnetic-air interface provided the magnetic surface force (1.39), which expression is similar to (1.45). Then, it is understandable that AGSF gives an approximation of the magnetic surface force that

apply on the tips of the teeth, assuming that the magnetic field changes very slightly in the air gap. Moreover, it assumes that volume force density has negligible contribution to vibration. Using cylindrical surface (and defining a 2D polar referential as in Annex C.5) gives that the normal direction $\mathbf{n}$ is opposite to the radial direction $\mathbf{e}_r$ when considering the force experienced by the external structure. Then, the AGSF can be decomposed as a sum of a radial and tangential (or circumferential) contribution $\forall\theta \in [0, 2\pi]$ and for all radius r inside the air-gap cylindrical band between R_s and R_r:

$$\mathbf{P}_{ag}(r,\theta) = P_r(r,\theta)\mathbf{e}_r + P_\theta(r,\theta)\mathbf{e}_\theta\,, \tag{1.46}$$

where P_r and P_θ can be expressed as:

$$P_r(r,\theta,t) = -\frac{1}{2\mu_0}\left(B_r^2(r,\theta,t) - B_\theta^2(r,\theta,t)\right), \text{ and} \tag{1.47}$$

$$P_\theta(r,\theta,t) = -\frac{1}{2\mu_0}B_r(r,\theta,t)B_\theta(r,\theta,t)\,. \tag{1.48}$$

An example of the radial AGSF along air-gap is presented in Fig. 1.13. The advantage of using (1.46) is that global force and torque are kept constant thanks to (1.43). However, the local surface force might not be correctly estimated. Indeed, the results depend on the radius of application as shown in Fig. 1.11-1.12.

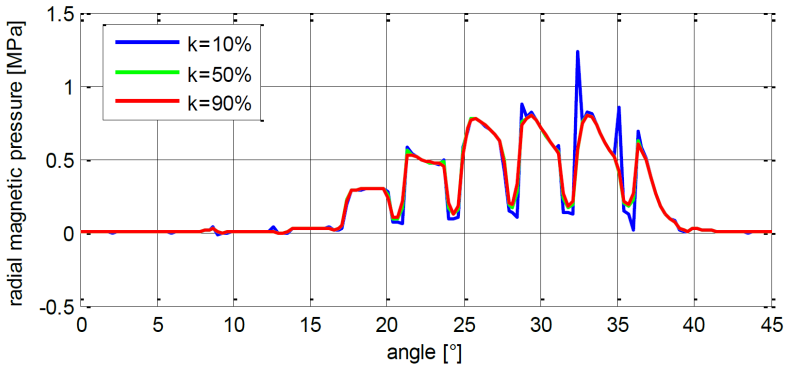

Figure 1.11 – Radial AGSF in an electrical machine depending on the radius of computation $k = \frac{r-R_s}{R_r-R_s}$ [Hallal et al., 2013]: $k = 10\%$ is near the stator and $k = 90\%$ is near the rotor.

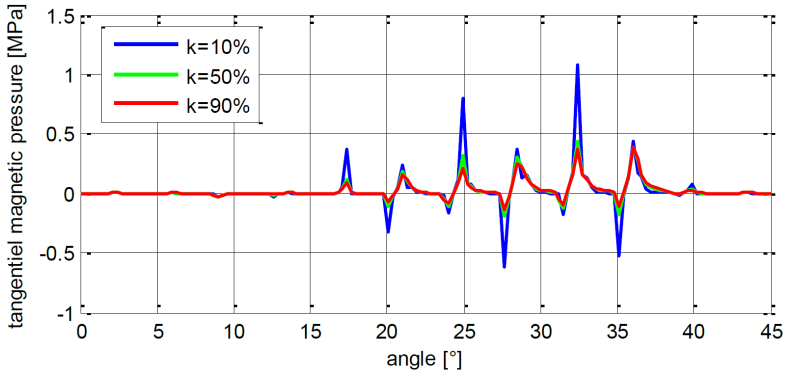

Figure 1.12 – Tangential AGSF in an electrical machine depending on the radius of computation $k = \frac{r-R_s}{R_r-R_s}$ [Hallal et al., 2013].

The AGSF is also a periodical signal in time and angular position. As a consequence,

the Fourier transform can be performed in both dimensions:

$$P_r(r,\theta,t) = \sum_n \sum_\omega \hat{P}_r(r,n,\omega) \exp^{j(n\theta+\omega t)}, \tag{1.49}$$

$$P_\theta(r,\theta,t) = \sum_n \sum_\omega \hat{P}_\theta(r,n,\omega) \exp^{j(n\theta+\omega t)}, \tag{1.50}$$

with ω the time harmonic, n the (angular) wavenumber, $\hat{P}_r$ and $\hat{P}_\theta$ the radial and tangential AGSF Fourier transform, and j the imaginary number. An illustration of decomposition per wavenumber is presented in Fig. 1.13. The wavenumbers are an important information to identify the main sources of noise in electrical machines. Indeed, the notion of wavenumber is linked to the spatial distribution of magnetic force in the machine, and thus the susceptibility to excite specific mechanical eigenmodes. This point is further discussed in Section 1.4.

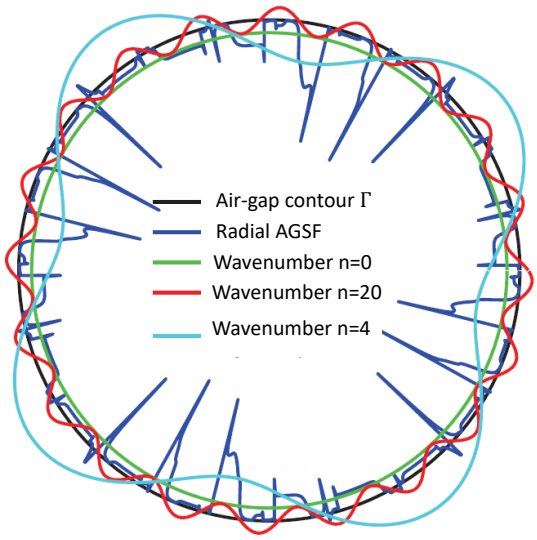

Figure 1.13 – Example of the radial AGSF distribution in an electrical machine including different wavenumbers [Boesing, 2013].

The AGSF is accurate for unbalanced magnetic global force (also called unbalanced magnetic pull) and torque by construction. Moreover, numerical harmonics can be filtered thanks to analytical knowledge [Verma and Balan, 1994; Kiyoumarsi and Zadeh, 2009; Le Besnerais et al., 2010; Azeem et al., 2019]. The problem of the point of application of the computed force is also remaining because the calculated AGSF is not associated with a mechanical surface. The AGSF is computed on a continuous surface in the air-gap while the stator has slots and is therefore not continuous along the air-gap [Boesing, 2013]. As a consequence a specific operation is required, often called "projection". More details about these issues are presented in Section 1.4.2. Despite these disadvantages, the AGSF is widely used because it is a simple method to understand the main force-structure interactions. It is usually applied in the middle of the air-gap for $r = R_{ag}$.

The different ways to apply MST have been presented. In particular the advantages of the AGSF have been highlighted for the vibro-acoustic of electrical machines. The fact that the AGSF are not computed on the stator bore radius R_s is one of the main drawback.

1.3.4 Virtual Work Principle

According to [Rafinéjad, 1977; Bathe, 1996], the concept of VWP is to derive a resultant force (or torque) applied to a deformable domain Ω from the variation of energy ΔE corresponding to a displacement Δx:

$$F \overset{\text{law}}{=} \frac{\Delta E}{\Delta x}. \tag{1.51}$$

A simple electromagnetic circuit as in Fig.1.14 is considered to illustrate this principle. Considering that the magnetic flux density is uniform in the small air-gap volume, then the variation of co-energy due to a small displacement Δx is:

$$\Delta E = A \Delta x \frac{B^2}{\mu_0}. \tag{1.52}$$

Using (1.51) leads to the classical result for the magnetic force in such electromagnetic circuit [Bekemans, 2006]:

$$F = A \frac{B^2}{\mu_0}, \tag{1.53}$$

which could be found back using the MST and (1.42).

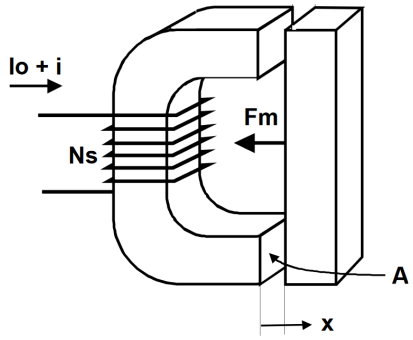

Figure 1.14 – Illustration of magneto-mechanical coupling in a simple case [Bekemans, 2006].

Now that the general principle of virtual work is introduced, it is applied to compute local magnetic force with a FE simulation. Considering an electromagnetic solution calculated on the (virtually) deformable domain Ω with its boundary $\partial\Omega$, the energy and co-energy can be defined as [Rafinéjad, 1977; de Medeiros et al., 1999; Fu et al., 2004]:

$$E_H \overset{\text{def}}{=} \int_\Omega \left(\int_{B_0}^{B} \mathbf{H} \cdot d\mathbf{B} + W_0 \right) dV, \tag{1.54}$$

$$E_B \overset{\text{def}}{=} \int_\Omega \left(\int_{B_0}^{H} \mathbf{B} \cdot d\mathbf{H} + W_0^* \right) dV, \tag{1.55}$$

where W_0 is the energy density and W_0^* the co-energy density of the initial operating point, with the corresponding magnetic solution $\mathbf{H_0}$ and $\mathbf{B_0}$. This initial operating point corresponds to the studied system isolated from external exciting sources. For example, it could be calculated for a permanent magnet alone in the void, isolated from any other magnetic source/material.

Then, [Rafinéjad, 1977; Coulomb, 1983] propose to define the following co-energy functional of the (virtual) displacement $\mathbf{u}$ in a direction s:

$$C_E(\mathbf{u}) \overset{\text{def}}{=} E_B + \int_{\partial\Omega} (\mathbf{B} \cdot \mathbf{n}) \mathbf{u} dS. \tag{1.56}$$

The difference between the magnetic co-energy (1.55) and the functional (1.55) is minimized for the following extremal conditions:

$$\frac{\partial \mathrm{C_E}}{\partial \mathbf{u}} = 0\,. \tag{1.57}$$

Hence, the VWP theorem applied with the co-energy functional gives an approximation of the force in the direction s acting on the rigid part of the domain:

$$\mathrm{F_s} = \frac{\mathrm{dC_E}}{\mathrm{d}s} = \frac{\partial \mathrm{C_E}}{\partial s} + \left(\frac{\partial \mathrm{C_E}}{\partial \mathbf{u}}^{\mathrm{T}} \cdot \frac{\partial \mathbf{u}}{\partial s} \right). \tag{1.58}$$

Looking for the optimal co-energy functional implies (1.57) such that

$$\mathrm{F_s} = \frac{\partial \mathrm{C_E}}{\partial s} = \frac{\partial}{\partial s} \left(\mathrm{E_B} + \int_{\partial\Omega} (\mathbf{B}\cdot\mathbf{n})\mathbf{u}\mathrm{dS} \right). \tag{1.59}$$

In order to simplify this last equation, it is important to highlight that an implicit "weak-coupling" hypothesis is used in [Coulomb, 1983] such that

$$\frac{\partial \mathbf{B}}{\partial \mathbf{u}} = 0\,. \tag{1.60}$$

Thus,

$$\frac{\partial}{\partial s} \left(\int_{\partial\Omega} (\mathbf{B}\cdot\mathbf{n})\mathbf{u}\mathrm{dS} \right) = \int_{\partial\Omega} (\mathbf{B}\cdot\mathbf{n})\mathrm{dS} \equiv 0\,, \tag{1.61}$$

such that only the first term is left:

$$\mathrm{F_s} = \frac{\partial \mathrm{E_B}}{\partial s}\,. \tag{1.62}$$

The issue of the initial operating point requires to make the distinction between intrinsic force density and interaction force density [de Medeiros et al., 1999; Fu et al., 2004]: intrinsic force density $\mathrm{F_s^0}$ is the distribution of forces at the initial operating point while interaction force density $\mathrm{F_s^{ext}}$ is due to interactions of the exterior medium:

$$\mathrm{F_s} = \mathrm{F_s^0} + \mathrm{F_s^{ext}}\,, \tag{1.63}$$

with

$$\mathrm{F_s^0} = \frac{\partial}{\partial s} \int_\Omega \omega_0^* \mathrm{d}\Omega \tag{1.64}$$

$$\mathrm{F_s^{ext}} = \frac{\partial}{\partial s} \int_\Omega \left(\int_{\mathrm{B_0}}^{\mathrm{H}} \mathbf{B}\cdot\mathrm{d}\mathbf{H} \right) \mathrm{d}\Omega\,. \tag{1.65}$$

For example, a magnet alone in the void will self-generate a magnetic field such that ω_0 is not null which implies the existence of intrinsic force density. On the opposite, ferromagnetic media alone does not have any magnetic energy such that the only possible magnetic force is due to the interactions. In the context of e-NVH studies, the interaction force $\mathrm{F_s^{ext}}$ is the quantity of interest. Indeed, machine designers are only interested in the dynamic force which creates the vibration. By definition, intrinsic force is static such that it can be filtered with a time Fourier decomposition.

The VWP is adapted to FE application since the previous integration domain Ω is naturally defined by each element that constitutes the mesh. To evaluate the energy derivation for each element e of the mesh, $\mathrm{F_s}$ can be expressed into the reference element to get the integral boundaries independent of any derivatives:

$$\mathrm{F_s} = \sum_e \int_{e_{\mathrm{ref}}} \frac{\partial}{\partial s} \left(\int_0^{\mathbf{H}} \mathbf{B}\,\mathrm{d}\mathbf{H}|\mathrm{J}| \right) \mathrm{de}\,, \tag{1.66}$$

where J is the jacobian matrix (of the element e) and |J| its determinant. The co-energy derivative under integral can be developed such that the magnetic VWP can be expressed with the solution of the electromagnetic field and the jacobian's derivatives [Coulomb, 1983; Coulomb and Meunier, 1984]:

$$\mathrm{F_s} = \sum_e \int_e \left(-\mathbf{B} \cdot \mathrm{J}^{-1} \cdot \frac{\partial \mathrm{J}}{\partial s} \cdot \mathbf{H} + \left(\int_0^{\mathbf{H}} \mathbf{B}\, d\mathbf{H} \right) |\mathrm{J}^{-1}| \frac{\partial |\mathrm{J}|}{\partial s} \right) \mathrm{de}. \tag{1.67}$$

The calculation of the Jacobian derivative is known to be the most difficult part of this method. Until (1.67), the expression is independent of the targeted node. However, the calculation of the Jacobian derivatives requires to choose the virtually moving node, and to assign the element computed resultant (1.67) to this node. In the following, the matrix of the coordinates of the element nodes is denoted S, and the matrix of shape functions in the element of reference is ω_{ref}. The Jacobian matrix of the element can be expressed as [Coulomb and Meunier, 1984; Boualem, 1997]:

$$\mathrm{J} = \boldsymbol{\nabla} \omega_{\mathrm{ref}} \mathrm{S}. \tag{1.68}$$

The derivatives of (1.68) can then be computed:

$$\frac{\partial \mathrm{J}}{\partial s}^{(i)} = \frac{\partial \boldsymbol{\nabla} \omega}{\partial s} \mathrm{S} + \boldsymbol{\nabla} \omega \frac{\partial \mathrm{S}}{\partial s}^{(i)}. \tag{1.69}$$

The left side of (1.69) can be calculated from the expression of shape function in the reference element. However, the right side of the equation is not straightforward. The idea proposed by [Coulomb, 1983] is to virtually perform an elementary displacement of each node, one by one, as illustrated in Fig. 1.15. Thus, the derivative now depends

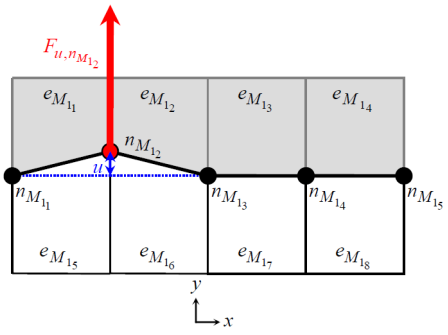

Figure 1.15 – Application of VWP: virtually moving each node to compute the Jacobian derivative of the element [Parent, 2008].

on the targeted node (i) and denoted $\frac{\partial}{\partial s}^{(i)}$. The matrix $\frac{\partial \mathrm{S}}{\partial s}^{(i)}$ is equal to zero everywhere except for one value - at the i^{th} line and column corresponding to the spatial direction s - equal to one. The calculation of the determinant derivative relies on the same principle. In order to compute determinant derivative, it is proposed to use the trace operator:

$$\frac{\partial |\mathrm{J}|}{\partial s}^{(i)} = \mathrm{Tr}\left(\mathrm{J}^{-1} \frac{\partial \mathrm{J}}{\partial s}^{(i)} \right) |\mathrm{J}|. \tag{1.70}$$

This last equation was not found in the analysed literature, but it enables simplified calculation and implementation compared to [Coulomb, 1983].

Finally, the application of (1.67) allows us to get a different resultant for each node of the element:

$$\mathrm{F}_{\mathrm{s},(i)} = \sum_e \int_e \left(-\mathbf{B} \cdot \mathrm{J}^{-1} \cdot \frac{\partial \mathrm{J}}{\partial s}^{(i)} \cdot \mathbf{H} + \left(\int_0^{\mathbf{H}} \mathbf{B}\, d\mathbf{H} \right) |\mathrm{J}^{-1}| \frac{\partial |\mathrm{J}|}{\partial s}^{(i)} \right) \mathrm{d}e\,. \tag{1.71}$$

Each element contributes to the surrounding nodes as illustrated in Fig. 1.16.

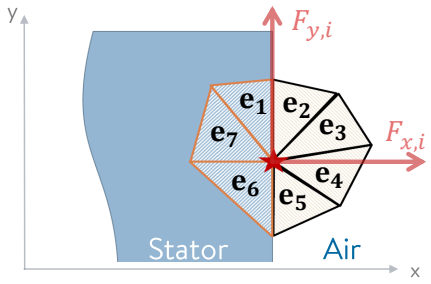

(a) Application for 2D triangular elements.

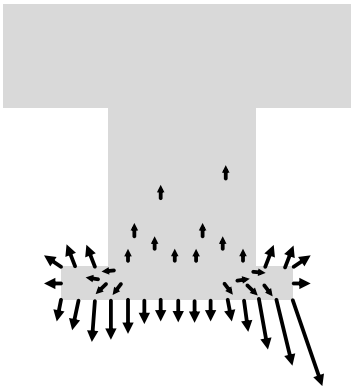

(b) Result on a stator tooth.

Figure 1.16 – Illustration of application of VWP.

The integral of magnetic co-energy can be performed numerically based on the input B-H curve, or it can be simplified by supposing a constant permeability in each element such that:

$$\int_0^{\mathbf{H}} \mathbf{B}\, \mathrm{d}\mathbf{H} \approx \frac{\mu}{2} |\mathbf{H}|^2\,. \tag{1.72}$$

If the electromagnetic FE analysis is performed by taking into account saturation, then μ would be different in each element, but this approximation could still lead to approximate the force inside the volume a illustrated in Fig. 1.17: the magnetic co-energy corresponds to the area under the curve which is underestimated with a linear hypothesis. The error of integration naturally increases with the saturation of the material.

Instead of using the VWP, one could integrate the divergence of the MST (1.42) on each element, with $\mathbf{T}_{\mathrm{mag}}$ from (1.28). This method is called Tooth Tip MST method (as illustrated in Fig. 1.18). It is theoretically equivalent to the VWP when using the approximation (1.72), but numerical implementation can introduce significant differences. For this reason, the AGSF (1.46) should lead to results which are equivalent to VWP if it is applied only on the air side (such as elements e_2, e_3, e_4, and e_5 in Fig. 1.16).

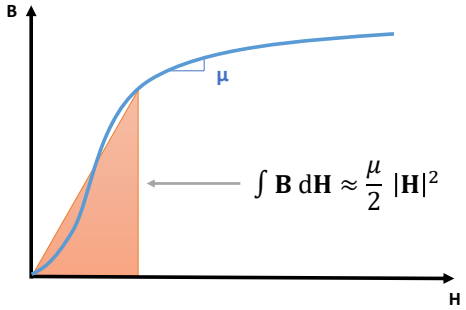

Figure 1.17 – Approximation of magnetic co-energy using constant permeability hypothesis in each element.

The nodal force (1.71) define a set of discrete force resultants acting on each node [Parent et al., 2008] (note a vectorial field). In Section 1.4.6.1, the methods to compute an equivalent force density will be presented. However, even with force density, the comparison with AGSF is not straightforward. Indeed, the calculation of spatial Fourier transforms is a key information for e-NVH troubleshoot (see Section 1.4.8). However, classical Fourier algorithms (such as Fast Fourier Transform) rely on regularly spaced mesh in all directions. In general, the initial magnetic/structural meshes are not suitable for the Fourier analysis and another projection must be performed [Kotter, 2019]. Nevertheless, the continuous air-gap domain of definition for AGSF is still different from the discrete tooth domain. As a consequence, the link between nodal force (1.71) and electromagnetic sources is not straightforward, such that it makes it more difficult to identify the root causes of e-NVH compared to AGSF.

1.3.5 Conclusion

The two main methods to compute magnetic force for e-NVH analysis have been presented: the AGSF based on MST and the nodal force based on VWP. The main advantages and disadvantages are summarized in Fig. 1.18.

These are not the only existing methods which can be found in the literature:

— Equivalent magnetic currents: The idea of this method is to replace the media by a fictive non-magnetic media through which currents flow. It allows us to define the force from Laplace's formula [Carpenter, 1960].

— Equivalent magnetic mass density: The idea of this method is to replace the media by a fictive non-magnetic media which has a magnetic mass density [Carpenter, 1960].

— Formulation with both magnetic currents and magnetic mass [Carpenter, 1960] which is equivalent to MST applied at the interface between materials.

— Energy derivation formulation [Carpenter, 1960] which leads to the VWP methods.

All these methods have been compared in several articles by numerical means [Muller, 1990; Sadowski et al., 1992; Ren, 1994] and more recently with experimental means [Barré et al., 2006]. The conclusions are that the formulations based on energy derivation (such as VWP) are the most accurate because it can take into account body-force density. The AGSF seems to be a reasonable approximation in most of applications for electrical machines as body-force density is limited [Curti et al., 2017]. However the main benefit of the AGSF is its interpretability for e-NVH troubleshoot. This last point is further developed in Section 1.4.8.

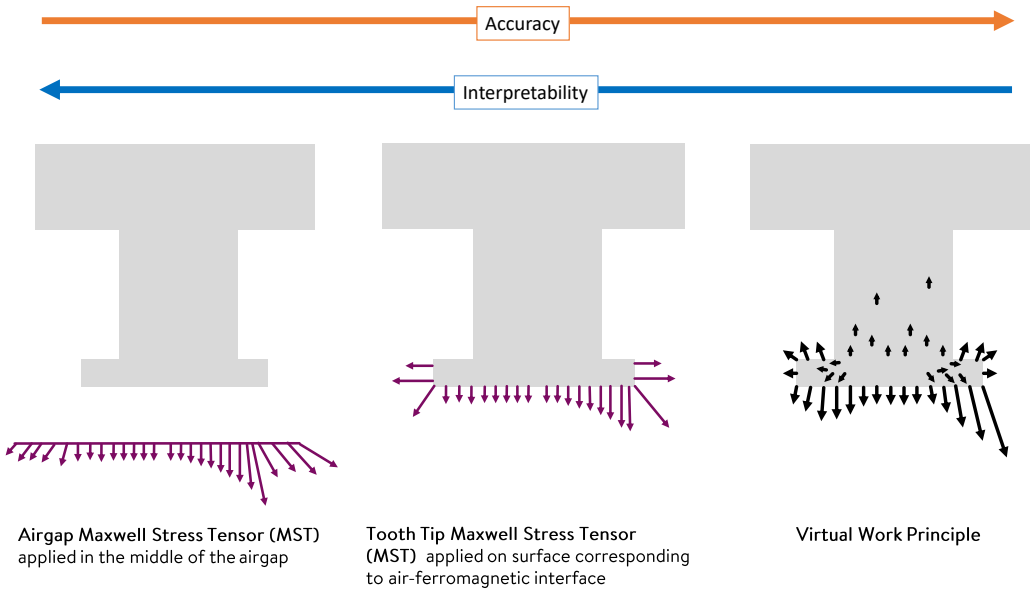

Figure 1.18 – Main methods to compute magnetic force for e-NVH: interpretability vs. accuracy.

1.4 Mechanical and Acoustic Modelling

The different methods to compute magnetic force have been presented. It is now necessary to review the different models available to compute the corresponding mechanical response.

The main output of interest is the displacement. A major issue of the magneto-mechanical coupling is the computational cost: a direct method would be to compute the response at every frequency for each electromagnetic load-case (i.e. rotation speed). It could represent an overwhelming number of simulations. To solve this issue, it is common to use both weak magneto-mechanical coupling and mechanical linearity assumptions:

— The first one enables the computation of all magnetic force load-cases independently of mechanical properties;

— The validity of the second assumption relies on the small displacement related to e-NVH issues (typically 1×10^{-3} mm). It allows us to reduce the mechanical simulations to a few significant normalized cases such that only one mechanical simulation is necessary for every magnetic load-case.

This thesis relies on both hypotheses. This section details the different methods to apply magnetic force and compute vibration. The projection methods, which are the techniques used to load the mechanical model depending on the magnetic force model, are introduced. The advantages and disadvantages of each method are presented, in particular the methods based on AGSF and VWP.

1.4.1 Modal Analysis & Frequency Response Function

1.4.1.1 Natural Frequency and Mode Shape

The modal analysis is the study of dynamic properties in the frequency domain. A simple 1D system to introduce the mechanical dynamic behaviour is a mass-spring os-

cillator as illustrated in Fig. 1.19. The position x of the mass-spring system can be ex-

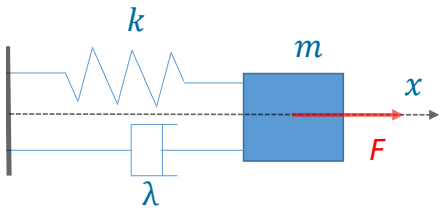

Figure 1.19 – Mass spring damping 1D mechanical system

pressed as function of time t according to:

$$m\frac{\partial^2 x}{\partial t^2} + c\frac{\partial x}{\partial t} + kx(t) = \mathrm{F}(t)\,, \tag{1.73}$$

where m is the mass, k is the spring stiffness, c the viscosity, and F the external load. Looking for this solution under complex form $x(t) = \mathrm{X}(\omega)\exp\left(j\omega t\right)$, with ω the pulsation, leads to the Frequency Response Function (FRF)

$$\mathrm{H}(\omega) = \frac{\mathrm{X}(\omega)}{\mathrm{F}(\omega)} = \frac{1/m}{\omega_n^2 + 2j\epsilon\omega_n\omega - \omega^2}\,, \tag{1.74}$$

with $\epsilon = \frac{c}{2\sqrt{km}}$ the reduced damping, and $\omega_n = \sqrt{\frac{k}{m}}$ the pulsation corresponding to the natural frequency $f_n = 2\pi\omega_n$. The transfer function H is plotted for several damping values for a pulsating force $\mathrm{F}(t) = \mathrm{F}_0\cos(\omega t)$ in Fig. 1.20: the maximum of vibration is reached when the excitation's frequency is matching the resonant frequency

$$\omega_r = \omega_n\sqrt{1-2\epsilon^2} \approx \omega_n\,. \tag{1.75}$$

In electrical machines, the damping ϵ of an orthotropic lamination is typically 2%. Therefore, the difference between the natural frequency and the corresponding resonant frequency is neglected in this work.

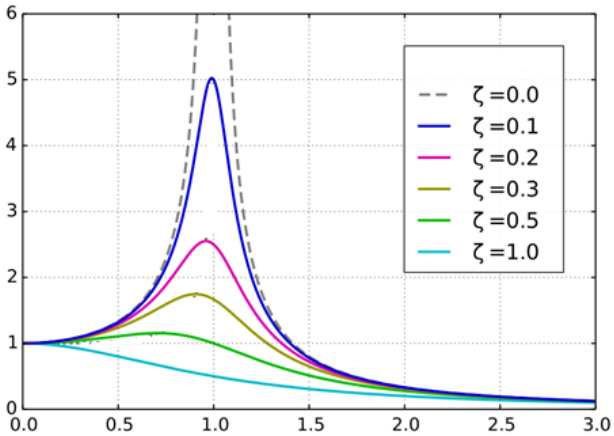

Figure 1.20 – FRF of a mass spring system to a cosine excitation.

The similarity between mass spring FRF and a typical stator yoke FRF excited by rotating AGSF can be observed by comparing Fig. 1.20 and Fig. 1.21. It motivates the use of analytical cylinder shell models for mechanical response.

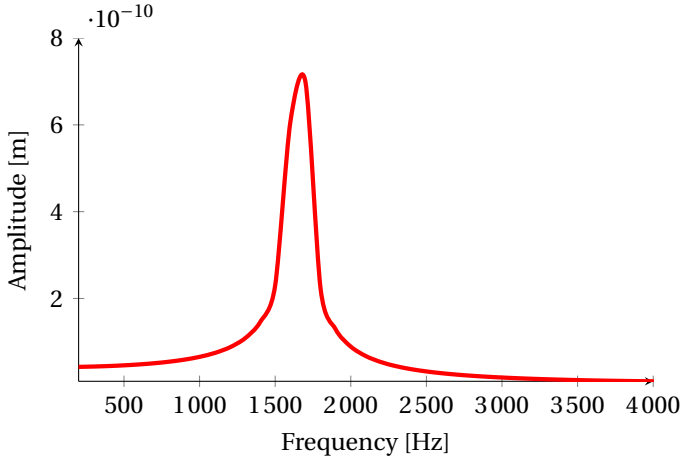

Figure 1.21 – FRF of the displacement on the yoke of a stator calculated with FE analysis for a normalized excitation of wavenumber $n = 2$.

As any complex mechanical structure, electrical machines stator lamination would have more than one mode shape as illustrated in Fig. 1.22. The main mode shapes of lamination are classified according to their natural frequency but also according to the periodicity of the mode denoted by a duo (n, m) or triplet (n, m, k) [Van der Giet, 2011; Kotter, 2019]:

— n denotes the radial periodicity of the mode,

— m denotes the axial periodicity of the mode,

— k denotes the tangential periodicity of the mode.

The last index is less used as it refers to torsional modes which have generally weak e-NVH impact. Torsional modes could be excited by tangential force leading to structure-borne noise in the operating environment. Nevertheless, this type of e-NVH issue is not studied in this thesis.

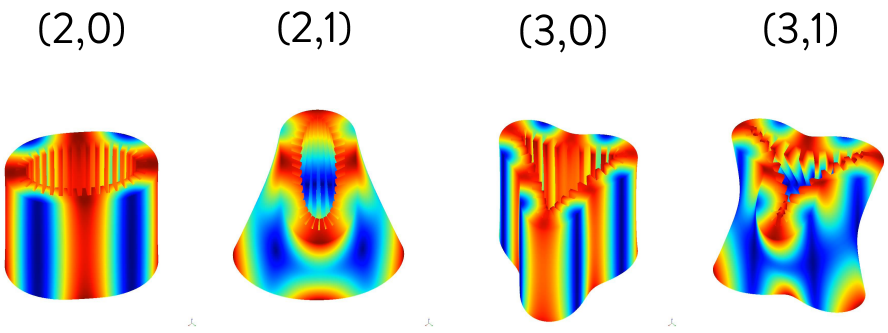

Figure 1.22 – First mode shapes of a stator lamination in free-free conditions obtained by FE analysis.

1.4.1.2 Analytical Modal Analysis

Analytical calculation of eigenmodes and their frequency starts with [Jordan, 1950; Alger, 1953; Alger and Erdelyi, 1956; Hartog, 1960; Timar, 1989]: the electrical machine is

approximated by an equivalent 2D circular beam (like the tube in Fig. 1) with relatively thin thickness, and the equations are simplified by using kinetic hypothesis. The teeth and windings contributions are considered by increasing mass density. The classical analytical modal shape is supposed to be a pure sine of the considered mode order. In general, the circumferential natural frequency are calculated for the order $n = 0$ according to [Boisson, 2014; Pellerey, 2012]:

$$\omega_0 = \frac{1}{R_y}\sqrt{\frac{E}{\rho_{eq}}}, \tag{1.76}$$

and for the orders $n > 1$ according to [Boisson, 2014; Pellerey, 2012]:

$$\omega_n = \frac{H_y}{2\sqrt{3}R_y}\frac{n(n^2-1)}{\sqrt{n^2+1}}\omega_0, \tag{1.77}$$

with the following parameters:

— E is the Young's modulus of the yoke,

— R_y is the radius of the yoke's neutral fiber (see Fig. 1.23),

— H_y is the thickness of the yoke,

— $\rho_{eq} = \rho\frac{M_y+M_t+M_w}{M_y}$ is the equivalent mass density of the yoke,

— M_y, M_t and M_w are the masses of (resp.) the yoke, the teeth and the windings.

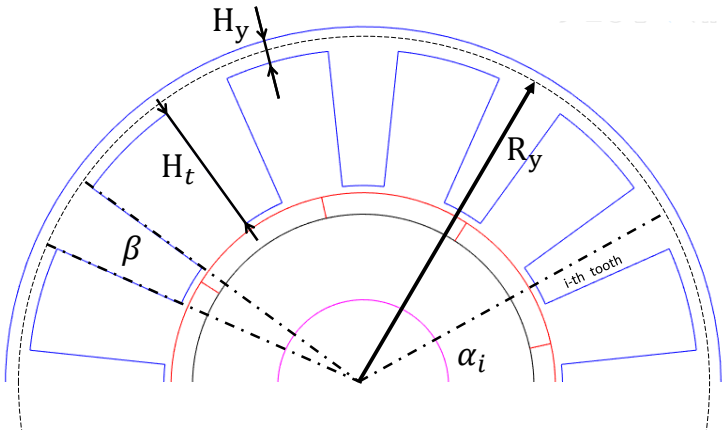

Figure 1.23 – Geometrical notations.

These classical formulae consider a relatively thin yoke [Verez and Espanet, 2016], typically $\frac{H_y}{R_y} < 0.1$. The extension of analytical calculation to higher thickness and taking into account teeth is presented in [Boisson, 2014].

The radial modes with low orders generally have the most influence on noise and vibrations, in particular ovalization mode (2,0), breathing mode (0,0) and bending mode (0,1). In fact, maximal displacement magnitude in function of circumferential wavenumbers decreases such as [Jordan, 1950]:

$$u_{max} \propto \frac{1}{\left(n^2-1\right)^2}. \tag{1.78}$$

Thus, the greater are the orders (n,m), the lower is the resonance peak and the higher is the natural frequency. However, higher modes may have an influence on noise and vibrations of large diameter machines [Traxler-Samek et al., 2012].

1.4.1.3 Modal Analysis

The mechanical response of laminations in electrical machines relies on the same principle. A more complex system can be discretized in small elements with elementary mass and stiffness. For each element, degrees of freedom (rotations & displacements) are set in a **X** vector of N elements such that:

$$-\omega^2\mathbf{M}\mathbf{X}(\omega) + j\omega\mathbf{C}\mathbf{X}(\omega) + \mathbf{K}\mathbf{X}(\omega) = \mathbf{F}(\omega) \tag{1.79}$$

with **M** the mass matrix, **C** the damping matrix, **K** the stiffness matrix, and **F** the excitation vector. This type of matrix system is solved in mechanical FE harmonic solvers.

The particular case without excitation is the free response:

$$\left(\mathbf{M}^{-1}\mathbf{K} - \omega^2\mathbf{I}\right)\mathbf{Q} = 0 \tag{1.80}$$

Considering a mesh with N numerical degrees of freedom, this equation has exactly N solutions $\mathbf{Q}_i$ which are called eigenvectors associated with natural frequencies ω_i and damping ϵ_i. The eigenvectors represents a particular shape of the vibration called mode shape. A modal analysis is the numerical or experimental method used to identify these modal shapes and their corresponding modal frequency.

The modal basis can also be reconstructed by experimental means [Allemang, 1981; Piranda, 2001; Avitabile, 2001]: FRF are measured on various points of the machine as illustrated in Fig. 1.24. Supposing a given number of significant modes, mass and stiffness matrix can be computed as in (1.80) using a fitting algorithm. However, this task can be rather complex on structures integrating electric motors because:

— some modes may have close natural frequencies,

— sometimes with similar modal shapes, and

— some modes may be difficult to excite with a shock hammer.

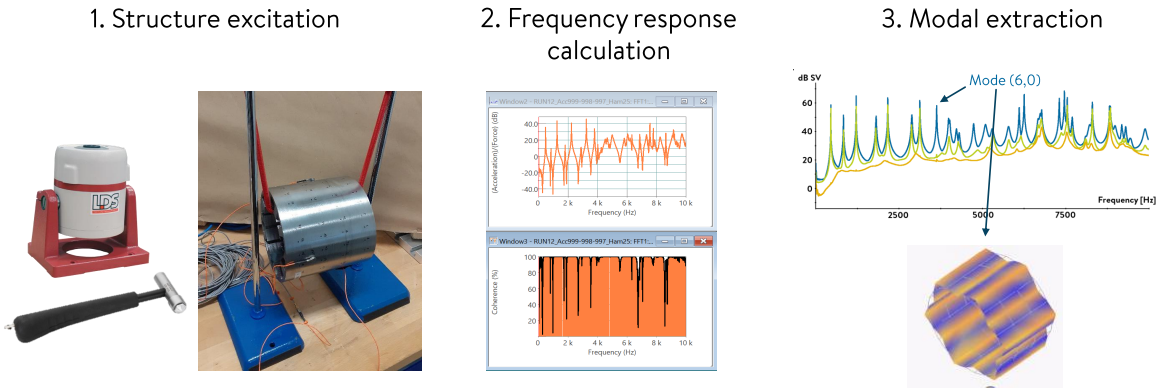

Figure 1.24 – Experimental protocol to get mode shapes and natural frequencies.

Many hypotheses on the mechanical properties are used when building a numerical model: material definition, contacts between pieces ... The common method consists in updating these mechanical properties in order to get natural frequencies comparable with an experimental modal analysis [Mottershead et al., 2011]. This finite element model updating is illustrated in Fig. 1.25.

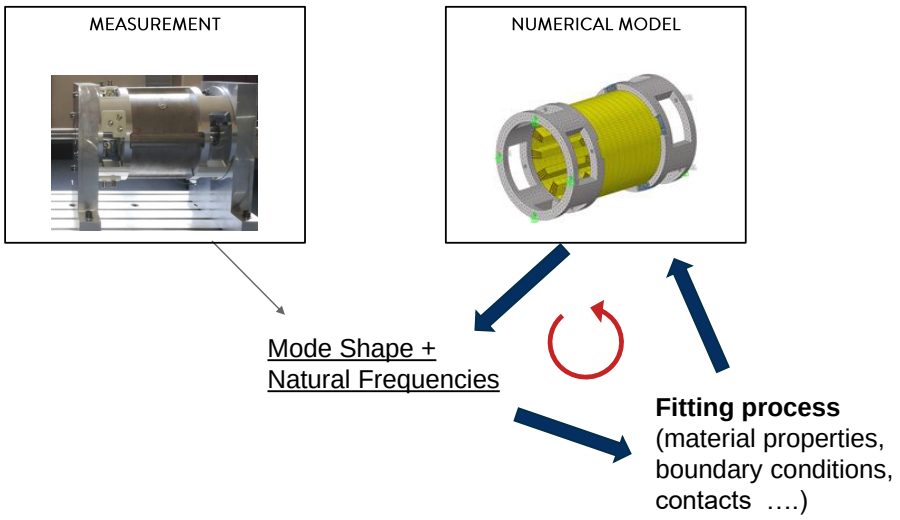

Figure 1.25 – FE model updating process based on experimental data.

1.4.1.4 Modal Superposition

Considering N eigenmodes, an excitation $\mathbf{F}(\omega)$ (in [N]) is applied to selected nodes of the modal basis mesh. The corresponding FRF can be synthesized according to the modal superposition method [MacNeal, 1971; Fiedler et al., 2010; Van der Giet, 2011]:

$$\mathbf{X}(\omega) = \sum_{i=1}^{N} \mathbf{Q}_i \frac{\mathbf{Q}_i \mathbf{F}(\omega)^T}{\omega_i + 2j\omega\epsilon_i\omega_i - \omega^2} \tag{1.81}$$

where the scalar $\mathbf{Q}_i\mathbf{F}(\omega)^T = \mathbf{Q}_i \cdot \mathbf{F}(\omega)$ is called the modal projection factor as it represents the capacity of the excitation to interact with each mode shape.

This method enables to compute FRF. An example is shown in Fig. 1.21. The method is valid under the assumption of mechanical linearity which has already been assumed in this thesis. This method is different from the so-called "direct" solving method, which consist in solving the variational formulation of structural mechanics equations including the external excitation. Indeed, the vibro-acoustic impact of the transient state is neglected with the modal superposition method. Moreover, using resultant force on each tooth might introduce local displacement error (compared to distributed nodal force), but the output of interest is the vibration on a radiating surface generally at a different location. Thus, this modal superposition method is selected to study the force-mode interactions in electrical machines in all mechanical simulations of this thesis work.

1.4.2 Magnetic Force Projection for Air-Gap Surface Force

This section presents the different techniques used for the magneto-mechanical coupling based on the AGSF. In every case, it is considered that the mechanical structure is excited by an AGSF such as (1.46). In this part, it is supposed that the AGSF is computed at a fixed radius $r = R_{ag}$ in the air-gap. The idea is to extrapolate the calculation of the global force (1.43). The next step is to attribute the force which corresponds to the i^{th} tooth at angular position α_i. To that end, several methods exist depending on the mechanical model. The next paragraphs detail the main methods.

1.4.2.1 Force Continuous in Air-Gap

The first method is to apply AGSF directly on the stator's yoke. Indeed, if the analytical frequency is calculated such as (1.77), the radial displacement wavenumbers of the outer yoke can be computed according to (1.81):

$$\mathrm{Y_r}(n,\omega) = \frac{\mathbf{Q}_n \cdot \left(\hat{\mathrm{P}}_\mathrm{r}(\mathrm{R_{ag}}, n, \omega)\mathbf{e}_\mathrm{r}\right)}{\omega_n + 2j\omega\epsilon_n\omega_n - \omega^2}. \tag{1.82}$$

Thus, it is implicitly supposed that a circumferential mode shape (n,0) can only be excited by a radial AGSF of wavenumber n. The numerator can be computed with structural analytical models [Amor et al., 1995; Gieras et al., 2005]. These models are mainly used for root-cause analysis and fast qualitative analysis at early-design stage [Rasmussen et al., 1999; Le Besnerais, 2008] because it is immediately compatible with electromagnetic analytical models.

1.4.2.2 Force Constant on Teeth

Another method is to compute a resultant force per tooth (also called lumped tooth force or simply tooth force). This model can be justified because radial and tangential forces act predominantly at the tip of the tooth and that the tip is so small and stiff that it can be considered to be point forces [Garvey, 1997]. As illustrated in Fig. 1.26, this is achieved by integrating radial and tangential forces $\mathrm{F_r}$ and $\mathrm{F_\theta}$ on a portion γ of the AGSF signal [Boesing, 2013; Saito et al., 2016]:

$$\mathrm{F}_{\mathrm{r},i}(t) = \mathrm{R_{ag}L_s}\int_{\alpha_i-\gamma/2}^{\alpha_i+\gamma/2}\left[\mathrm{P_r}(\mathrm{R_{ag}},\theta)\mathbf{e}_\mathrm{r}(\theta) + \mathrm{P_\theta}(\mathrm{R_{ag}},\theta)\mathbf{e}_\theta(\theta)\right]\cdot\mathbf{e}_\mathrm{r}(\alpha_i)\,\mathrm{d}\theta\,, \tag{1.83}$$

and

$$\mathrm{F}_{\theta,i}(t) = \mathrm{R_{ag}L_s}\int_{\alpha_i-\gamma/2}^{\alpha_i+\gamma/2}\left[\mathrm{P_r}(\mathrm{R_{ag}},\theta)\mathbf{e}_\mathrm{r}(\theta) + \mathrm{P_\theta}(\mathrm{R_{ag}},\theta)\mathbf{e}_\theta(\theta)\right]\cdot\mathbf{e}_\theta(\alpha_i)\,\mathrm{d}\theta\,, \tag{1.84}$$

with $\mathrm{L_s}$ the considered length of the lamination.

The integration path is always centered around each tooth, but two main values can be found in the scientific literature for the angle of integration γ as illustrated in Fig. 1.27:

— The angle γ can be chosen equal to the tooth tip width β in [Weh, 1964; Wang et al., 2020; Liang, 2017] because it matches with the physical location of the magnetic force.

— The angle γ can be chosen equal to the slot pitch $\gamma = \frac{2\pi}{Z_s}$ with Z_s the number of stator teeth. as in [Saito et al., 2016; Boesing, 2013]. The unbalanced magnetic force acting on the stator is accurate since there is no signal leak [Boesing, 2013]. However, the tooth geometry (in particular tooth tip width) is not taken into account by the integration method. Nevertheless, the tooth geometry is linked to the magnetic field spectrum such that it has an indirect effect on the force.

In any case, a Fourier transform in time is applied to (1.83) and (1.84) in order to get a result compatible with (1.81).

A more advanced technique considers independently each wavenumber n independently by assuming the mechanical linearity [Boesing, 2013]. Using (1.49), each AGSF wavenumber can be integrated as an equivalent lumped tooth force:

$$\hat{\mathrm{F}}_{\mathrm{r},i}(n,\omega) = \mathrm{R_{ag}L_s}\int_{\alpha_i-\gamma/2}^{\alpha_i+\gamma/2}\left[\hat{\mathrm{P}}_\mathrm{r}(\mathrm{R_{ag}},n,\omega)\mathbf{e}_\mathrm{r}(\theta) + \hat{\mathrm{P}}_\theta(\mathrm{R_{ag}},n,\omega)\mathbf{e}_\theta(\theta)\right]\cdot\mathbf{e}_\mathrm{r}(\alpha_i)\mathrm{e}^{n\theta}\,\mathrm{d}\theta\,, \tag{1.85}$$

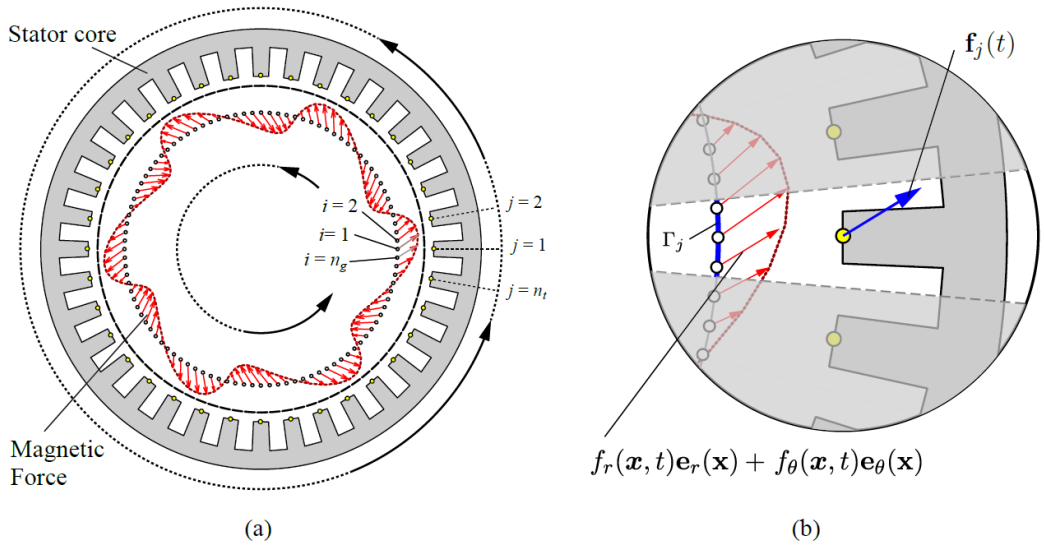

Figure 1.26 – Schematics of magnetic force: (a) AGSF, (b) relationship between AGSF and its resultant tooth force [Saito et al., 2016].

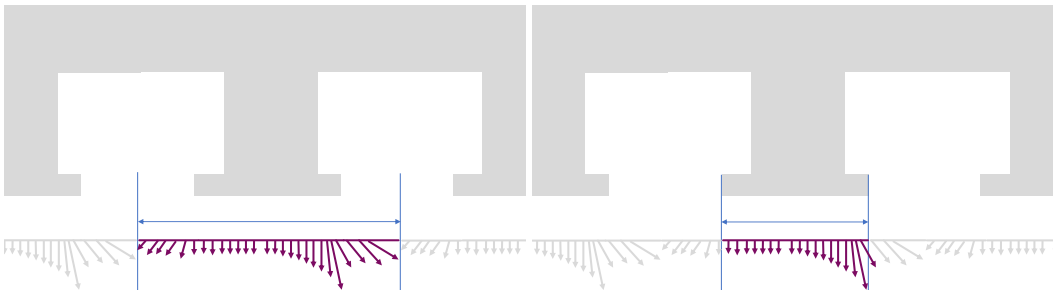

Figure 1.27 – Illustration of the different integration paths for lumped tooth force.

$$\hat{\mathrm{F}}_{\theta,i}(n,\omega) = \mathrm{R_{ag}L_s}\int_{\alpha_i-\gamma/2}^{\alpha_i+\gamma/2}\left[\hat{\mathrm{P}}_\mathrm{r}(\mathrm{R_{ag}},n,\omega)\mathbf{e}_\mathrm{r}(\theta)+\hat{\mathrm{P}}_\theta(\mathrm{R_{ag}},n,\omega)\mathbf{e}_\theta(\theta)\right]\cdot\mathbf{e}_\theta(\alpha_i)\mathrm{e}^{n\theta}\,\mathrm{d}\theta\,. \quad (1.86)$$

It is generally supposed that the deviation from the radial direction at the center of the tooth is small such that

$$\mathbf{e}_\theta(\theta)\cdot\mathbf{e}_\mathrm{r}(\alpha_i)\approx 0\,, \quad (1.87)$$
$$\mathbf{e}_\mathrm{r}(\theta)\cdot\mathbf{e}_\theta(\alpha_i)\approx 0\,, \quad (1.88)$$

It leads to the following result [Weh, 1964; Boesing, 2013; Fang et al., 2019]:

$$\hat{\mathrm{F}}_{r,i}(n,\omega) = \mathrm{R_{ag}L_s}\frac{2}{n}\sin\left(n\frac{\gamma}{2}\right)\hat{\mathrm{P}}_\mathrm{r}(\mathrm{R_{ag}},n,\omega)\mathrm{e}^{jn\alpha_i}\,, \quad (1.89)$$
$$\hat{\mathrm{F}}_{\theta,i}(n,\omega) = \mathrm{R_{ag}L_s}\frac{2}{n}\sin\left(n\frac{\gamma}{2}\right)\hat{\mathrm{P}}_\theta(\mathrm{R_{ag}},n,\omega)\mathrm{e}^{jn\alpha_i}\,, \quad (1.90)$$

which is continuously extended to the case $n = 0$ using a Taylor development of the sinus function. This results is not exactely a Fourier transform. The lumped tooth force is

a punctual load (not a continuous quantity), so the Fourier decomposition cannot be properly defined. Nevertheless, the interpretation for e-NVH troubleshooting can be done exactly as if it was a (fictive) Fourier decomposition because it allows us to make the link between the AGSF wavenumbers and the excitation of the structure.

Next, several FE harmonic simulations are performed for each wavenumber n of interest with all teeth loaded according to (1.89) and (1.90), or with an equivalent surface force which is constant on each tooth tip as illustrated in Fig. 1.28.

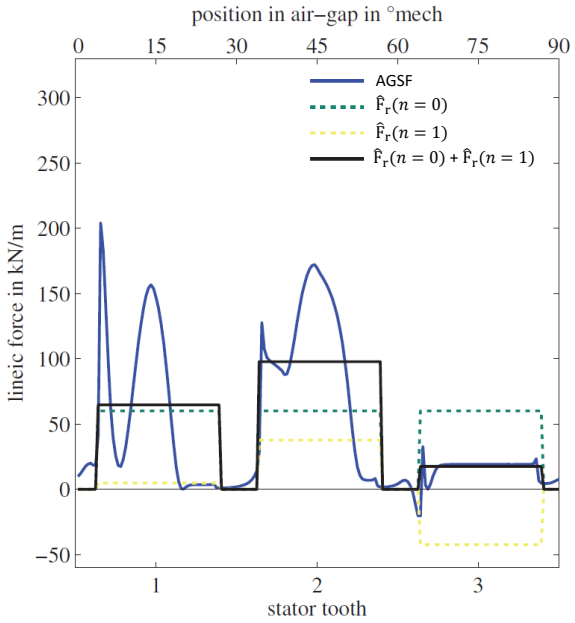

Figure 1.28 – Example of AGSF and its tooth approximation at one point in time [Boesing, 2013].

1.4.2.3 Continuous Tooth Force

The principle of this method is to perform a bijective projection between the air-gap signal and the tooth tip domain. Indeed the AGSF Fourier transform (1.49) and (1.50) are mathematically valid because they are defined on a continuous contour in the air-gap. However, the AGSF only acts close to the tooth surface. One idea is to choose the domain for force decomposition in order to encompass only the piecewise continuous stator tooth surface along the air-gap [Boesing, 2013]. The bijectivity of the transformation keep all the spectrum energy. This surface force spectrum is called tsine and denoted $\hat{P}_r^*(R_{ag}, n, \omega)$. It is obtained by applying for each tooth a door function to the AGSF and shifting the result in front of the corresponding tooth [Boesing, 2013]:

$$\hat{P}_r^*(R_s, n, \omega) = \sum_{i=1}^{Z_s} \left(H_{door,i}(n) \circledast \hat{P}_r(R_{ag}, n, \omega)\right) H_{shift,i}(n)\,. \tag{1.91}$$

After calculations, it leads to the following result:

$$\hat{P}_r^*(R_s, n, \omega) = \sum_m K_{m,n} \hat{P}_r(R_{ag}, m, \omega) \tag{1.92}$$

where $K_{m,n}$ takes different values depending on the relation between n and m. If $\exists k \in \mathbb{Z}$ such that $n = m + k$, then

$$K_{m,n} = 2\frac{\beta}{\alpha} \frac{\sin\left((\beta n - \alpha m)/2\right)}{\beta n - \alpha m} \tag{1.93}$$

and otherwise

$$K_{m,n} = 0\,. \tag{1.94}$$

An illustration of the tsine decomposition is presented in Fig. 1.29. It can be observed that each tsine wavenumber is continuous in the tooth domain of definition.

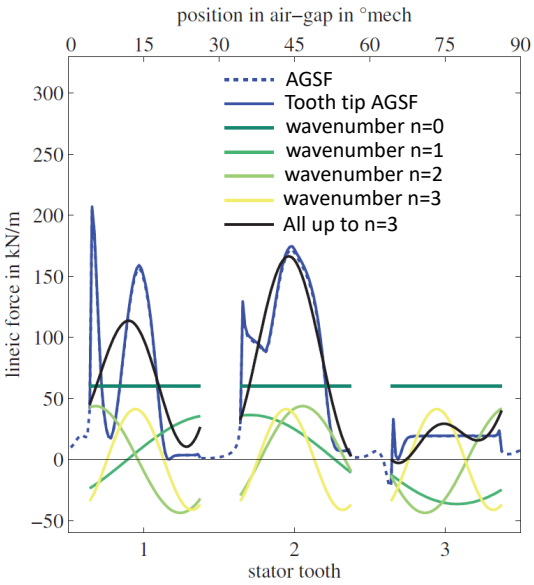

Figure 1.29 – Example of AGSF and its tsine approximation at one point in time [Boesing, 2013].

1.4.2.4 Continuous Yoke Force

The principle of this approach is to define a force which could be equivalently applied on the yoke as illustrated in Fig. 1.30.

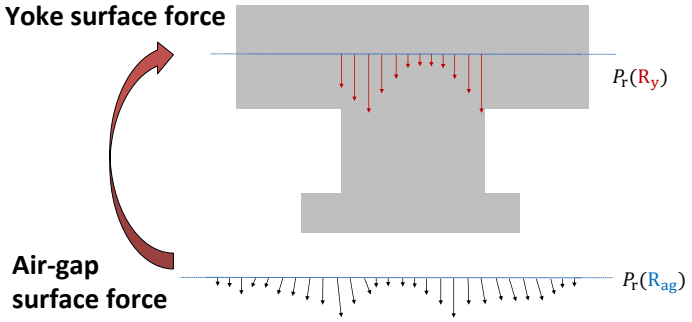

Figure 1.30 – Yoke surface force build from the spectrum of the AGSF.

Thus, this method is even more in accordance with most analytical models. Several attempts to compute this equivalent yoke surface force are presented in [Liang, 2017]. For example:

$$\hat{P}_r^*(R_y, n, \omega) = \sum_m K_{m,n}^* \hat{P}_r(R_{ag}, m, \omega) \tag{1.95}$$

with

$$K_{m,n}^* = \frac{1}{k\pi} \sin\left(\frac{Z_s k\beta}{2}\right) \tag{1.96}$$

if $\exists k \in \mathbb{Z}$ such that $n = m + k$, and otherwise

$$K^*_{m,n} = 0 \tag{1.97}$$

Another issue of the analytical cylindrical models is the contribution of tangential AGSF to the vibration. In fact, tangential force harmonics applied on a cylindrical structure generate radial yoke deflection, which might be emphasized due to tooth bending motion (or tooth rocking) as illustrated in Fig. 1.31, especially in machines with large tooth height to yoke thickness ratio [Garvey, 1997; Roivainen, 2009]. According

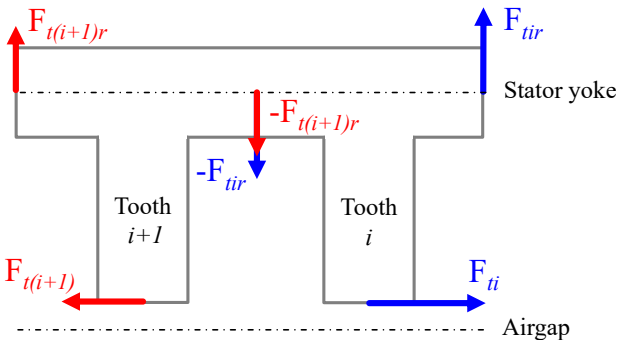

Figure 1.31 – Schematics of magnetic tangential force tooth bending and equivalent yoke radial force [Roivainen, 2009; Devillers, 2018].

to [Roivainen, 2009], this tooth bending effect can be taken into account by building the following equivalent radial yoke surface force spectrum:

$$\hat{P}^*_r(R_y, n, \omega) = -2jZ_s \frac{2H_t + H_y}{4\pi R_s} \sin\left(\frac{n\pi}{Z_s R_s}\right) \hat{P}_\theta(R_{ag}, n, \omega) \tag{1.98}$$

where H_t is the tooth height as defined in Fig. 1.23.

1.4.3 Unit Wave Frequency Response Function

The simulations must be performed on a wide range of frequencies and rotation speeds to perform a complete e-NVH diagnostic of an electrical machine, [Boesing et al., 2010; Le Besnerais et al., 2010; Le Besnerais and Souron, 2016]. To reduce the computation cost of the mechanical simulation, a technique is to inject a normalized amplitude and to weight the results by the operational magnitude of the force.

Indeed, the wave-FRF method considers that the stator is excited with an AGSF such as (1.49) and (1.50) computed from an electromagnetic model. Assuming the mechanical linearity, each wavenumber n can be considered independently. Hence, a harmonic FE mechanical simulation is performed for each wavenumber n of interest and for each direction (radial/tangential) with all teeth loaded with 1 [N] wave amplitude:

$$F_{r,i}(n, \omega) = e^{jn\alpha_i}, \tag{1.99}$$

$$F_{\theta,i}(n, \omega) = e^{jn\alpha_i}. \tag{1.100}$$

The normalized complex displacement on the radiating surface $FRF_r(n, \omega)$ and $FRF_\theta(n, \omega)$ is the output value of interest. An illustration of the obtained displacement is shown in Fig. 1.21. For the cost of one mechanical harmonic FE analysis, the whole speed range N response can be simulated by weighting the result by the amplitude of the corresponding

force wavenumbers [Boesing et al., 2010]. For example, considering the lumped tooth force amplitudes (1.89) and (1.90) :

$$\mathrm{Y_r}(\omega) = \mathrm{R_{ag}L_s}\sum_n \frac{2}{n}\sin\left(n\frac{\gamma}{2}\right)\left(\hat{\mathrm{P}}_\mathrm{r}(\mathrm{R_{ag}},n,\omega)\ \mathrm{FRF_r}(n,\omega)\right), \tag{1.101}$$

$$\mathrm{Y_\theta}(\omega) = \mathrm{R_{ag}L_s}\sum_n \frac{2}{n}\sin\left(n\frac{\gamma}{2}\right)\left(\hat{\mathrm{P}}_\theta(\mathrm{R_{ag}},n,\omega)\ \mathrm{FRF_\theta}(n,\omega)\right). \tag{1.102}$$

1.4.4 Tooth Frequency Response Function

The tooth-FRF considers that only one tooth is loaded per simulation with a normalized load:

$$\mathrm{F}_{\mathrm{r},i}(n,\omega) = \exp^{j\omega}, \tag{1.103}$$

$$\mathrm{F}_{\theta,i}(n,\omega) = \exp^{j\omega}. \tag{1.104}$$

The number of FRF to be performed depends on the symmetries. For example, only one tooth is necessary when considering the cyclical symmetry of the stator alone. In non-simplified system without obvious symmetries (electric motor with the casing, fixations, etc.), all the teeth should be tested.

The tooth-FRF can also be obtained experimentally by impacting a tooth with an impact hammer and measuring external yoke structural response with an accelerometer normalized by the injected force [Saito et al., 2016]. The external yoke complex displacement per tooth $\mathrm{Y}_{i,k}(\omega)$ is the output value of interest, with $i \in [1, \mathrm{Z_s}]$ identifying the tooth number and $k \in [1, \mathrm{K_h}]$ identifying a point on the radiating surface.

This method based on tooth-FRF predicts the vibration, but it is less efficient than the wave-FRF for troubleshooting the main sources of magnetic noise and vibrations (see Section 1.4.8). Indeed, several AGSF wavenumbers can co-exist at the same frequency, and the strategy to reduce the force amplitude often depends on the targeted wavenumber.

1.4.5 Tooth Mechanical Modulation Effect

The concept of tooth mechanical modulation effect - or slot aliasing effect - is the principle that displacement generated by some high wavenumbers wave-FRF is more or less equivalent to a specific lower wavenumbers wave-FRF. The first one to discuss this issue was [Weh, 1964]: the proposed model performs a sampling of the AGSF signal by the teeth. As a consequence, any wavenumber $|n| > \frac{\mathrm{Z_s}}{2}$ is under-sampled such that it is seen by the stator yoke as a lower wavenumber

$$m = n - k\mathrm{Z_s}, \tag{1.105}$$

where $k \in \mathbb{Z}$ such that $|m| \leq \frac{\mathrm{Z_s}}{2}$. This principle is illustrated in Fig. 1.32: the AGSF of wavenumber $n = 10$ in a 12 slots machine could be modelled by a lumped tooth force of apparent wavenumber $n = -2$. Thus, an equivalent modulated magnetic tooth force of wavenumbers m from an AGSF of wavenumbers n is

$$\mathrm{F}_{r,i}(m,\omega) = \mathrm{R_{ag}L_{st1}}\frac{2}{n}\sin\left(n\frac{\gamma}{2}\right)\hat{\mathrm{P}}_\mathrm{r}(\mathrm{R_{ag}},n,\omega)\mathrm{e}^{jm\alpha_i}. \tag{1.106}$$

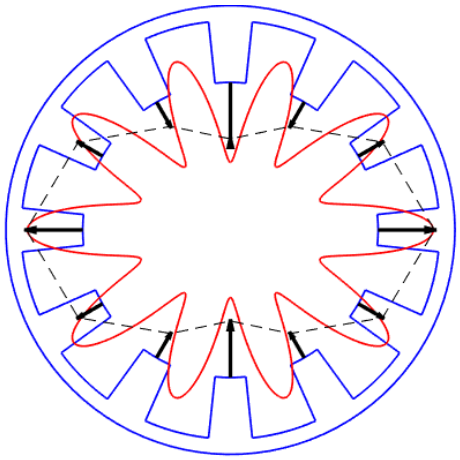

Figure 1.32 – Lumped Tooth force (black) corresponding to radial AGSF wavenumber $n = 10$ (red).

It can be deduced by comparing (1.106) and (1.89) that the displacement caused by an AGSF of wavenumbers n can be deduced from the displacement caused by an AGSF of wavenumbers m:

$$Y_n(\omega) = K_{n,m} Y_m(\omega), \tag{1.107}$$

with $K_{n,m}$ the modulation effect coefficient. For example, [Boesing, 2013; Fang et al., 2019] proposes

$$K_{n,m} = \frac{m}{n} \frac{\sin\left(n\frac{\gamma}{2}\right)}{\sin\left(m\frac{\pi}{Z_s}\right)} \tag{1.108}$$

if $m = n - kZ_s$, and $K_{n,m} = 0$ otherwise.

This proposition enables the reduction of the calculation time for the mechanical simulations: a normalized simulation for the lowest wavenumber can be extrapolated to the other wavenumbers using (1.107). This effect has been experimentally observed recently [Wang et al., 2020; Fang et al., 2019], and different attempts to model the modulation effect are available. In [Liang, 2017], the different attempts to define the yoke equivalent surface force such as (1.95) are used in order to model the modulation effect. If the distribution of forces on tooth tip is taken into account, the AGSF is also cut on a portion β. In conclusion, the key parameter is the angle of integration γ as introduced in Section 1.4.2.2. This issue is discussed in Chapter 3.

1.4.6 Magnetic Force Projection for Nodal Forces

The nodal forces computed with VWP can be summed over the nodes of each tooth in order to get a lumped tooth force with similar application as in Section 1.4.2.2. However the accuracy of the model can be improved as the nodal forces map the load everywhere on the tooth in the magnetic model. The main issue is to adapt this load to be compatible with the mechanical model.

Indeed, the electromagnetic FE analysis mainly is based on triangle mesh in 2D (or tetrahedron in 3D) while the mechanical FE analysis is mainly based on hexahedron (cuboid). Unfortunately, the use of tetrahedron or prismatic elements for mechanical FE analysis significantly increase the computational cost for the same precision [Chandrupatla et al., 2002; Cook et al., 2007]. Moreover, the thinness of the electromagnetic

mesh on the tooth tip is unsuitable for the mechanical simulation and the natural frequency fitting. This is an issue when considering e-NVH optimisation: a high number of mechanical simulations must be performed, and the mechanical numerical model must be accurately fitted (in particular, natural frequencies). Since the magnetic mesh is unsuitable, then it is common to perform a mesh-to-mesh projection using for instance Ritz-Galerkin method [Parent et al., 2008; Journeaux et al., 2013]. The next Sections 1.4.6.1-1.4.6.2 present the different steps to load the mechanical simulation with VWP results using mesh-to-mesh projection.

1.4.6.1 Calculation of Nodal Magnetic Force Density

As seen in Section 1.3.4, the VWP calculations give a nodal resultant force which depends on the vicinity of the mesh [Parent et al., 2008]. This is an important restriction because the mesh used for electromagnetic model is not suitable for mechanical problem solving. Indeed, the electromagnetic mesh compared to the mechanical mesh is generally too thin on the tip of the teeth, and sometimes too coarse on the yoke. The most accurate method to compute the equivalent magnetic force on the mechanical mesh requires two numerical operations: first the magnetic force density must be computed (to have continuous interpolable quantity), then this force density is projected on the mechanical mesh by a mesh-to-mesh projection approach (for example Ritz-Galerkin projection) [Geuzaine et al., 1999; Parent et al., 2008; Journeaux et al., 2013; Wang et al., 2016; Kotter et al., 2017; Kotter, 2019].

The nodal magnetic forces F_s^i calculated with (1.67) cannot be interpolated since it is the amplitude associated with a dirac function defined with respect to the point of application. Considering that this nodal resultant F_s^i comes from a continuous force field f_s defined on a discrete shape function basis ϕ_i such that

$$f_\mathrm{s}(x) = \sum_{k=1}^{\mathrm{N}} \phi_k(x) f_{s,k}\,, \tag{1.109}$$

then the link between F_s^i and f_s is the integration of the force field interpolated by all the shape functions [Parent et al., 2008]:

$$\sum_{k=1}^{\mathrm{N}} f_{s,k} \int_{\mathrm{D_{mag}}} \phi_i \phi_k \, d\tau = \mathrm{F}_s^i\,, \tag{1.110}$$

where $\mathrm{D_{mag}}$ is the domain of definition in the magnetic source mesh, and N the total number of nodes. Considering all the possible combinations of i and k, (1.110) leads to a linear matrix system of size N to be solved:

$$[\mathrm{A}]\,[f_\mathrm{s}] = [\mathrm{F_s}]\,, \tag{1.111}$$

with

$$\mathrm{A}_{i,k} = \int_{\mathrm{D_{mag}}} \phi_i \phi_k \, d\tau\,. \tag{1.112}$$

Note that the choice of the basis ϕ_i is arbitrary. A natural and efficient choice for this basis ϕ_i is to use the electromagnetic FE shape functions [Journeaux et al., 2013; Wang et al., 2016; Kotter et al., 2017].

At this point, the physical dimension $f_{s,k}$ depends on the types of elements which are considered as illustrated in Fig. 1.33. On one hand, $f_{s,k}$ is a surface force density when considering only surface elements in 3D (or edge elements in 2D). On the other hand,

$f_{s,k}$ can be a volume force density considering volume elements in 3D (or facet elements in 2D). The choice depends on the loading condition of the electrical machines: with low magnetic saturation, magnetic forces concentrate at the ferromagnetic-air interface such that the surface force model is more accurate. However, a highly saturated case creates resultant forces from (1.67) inside the volume which can be then converted into volume force density. According to [Curti et al., 2017; Kotter, 2019], the forces inside the ferromagnetic volume have small contribution to the forces and torque as illustrated in Fig. 1.34.

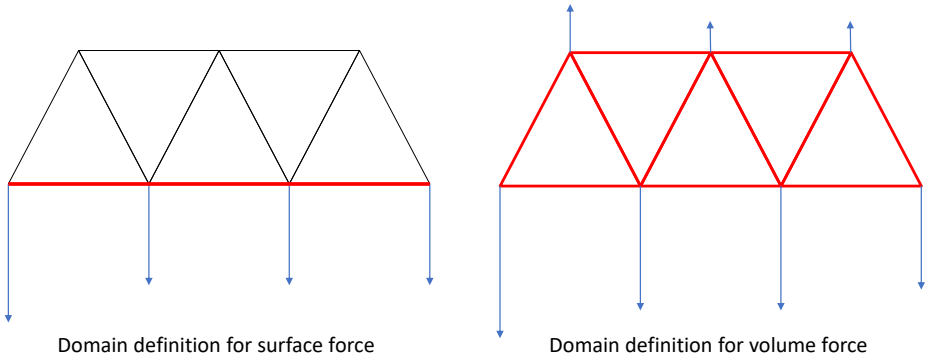

Figure 1.33 – Domain of definition (red) for force density calculation: the same nodal forces would lead to a different result depending on the chosen domain of definition (surface or volume).

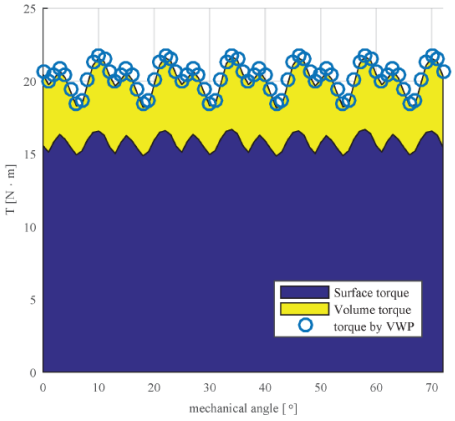

Figure 1.34 – Relative contribution of volume and surface forces to the electromagnetic torque [Curti et al., 2017].

1.4.6.2 Mesh-to-Mesh Projection

The goal of this section is to present the methods to project the discrete magnetic force field $f_{s,k}$ on the mechanical mesh as a new discrete field $\hat{f}_{s,k}$. The criteria for the choice of a method concern precision, conservation of total forces and calculation time.

Most of the mesh-to-mesh projection techniques rely on the Galerkin method because it ensures the uniqueness of the solution. Moreover, the error is orthogonal to the chosen subspace [Bossavit, 1998; Geuzaine et al., 1999; Wang et al., 2016] and this ensures an accuracy that decreases with the size of the target mesh. The Galerkin method gives a new field distribution $\hat{f}_{s,k}$ on the mechanical mesh using a weak-formulation:

$$\langle \psi, \hat{f}_{s,k} \rangle = \langle \psi, f_{s,k} \rangle \,, \tag{1.113}$$

where ψ is a test function that belongs to a Sobolev space, and $\langle \cdot, \cdot \rangle$ a scalar product which corresponds to the same Sobolev space. With this weak-formulation, an error minimization of $\|\hat{f}_s - f_s\|$ is achieved in the sense of the norm defined on the Sobolev space. In this case, the choice of $\mathbf{L}^2$ for the Sobolev space is adapted for the conservation of the total force [Journeaux et al., 2013]:

$$\|\hat{f}_s\|_{\mathbf{L}^2} = \int_{D_{mech}} \hat{f}_s^2 \, d\tau \,. \tag{1.114}$$

Indeed, the integration of nodal forces (1.110) implicitly uses a $\mathbf{L}^2$ scalar product such as

$$\langle \hat{f}_{s,1}, \hat{f}_{s,2} \rangle_{\mathbf{L}^2} = \int_{D_{mech}} \hat{f}_{s,1} \hat{f}_{s,2} \, d\tau \,. \tag{1.115}$$

Moreover, the input for the mechanical simulation is directly the projected force density (not its gradient/divergence/rotational). Therefore, the use of Hilbert spaces instead of $\mathbf{L}^2$ is useless in the context of force projection.

The test function ψ must be chosen wisely in order to avoid ill-conditioned problem. Thus, the Ritz-Galerkin is often preferred [Parent et al., 2008; Journeaux et al., 2013; Wang et al., 2016]: the test function is also the target shape function basis of the mechanical mesh $\psi = \chi_i$.

Then, the previous weak-formulation can be written as another linear matrix system to be solved:

$$[C][\hat{f}] = [f] \,, \tag{1.116}$$

with

$$C_{i,k} = \int_{D_{mech}} \chi_i \chi_k \, d\tau \tag{1.117}$$

and

$$\hat{f}_i = \sum_{k=1}^{N} f_k \int_{D_{mech}} \chi_i \phi_k \, d\tau \,, \tag{1.118}$$

where D_{mech} is the domain of definition in the mechanical target mesh. The matrix [C] is symmetric positive definite matrix so the problem (1.116) has a unique solution.

Depending on the physical properties of the projected quantity, the chosen Sobolev space and test function can be adapted. Another example of the test function ψ is the bi-orthogonal shape function [Wang, 2013]. The bi-orthogonal test function are built according to

$$\int_{D_{mech}} \psi_i \phi_k \, d\tau = \delta_{i,k} \,. \tag{1.119}$$

Thus, the matrix [C] is diagonal and the system (1.116) is analytically invertible. This kind of method is interesting when the size of the system becomes relatively important, with many elements (such as in 3D meshes).

1.4.6.3 Numerical Integration

The calculation of each integral is a recurrent issue for the mesh-to-mesh projection as it often implies non-matching meshes.

The classical methods are using the Gaussian quadrature [Stroud and Secrest, 1966] (or equivalent quadrature) on the mechanical mesh. Thus, the integration of (1.117) is accurate since Gaussian quadrature is exact for polynomials functions. However, the integration of (1.118) is not exact as illustrated in Fig. 1.35: seen by a mechanical mesh

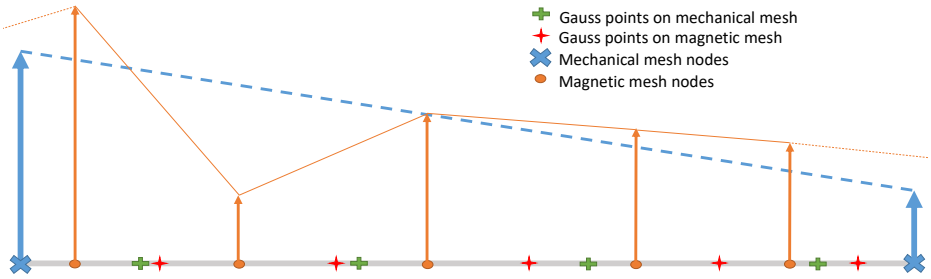

Figure 1.35 – Gauss quadrature between two 1D non-matching meshes.

element, the force density field on the magnetic mesh is $\mathbf{C}^1$ piece-wise such that the Gaussian quadrature is only an approximation.

A first solution relies on the concept of super-mesh [Farrell and Maddison, 2011; Kotter, 2019]: the idea is to build an intersected mesh - called super-mesh - between the source and the target meshes. Every element of this intersected super-mesh are defined inside of the elements of both source and target meshes as illustrated in Fig. 1.36. Then, both target and source shape functions are always polynomials such that the quadrature methods are accurate. The main drawback of this method is the computational cost and algorithm complexity for building and integrating the super-mesh.

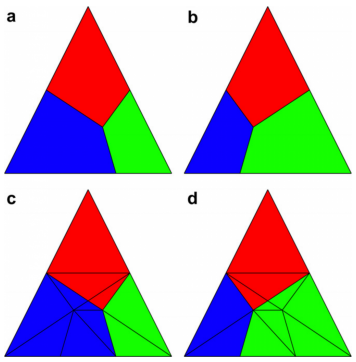

Figure 1.36 – (a) and (b): Input meshes. (c) The super-mesh of (a) and (b), coloured to show the elements of (a). (d): The same super-mesh as (c), coloured to show the elements of (b) [Farrell and Maddison, 2011].

Another solution is to simply increase the number of Gauss points. It allows us to reduce significantly the integration error with a relatively low computational cost [Wang et al., 2016]. Then, (1.118) can be approximated with a "high" N_g number of Gauss points such that:

$$f_i \approx \sum_{k=1}^{N} f_{s,k} \sum_{m=1}^{N_g} \phi_i(x_m)\omega_k(x_m)p_m\,, \tag{1.120}$$

with x_m the Gauss points and p_m Gauss weights. The question that remains is the accuracy required for the projection to avoid exciting modes by purely numerical noise.

1.4.7 Acoustic Noise generation

The acoustic noise generation process is not investigated in this thesis. The present subsection only aims at defining the different quantities used to evaluate the acoustic properties of electrical machines. Acoustic noise results from the travelling of coupled pressure/velocity waves in the air around an observer (person or microphone). Between the entity causing the noise (e.g. the electric motor) and the observer, there is usually not only air but also solid elements that make up the environment (e.g. car interior, chassis, etc.) with various acoustic properties.

Thus, a distinction is made between structure-borne noise and airborne noise as illustrated in Fig. 1.37: the structure-borne noise is transmitted through fixations of the electrical machine while the air-borne noise is directly emitted from the electrical machine surface. Each path taken by the vibration, called transfer path, is modelled by a transfer functions. In any case, the pressure waves originate from the local velocity (or vibration) of air particles in contact with the vibrating structures, which are subject to excitations such as the magnetic forces.

In order to compare the different noise sources, the concept of acoustic intensity is introduced as

$$\mathbf{I} = < p\mathbf{v} >_T , \tag{1.121}$$

where $\mathbf{v}$ is the velocity wave and p the pressure wave, averaged over a wave period T. The acoustic intensity magnitude decreases with distance r from source, as spherical vibration waves decay in $\frac{1}{r}$. In free field - no sound reflections - and far away from the acoustic source, velocity $\mathbf{v}$ and pressure p are proportional and linked to sound speed in the air, noted c_0 and air density ρ_0. Therefore, acoustic intensity is quadratically proportional to pressure or vibration level [Fahy and Gardonio, 2007]:

$$I = |\mathbf{I}| \propto < \rho_0 c_0 |\mathbf{v}|^2 >_T \propto < \frac{p^2}{\rho_0 c_0} >_T . \tag{1.122}$$

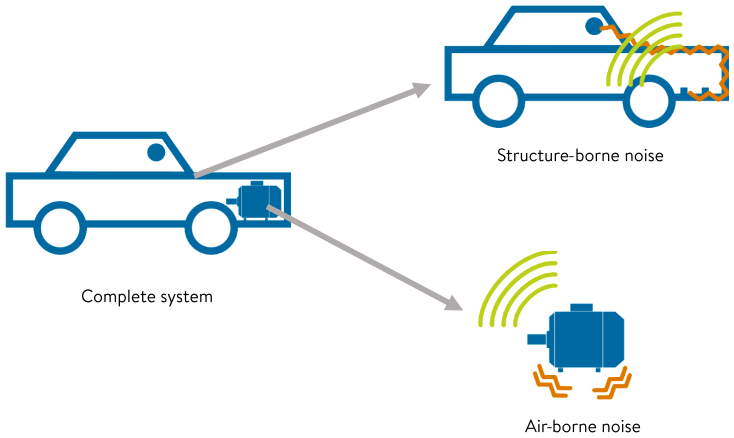

Figure 1.37 – Illustration of transfer path differences between structure borne noise and airborne noise.

From acoustic intensity, noise level is physically represented by two quantities: sound pressure level and sound power level [Yang, 1981]. Such as acoustic intensity, sound pressure level quantifies the sound level perceived at specific position regarding the

acoustic source, and therefore decreases with distance from the source. This is the physical quantity perceived by human ear. Sound pressure level, noted L_p, is expressed in dB as a logarithmic function of the acoustic intensity:

$$L_p = 10\log_{10}\left(\frac{I}{I_0}\right) = 20\log_{10}\left(\frac{p_{RMS}}{p_0}\right), \tag{1.123}$$

where $I_0 = 1.0\times10^{-12}\,W{\cdot}m^{-2}$ is the reference intensity, p_{RMS} is the Root Mean Square (RMS) value of the acoustic pressure wave, and $p_0 = 2.0\times10^{-5}\,Pa$ is the reference pressure [Ellison and Moore, 1968].

Sound power level quantifies the overall sound power level radiated by the acoustic source in the whole space. Sound power level is independent from the position and characterizes the intrinsic noise level of the source. It enables to compare the NVH performances of different electrical machines, regardless of the context [Ennassiri, 2018]. Sound power level, noted L_w, is also expressed in dB as a logarithmic function of the acoustic power:

$$L_w = 10\log_{10}\left(\frac{W}{W_0}\right), \tag{1.124}$$

where W is the acoustic power value, and $W_0 = 1.0\times10^{-12}\,W$ is the reference acoustic power. The acoustic power is obtained by integrating the acoustic intensity on any surface S enclosing the electrical machine [Yang, 1981]:

$$W = \int_S \mathbf{I}.\mathbf{dS}. \tag{1.125}$$

Besides, pressure amplitude is proportional to vibration amplitude. At a given frequency ω, vibration is also proportional to excitations (see Section 1.4.1). Therefore, sound pressure level and sound power level are also logarithmic functions of vibrations and excitations:

$$L_p(\omega) \propto 20\,\log_{10}\left(\frac{v_{RMS}(\omega)}{v_0}\right) \propto 20\log_{10}\left(\frac{F(\omega)}{F_0}\right), \tag{1.126}$$

with v the velocity, v_0 a reference velocity, F the magnetic excitation amplitude, and F_0 a reference magnetic force.

As explained in [Devillers, 2018], the use of logarithmic scale is explained by human audition physiology, which has a logarithmic behavior in magnitude. The physical value of sound pressure level can be corrected to account for human's ear sensitivity limited to [20, 20000] Hz. The most used weighting curve is the A-weighting curve [IEC61672-1, 2013] which is presented in Fig. 1.38. The resulting A-weighting sound pressure level is expressed in dBA. For example, 100 dB at 100 Hz equals to 80 dBA as human's ear damps low frequencies. The maximum ear sensitivity is around 2500 Hz.

In addition, it is worth noting that two similarly noisy machines increase by 3 dB the overall noise level compared to the same machine alone. Indeed, multiplying by two the acoustic power increases by 3 dB the sound power level:

$$10\log_{10}\left(\frac{2W}{W_0}\right) = 10\log_{10}\left(\frac{W}{W_0}\right) + 10\log_{10}(2) \approx 10\log_{10}\left(\frac{W}{W_0}\right) + 3\text{dB}. \tag{1.127}$$

It means that two identical machines have almost the same noise as a single machine for the human ear.

In conclusion, the vibration results from Chapter 3 will be mainly presented using the velocity v, but also acceleration a or displacement u, and analyzed with logarithmic scale to better fit with the perception of human hear. In particular, comparison between two vibration level will be expressed in dB using for example $20\log_{10}(v_{RMS})$.

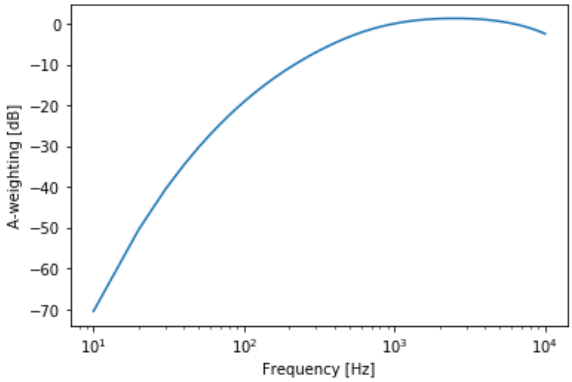

Figure 1.38 – A-weighting curve to account for human's ear sensitivity depending on frequency.

1.4.8 Troubleshooting Methods

The goal of this section is to highlight the interest of AGSF decomposition on Fourier basis to analyse and troubleshoot e-NVH issues.

1.4.8.1 Diagrams for e-NVH Analysis

The harmonic content of the AGSF can be analytically predicted and ranked for most of radial flux topology [Devillers, 2018; Le Besnerais et al., 2010], even considering saturation [Le Besnerais et al., 2009]. It mainly consists in decomposing the magnetic force harmonic from its quadratic relation with magnetic flux density. The magnetic flux density harmonic content is known from analytical methods presented in Section 1.2.4. Thus, the AGSF (1.47) is a function of rotor and stator flux densities:

$$P_r = -\frac{1}{2\mu_0}\left[\left(B_r^R + B_r^S\right)^2 - \left(B_t^R + B_t^S\right)^2\right], \tag{1.128}$$

with $B_{r,t}^R$ the rotor radial/tangential air-gap flux density and $B_{r,t}^S$ the stator radial/tangential air-gap flux density. Then, there are three origins of force harmonics:

— Rotor to Rotor flux harmonics interactions: $B^R B^R$.

— Stator to Rotor flux harmonics interactions: $B^S B^R$.

— Stator to Stator flux harmonics interactions: $B^S B^S$.

However, the main source of e-NVH among these three combinations depends on the machine topology and operational conditions. The main type of electrical machine (Permanent Magnet Synchronous Machine (PMSM), Wound Rotor Synchronous Machine (WRSM), Squirrel Cage Induction Machine (SCIM), Switched Reluctance Machine (SRM), Synchro-Reluctant Machine (SynRM)) and their main contributions are presented in Table 1.1.

It enables qualitative figures such as the Campbell diagram in Fig. 1.39: the main AGSF harmonics are functions of rotation speed and frequency. Each line corresponds to a force harmonics as function of speed and frequency, called order. The excitations in electrical machine are proportional to both mechanical frequency

$$H = \frac{N}{60}, \tag{1.129}$$

Table 1.1 – Contribution of stator and rotor flux densities to magnetic forces in different operating cases and topologies.

	PMSM	WRSM	SCIM	SRM	SynRM
Open-circuit / no load	$B^R B^R$	$B^R B^R$	$B^S B^S$	$B^S B^S$	$B^S B^S$
Full load	$B^R B^R$ $B^S B^R$	$B^R B^R$ $B^S B^R$	$B^S B^S$ $B^R B^S$	$B^S B^S$	$B^S B^S$
Rotor-driven / null stator & rotor current	$B^R B^R$	-	-	-	-

and the electrical frequency

$$f_s = p\frac{\mathrm{N}}{60}, \tag{1.130}$$

with p the pole pair number and N the rotation speed. This property enables to number each line. For example, the left-most order in Fig. 1.39, denoted H8 (or $2f_s$) is proportional to 8 times the mechanical frequency (or 2 times the electrical frequency). Analytical calculation allows us to guess the lowest wavenumber occurring at this order by knowing the number of teeth Z_s, the number of pole pairs p, and the machine type. The interactions of stator and rotor flux harmonics from Table 1.1 can also be added as in Fig. 1.39 to improve the analysis.

Thus, one can identify the risk of a resonance at a given speed for a set of modes and natural frequency. It is interesting to note that the Campbell diagram can be calculated with only the main parameters (notably slot pole combination). Thus, this analysis can be performed at early design stage, but it is also a tool to quickly identify the root-cause of e-NVH. It is a classic tool for e-NVH engineers.

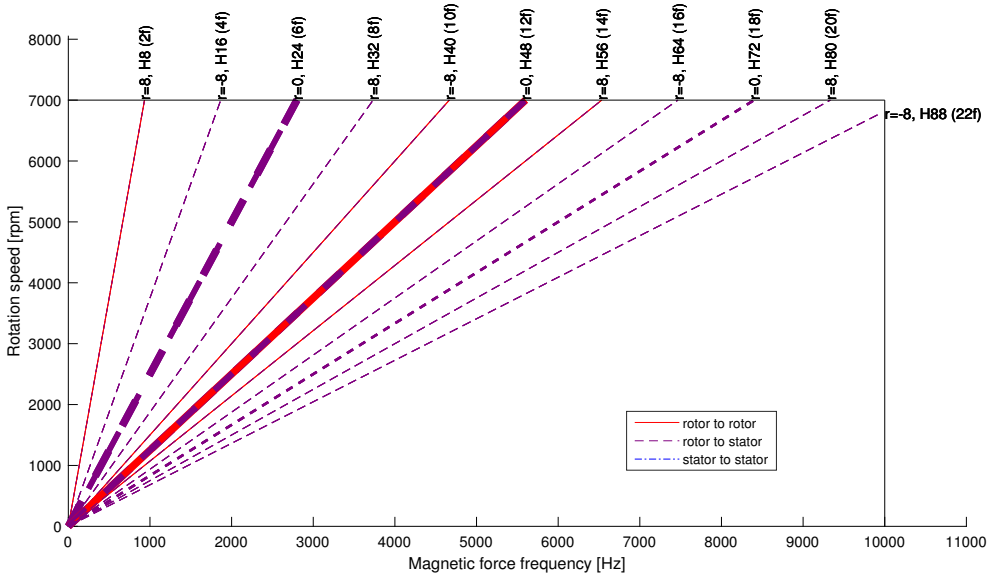

Figure 1.39 – Campbell diagram for a permanent magnet synchronous machine generated with MANATEE [EOMYS ENGINEERING, 2020]. ($Z_s = 48, p = 4$).

In order to go more deeply into details such as the relative amplitude of each order, one can compute a spectrogram as illustrated in Fig. 1.40. It can be applied to vibration, sound pressure level (1.123), etc. The spectrogram enables the identification of critical frequencies and rotation speeds for e-NVH. For example, a resonance is observed

around 6500 rpm with the harmonic at $12 f_s$ in Fig. 1.40. The spectrogram can be generated from both simulations and measurements during a run-up on a given speed range [Boesing et al., 2010; Le Besnerais et al., 2010]. It can also be generated by an hybrid method in which the mechanical FRF is measured and the electromagnetic excitation is simulated [Saito et al., 2016].

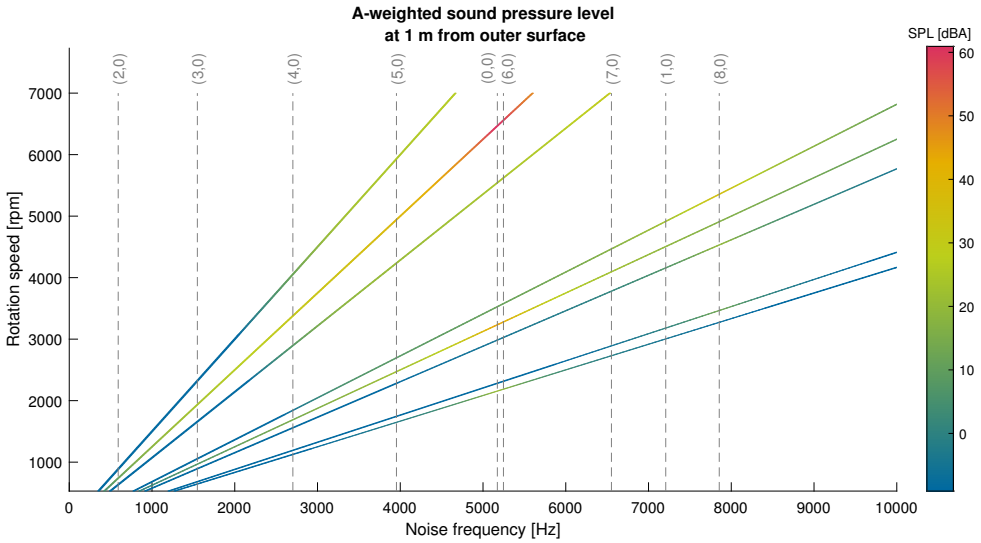

Figure 1.40 – Spectrogram for A-weighted sound pressure level at 1 m from outer surface for PMSM ($Z_s = 48, p = 4$). Mechanical modes are indicated with dashed grey lines. Generated with MANATEE [EOMYS ENGINEERING, 2020].

An even more advanced tool is the notion of spatiogram, as illustrated in Fig. 1.41. The concept is to represent one spectrogram for each excitation wavenumber using wave-FRF. Indeed, overlaying both wavenumbers $r = 0$ and $r = 8$ in Fig. 1.41 would almost lead to the result in Fig. 1.40. It allows us to identify the most problematic wavenumbers. It is particularly useful to discriminate several wavenumbers occurring at the same frequency. However, it is only available from numerical simulation in the literature. Indeed, it is hardly achievable to create a direct sinusoidal excitation on the tip of the teeth with vibrating pot or impact hammers. So, the classical method requires to fit a FE model with experimental modal analysis to get the wave-FRF.

Plotting spectrogram and spatiogram requires to perform an electromagnetic simulation with one of the method presented in Section 1.2 for every frequency and every rotation speed. Then, the vibro-acoustic simulation must be performed as well to get the vibrations and noise. If this can be done in a few seconds with a combination of electromagnetic and mechanical analytical models, the calculation time with full numerical magneto-mechanical coupling can quickly explode. However, accurate solutions are difficult to get without numerical simulations [Devillers, 2018]: fast analytical models are preferred at early-design stage while the FE analysis enables complete design optimization. It points out the need for model reduction when considering advanced e-NVH design of electrical machines.

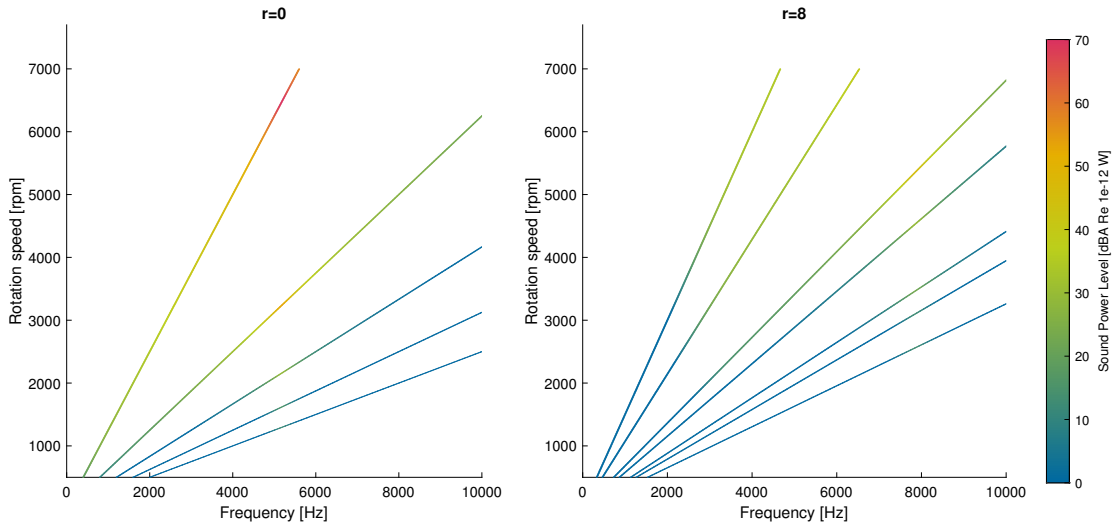

Figure 1.41 – Spatiograms with wavenumbers $r = 0$ and $r = 8$ for A-weighted sound pressure level at 1 m from outer surface for PMSM ($Z_s = 48, p = 4$). Generated with MANATEE [EOMYS ENGINEERING, 2020].

1.4.8.2 Forced Response and Resonance

In e-NVH studies of electrical machines, the distinction is made between two types of noisy magneto-mechanical interactions:

— A forced response: the magnetic force are actively exciting a particular mode, but the amplitude of the excitation is sufficiently high to create audible noise.

— A resonance: the magnetic force is actively interacting with a mode such that the resulting vibrations is significant. It corresponds to the peak-value of displacement as in Fig. 1.21.

Both cases are represented in Fig. 1.42.

In vibroacoustic references based on a structural cylindrical model of the stator structure [Jordan, 1950; Alger, 1953; Timar, 1989; Gieras et al., 2005], the resonance occurs if three conditions are fulfilled for an existing AGSF harmonic:

— The rotating frequency ω is close to the natural frequency of a structural mode.

— The AGSF wavenumber n is equal to the circumferential mode order m. This point can be discussed as some mode shape can be excited by other circumferential wavenumbers [Braunisch et al., 2013; Kotter, 2019] but it gives an idea of the main issues.

— The amplitude of the AGSF must be sufficient to reach significant vibration level.

It can also happen for longitudinal modes excited by non-uniform magnetic forces in the length of the machine. It mainly occurs when the machine is skewed [Piriou and Razek, 1990; Despret et al., 2016]: skewing is generally used to reduce torque pulsation (meaning pulsating tangential force) due to magneto-motive force and slotting harmonics. However, it can also reduce other harmonics of radial AGSF. This kind of reduction techniques are not studied in this thesis.

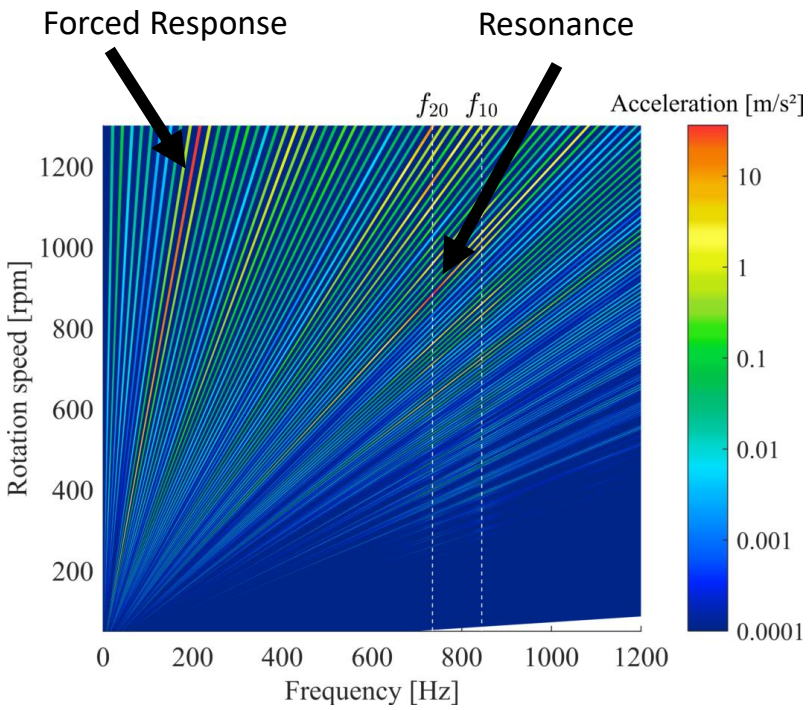

Figure 1.42 – Illustration of forced response and resonance on the spectrogram of 12s10p PMSM [Devillers, 2018].

1.5 Conclusion, Scientific gap and Research Agenda

In the context of e-NVH, the main methods for computing magnetic field, magnetic forces and vibro-acoustic response have been presented. In particular, the relevance of wavenumber decomposition has been highlighted: it allows us to identify the electromagnetic source, and to discriminate forced response from resonance.

Several scientific gaps have been raised:

— Quantifying the uncertainty of AGSF application, especially when the air-gap size and wavenumbers are increased.

— The adequate integration angle to compute lumped tooth force.

— Performing unit-wave FRF based on experimental measurements for the mechanical modelling.

— The risk of introducing purely numerical excitations after mesh-to-mesh projection.

— The application of the tooth modulation effect to reduce the mechanical model.

The Chapter 2 addresses the first issue using analytical calculation and numerical applications. The Chapter 3 addresses the remaining uncertainties using analytical calculation, numerical simulations and experimental measurements.

Chapter 2

Spatial Fourier Analysis of Air-Gap Surface Force

Contents

2.1 Introduction

The main issue discussed in this chapter is the concept of Air-Gap Surface Force (AGSF) transfer, i.e. the variation of the AGSF between the middle air-gap radius and the tooth tip radius. As seen in Section 1.3, the MST method based on a closed surface is historically used to accurately compute the electromagnetic torque and the global forces in electrical machines, and recent developments in the field of electromagnetic vibrations for electrical machines show a preference for estimating magnetic forces based on the MST in the air-gap.

As explained in Section 1.3.3, the AGSF method based on MST consists in computing equivalent magnetic surface forces on a cylindrical shell in the middle of the air-gap, and then projecting the forces on the teeth as explained in Section 1.4.2. The AGSF is based on the assumption that the air-gap is relatively thin in electrical machines, and that the differences between the forces in the middle of the air-gap and the actual forces on the teeth are negligible for e-NVH analysis. Said differently, it is generally supposed that the AGSF is independent of the radius.

This chapter proposes to discuss these assumptions. The variation of AGSF as a function of radius was mainly studied numerically [Hallal et al., 2013]: the radius where the AGSF is computed has an effect on vibration results at high frequency. The analytical calculation of global forces and torque - which corresponds to the integral of the 0^{th} AGSF wavenumber - has been studied in [Meessen et al., 2013; Bjørk et al., 2010]. The analytic study of higher AGSF wavenumbers is one objective of this chapter.

In the following sections, the complexity of the problem is gradually increased. First a slotless machine is studied in Section 2.2; The results are then extended to any slotted topology in Section 2.3. Finally three numerical applications are performed in Section 2.4.

2.2 Analytical Study of a Slot-Less Case

The magnetic field inside an electrical machine is influenced by various sources of spatial harmonics combination. These harmonics result from saturation effect, complex/sharp geometries including slotting effect, space harmonics, magneto-motive force harmonics ... In this study, these artifacts prevent understanding the transfer of AGSF. Thus, a specific case is defined to avoid these artifacts with the following constraints:

— Slotless stator and rotor to avoid sharp geometries and slotting effect;

— Single-wave excitation to avoid interference between difference wavenumbers;

— Analytical solving to avoid meshing and numerical errors.

The case presented in Fig. 2.1 proposes to fulfill all these constraints. The results of this section are published in [Pile et al., 2018b].

2.2.1 Electromagnetic Problem

In order to have only one magnetic wave-number, the magnetic potential z-component A_z is imposed at radius R_{ag} such that

$$A_z(R_{ag},\theta) = \beta_n \sin\left(n\theta + \phi_n\right), \forall \theta \in [0, 2\pi], \text{and } n \in \mathbf{N}^* . \tag{2.1}$$

The external boundary condition is

$$A_z(R_e, \theta) = 0 \tag{2.2}$$

to ensure uniqueness of the solution. Finally, the conservation of normal magnetic flux density and tangential magnetic field comes directly from Maxwell equations and can be expressed with the magnetic potential at the interface between the air (permeability μ_0) and ferromagnetic media (relative permeability μ_r), $\forall \theta \in [0, 2\pi]$:

$$A_z(R_s^-, \theta) = A_z(R_s^+, \theta), \tag{2.3}$$

$$\frac{1}{\mu_0}\frac{\partial A_z}{\partial r}(R_s^-, \theta) = \frac{1}{\mu_r \mu_0}\frac{\partial A_z}{\partial r}(R_s^+, \theta). \tag{2.4}$$

The electromagnetic potential A_z is a solution of the 2D Poisson's equation (1.22). In this case, a solution exists and is unique for the previous system [Landau and Lifshitz, 1975] and it can be solved analytically [Lubin et al., 2010; Bekemans, 2006]. Thus, magnetic potential, magnetic flux density and magnetic field can be analytically computed in the studied domain. In the following, calculation steps are detailed.

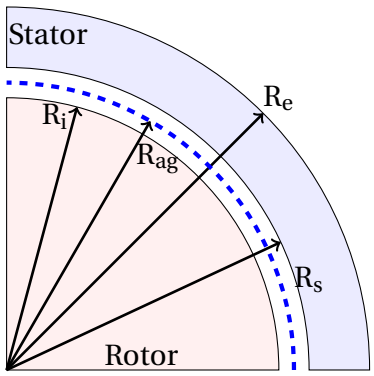

Figure 2.1 – Slotless electrical machine used to compare magnetic pressure on the stator and in the air-gap

Then, a method consists to state a function A_z and to check if it fulfills the boundary conditions. A solution similar to [Lubin et al., 2010] is searched for each part of the machine: the slotless stator, the two half of the airgap and the rotor. For clarity, two polynomial functions are defined $(x, y) \in \mathbb{R}^2$:

$$E_n : (r, R) \rightarrow \left(\frac{r}{R}\right)^n - \left(\frac{R}{r}\right)^n, \tag{2.5}$$

$$F_n : (r, R) \rightarrow \left(\frac{r}{R}\right)^n + \left(\frac{R}{r}\right)^n. \tag{2.6}$$

These polynomial functions have the following useful properties:

$$\begin{aligned} E_n(r,R)E_m(r,R) &= F_{n+m}(r,R) - F_{n-m}(r,R), \\ F_n(r,R)F_m(r,R) &= F_{n+m}(r,R) + F_{n-m}(r,R), \\ F_n(r,R)E_m(r,R) &= E_{n+m}(r,R) - E_{n-m}(r,R). \end{aligned} \tag{2.7}$$

For the upper side of the air-gap, a solution A_z is searched $\forall \theta \in [0, 2\pi]$ and $\forall r \in [R_{ag}, R_s]$ under the form

$$A_z(r, \theta) = \left(\gamma_n \frac{E_n(r, R_s)}{E_n(R_{ag}, R_s)} + \alpha_n \frac{E_n(R_{ag}, r)}{E_n(R_{ag}, R_s)}\right) \sin\left(n\theta + \phi_n\right). \tag{2.8}$$

First, satisfying the boundary condition (2.1) in the air-gap leads to

$$\gamma_n = \beta_n \,. \tag{2.9}$$

In the same way, for the stator ring $\forall \theta \in [0, 2\pi]$ and $\forall r \in [R_s, R_e]$:

$$A_z(r,\theta) = \left(\zeta_n \frac{E_n(r, R_e)}{E_n(R_s, R_e)} + \chi_n \frac{E_n(R_s, r)}{E_n(R_s, R_e)} \right) \sin\left(n\theta + \phi_n\right). \tag{2.10}$$

The second boundary condition (2.2) leads to

$$\chi_n = 0 \,. \tag{2.11}$$

The interface conditions (2.3) can be used to determine α_n and ζ_n:

$$\alpha_n = \zeta_n \,, \tag{2.12}$$

$$\frac{\left(\beta_n \frac{\partial E_n}{\partial r}(r = R_s, R_s) + \alpha_n \frac{\partial E_n}{\partial r}(R_{ag}, r = R_s) \right)}{E_n(R_{ag}, R_s)} = \frac{\zeta_n \frac{\partial E_n}{\partial r}(r = R_s, R_y)}{\mu_r E_n(R_s, R_y)} \,. \tag{2.13}$$

The partial derivatives of the polynomial E can be expressed the following way:

$$\frac{\partial E_n(r, R)}{\partial r} = \frac{n}{r} F_n(r, R) \,, \tag{2.14}$$

$$\frac{\partial E_n(R, r)}{\partial r} = -\frac{n}{r} F_n(r, R) \,. \tag{2.15}$$

Then, (2.13) leads to

$$\alpha_n = \frac{2\beta_n}{F_n(R_a, R_s) + \frac{F_n(R_s, R_e) E_n(R_a, R_s)}{\mu_r E_n(R_s, R_e)}} \,. \tag{2.16}$$

For the other half of the air-gap, a solution A_z is searched under the form $\forall \theta \in [0, 2\pi]$ and $\forall r \in [R_i, R_{ag}]$:

$$A_z(r,\theta) = \left(\kappa_n \frac{E_n(r, R_i)}{E_n(R_{ag}, R_i)} + \tau_n \frac{E_n(R_{ag}, r)}{E_n(R_{ag}, R_i)} \right) \sin\left(n\theta + \phi_n\right). \tag{2.17}$$

Satisfying the continuity equations in the middle of the air-gap leads to:

$$\kappa_n = \beta_n \,, \tag{2.18}$$

$$\tau_n = \alpha_n \,. \tag{2.19}$$

At this point there are no unknowns left. The rotor is seen as a "blackbox" excitation generating a sine potential wave in the air-gap. It could be generated by an adapted cylindrical magnet, or by an equivalent current sheet [Lubin et al., 2010]. In the following, the "current sheet" solution is presented. A current sheet $\mathbf{J}(\theta) = J_n \sin(n\theta)\mathbf{e}_z$ is located at radius R_i. Then, a solution A_z is searched $\forall \theta \in [0, 2\pi]$, $\forall r \in [0, R_i]$ under the form

$$A_z(r,\theta) = D_n r^n \sin\left(n\theta + \phi_n\right). \tag{2.20}$$

The potential continuity gives

$$D_n R_i^n = \tau_n = \alpha_n \,. \tag{2.21}$$

Under this form, the vector A_z is satisfying (1.19) everywhere and all the boundary conditions. By unicity of the solution to (1.19), $A(r,\theta)$ must be the unique solution of the electromagnetic problem. Then, the magnetic flux density is derived with

$$\mathbf{B} = \mathbf{curl}(\mathbf{A}) = \frac{1}{r}\frac{\partial A_z}{\partial \theta}\mathbf{e_r} - \frac{\partial A_z}{\partial r}\mathbf{e}_\theta = B_r\mathbf{e_r} + B_\theta\mathbf{e}_\theta\,. \tag{2.22}$$

Thus, radial and tangential components of the magnetic flux density can be analytically expressed. For example, the analytical flux in the air-gap is:

$$B_r(r,\theta) = \frac{n}{r}\left(\beta_n\frac{E_n(r,R_s)}{E_n(R_{ag},R_s)} + \alpha_n\frac{E_n(R_{ag},r)}{E_n(R_{ag},R_s)}\right)\cos\big(n\theta+\phi_n\big)\,, \tag{2.23}$$

$$B_\theta(r,\theta) = -\frac{n}{r}\left(\beta_n\frac{F_n(r,R_s)}{E_n(R_{ag},R_s)} - \alpha_n\frac{F_n(R_{ag},r)}{E_n(R_{ag},R_s)}\right)\sin\big(n\theta+\phi_n\big)\,. \tag{2.24}$$

Note that considering infinite permeability in the ferromagnetic media leads to

$$\alpha_n = \frac{2\beta_n}{F_n(R_a,R_s)} \tag{2.25}$$

such that the solution in the air-gap becomes independent of the stator's thickness:

$$B_r(r,\theta) = \frac{n}{r}\beta_n\left(\frac{E_n(r,R_s)}{E_n(R_{ag},R_s)} + \frac{2}{F_n(R_a,R_s)}\frac{E_n(R_{ag},r)}{E_n(R_{ag},R_s)}\right)\cos\big(n\theta+\phi_n\big)\,, \tag{2.26}$$

$$B_\theta(r,\theta) = -\frac{n}{r}\beta_n\left(\frac{F_n(r,R_s)}{E_n(R_{ag},R_s)} - \frac{2}{F_n(R_a,R_s)}\frac{F_n(R_{ag},r)}{E_n(R_{ag},R_s)}\right)\sin\big(n\theta+\phi_n\big)\,. \tag{2.27}$$

H_r or H_θ are obtained with the closure relation $\mathbf{H} = \mathbf{B}/\mu$. The analytical magnetic flux (2.26) is compared to the numerical result computed with FE analysis in the middle of the airgap ($R_{ag} = 42.5\,\text{mm}$) and close to the stator bore radius $R_s = 44.95\,\text{mm}$ in Fig. 2.2 when the magnetic potential is injected on the rotor bore radius R_i. The error is plotted as function of radius in Fig. 2.3. As discussed in Section 1.3.3, the tangential flux is locally less accurate close to the stator bore radius with FE method because the weak formulation cannot impose both B_r and H_t continuity. Thus a sudden change of permeability is source of numerical errors [Ren, 1994; Li and Lowther, 2009].

The behaviour of the magnetic field is linear. It means the electromagnetic solution for a multi-harmonic excitation is the sum of the previous solution for different values of n, which are independent from each other. Nevertheless, the magnetic force is proportional to the square of the flux such that it does not conserve the electromagnetic linearity. In order to better understand the behaviour of the AGSF in these conditions, a single magnetic wave solution is first studied in the next section before increasing the complexity with several magnetic wavenumbers.

2.2.2 Surface Force Transfer with Single Magnetic Wave

A function of the radius and the angle is defined from the radial AGSF based on MST (1.46):

$$P : \begin{cases} [R_{ag},R_s]\times[0,2\pi] & \rightarrow & \mathbb{R}^+ \\ (r,\theta) & \rightarrow & \frac{1}{2\mu_0}\left(B_r^2(r,\theta) - B_\theta^2(r,\theta)\right) \end{cases} \tag{2.28}$$

As previously discussed, the magnetic force computed with this function is only valid when $r = R_s$. However the comparison is not straightforward because it depends on

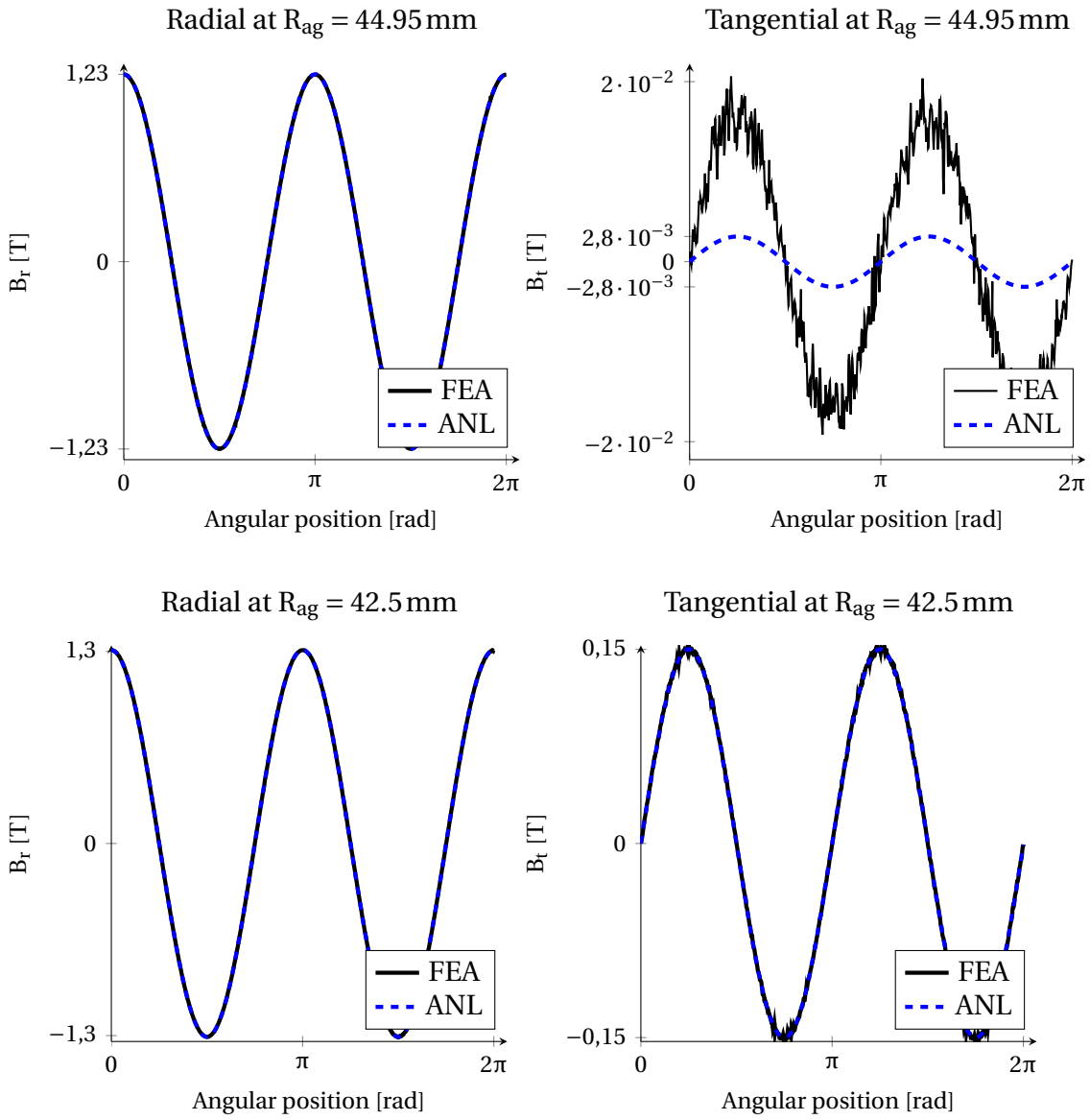

Figure 2.2 – Comparison between analytical (ANL) and numerical (FEA) computation of the magnetic flux density B for the wavenumber $n = 2$ and $\beta_n = 0.0283$ injected at R_i.

the angle. In order to better understand the AGSF transfer, a Fourier decomposition is performed. Since only one magnetic excitation wavenumber n is imposed from (2.1), it leads to

$$P(r,\theta) = P_0(r) + P_{2n}(r)\cos\big(2n\theta + 2\phi_n\big). \tag{2.29}$$

The amplitude of magnetic flux is introduced as

$$B_r(r,\theta) = B_{r,n}(r)\cos\big(n\theta + \phi_n\big), \tag{2.30}$$

$$B_\theta(r,\theta) = B_{\theta,n}(r)\sin\big(n\theta + \phi_n\big). \tag{2.31}$$

Then, the AGSF can be decomposed under the form

$$P(r,\theta) = \frac{B_{r,n}^2(r) - B_{\theta,n}^2(r)}{4\mu_0} + \frac{B_{r,n}^2(r) + B_{\theta,n}^2(r)}{4\mu_0}\cos\big(2n\theta + 2\phi_n\big). \tag{2.32}$$

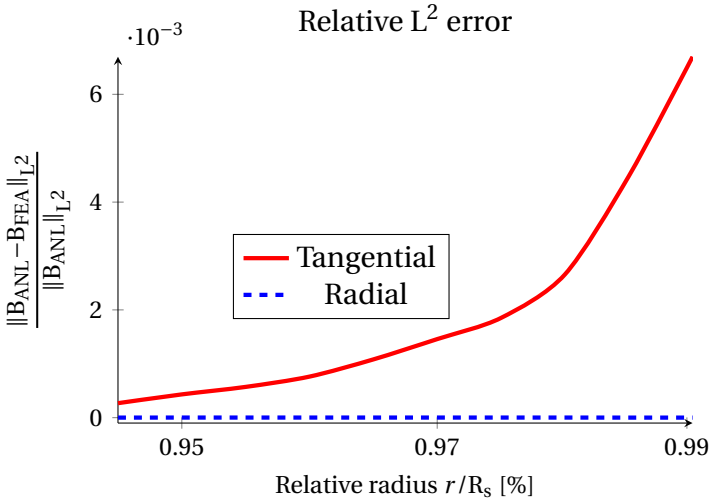

Figure 2.3 – Comparison between analytical (ANL) and numerical (FEA) computation of the magnetic flux density components B_r and B_t depending on the radius with a slotless machine for a wavenumber $k = 2$.

This is a classical result: a magnetic wavenumber n in the air-gap is recomposed into AGSF wavenumbers 0 and $2n$. In order to avoid θ dependency, the amplitude of each harmonic is compared independently such that two ratio can be defined:

$$R_0 = \frac{B_{r,n}^2(R_{ag}) - B_{\theta,n}^2(R_{ag})}{B_{r,n}^2(R_s) - B_{\theta,n}^2(R_s)}, \tag{2.33}$$

$$R_{2n} = \frac{B_{r,n}^2(R_{ag}) + B_{\theta,n}^2(R_{ag})}{B_{r,n}^2(R_s) + B_{\theta,n}^2(R_s)}. \tag{2.34}$$

It can be noted that $B_{\theta,n}(R_s) = 0$ in this configuration since an infinite permeability is assumed for the stator. These functions allow us to rewrite the AGSF as

$$P(R_{ag},\theta) = R_0 P_0(R_s) + R_{2n} P_{2n}(R_s)\cos\left(2n\theta + \phi_n\right). \tag{2.35}$$

If the AGSF is equivalent to its theoretical application on the stator (slotless) surface, then both R_0 and R_{2n} should be almost equal to 1. The next step is to introduce the analytic solution of the magnetic flux (2.23) into (2.33) in order to get the analytic expression of each function R_0 and R_{2n}. The definition (2.33) can be developed using (2.26):

$$R_0 = \frac{R_s^2}{R_{ag}^2}\left(\frac{E_n(R_{ag},R_s)^2 - \left(F_n(R_{ag},R_s) - \frac{4}{F_n(R_{ag},R_s)}\right)^2}{\left(\frac{2E_n(R_{ag},R_s)}{F_n(R_{ag},R_s)}\right)^2}\right). \tag{2.36}$$

For more readability, the following notations are used:

$$\begin{aligned} E_n &= E_n(R_{ag},R_s), \\ F_n &= F_n(R_{ag},R_s). \end{aligned} \tag{2.37}$$

Using the properties (2.7):

$$\begin{aligned}\frac{R_{ag}^2}{R_s^2}R_0 &= \frac{E_n^2F_n^2-\left(F_n^2-4\right)^2}{(2E_n)^2}\\ &= \frac{(F_{2n}-2)(F_{2n}+2)-(F_{2n}-2)^2}{4(F_{2n}-2)}\\ &= \frac{F_{2n}^2+2F_{2n}-2F_{2n}-4-F_{2n}^2+4F_{2n}-4}{4(F_{2n}-2)}\\ &= \frac{4F_{2n}-8}{4(F_{2n}-2)}\\ &= 1\,.\end{aligned} \tag{2.38}$$

The same method is applied for R_{2n} from the definition (2.33) using (2.26), (2.7) and (2.37):

$$\begin{aligned}\frac{R_{ag}^2}{R_s^2}R_{2n} &= \frac{(F_{2n}-2)(F_{2n}+2)+(F_{2n}-2)^2}{4(F_{2n}-2)}\\ &= \frac{F_{2n}^2+2F_{2n}-2F_{2n}-4+F_{2n}^2-4F_{2n}+4}{4(F_{2n}-2)}\\ &= 2F_{2n}\frac{F_{2n}-2}{4(F_{2n}-2)}\\ &= \frac{F_{2n}}{2}\,.\end{aligned} \tag{2.39}$$

Finally, the relation between the AGSF at position $r = R_{ag}$ and the theoretic surface force at position $r = R_s$ can be established:

$$P(R_{ag},\theta) = \frac{R_s^2}{R_{ag}^2}\left(P_0(R_s)+P_{2n}(R_s)\frac{F_{2n}}{2}\cos\left(2n\theta+2\phi_n\right)\right). \tag{2.40}$$

The differences between theoretical surface force and air-gap surface force depend on the geometry, the radius of application and the wavenumber. It is worth mentioning that it does not depend on θ or β. Fig. 2.4 shows how these coefficients can affect magnetic surface force harmonics depending on the radius of calculation. The effect of the

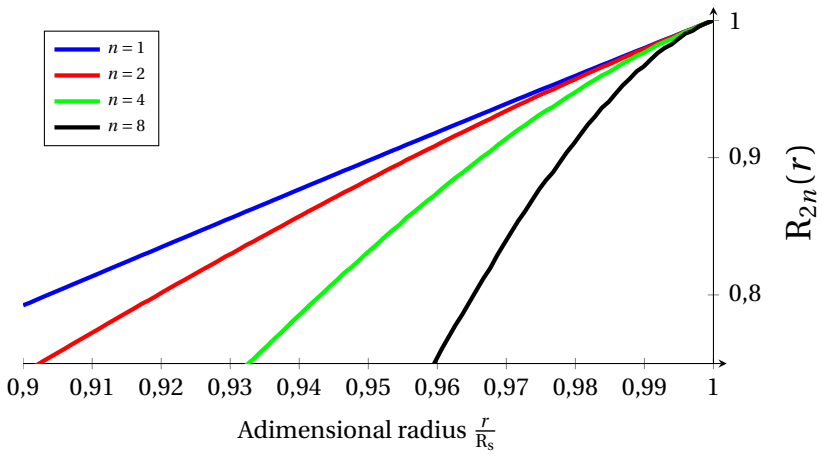

Figure 2.4 – Comparing stator and air-gap surface force for the harmonic $2n$

transfer from the airgap to the stator bore radius for the AGSF is not negligible even when

considering a single magnetic wavenumber. In this case, the analytic magnetic surface force can be computed from the AGSF by inverting the formula (2.40):

$$P(R_s,\theta) = \frac{R_{ag}^2}{R_s^2}\left(P_0(R_{ag}) + P_{2n}(R_{ag})\frac{2}{F_{2n}}\cos\left(2n\theta+\phi_n\right)\right) \tag{2.41}$$

2.2.3 Surface Force Transfer in Multi-Harmonic Case

2.2.3.1 Analytical Multi-Harmonic Magnetic Flux Density

The result (2.26) is generalizable to a multi-wavenumber magnetic problem thanks to the linear property of the Poisson Equation [Green, 1828; Landau and Lifshitz, 1975]: a linear combination of solutions of the form (2.26) for different values of n is still a solution of (1.20). Using the complex notation

$$\underline{B_{r,k}} = B_{r,k}e^{j\phi_{r,k}}, \tag{2.42}$$

$$\underline{B_{\theta,k}} = B_{\theta,k}e^{j\phi_{\theta,k}}, \tag{2.43}$$

the magnetic flux on the stator bore radius can be decomposed as complex Fourier series:

$$B_r(R_s,\theta) = \sum_{k=-\infty}^{k=+\infty} \underline{B_{r,k}}e^{jk\theta} \tag{2.44}$$

Note that the time variation is included in the phase $\phi_{\theta,k}$ and that the tangential flux is null on the stator bore radius. Then the magnetic flux in the airgap can be expressed with (2.26) and the notations (2.37):

$$B_r(R_{ag},\theta) = \frac{R_{ag}}{R_s}\sum_{k=-\infty}^{k=+\infty}\frac{1}{2}F_k\underline{B_{r,k}}e^{jk\theta} \tag{2.45}$$

$$B_\theta(R_{ag},\theta) = \frac{R_{ag}}{R_s}\sum_{k=-\infty}^{k=+\infty}j\frac{1}{2}E_k\underline{B_{r,k}}e^{jk\theta} \tag{2.46}$$

2.2.3.2 Magnetic Force Transfer in the Airgap

The multi-harmonic case is much more complex to solve. Indeed, for a duo of magnetic wavenumbers (m,n), a magnetic force of wavenumbers (m-n,m+n) exists, and this applies to all possible harmonic duos. In order to properly solve the problem, the convolution product $\circledast$ is required. It allows us to develop the complex Fourier transform of P_r:

$$\hat{P}_r(R_{ag},n) = -\frac{\left[\hat{B}_r \circledast \hat{B}_r\right](R_{ag},n) - \left[\hat{B}_\theta \circledast \hat{B}_\theta\right](R_{ag},n)}{2\mu_0} \tag{2.47}$$

where $\hat{B}_r$ and $\hat{B}_\theta$ are the complex Fourier transform of B_r and B_θ. Using properties of convolution product, $\hat{P}_r$ is written as

$$\hat{P}_r(R_{ag},n) = -\left(\frac{R_{ag}}{R_s}\right)^2\frac{1}{8\mu_0}\sum_{k=-\infty}^{k=+\infty}P_{r,k,n}\,e^{jn\theta} \tag{2.48}$$

where $P_{r,k,n}$ is expressed using (2.45):

$$P_{r,k,n} = (F_kF_{n-k} + E_kE_{n-k})\,\underline{B_{r,k}}\,\underline{B_{r,n-k}}. \tag{2.49}$$

Using polynomials properties of F_k and E_k, it can be shown:

$$F_kF_{n-k} + E_kE_{n-k} = 2F_n \tag{2.50}$$

Table 2.1 – Injected magnetic potential spectrum for the validation case with $R_{ag} = 42.5\,mm$ and $R_s = 45.0\,mm$.

Wavenumber k	5	7	15	17	19
Amplitude β [T.m]	5.2615	0.6861	0.2119	0.2725	0.1926
Phase ϕ [rad]	3.8893	0.7100	0.4700	0.6849	0.5410

such that the dependency on magnetic flux wavenumbers recombination vanishes:

$$\hat{P}_r(R_{ag}, n) = -\left(\frac{R_{ag}}{R_s}\right)^2 \frac{F_n}{2} \frac{1}{2\mu_0} \sum_{k=-\infty}^{k=+\infty} \underline{B_{r,k}}\, \underline{B_{r,n-k}}\, e^{jn\theta}. \tag{2.51}$$

The convolution product of the magnetic flux on the stator bore radius can be identified:

$$\hat{P}_r(R_{ag}, n) = -\left(\frac{R_{ag}}{R_s}\right)^2 \frac{F_n}{2} \frac{\left[\hat{B}_r \circledast \hat{B}_r\right](R_s, n)}{2\mu_0} \tag{2.52}$$

which leads to the final result

$$\hat{P}_r(R_{ag}, n) = R_n \hat{P}_r(R_s, n) \tag{2.53}$$

with the transfer coefficient

$$R_n = \left(\frac{R_{ag}}{R_s}\right)^2 \frac{F_n}{2}. \tag{2.54}$$

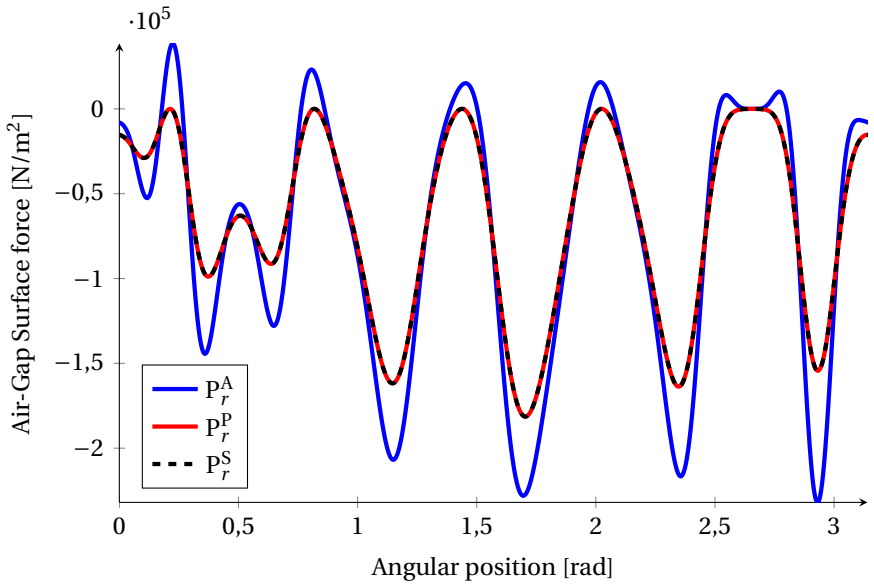

Figure 2.5 – Comparison of several methods for surface force density using Maxwell Tensor

2.2.3.3 Validation

The result (2.53) has an important physical meaning: the transfer of the AGSF does not depend on the nature of the electromagnetic excitation or the magnetic spectrum recombination, but only on the AGSF spectrum.

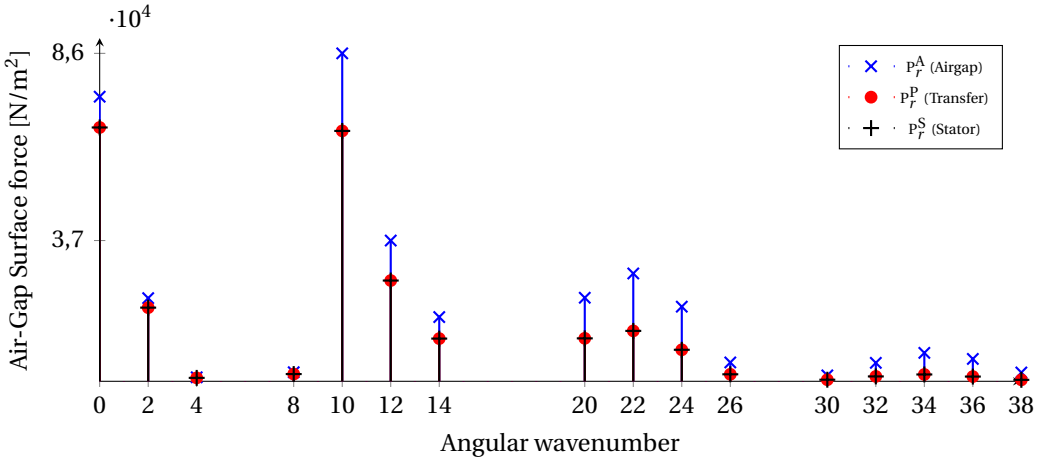

Figure 2.6 – Comparison of several methods for Fourier transform of surface force density using Maxwell Tensor

As in the single magnetic wave case, the analytic magnetic surface force wavenumbers can be computed from the AGSF with the formula (2.53) for any n. The effect of the transfer coefficients (2.54) is studied for the same slotless case in Fig. 2.1. Thus, the magnetic flux is entirely solved analytically using a linear combination of (2.26). The numerical inputs of this validation case are presented in Table 2.1. The results are shown in Figs. 2.5-2.6: $\mathrm{P_r^A}$ denotes the application of (1.47) at $r = \mathrm{R_{ag}}$, $\mathrm{P_r^T}$ denotes the application of the transfer based on the knowledge of $\mathrm{P_r^A}$:

$$\hat{\mathrm{P}}_\mathrm{r}(\mathrm{R_s}, n) = \frac{\hat{\mathrm{P}}_\mathrm{r}(\mathrm{R_{ag}}, n)}{\mathrm{R}_n} \tag{2.55}$$

and $\mathrm{P_r^S}$ denotes the exact value of magnetic surface force density obtained with (1.47) at $r = \mathrm{R_s}$. Comparing the L^2-norm of the two signals with respect to the stator surface forces:

$$\|\mathrm{P_r^T} - \mathrm{P_r^S}\|_{\mathrm{L}^2} \approx 10^{-5} \|\mathrm{P_r^A} - \mathrm{P_r^S}\|_{\mathrm{L}^2} \tag{2.56}$$

Thus, there is an excellent match between the analytical transfer $\mathrm{P_r^P}$ and the numerical reference $\mathrm{P_r^S}$. This last result enables the partial use of these coefficients for slotted electrical machine: all the previous results hold when the angular domain is restricted. Thus supposing the previous reasoning is applied on the angular opening of an electrical machine stator's tooth - with infinite ferromagnetic permeability - then the transfer method (2.55) can be applied on this restricted angular opening. Nevertheless, the transfer of the AGSF in front of the slotted area might not be properly predicted by these coefficients. It motivates the generalization proposed in the next section.

2.3 Generalization to Slotted Machines

The aim of this section is to generalize the previous transfer law (2.55) to slotted electrical machines. The results of this section are published in [Pile et al., 2020c].

2.3.1 Magnetic field in the air-gap

It is supposed that the magnetic flux density is computed on a circular contour in the air-gap such as the blue contour Γ in Fig. 1.9. The domain required for the problem is reduced to the cylindrical air-gap band. At first, a single magnetic flux density wave of order k is considered as the boundary condition in the air-gap at the radius $r = R_{ag}$:

$$\begin{aligned} B_r(R_{ag},\theta) &= B_{r,k}\cos\left(k\theta+\phi_{r,k}\right), \\ B_\theta(R_{ag},\theta) &= B_{\theta,k}\cos\left(k\theta+\phi_{\theta,k}\right). \end{aligned} \tag{2.57}$$

It is equivalent to say that an ideal excitation is considered. It can be produced by any kind of component (windings, permanent magnets ...) but it has no importance for the following. Note that the radius R_{ag} is arbitrarily chosen in the domain of definition.

In these conditions, the fundamental equation for the electromagnetic field is the Poisson's equation (1.22) for the 2D magnetic vector potential component A_z in polar coordinates $\forall\theta\in[0,2\pi]$, $\forall r\in[R_{ag},R_s]$. A solution exists and is unique for the previous system [Landau and Lifshitz, 1975]. Then, a function A_z which fulfils the boundary conditions is sought as in Section 2.2 for the upper cylindrical air-gap band $\forall\theta\in[0,2\pi]$ and $\forall r\in[R_{ag},R_s]$:

$$A(r,\theta) = \frac{\gamma_k E_k(r,R_s)+\alpha_k E_k(R_{ag},r)}{E_k(R_{ag},R_s)}\sin\left(k\theta+\phi_{r,k}\right) + \frac{\zeta_k E_k(r,R_s)+\chi_k E_k(R_{ag},r)}{E_k(R_{ag},R_s)}\cos\left(k\theta+\phi_{\theta,k}\right) \tag{2.58}$$

where the unknowns γ_k, α_k, ζ_k and χ_k depend on the geometry, the wavenumber and the boundary conditions. The next step is to link the magnetic flux density with the magnetic potential:

$$B_r(r,\theta) = \frac{1}{r}\frac{\partial A}{\partial\theta}(r,\theta), \tag{2.59}$$

$$B_\theta(r,\theta) = -\frac{\partial A}{\partial r}(r,\theta). \tag{2.60}$$

Then, the boundary condition (2.57) enables to determine the previous unknowns:

$$\gamma_k = \frac{R_{ag}}{k}B_{r,k}, \tag{2.61}$$

$$\alpha_k = \frac{R_{ag}}{k}B_{r,k}\frac{F_k(R_{ag},R_s)}{2}, \tag{2.62}$$

$$\zeta_k = 0, \tag{2.63}$$

$$\chi_k = \frac{R_{ag}}{k}B_{\theta,k}\frac{E_k(R_{ag},R_s)}{2}. \tag{2.64}$$

Thus, the magnetic potential inside the air-gap band is entirely determined. The corresponding magnetic flux density is deduced from the knowledge of (2.58) and (2.61):

$$B_r(R_s,\theta) = \frac{R_{ag}}{R_s}\left(B_{r,k}\frac{F_k(R_{ag},R_s)}{2}\cos\left(k\theta+\phi_{r,k}\right) - B_{\theta,k}\frac{E_k(R_{ag},R_s)}{2}\sin\left(k\theta+\phi_{\theta,k}\right)\right), \tag{2.65}$$

$$B_\theta(R_s,\theta) = \frac{R_{ag}}{R_s}\left(B_{r,k}\frac{E_k(R_{ag},R_s)}{2}\sin\left(k\theta+\phi_{r,k}\right) + B_{\theta,k}\frac{F_k(R_{ag},R_s)}{2}\cos\left(k\theta+\phi_{\theta,k}\right)\right). \tag{2.66}$$

This result is generalizable to a multi-wavenumbers magnetic problem thanks to the linear property of the Poisson's equation [Green, 1828; Landau and Lifshitz, 1975]: a linear combination of solutions of the form (2.65) and (2.66) for different values of n is still a

solution of (1.20). Using again the complex notations, the air-gap magnetic flux density can be again decomposed as complex Fourier series

$$\begin{aligned} B_r(R_{ag},\theta) &= \sum_{k=-\infty}^{k=+\infty} \underline{B_{r,k}} e^{jk\theta}, \\ B_\theta(R_{ag},\theta) &= \sum_{k=-\infty}^{k=+\infty} \underline{B_{\theta,k}} e^{jk\theta}. \end{aligned} \tag{2.67}$$

In the rest of the demonstration, the following notations are used again:

$$\begin{aligned} F_k &= F_k(R_{ag},R_s), \\ E_k &= E_k(R_{ag},R_s). \end{aligned} \tag{2.68}$$

Then, the magnetic flux density can be expressed on the stator bore radius R_s as

$$B_r(R_s,\theta) = \frac{1}{2}\frac{R_{ag}}{R_s}\sum_{k=-\infty}^{k=+\infty} F_k \underline{B_{r,k}} + jE_k \underline{B_{\theta,k}} e^{jk\theta}, \tag{2.69}$$

$$B_\theta(R_s,\theta) = \frac{1}{2}\frac{R_{ag}}{R_s}\sum_{k=-\infty}^{k=+\infty} F_k \underline{B_{\theta,k}} - jE_k \underline{B_{r,k}} e^{jk\theta}. \tag{2.70}$$

The theoretic magnetic flux density on the stator bore radius R_s is obtained thanks to (2.69) and (2.70) which are based on the air-gap boundary condition (2.67). The expression (2.69) is different from what can be found in the literature because it is based on the magnetic flux density instead of magnetic potential [Lee et al., 1991; Lubin et al., 2010]. However, to solve the issue of AGSF transfer, it is more convenient to use the magnetic flux density since the AGSF expression (1.47) and (1.48) are based on the air-gap flux density.

Thus, (2.69) and (2.70) give the theoretical spatial transfer of the magnetic flux density **B** from the air-gap radius R_{ag} to the stator bore radius R_s. The goal of the next sections is to deduce from (2.69) and (2.70) the theoretical spatial transfer law for the AGSF radial component.

2.3.2 Radial magnetic surface forces

The magnetic radial surface force density experienced by the outer structure (stator or rotor) is computed according to the AGSF formulae (1.47) on a contour of radius R_s corresponding to the stator teeth tip radius as in Fig.1.9:

$$P_r(R_s,\theta) = -\frac{B_r(R_s,\theta)^2 - B_\theta(R_s,\theta)^2}{2\mu_0}. \tag{2.71}$$

The complex Fourier transform of P_r is performed using the convolution product:

$$\hat{P}_r(R_s,n) = -\frac{\left[\hat{B}_r \circledast \hat{B}_r\right](R_s,n) - \left[\hat{B}_\theta \circledast \hat{B}_\theta\right](R_s,n)}{2\mu_0} \tag{2.72}$$

where $\hat{B}_r$ and $\hat{B}_\theta$ are the complex Fourier transform of B_r and B_θ. Using properties of convolution product, $\hat{P}_r$ is written as:

$$\hat{P}_r(R_s,n) = -\left(\frac{R_{ag}}{R_s}\right)^2 \frac{1}{8\mu_0}\sum_{k=-\infty}^{k=+\infty} P_{r,k,n}\, e^{jn\theta} \tag{2.73}$$

where $P_{r,k,n}$ is expressed using (2.69):

$$\begin{aligned} P_{r,k,n} = &(F_k F_{n-k} + E_k E_{n-k})\, \underline{B_{r,k}}\, \underline{B_{r,n-k}} \\ &- (F_k F_{n-k} + E_k E_{n-k})\, \underline{B_{\theta,k}}\, \underline{B_{\theta,n-k}} \\ &+ j\,(F_k E_{n-k} + E_k F_{n-k})\, \underline{B_{r,k}}\, \underline{B_{\theta,n-k}} \\ &+ j\,(F_k E_{n-k} + E_k F_{n-k})\, \underline{B_{r,n-k}}\, \underline{B_{\theta,k}}\,. \end{aligned} \tag{2.74}$$

At this point, the spatial variation of each AGSF wavenumber is complex because it depends on the recombination of several magnetic flux density waves. Nevertheless, using polynomial properties of F_k and E_k, it can be shown that

$$\begin{aligned} F_k F_{n-k} + E_k E_{n-k} &= 2F_n\,, \\ F_k E_{n-k} + E_k F_{n-k} &= 2E_n\,, \end{aligned} \tag{2.75}$$

such that $P_{r,k,n}$ can be factorized:

$$P_{r,k,n} = 2F_n \left(\underline{B_{r,k}}\, \underline{B_{r,n-k}} - \underline{B_{\theta,k}}\, \underline{B_{\theta,n-k}} \right) + j2E_n \left(\underline{B_{r,k}}\, \underline{B_{\theta,n-k}} + \underline{B_{r,n-k}}\, \underline{B_{\theta,k}} \right). \tag{2.76}$$

The convolution product is used to factorize the sum under the form

$$\begin{aligned} \sum_{k=-\infty}^{k=+\infty} P_{r,k,n} = &2F_n \left[\hat{B}_r \circledast \hat{B}_r \right](R_{ag}, n) + 2F_n \left[\hat{B}_\theta \circledast \hat{B}_\theta \right](R_{ag}, n) \\ &+ j4E_n \left[\hat{B}_r \circledast \hat{B}_\theta \right](R_{ag}, n)\,. \end{aligned} \tag{2.77}$$

Replacing this intermediate result in (2.73) leads to

$$\begin{aligned} \hat{P}_r(R_s, n) = &-\frac{1}{2}\left(\frac{R_{ag}}{R_s}\right)^2 F_n \frac{1}{2\mu_0} \left(\left[\hat{B}_r \circledast \hat{B}_r \right](R_{ag}, n) - \left[\hat{B}_\theta \circledast \hat{B}_\theta \right](R_{ag}, n) \right) \\ &- j\frac{1}{2}\left(\frac{R_{ag}}{R_s}\right)^2 E_n \frac{1}{\mu_0} \left[\hat{B}_r \circledast \hat{B}_\theta \right](R_{ag}, n)\,. \end{aligned} \tag{2.78}$$

Then the air-gap MST terms (1.47) and (1.48) are identified:

$$\hat{P}_r(R_s, n) = \left(\frac{R_{ag}}{R_s}\right)^2 \frac{F_n \hat{P}_r(R_{ag}, n) + jE_n \hat{P}_\theta(R_{ag}, n)}{2}\,. \tag{2.79}$$

Introducing the self-transfer coefficient

$$S_n = \left(\frac{R_{ag}}{R_s}\right)^2 \frac{F_n}{2} = \frac{1}{2}\left(\frac{R_{ag}}{R_s}\right)^{n+2} + \frac{1}{2}\left(\frac{R_{ag}}{R_s}\right)^{-n+2} \tag{2.80}$$

and the cross-transfer coefficient

$$C_n = \left(\frac{R_{ag}}{R_s}\right)^2 \frac{E_n}{2} = \frac{1}{2}\left(\frac{R_{ag}}{R_s}\right)^{n+2} - \frac{1}{2}\left(\frac{R_{ag}}{R_s}\right)^{-n+2} \tag{2.81}$$

the formula (2.79) can be rewritten under the final form:

$$\hat{P}_r(R_s, n) = S_n \hat{P}_r(R_{ag}, n) + jC_n \hat{P}_\theta(R_{ag}, n)\,. \tag{2.82}$$

This last result means the radial AGSF spectrum can be accurately compute on the stator bore radius from the knowledge of the AGSF spectrum in the middle of the air-gap. Note that the limit case $R_{ag} = R_s$ leads to $S_n = 1$ and $C_n = 0$ such that $\hat{P}_r(R_s, n) = \hat{P}_r(R_{ag} = R_s, n)$. Thus, the formula stays valid.

2.3.3 Tangential magnetic surface forces

The magnetic tangential surface force experienced by the outer structure is computed according to (1.48):

$$P_\theta(R_s,\theta) = -\frac{B_r(R_s,\theta)B_\theta(R_s,\theta)}{\mu_0}. \tag{2.83}$$

The methodology is very similar to the radial case. The complex Fourier transform of P_θ is performed using the convolution product:

$$\hat{P}_r(R_s,n) = -\frac{\left[\hat{B}_r \circledast \hat{B}_\theta\right](R_s,n)}{\mu_0} \tag{2.84}$$

which can be rewritten as

$$\hat{P}_\theta(R_s,n) = -\frac{1}{4\mu_0}\left(\frac{R_{ag}}{R_s}\right)^2 \sum_{k=-\infty}^{k=\infty} P_{\theta,k,n}\, e^{jn\theta}. \tag{2.85}$$

Then, $P_{\theta,r,n}$ is expressed using (2.69):

$$\begin{aligned} P_{\theta,k,n} =& 2F_n \underline{B_{r,k}}\,\underline{B_{\theta,n-k}} \\ &- jE_n\left(\underline{B_{r,k}}\,\underline{B_{r,n-k}} - \underline{B_{\theta,k}}\,\underline{B_{\theta,n-k}}\right). \end{aligned} \tag{2.86}$$

Replacing this intermediate result in (2.85) leads to

$$\begin{aligned} \hat{P}_\theta(R_s,n) = -\left(\frac{R_{ag}}{R_s}\right)^2 \Bigg(& E_n \frac{1}{2\mu_0}\left[\hat{B}_r \circledast \hat{B}_\theta\right](R_{ag},n) \\ & + jF_n \frac{1}{4\mu_0}\left(\left[\hat{B}_r \circledast \hat{B}_r\right](R_{ag},n)\right. \\ & \left. - \left[\hat{B}_\theta \circledast \hat{B}_\theta\right](R_{ag},n)\right)\Bigg). \end{aligned} \tag{2.87}$$

Finally, identifying air-gap MST terms and using coefficients (2.80) and (2.81) allows us to get the final equation

$$\hat{P}_\theta(R_s,n) = S_n \hat{P}_\theta(R_{ag},n) - jC_n \hat{P}_r(R_{ag},n). \tag{2.88}$$

This last result means the tangential AGSF spectrum can be accurately compute on the stator bore radius from the knowledge of the AGSF spectrum in the middle of the air-gap. Note that the limit case $R_{ag} = R_s$ leads to $S_n = 1$ and $C_n = 0$ such that $\hat{P}_\theta(R_s,n) = \hat{P}_\theta(R_{ag} = R_s,n)$. Thus, the formula stays valid.

2.3.4 Discussion

This section aims to analyze the previous results in order to determine how it could affect the computed AGSF. In order to obtain the equations (2.82) and (2.88), an electrical machine with a cylindrical air-gap band was considered. A particular example with polar teeth was given in Fig. 1.9 but any radial flux machine topology could be considered. The complete AGSF transfer law can be written as:

$$\begin{aligned} \hat{P}_r(R_s,n) &= S_n \hat{P}_r(R_{ag},n) + jC_n \hat{P}_\theta(R_{ag},n), \\ \hat{P}_\theta(R_s,n) &= S_n \hat{P}_\theta(R_{ag},n) - jC_n \hat{P}_r(R_{ag},n), \end{aligned} \tag{2.89}$$

with S_n the self-transfer coefficient and C_n the cross-transfer coefficient given by

$$\begin{aligned} S_n &= \frac{1}{2}\left\{\left(\frac{R_{ag}}{R_s}\right)^{n+2} + \left(\frac{R_{ag}}{R_s}\right)^{-n+2}\right\}, \\ C_n &= \frac{1}{2}\left\{\left(\frac{R_{ag}}{R_s}\right)^{n+2} - \left(\frac{R_{ag}}{R_s}\right)^{-n+2}\right\}. \end{aligned} \tag{2.90}$$

These coefficients S_n and C_n only depend on the considered magnetic surface force wavenumber n and the adimensional radius ratio $r = \frac{R_{ag}}{R_s}$. Thus the spatial variation of AGSF does not depend on a particular combination of magnetic flux density k^{th} wavenumbers but only on the considered AGSF wavenumber n. It also confirms that radial and tangential magnetic surface force are strongly correlated.

This result is a generalization of the simplified coefficients for the multiharmonic slotless case (2.55). The results of the multiharmonic slotless case (2.53) can be found back when $P_\theta(R_s, \theta) = 0$.

Fig. 2.7-2.8-2.9 illustrate the variation of the transfer coefficients (2.90) with the wavenumber n and the adimensional radius r. In particular, Fig. 2.7 highlights that

$$\begin{aligned} \lim_{|n|\to\infty} |S_n| &= \infty, \\ \lim_{|n|\to\infty} |C_n| &= \infty. \end{aligned} \tag{2.91}$$

Physically, the spectrum energy is not infinite such that

$$\begin{aligned} \lim_{|n|\to\infty} |S_n \hat{P}_r(R_{ag}, n) + jC_n \hat{P}_\theta(R_{ag}, n)| &= 0, \\ \lim_{|n|\to\infty} |S_n \hat{P}_\theta(R_{ag}, n) - jC_n \hat{P}_r(R_{ag}, n)| &= 0. \end{aligned} \tag{2.92}$$

Nevertheless, a Fourier transform does not provide an exact zero at every non-physical frequency in numerical applications. Then it is recommended to take precautions to avoid numerical noise amplification at high wavenumbers.

As illustrated in Fig. 2.7, the transfer coefficients have the following symmetry properties:

$$\begin{aligned} S_{-n} &= S_n, \\ C_{-n} &= -C_n. \end{aligned} \tag{2.93}$$

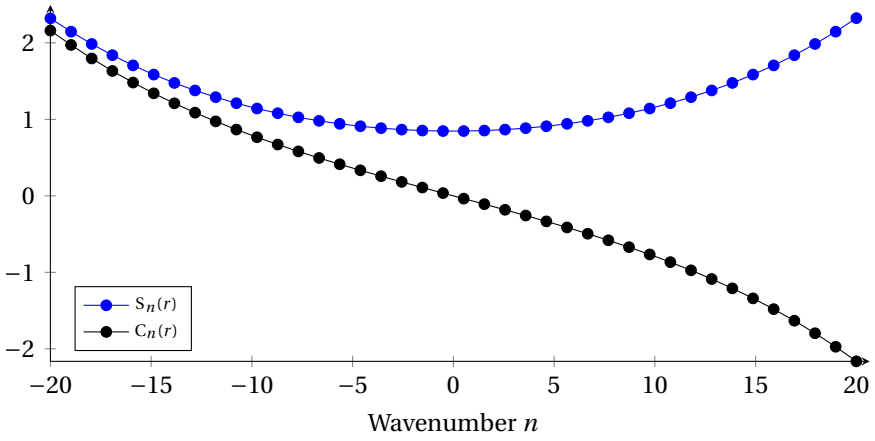

Figure 2.7 – Transfer coefficients at a fixed relative radius $r = \frac{R_{ag}}{R_s} = 0.96$

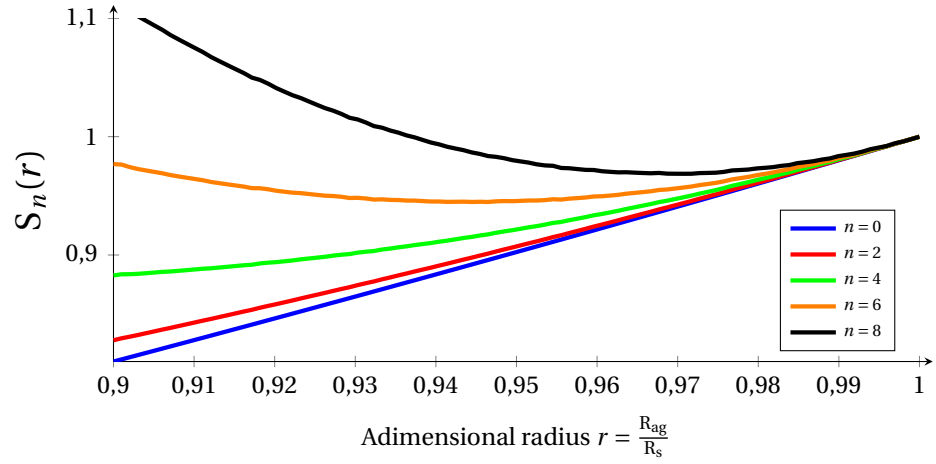

Figure 2.8 – Self-transfer coefficient $S_n(r)$ as a function of adimensional radius r

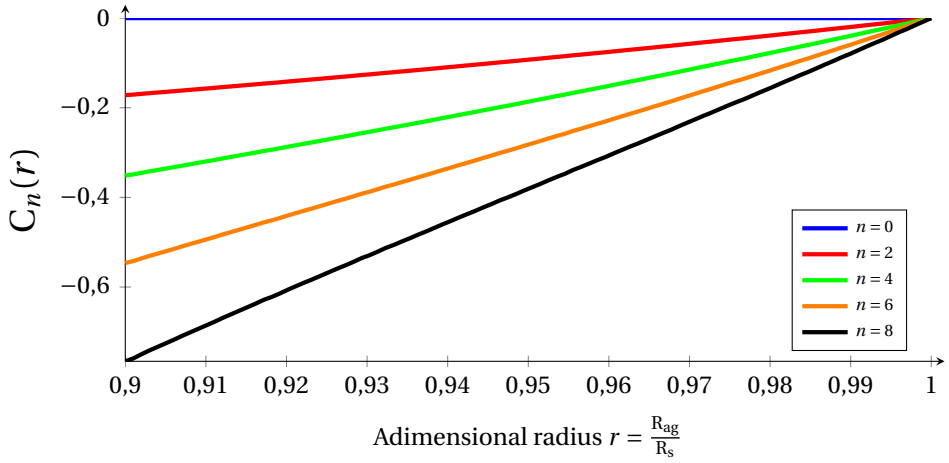

Figure 2.9 – Cross-transfer coefficient $C_n(r)$ as a function of adimensional radius r

The average radial force F_r or average tangential F_t force computed with AGSF depends linearly on the radius:

$$\begin{aligned} F_r(R_s) &= \int_0^{2\pi} P_r(R_s,\theta)\, R_s\, d\theta \\ &= 2\pi \hat{P}_r(R_s,0)\, R_s \\ &= 2\pi \left(\frac{R_{ag}}{R_s}\right)^2 \hat{P}_r(R_{ag},0)\, R_s \quad = \frac{R_{ag}}{R_s} F_r(R_{ag}) \end{aligned} \tag{2.94}$$

and similarly

$$F_\theta(R_s) = \frac{R_{ag}}{R_s} F_\theta(R_{ag}) \tag{2.95}$$

The Stoke's theorem predict that global forces F_x and F_y and torque M_z in the fixed Cartesian coordinate frame are independent from the radius of computation. This result can be found back:

$$\begin{aligned} F_x(R_s) &= \int_0^{2\pi} (P_r(R_s,\theta)\cos(\theta) - P_\theta(R_s,\theta)\sin(\theta))\, R_s\, d\theta = F_x(R_{ag})\,, \\ F_y(R_s) &= \int_0^{2\pi} (P_r(R_s,\theta)\sin(\theta) + P_\theta(R_s,\theta)\cos(\theta))\, R_s\, d\theta = F_y(R_{ag})\,, \end{aligned} \tag{2.96}$$

and

$$\begin{aligned} M_z(R_s) &= \int_0^{2\pi} P_\theta(R_s,\theta) R_s^2 \, d\theta \\ &= 2\pi \hat{P}_\theta(R_s,0) R_s^2 \\ &= 2\pi \left(\frac{R_{ag}}{R_s}\right)^2 \hat{P}_\theta(R_{ag},0) R_s^2 \quad = M_z(R_{ag}) \,. \end{aligned} \tag{2.97}$$

Nevertheless, in most of electrical machines $\frac{R_{ag}}{R_s} \approx 1$ such that the approximations $F_r(R_s) \approx F_r(R_{ag})$ and $F_\theta(R_s) \approx F_\theta(R_{ag})$ can be used accurately for vibroacoustic assessment [Boesing et al., 2010; Saito et al., 2016]. Indeed the air-gap cylindrical band thickness g is generally very small compared to the stator bore radius R_s such that the following approximations can be made:

$$\begin{aligned} S_n &\approx 1 \,, \\ C_n &\approx -n \frac{g}{R_s} \,. \end{aligned} \tag{2.98}$$

These approximations give an a priori estimation of the transfer error on the computed AGSF. To illustrate the relevance of this estimation, an electrical machine with a single wavenumber excitation n is considered:

$$\begin{aligned} \hat{P}_r(R_s,n) &= jM\hat{P}_\theta(R_{ag},n) \\ \frac{g}{R_s} &= \frac{1}{Q} \end{aligned} \tag{2.99}$$

where $M \gg 1$ and $Q \gg 1$ are adimensional coefficients. Introducing (2.98) in (2.82) and (2.88) leads to:

$$\begin{aligned} |\hat{P}_r(R_s,n)| &\approx |\hat{P}_r(R_{ag},n)| \\ |\hat{P}_\theta(R_s,n)| &\approx \left(1 + n\frac{M}{Q}\right) |\hat{P}_\theta(R_{ag},n)| \end{aligned} \tag{2.100}$$

It means that depending on the $\frac{M}{Q}$ ratio, the transfer coefficients could have a great influence on the tangential magnetic force. A quick numerical application with the 12s10p topology from Annex A.1 shows that $\frac{M}{Q} \approx \frac{1}{10}$ such that there could be a 40% error on the 4^{th} wavenumber.

In summary, the transfer law (2.89) was demonstrated. Then, the transfer coefficients were analysed. In particular, Taylor expansions were performed to show that the transfer law effect on AGSF is not necessarily negligible. Consequently, more detailed numerical studies are carried out in the following section.

2.4 Numerical Applications

The purpose of this section is to quantify the differences that AGSF transfer law (2.89) can cause for radial flux electrical machine. It was possible to compare and validate the results to analytical solution in Section 2.2. However, electromagnetic field in radial flux slotted machines is less accurate with analytical methods than FE analysis. In order to perform a validation of the AGSF transfer law with numerical simulation, two different approached are used:

— First, the AGSF is calculated at a given radius with or without the transfer, and with different mesh sizes.

— Then, the AGSF transfer law is used to compute magnetic force on the stator bore radius R_s and compare to an equivalent AGSF calculated from VWP results.

The simulations are performed with 2D electromagnetic FE analysis using MANATEE-FEMM coupling EOMYS ENGINEERING [2020]; Le Besnerais [2016]; Meeker [2019] (potential vector A-formulation). The magnetic surface forces are computed according to the different methods named as follow:

— AGSF-TR(r): AGSF calculated at radius r based on (1.46) applied at R_{ag} then using transfer coefficients (2.89);

— AGSF(r): AGSF based on (1.46) applied on a circular contour at radius R.

2.4.1 Validation with SPMSM 12s10p

In this section, the simulations are performed on the 12s10p machine described in Annex A.1. This electrical machine is convenient for this study because it has a relatively wide air-gap. The validation cases consist in comparing the application of the transfer law (based the AGSF computed at R_{ag}) with the direct calculation of the AGSF at desired radius r. The first comparison is performed at $r = 0.994R_s$ (which corresponds to $k = (r - R_r)/(R_s - R_r) = 90\%$) of the air-gap length). The results are presented in Fig. 2.10: the AGSF-TR(R_s) method provide amplitudes very close from the AGSF(R_s) method (around 1% or 2% relative error on the main peaks) compared to the classical AGSF(R_{ag}).

The interest of the method can be further highlighted by using two different mesh sizes and three methods:

— AGSF(R_s) computed on the coarse mesh,

— AGSF-TR(R_s) computed on the coarse mesh,

— AGSF(R_s) computed on the fine mesh (the reference).

The number of elements is multiplied by a factor 4 between the coarse mesh and the fine mesh. The results are presented on the Fig. 2.11: the AGSF-TR is closer from the reference than the direct method on the coarse mesh for the main peaks. This result can be linked to the observations made in Fig 2.2 and in [Li and Lowther, 2009]: the numerical errors are more likely to occur near the ferromagnetic-air interface. As a consequence, the AGSF transfer law can be used to improve the accuracy/cost balance.

2.4.2 Virtual Work Principle equivalent surface force

As discussed in Section 1.3, the nodal forces from VWP can be considered as a reference method in the context of e-NVH. However, the VWP output is located on the magnetic mesh nodes corresponding to the stator. Moreover, the physical unit is a resultant

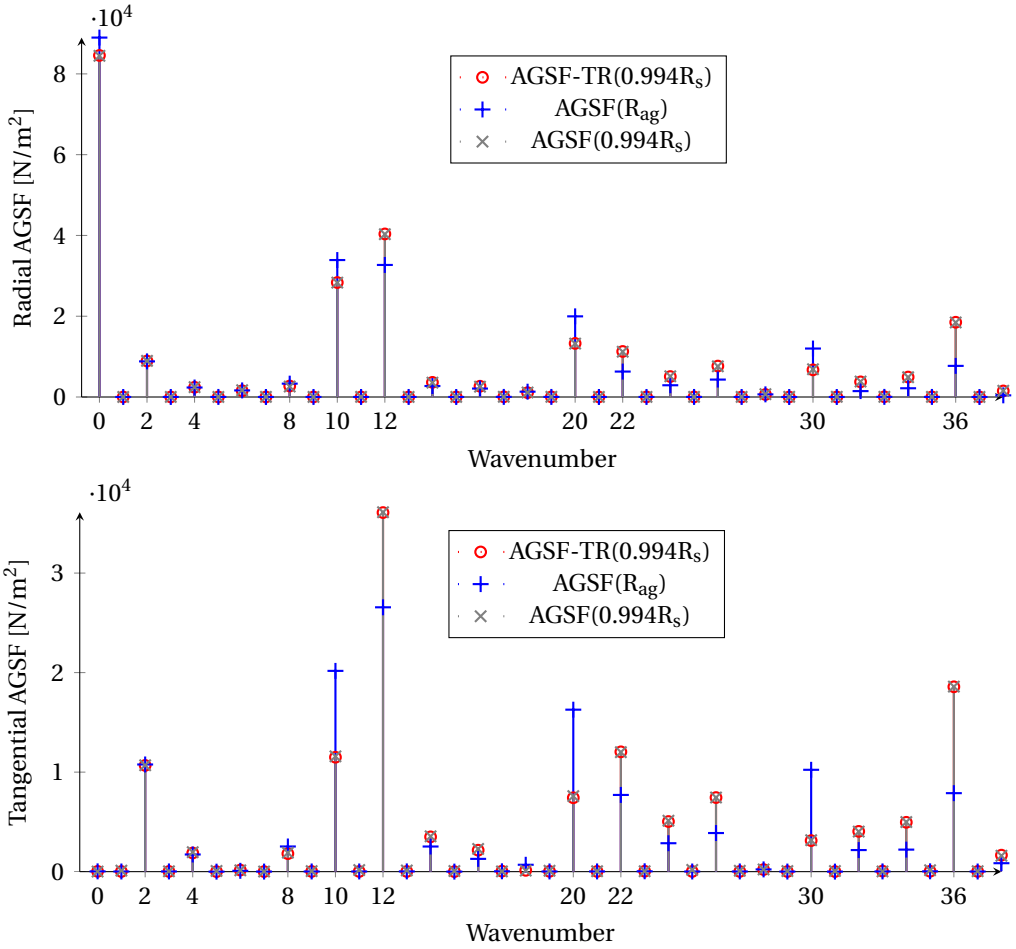

Figure 2.10 – Comparison of different AGSF angular spectrum at fixed time step.

force i.e. [N/m] for a 2D simulation. Then, AGSF and VWP results are not immediately comparable. The next Section 2.4.2 proposes a methodology to build an equivalent AGSF from VWP results.

According to Parent et al. [2008], the nodal magnetic forces based on VWP concentrate the effects of the actual force density in the direct vicinity of the node. As a consequence, a nodal force is meaningful only on its original mesh. Then VWP nodal forces must be converted in order to be compared with the AGSF which is a surface force density defined on a contour in the air-gap.

The proposed method consists in summing all the nodal forces included in an angular opening $d\theta$ to get the corresponding total force $F_{d\theta}$ as shown in Fig. 2.12. Then the obtained force is divided by the equivalent air-gap elementary surface:

$$P_{d\theta} = \frac{F_{d\theta}}{R_s d\theta} \tag{2.101}$$

The idea is to apply this process according to the discretization of the AGSF such that a surface force density $P_{vwp}(\theta)\ \forall\theta \in [0, 2\pi]$ is obtained on the stator bore radius R_s. This method is called VWP-S in the following.

In addition to the use as a reference in this chapter, this method can be interesting for e-NVH troubleshooting. Indeed, it allows us to decompose into wavenumbers the results of the VWP, and thus to use all the methods described in Section 1.4.8.

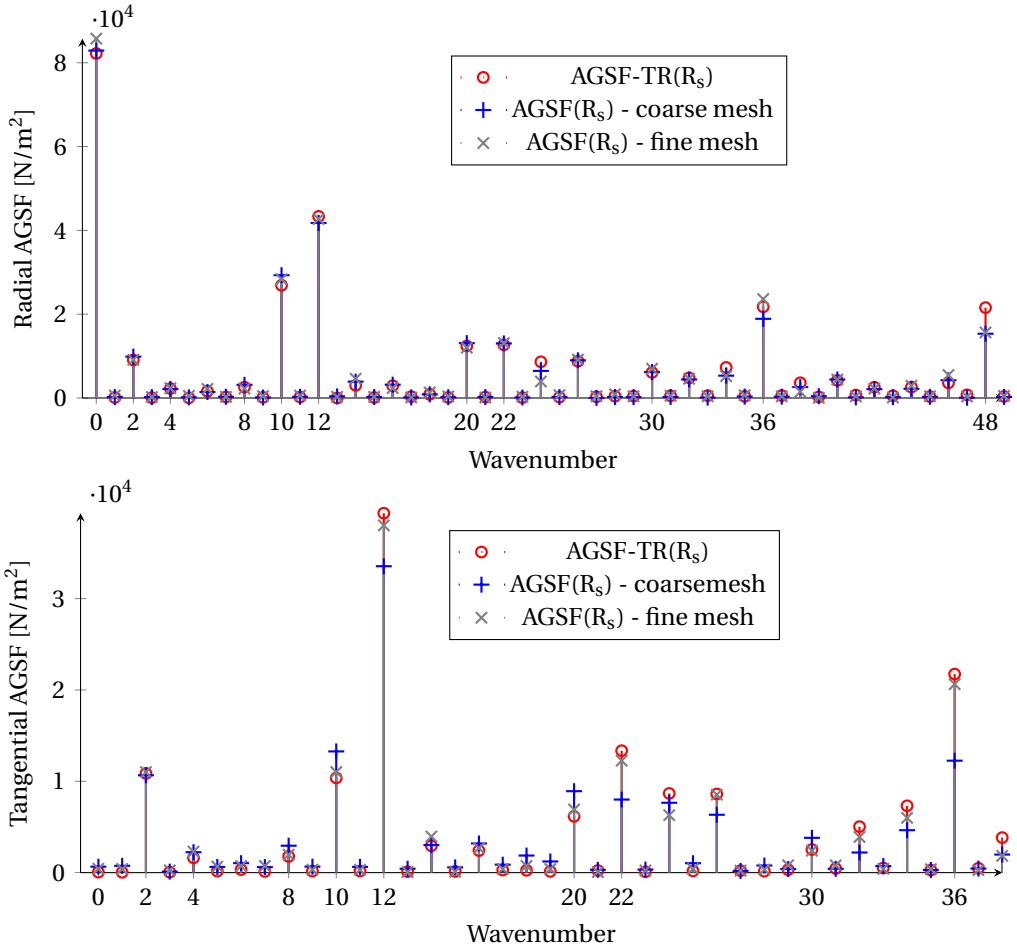

Figure 2.11 – Comparison of different AGSF angular spectrum at fixed time step.

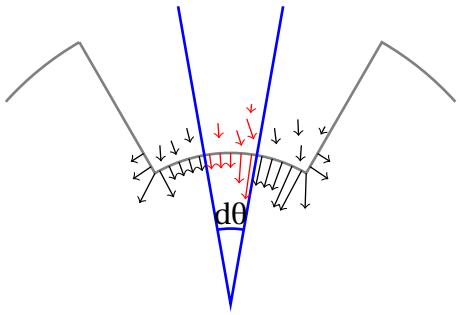

Figure 2.12 – Summing all nodal forces (red arrows) on an angular opening dθ to get an equivalent surface force density at stator bore radius.

Once this method is available, the effect of the transfer law (2.89) can be studied for three different electrical machines in Sections 2.4.3 and 2.4.4:

— a SCIM with a constructive effect of (2.89);

— a SPMSM with a destructive effect of (2.89);

— a turbo-alternator application considering modulation effect.

2.4.3 Validation with SCIM

A topology with which AGSF is commonly used to compute magnetic forces is the SCIM characterized by a thin cylindrical air-gap band ($\frac{g}{R_s} \approx 1\%$). In particular, the studied SCIM topology is presented in Fig. 2.13.

The results are presented in Fig. 2.14 for the radial direction and in Fig. 2.15 for the tangential direction. In particular Fig. 2.16 focuses on the force lower wavenumbers of interest for vibro-acoustic analysis.

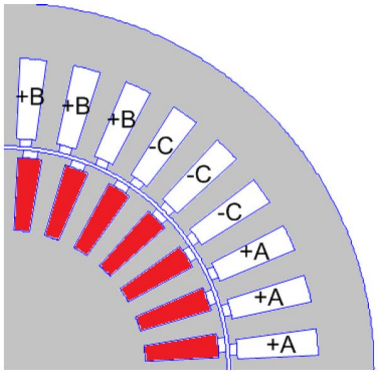

Figure 2.13 – Analyzed cage rotor induction machine with single layer winding and stator/rotor semiclosed slots (one pole). Boughrara et al. [2015]

A global observation of the results indicates that the AGSF-R_{ag} is giving more accurate radial surface force than AGSF-R_s for low wavenumbers. However the AGSF-R_s is more accurate than AGSF-R_{ag} for tangential surface force. In both directions, the AGSF-TR is accurate. In order to quantify these observations, a norm is defined to quantify the deviation from the VWP-S method:

$$\|\hat{P} - \hat{P}_{vwp}\|_N = \sum_{k=-N}^{k=+N} |\hat{P}(k) - \hat{P}_{vwp}(k)| \tag{2.102}$$

The 8 first wavenumbers have the main contribution to the total vibration. Then, two applications of (2.102) can be defined:

— $\|.\|_8$ with the 8 first wavenumbers.

— $\|.\|_{254}$ with all available wavenumbers.

It leads to the numerical values of Table 2.2 for radial AGSF and Table 2.3 for tangential AGSF. In all case, the most accurate method is the AGSF-TR based on the new transfer law (2.89).

Table 2.2 – Deviation of the magnetic surface force [N/m^2] with respect to the VWP-S in the radial direction compute with (2.102).

Method	$\|.\|_8$	$\|.\|_{254}$
AGSF-TR	1.3e+4	4.7e+5
AGSF-R_{ag}	1.8e+4	8.8e+5
AGSF-R_s	6.3e+4	6.3e+5

The benefits of the transfer coefficients used with AGSF-TR is particularly well shown in Fig. 2.16 where the 4^{th} wavenumber of the tangential AGSF is initially wrongly estimated with the AGSF-R_{ag} method. When using the AGSF-TR method based on (2.89),

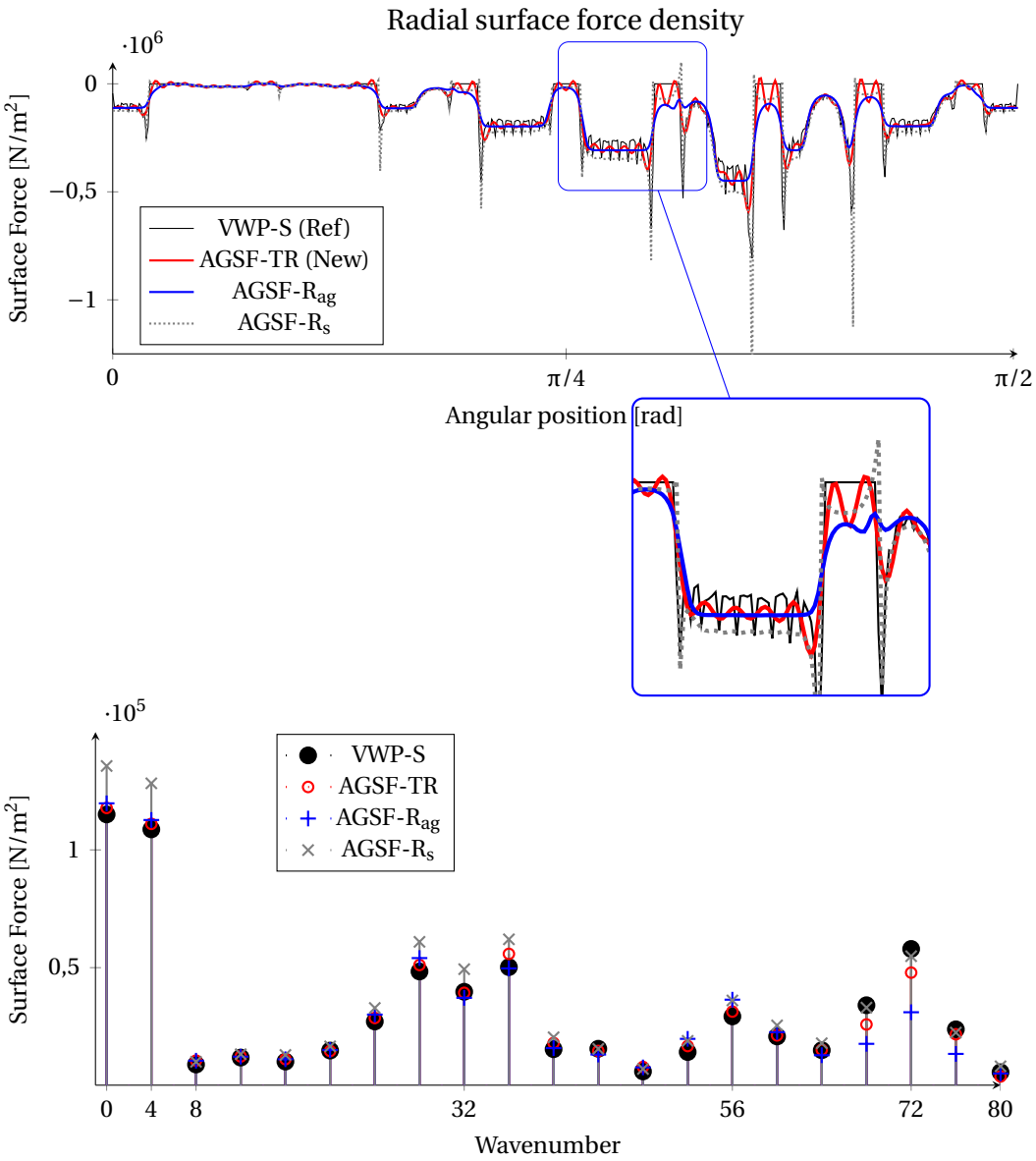

Figure 2.14 – Comparison of several methods for radial surface force density using air-gap MST and VWP for SCIM topology.

the 4^{th} wavenumber of the radial surface force has a constructive interference with the 4^{th} wavenumber of the tangential surface force in the air-gap thanks to the cross-transfer coefficient.

As the air gap is thin, the previous results shows that the effect of transfer law (2.89) remains weak on the radial AGSF. However, the effect of the transfer law is not negligible on the tangential AGSF and leads to a clear improvement.

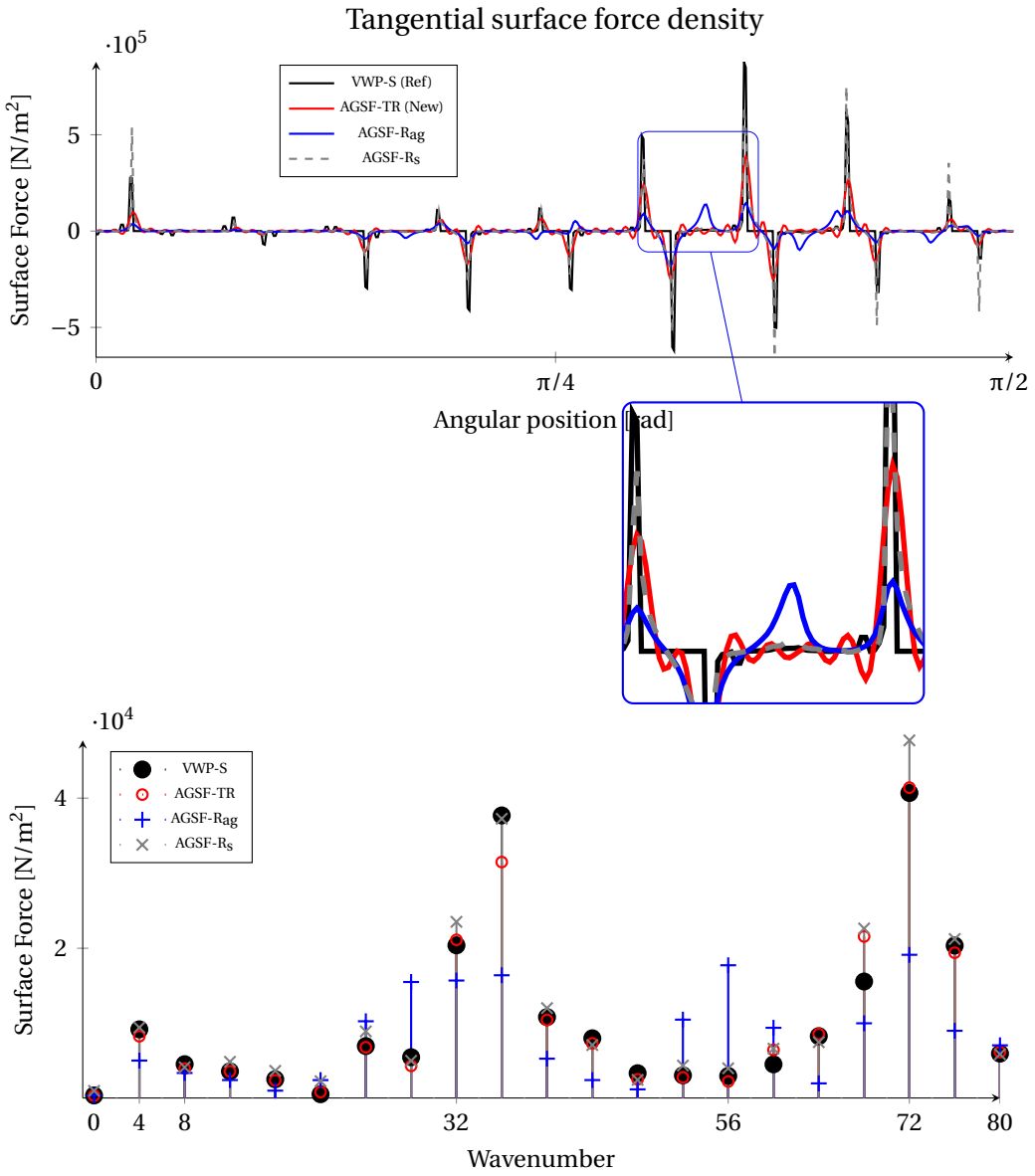

Figure 2.15 – Comparison of several methods for tangential surface force density using air-gap MST and VWP for SCIM topology.

Table 2.3 – Deviation of the magnetic air-gap surface force [N/m^2] with respect to the VWP-S in the tangential direction computed with (2.102).

Method	$\|.\|_8$	$\|.\|_{254}$
AGSF-TR	3.3e+3	4.1e+5
AGSF-R$_{ag}$	1.1e+4	8.9e+5
AGSF-R$_s$	4.0e+3	5.0e+5

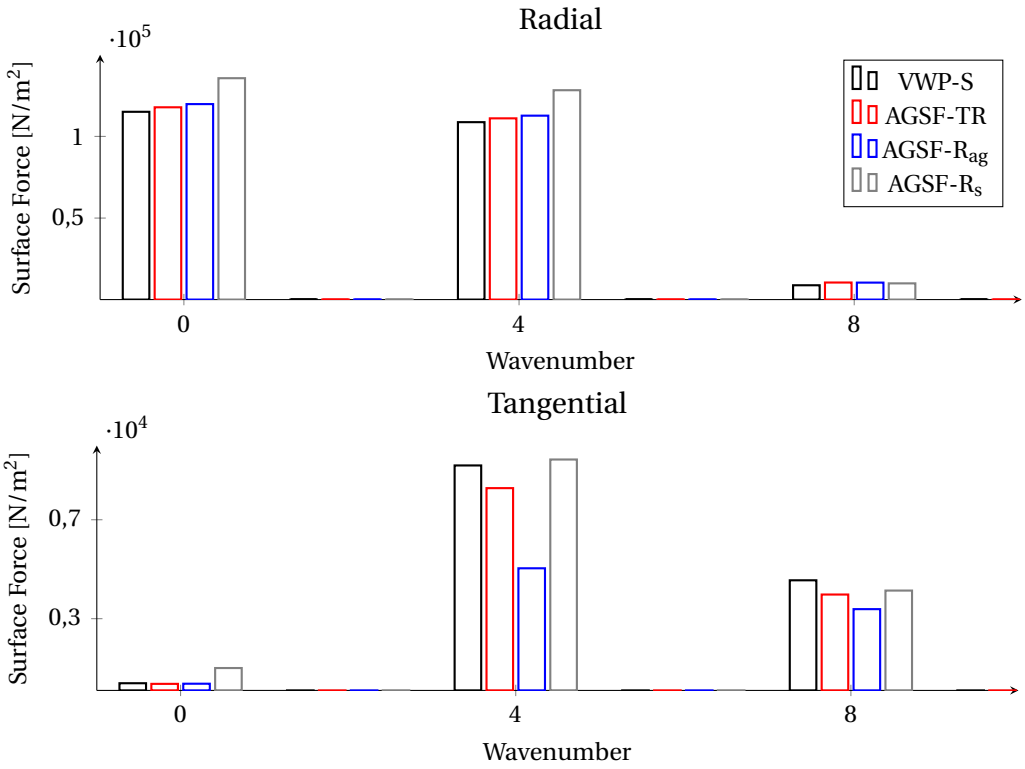

Figure 2.16 – Comparison of several methods for surface force density for low wavenumbers with SCIM topology.

2.4.4 Validation with SPMSM 12s8p

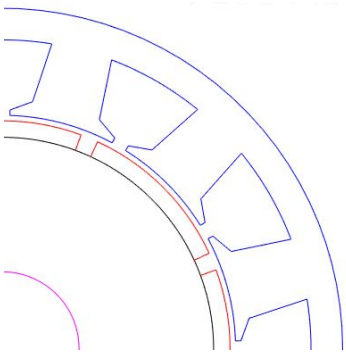

Figure 2.17 – Analyzed surface permanent magnet synchronous machine with 12 slots and 8 poles

This section proposes to compare the result of the different methods with a SPMSM topology. This kind of topology has wider air-gap than the SCIM which should influence the AGSF transfer law. The topology used for this application is similar to Fang et al. [2019], except that the pole pairs number was fixed at 8 and the simulation was performed at no-load as shown in Fig. 2.17. In these conditions, Fig. 2.18 and Fig. 2.19 give an image of the magnetic AGSF. The impact of the cross-transfer coefficients is noticeable: the 8^{th} wavenumber of the radial AGSF in Fig. 2.18 has a destructive interference with the 8^{th} wavenumber of the tangential surface force in the air-gap. Thus the contribution of the cross-transfer coefficient (2.90) is again not negligible.

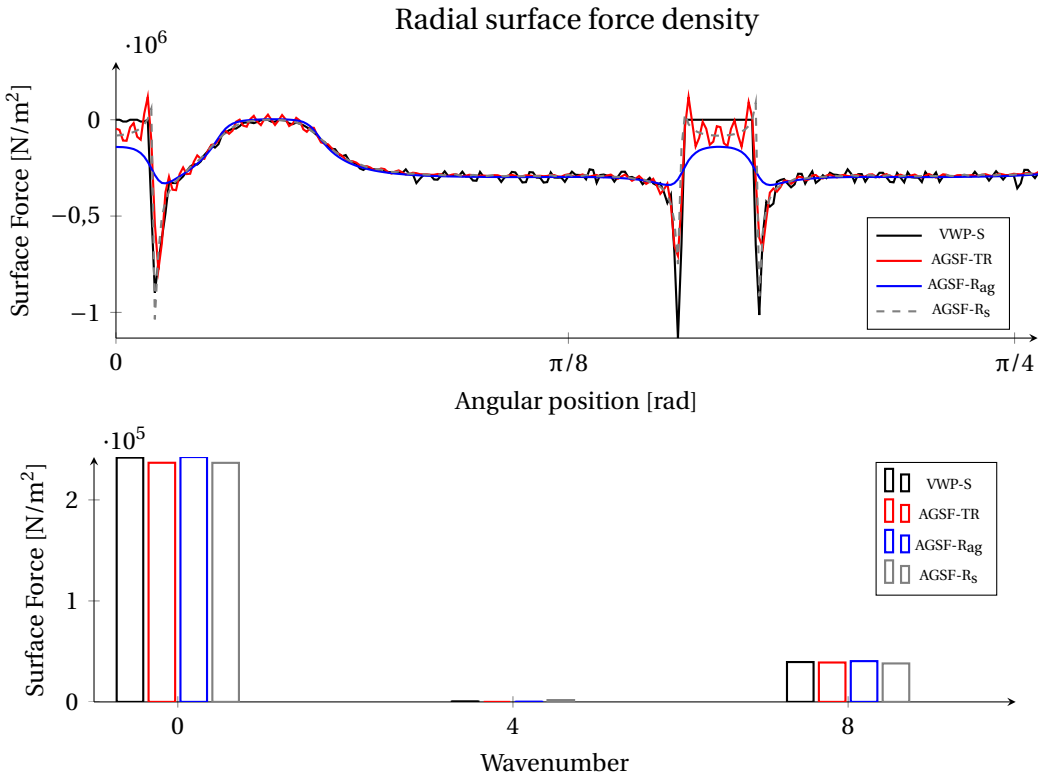

Figure 2.18 – Comparison of several methods for radial surface force density using AGSF and VWP for SPMSM topology..

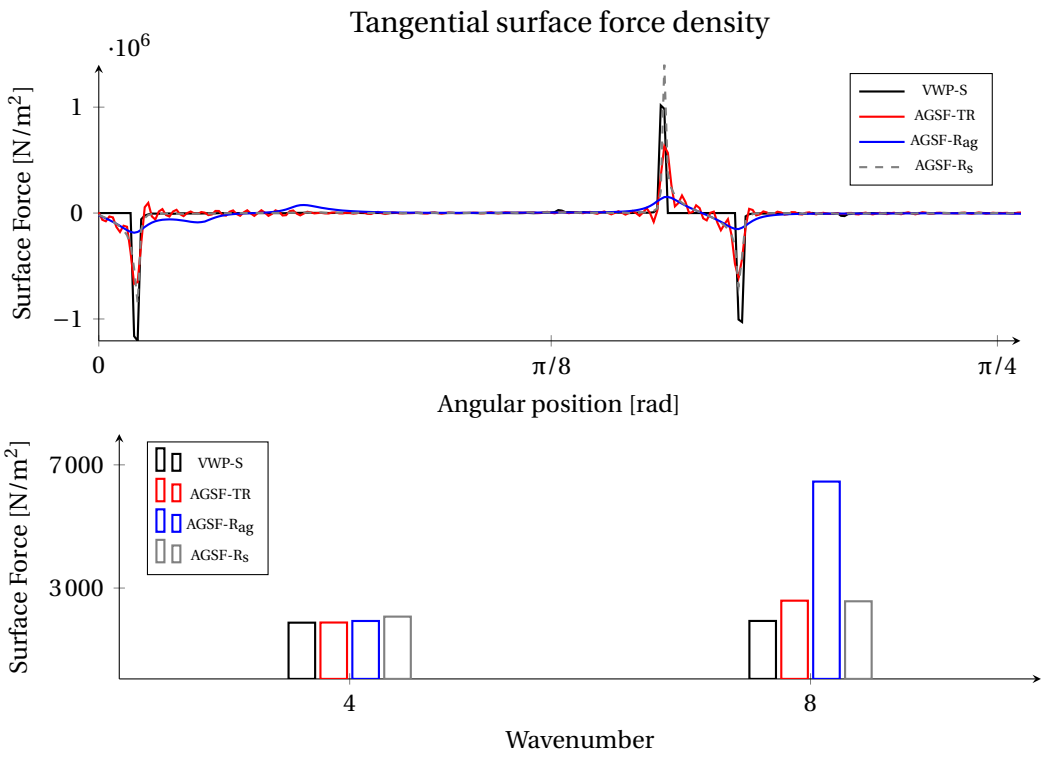

Figure 2.19 – Comparison of several methods for tangential surface force density using AGSF and VWP for SPMSM topology.

2.4.5 Application with Modulation Effect

The AGSF transfer law is mainly acting on the highest wavenumbers as shown by previous applications. In Section 1.4.5, the notion of modulation effect was introduced: it performs a spectral folding of high wavenumbers onto low wavenumbers. The question then arises as to whether the modulation effect is amplified (or decreased) by the transfer law. The results of this section are published in the article [Pile et al., 2020].

Then, this section proposes a numerical application in order to estimate the impact on vibroacoustic results. In this section, the application of the transfer law (2.89) is denoted **TR**. Moreover, considering the modulation effect described in Section 1.4.5, one can build an equivalent AGSF such that:

$$\hat{\mathrm{P}}(n,\omega) = \sum_m \mathrm{K}_{n,m}\left(\hat{\mathrm{P}}_\mathrm{r}(m,\omega) + \hat{\mathrm{P}}_\mathrm{r}^*(m,\omega)\right), \tag{2.103}$$

where $\hat{\mathrm{P}}^*$ is the equivalent radial force created by the tangential AGSF computed with (1.98), and $\mathrm{K}_{n,m}$ the modulation effect coefficient (1.108). This equivalent yoke surface force method is denoted **MOD**. It gives an image of the magnetic force signal seen from the yoke (after the tooth sampling). Finally, the successive application of **TR** then **MOD** is called **TRMOD**. This idea is summarized in Fig. 2.20.

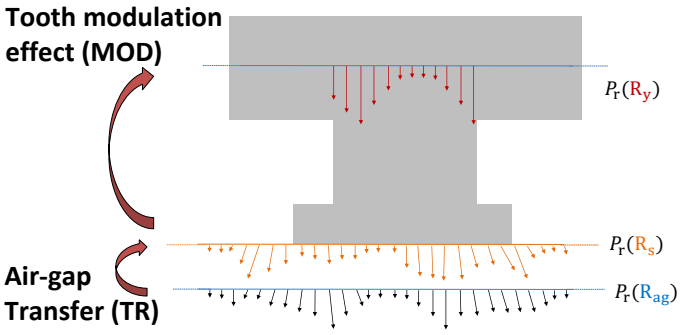

Figure 2.20 – Magnetic surface force equivalent spectrum from air-gap to yoke

To study the combination of both effects, a turbo-alternator topology described in Annex A.4 and in Fig. 2.21 is considered. For this topology:

— The relatively wide air-gap increases the impact of the AGSF transfer.

— The high number of teeth suggests that the modulation effect should stay negligible according to previous research Weh [1964]; Fang et al. [2019].

Regarding the time-dependency, the AGSF transfer (2.89) and the modulation effect (1.107) are independent of temporal harmonics, this aspect is omitted. Although the vibration spectrum should depend on the excitation's frequency, the goal of this numerical study is to have a qualitative analysis of the **TRMOD** method. Then, the simulation is performed using FEMM software Meeker [2019] at only one time-step. It removes the uncertainty due to time discretization and the approach used to take into account the rotation of the mesh.

Fig. 2.22 focuses on magnetic surface force density wavenumbers of interest for vibroacoustic. All previous methods are compared on the turbo-alternator topology. It can be observed in Fig. 2.22 that **TR** transformation alone has little impact on the surface force wavenumbers, in particular the 4^{th} wavenumber. However, it can be observed with **TRMOD** that the modulation can amplify the effect of the transfer law **TR**. The 4^{th} wavenumber is increased of approximately 20% (< 2dB) compared to the **MOD** method

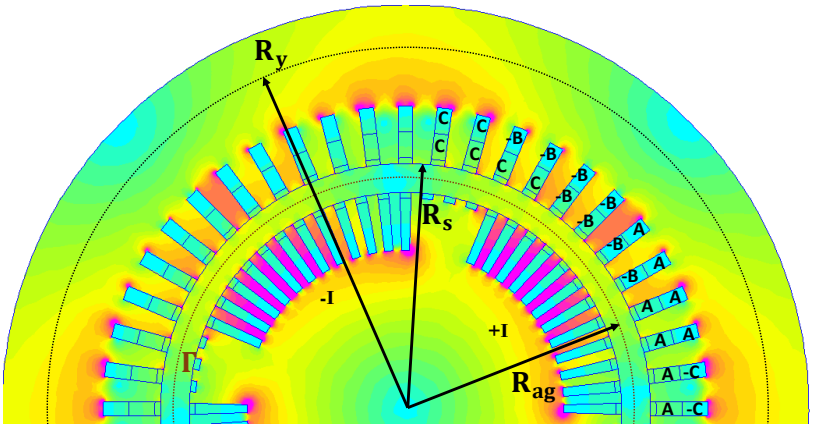

Figure 2.21 – Turbo-alternator topology with a relatively wide air-gap for numerical study of air-gap transfer and modulation effect. The three stator phases are indicated with signed letters A,B,C. The rotor poles are indicated by letters -I and +I.

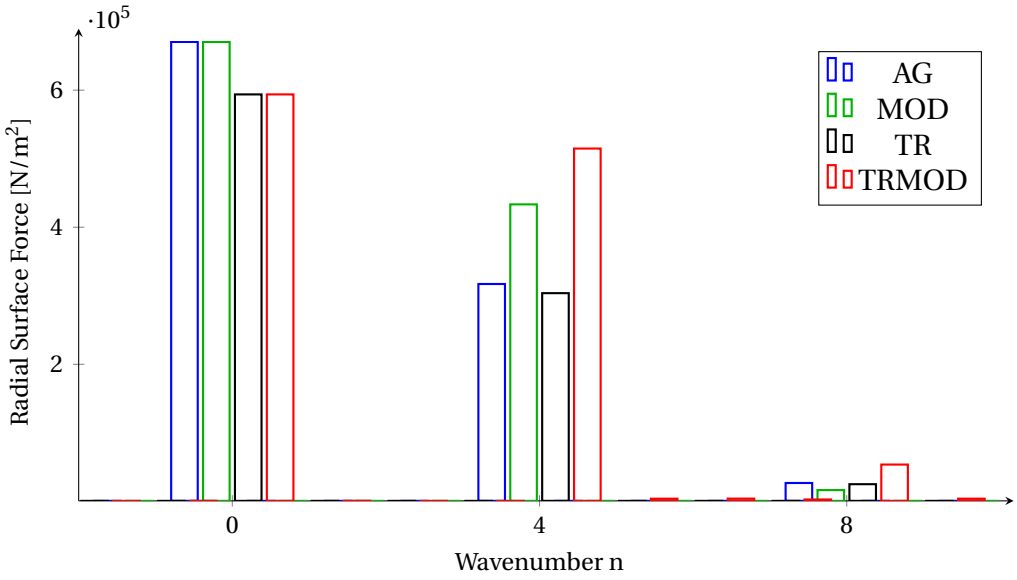

Figure 2.22 – Comparison of several methods for magnetic surface force to be applied on the teeth tips.

alone. The 8^{th} wavenumber is expected to decrease with **MOD** while it is increasing with **TRMOD** (almost +100%, or 6 dB). So the AGSF transfer could not only amplified modulation effect, but also change the expected behaviour (destructive or constructive).

2.5 Conclusion

In this Chapter, the dependency of AGSF with the radius of application in the air-gap was discussed for 2D model of radial flux electrical machines. At first, an analytical slotless case was studied. It has led to a first AGSF transfer law for the radial direction limited to infinite permeability and neglecting the effect of slots. Although this first version was very restrictive, this study allowed us to understand the mathematical equations that govern the behaviour of the AGSF depending on the radius and wavenumbers.

Then, the AGSF transfer law was generalized to any topology of radial flux electrical machines with a cylindrical air-gap band. This transfer law allows us to understand how the magnetic force wavenumbers depends on the air-gap radius of computation. In particular the two following properties are deduced:

— The amplitude and phase of each wavenumber depends on the radius, but the transfer to another radius does not add (or remove) any wavenumber.

— Air-gap radial and tangential surface forces are depending on each other when considering the transfer.

It also explains several observations made by Hallal et al. [2013] (see Figs. 1.11-1.12). The transfer law can be applied for electrical machines with saturation, but it does not change the limitations of AGSF modelling (in particular, neglecting volume force).

In order to estimate the impact on e-NVH studies, some applications with different topologies were proposed. The effect of AGSF transfer was observed and the improvement for reducing numerical noise in electromagnetic force spectrum was highlighted, in particular for the tangential force. However, the impact of this effect alone seems limited on the vibroacoustic result: 5% difference on the amplitude of radial force would change the noise result by less than 1dB as explained in Section 1.4.7. Nevertheless, the last application shows that the AGSF transfer could play a role when combined with the modulation effect study. Indeed, the result was significantly modified for some wavenumbers. It could lead to a difference of 6dB on the noise result for the proposed application. Therefore, both phenomena must be taken into account to study the vibroacoustic impact of high wavenumbers.

In conclusion, the transfer coefficients are of interest when the vibration effect of high wavenumbers is important. This can occur with the modulation effect, but also when the relative thickness of the yoke is small (e.g. with certain wind turbine generators). From now on, the transfer coefficients are systematically used to calculate AGSF based on MST. Now that the errors in the air gap have been quantified, the accuracy of the model based on lumped tooth force is going to be studied for magneto-mechanical coupling.

Chapter 3

Study of Lumped Tooth Force Modelling for Magneto-Mechanical Coupling

Contents

3.1 Introduction

The main goal of this chapter is to discuss the validity of the lumped tooth force (i.e. one resultant force per tooth) to perform magneto-mechanical coupling for e-NVH predictions. This topic was the subject of preliminary research work published in [Pile et al., 2018a].

The previous chapter proposed to discuss the model of the Air-Gap Surface Force (AGSF), and the influence on the modulation effect was highlighted. However, the modulation effect is still under discussion in the literature. As detailed in Section 1.4.5, the main idea is to use lumped tooth forces to model the response of the external structure - generally the stator - of the machine. Then, the wavenumbers which are higher than half the number of teeth $Z_s/2$ are under-sampled. In order to take into account the vibroacoustic contribution of these high wavenumbers, different methods are proposed in the literature Weh [1964]; Wang et al. [2020]; Fang et al. [2019]. Several assumptions have been identified to model the modulation effect:

1. The angle of integration γ in (1.106) is different between models (see Sections 1.4.2.2-1.4.5);
2. The small angle hypothesis is not discussed;

These scientific uncertainties are discussed in next Section 3.2 with different ways to integrate lumped tooth force from AGSF spectrum. Once these considerations have been made, an hybrid method based on lumped tooth force is proposed to predict vibration in electrical machine in Section 3.3: magnetic lumped tooth forces are computed numerically but the mechanical model relies on measurements only. Differences between prediction and measurements are observed. The last Section 3.4 discusses whether these differences could be due to the tooth force model. Thus, the mesh-to-mesh projection workflow is compared to the lumped tooth force workflow to predict the vibration at variable speed.

3.2 Lumped Tooth Force Integration

3.2.1 Analytical Integration

The goal of this section is to determine the correct angle of integration γ in (1.106) to accurately compute the lumped tooth forces corresponding to each AGSF wavenumber, as illustrated in Fig. 3.1.

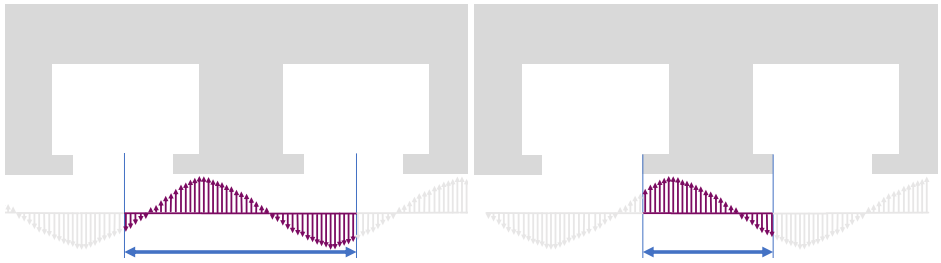

(a) $\gamma = 2\pi/Z_s$ (b) $\gamma = \beta$

Figure 3.1 – Two different integration paths for lumped tooth forces.

In order to have an exact comparison, it is necessary to remove every source of differences. It starts with the projection of the AGSF on each tooth radial/tangential direction,

which supposes small angles in the literature. This hypothesis can be lifted with the following calculations. First, the lumped tooth force calculation from (1.85) and (1.86) are recalled:

$$\hat{\mathrm{F}}_{\mathrm{r},i}(n,\omega) = \mathrm{R_s L_s}\int_{\alpha_i-\gamma/2}^{\alpha_i+\gamma/2}\left(\hat{\mathrm{P}}_\mathrm{r}(\mathrm{R_s},n,\omega)\mathbf{e}_\mathrm{r}(\theta)+\hat{\mathrm{P}}_\theta(\mathrm{R_s},n,\omega)\mathbf{e}_\theta(\theta)\right)\mathbf{e}_\mathrm{r}(\alpha_i)\exp^{n\theta}\,\mathrm{d}\theta\,,$$
$$\hat{\mathrm{F}}_{\theta,i}(n,\omega) = \mathrm{R_s L_s}\int_{\alpha_i-\gamma/2}^{\alpha_i+\gamma/2}\left(\hat{\mathrm{P}}_\mathrm{r}(\mathrm{R_s},n,\omega)\mathbf{e}_\mathrm{r}(\theta)+\hat{\mathrm{P}}_\theta(\mathrm{R_s},n,\omega)\mathbf{e}_\theta(\theta)\right)\mathbf{e}_\theta(\alpha_i)\exp^{n\theta}\,\mathrm{d}\theta\,.$$

Remember that α_i is the angle of the tooth. Instead of using the small angles hypothesis (1.87) and (1.88), one can compute the contribution of the tangential AGSF on the radial tooth force and the radial AGSF on the tangential tooth force. The intermediary calculations of the scalar products lead to

$$\int_{\alpha_i-\gamma/2}^{\alpha_i+\gamma/2}\mathbf{e}_\mathrm{r}(\theta)\cdot\mathbf{e}_\mathrm{r}(\alpha_i)\exp^{n\theta}\,\mathrm{d}\theta = \mathrm{A}_n^{\mathrm{rr}}\exp^{n\alpha_i}\,, \tag{3.1}$$
$$\int_{\alpha_i-\gamma/2}^{\alpha_i+\gamma/2}\mathbf{e}_\theta(\theta)\cdot\mathbf{e}_\mathrm{r}(\alpha_i)\exp^{n\theta}\,\mathrm{d}\theta = j\mathrm{A}_n^{\mathrm{rt}}\exp^{n\alpha_i}\,, \tag{3.2}$$
$$\int_{\alpha_i-\gamma/2}^{\alpha_i+\gamma/2}\mathbf{e}_\mathrm{r}(\theta)\cdot\mathbf{e}_\theta(\alpha_i)\exp^{n\theta}\,\mathrm{d}\theta = -j\mathrm{A}_n^{\mathrm{rt}}\exp^{n\alpha_i}\,, \tag{3.3}$$
$$\int_{\alpha_i-\gamma/2}^{\alpha_i+\gamma/2}\mathbf{e}_\theta(\theta)\cdot\mathbf{e}_\theta(\alpha_i)\exp^{n\theta}\,\mathrm{d}\theta = \mathrm{A}_n^{\mathrm{rr}}\exp^{n\alpha_i}\,, \tag{3.4}$$

with the following values for $n\neq 0$ and $\|n\|\neq 1$:

$$\mathrm{A}_n^{\mathrm{rr}} = 2\frac{n\cos\left(\frac{\gamma}{2}\right)\sin\left(n\frac{\gamma}{2}\right)-\sin\left(\frac{\gamma}{2}\right)\cos\left(n\frac{\gamma}{2}\right)}{n^2-1}\,, \tag{3.5}$$
$$\mathrm{A}_n^{\mathrm{rt}} = 2\frac{n\sin\left(\frac{\gamma}{2}\right)\cos\left(n\frac{\gamma}{2}\right)-\cos\left(\frac{\gamma}{2}\right)\sin\left(n\frac{\gamma}{2}\right)}{n^2-1}\,, \tag{3.6}$$

and if $|n|=1$

$$\mathrm{A}_1^{\mathrm{rr}} = \frac{1}{2}\left(\gamma+\sin(\gamma)\right)\,, \tag{3.7}$$
$$\mathrm{A}_1^{\mathrm{rt}} = -n\left(\gamma-\sin(\gamma)\right)\,, \tag{3.8}$$

and finally if $n=0$

$$\mathrm{A}_0^{\mathrm{rr}} = 2\sin\left(\frac{\gamma}{2}\right), \tag{3.9}$$
$$\mathrm{A}_0^{\mathrm{rt}} = 0\,. \tag{3.10}$$

Then, the lumped tooth forces can be expressed for each wavenumber:

$$\hat{\mathrm{F}}_{\mathrm{r},i}(n,\omega) = \mathrm{R_s L_s}\left(\mathrm{A}_n^{\mathrm{rr}}\hat{\mathrm{P}}_\mathrm{r}(\mathrm{R_s},n,\omega)+j\mathrm{A}_n^{\mathrm{rt}}\hat{\mathrm{P}}_\theta(\mathrm{R_s},n,\omega)\right)\exp^{n\alpha_i}\,, \tag{3.11}$$
$$\hat{\mathrm{F}}_{\theta,i}(n,\omega) = \mathrm{R_s L_s}\left(-j\mathrm{A}_n^{\mathrm{rt}}\hat{\mathrm{P}}_\mathrm{r}(\mathrm{R_s},n,\omega)+\mathrm{A}_n^{\mathrm{rr}}\hat{\mathrm{P}}_\theta(\mathrm{R_s},n,\omega)\right)\exp^{n\alpha_i}\,. \tag{3.12}$$

This result is more general than the formulae (1.89) and (1.90) of the scientific literature, which can be found back by using $\gamma\ll 1$ and Taylor developments such that

$$\mathrm{A}_n^{\mathrm{rr}} \approx 2\frac{\sin\left(n\frac{\gamma}{2}\right)}{n}\,, \tag{3.13}$$
$$\mathrm{A}_n^{\mathrm{rt}} \approx 0\,. \tag{3.14}$$

It is important to note that the coefficients could be very small for some specific wavenumbers which depends on the angle γ. For example, $A_n^{rr} \approx 0$ when $n \propto Z_s$ with $\gamma = 2\pi/Z_s$. It means that the chosen angle of integration could have significant effect on the interpretation of magnetic force wavenumbers contribution to vibration.

Similar calculation can be performed in order to take the tooth tip moments per wavenumber into account as detailed in Annex C.3. Only [Fang et al., 2019] has proposed to take tooth tip moments into account using the small angle hypothesis, but the contribution of the moments to vibration has yet to be demonstrated.

3.2.2 Numerical Study with VWP

The two following sections focus on different issues related to lumped tooth force integration:

— Section 3.2.2.1 focuses on the angle of integration γ by comparing the two different possibilities using a 36s36p machine specifically designed for this issue.

— Sections 3.2.2.2 studies the computation of lumped tooth force from AGSF with a reference based on VWP.

3.2.2.1 Validation with 36s36p

The different aspects of lumped tooth force integration are discussed with a numerical application on a SPMSM. The geometrical and numerical parameters of the 36s36p machine used in the magnetostatic simulation are presented in Annex A.2. The results of this section were submitted and accepted for the national conference Symposium de Génie Electrique (SGE) [Pile et al., 2020b].

The VWP is used as a reference: the sum of all nodal forces over each tooth gives a lumped force, which can be compared to the different transformations. However, differences remain with AGSF based on MST despite the use of AGSF transfer laws as discussed in Chapter 2. To solve this issue, the same technique as in Section 2.4.2 is applied: an equivalent AGSF is build from the VWP results and denoted VWP-S. Then, the differences can only be attributed to the integration method of lumped tooth forces.

The goal of this section is to determine the correct angle γ for integration of lumped tooth forces and to discuss the differences between coefficients. The topology has been designed to study the case where $A_n^{rr} \ll 1$ by directly comparing the VWP nodal forces with the lumped tooth force method. Only radial force are considered for this section.

The magnetic saturation of the material is low, making this machine a good candidate to compare AGSF with VWP. The force spectrum corresponding to this machine is shown in Fig. 3.2. From the modulation effect of Section 1.4.5, this machine has a pulsating tooth force (wavenumber $n = 0$) that can have two origins:

— either due to the pole/slot interaction $Z_s - 2p = 0$,

— or at the fundamental $2p = 36$, by the modulation effect.

The magnetostatic FE simulation is performed with a 2D triangle mesh using the coupling between FEMM software [Meeker, 2019] and MANATEE software [EOMYS ENGINEERING, 2020]. Thanks to the periodicity conditions, the simulation is reduced to a single tooth pitch: this enables to symmetrize the mesh in order to reduce the numerical noise on the mechanical FE simulation. For the same reason, a large number of elements are used: 306000 triangular faces in total.

However, the two different integration methods give significantly different results as shown in Fig. 3.3. The goal is to estimate the impact on the vibration. In a first step,

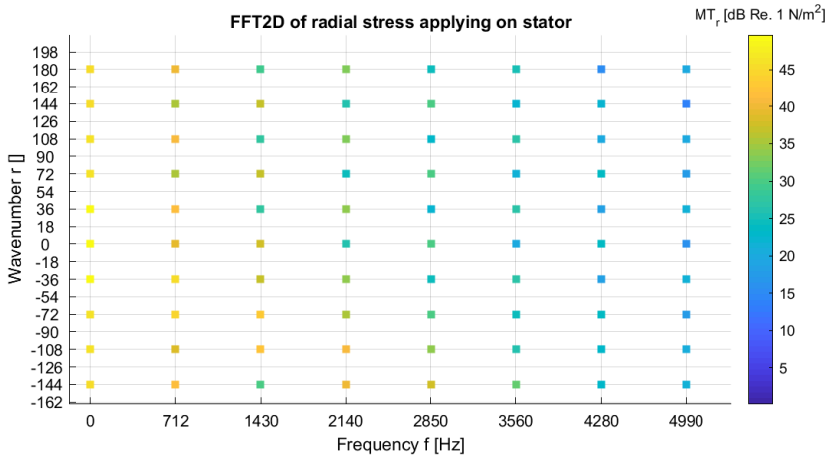

Figure 3.2 – AGSF spectrum of a 36s36p machine using MANATEE software.

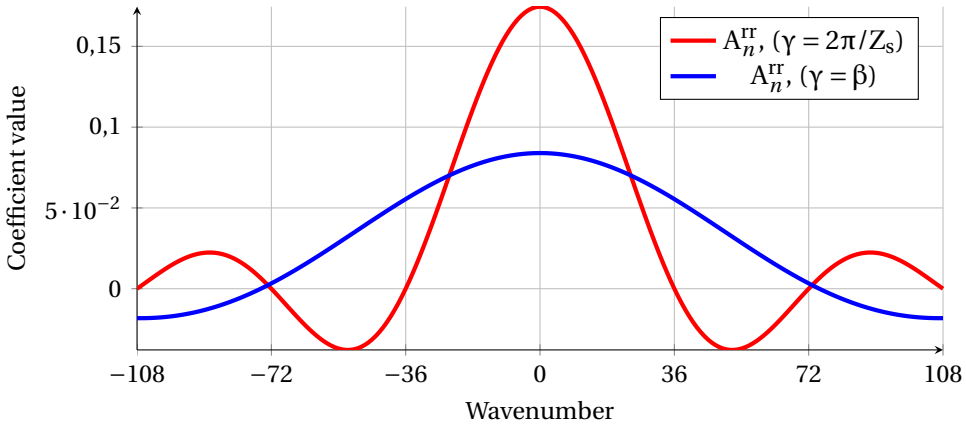

Figure 3.3 – Integration coefficients per wavenumber for lumped tooth force ($Z_s = 36$, $\beta = 4.81$ [deg]).

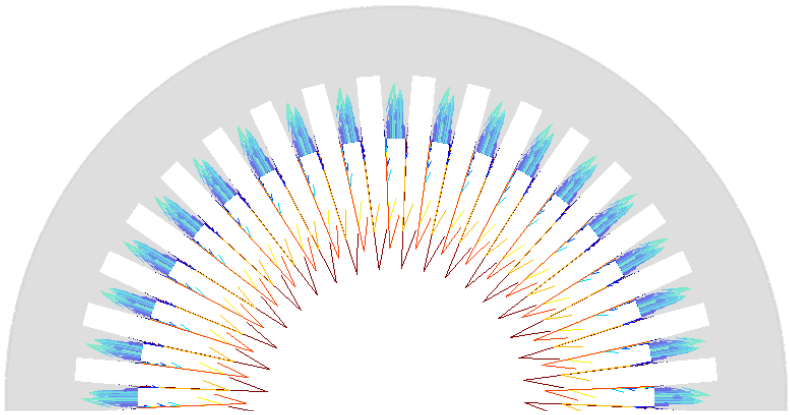

Figure 3.4 – Nodal forces calculated with VWP at 712 Hz.

the approximation of small angles (3.13) is used to simplify the interpretation such that when $n \propto Z_s$:

— For $\gamma = 2\pi/Z_s$, then $A_n^{rr} \approx 2\frac{\sin(n\pi)}{n} \approx 0$

— For $\gamma = \beta$ then $A_n^{rr} \neq 0$.

Formulated differently, the AGSF wavenumber $n \propto \pm 36$ contributes significantly to the vibration in only one model ($\gamma = \beta$).

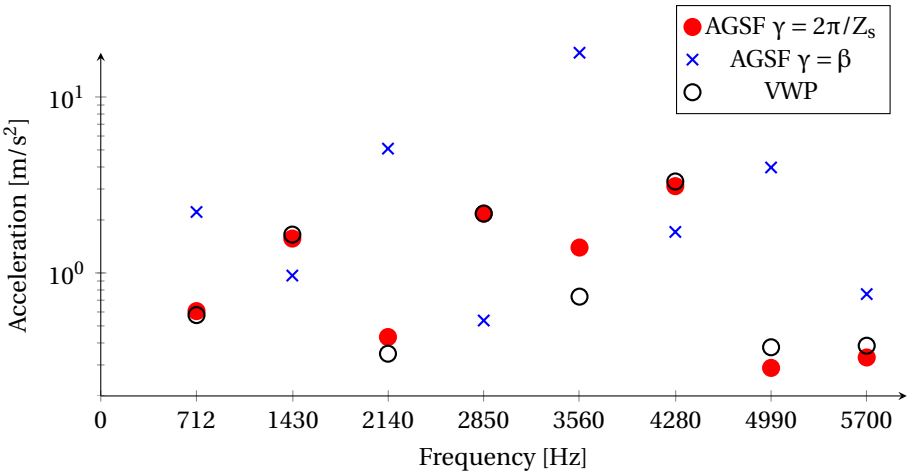

Figure 3.5 – Amplitude of acceleration (RMS) as function of frequency for different methods.

In order to test the two different angles of integration, these lumped tooth force models are compared with VWP in term of acceleration results. The 2-D triangle mesh is extruded in 3-D on 8 layers of the same length, leading to a prismatic mesh as shown in Fig. A.5. The VWP loading is then duplicated on the nodes along the length. The result of the mechanical FE simulation is the calculated harmonic displacement on the outer surface of the cylinder head. An example of the result of radial forces from the VWP at one time step obtained for this study is presented in Fig. 3.4. The wavenumber $n = 36$ can be observed in Fig. 3.4 with the same distribution of forces on all the 36 teeth.

The acceleration based on AGSF is obtained through three steps based on the wave-FRF method from Section 1.4.3:

— First, the FRF for a unit excitation $\mathrm{FRF}_r(0,\omega)$ of wavenumber $n = 0$ is simulated as explained in Section 1.4.3;

— Then, the displacement $\mathrm{Y}(0,\omega)$ due to the actual force of wavenumber 0 is calculated;

— Finally, the displacement $\mathrm{Y}(m,\omega)$ due to the higher wavenumbers $n \propto 36$ using $\mathrm{Y}(0,\omega)$ and (1.107) is calculated according to the modulation effect described in Section 1.4.5.

This leads to the operational displacement based on the lumped tooth force calculated with AGSF:

$$\mathrm{Y}(\omega) = \sum_{n \propto \pm \mathrm{Z_s}} \mathrm{A}^{\mathrm{rr}}_n(\gamma)\hat{\mathrm{P}}_{\mathrm{r}}(\mathrm{R_{ag}}, n, \omega)\mathrm{FRF}_r(0,\omega) \tag{3.15}$$

The displacement calculated with (3.15), for both $\gamma = 2\pi/\mathrm{Z_s}$ and $\gamma = \beta$, is compared to the VWP results in Fig. 3.5. It can be seen that the method based on $\gamma = 2\pi/\mathrm{Z_s}$ gives a result much closer to the reference calculated with the VWP, especially for the order at $10 f_s = 3564$ [Hz] where $\gamma = \beta$ gives a 22 dB error. The conclusion of this first part is that the angle of integration $\gamma = \beta$ leads to an incorrect estimation of the contribution of each wavenumber to the vibration.

However, using the approximation (3.13) is in contradiction with the experimental results obtained in [Wang et al., 2020]: the 0^{th} order alone cannot explain the vibration results. To solve this issue, the proposed approach is to use instead the non-simplified formulae (3.5) and (3.6) with $\gamma = 2\pi/\mathrm{Z_s}$. Then, $\mathrm{A}^{\mathrm{rr}}_n \neq 0$ when $n \propto \pm \mathrm{Z_s}$ which allows us to

take into account the contribution of all wavenumbers proportional to the number of teeth Z_s.

Then, all wavenumbers can be taken into account in the presented 36s36p application case and the integration coefficient (3.5) is used without the small angle hypothesis. It enables to compute the contribution of each wavenumbers to the resulting radial tooth force:

$$F_{r,i}(\omega) = R_s L_s \sum_n \left(A_n^{rr} \hat{P}_r(R_s, n, \omega) + j A_n^{rt} \hat{P}_\theta(R_s, n, \omega) \exp^{n\alpha_i} \right) \tag{3.16}$$

This last equation can be seen as a generalization to lumped tooth force of the work [Spargo et al., 2014] that makes it possible to find the contribution of each wavenumber to the average torque. The decomposition of the pulsating lumped tooth force according to (3.16) is compared to the resultant (taken as the reference) at $10 f_s$ can be seen in Fig. 3.6: all AGSF wavenumbers are stacked to represent their relative contribution to the resultant tooth force wavenumber (here only $n = 0$). The 4 main contributing wavenumbers are sorted by constructive (positive values) and destructive (negative values) interferences. The reference resultant (coloured in black) is directly computed from the VWP results. The resultant has the same value on both Fig. 3.6a and Fig. 3.6b. It can be observed that the tooth force is radically overestimated (+22dB) when using $\gamma = \beta$ but almost exact with $\gamma = \frac{2\pi}{Z_s}$. Thus, it explains the previous results in Fig. 3.5. It is interesting to underline that the very "high" wavenumbers such as $n = -180$ would have been neglected in classical methodologies. This is a significant contribution of this thesis.

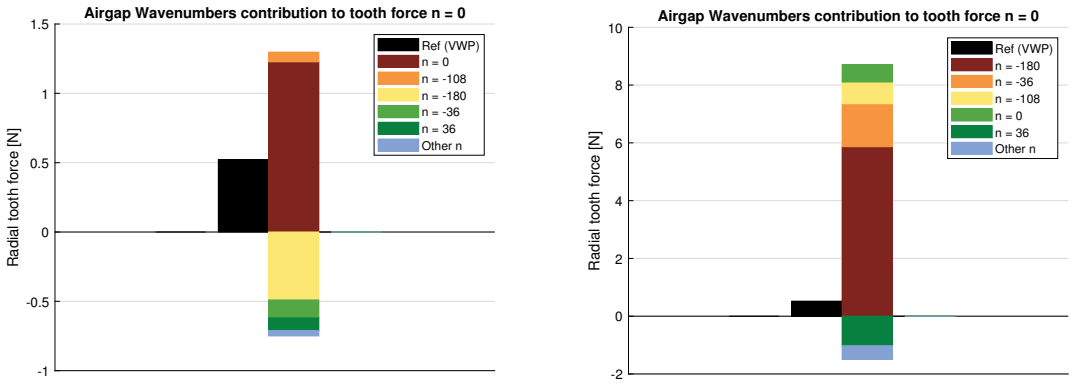

(a) $\gamma = \frac{2\pi}{Z_s}$ (b) $\gamma = \beta$

Figure 3.6 – Radial Lumped Tooth Force decomposition at 3564 Hz using MST compared to the resultant.

In conclusion, the tooth force model based on the integration of AGSF with an angle $\gamma = 2\pi/Z_s$ (slot pitch) is more accurate than $\gamma = \beta$ (tooth tip opening). However, it is only possible to take into account wavenumbers n proportional to Z_s when using the proposed formulae (3.5) and (3.6) instead of the usual small angle approach (3.13).

3.2.2.2 Application with 12s10p

The aim of this section is quantify the errors when using MST to compute lumped tooth force decomposition for the 12s10p benchmark machine presented in Annex A.1. For this purpose, a reference AGSF is computed with the VWP according to the method presented in Section 2.4.2.

This 12s10p electrical machine will be used for all the experimental validations in the following sections. Thus, it is important to study the potential uncertainties raised by each calculation step. In particular, the magnetic forces harmonics $2f_s$ (92 Hz at nominal speed) and $10f_s$ (460 Hz at nominal speed) are the most significant for the e-NVH behaviour of this machine: these harmonics include AGSF of wavenumber $n = \pm 2$ as shown in Fig. 3.7. As discussed in Section 1.1.2, this is a common cause of significant vibration by exciting mechanical modes (2,0) of the stator. Moreover, these harmonics are subject to the modulation effect described in Section 1.4.5. It is therefore interesting to study the contribution of the highest wavenumbers to lumped tooth forces at different frequencies before further analysis.

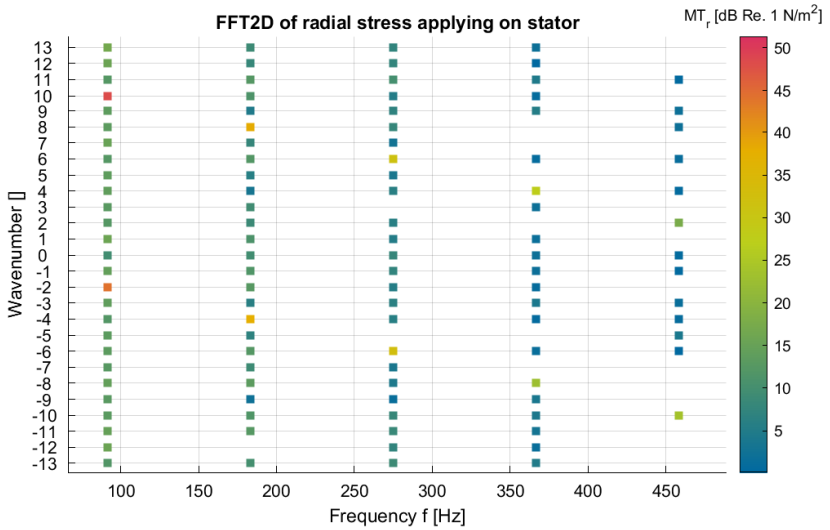

Figure 3.7 – AGSF spectrum based on MST of the 12s10p machine.

As observed in Fig. 3.8, the small angles hypothesis has globally a small effect on the A_n^{rr} coefficient with the exception of the wavenumber $n \propto Z_s$ (in this case, (3.13) is strictly equal to zero). This issue was already discussed in the previous Section 3.2.2. Nevertheless, for other kind of wavenumbers, if the magnetic tangential AGSF is negligible compared to radial AGSF, then the small angles approximation is legitimate.

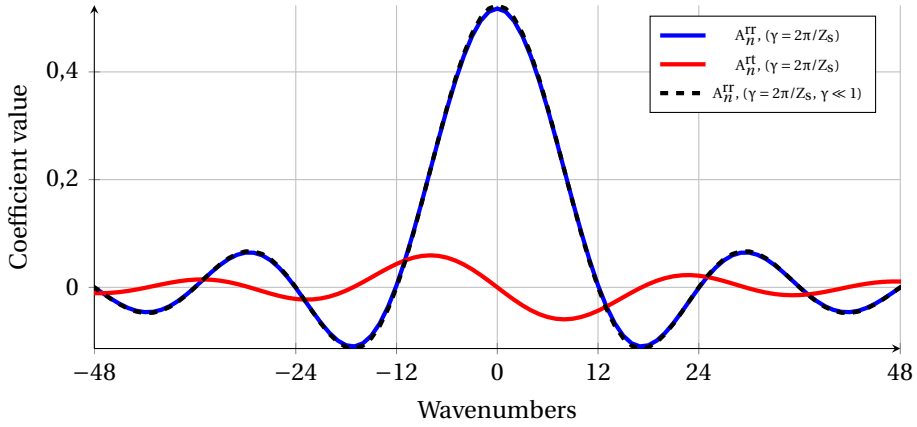

Figure 3.8 – Integration coefficients per wavenumber for lumped tooth force ($Z_s = 12$, $\beta = 12$ [deg]).

Then, the radial and tangential lumped tooth force $2f_s$ harmonic are compared with the reconstruction based on the wavenumber decomposition (3.11) and (3.12). The re-

sults are presented in Fig. 3.9 for the radial direction and in Fig. 3.10 for the tangential direction. The wavenumbers are sorted by constructive (positive values) and destructive (negative values) interferences. There is a good agreement between MST and VWP with a difference of less than 5% for the radial direction, and less than 10% on the tangential direction. Moreover, the significant wavenumbers are ordered similarly with both methods.

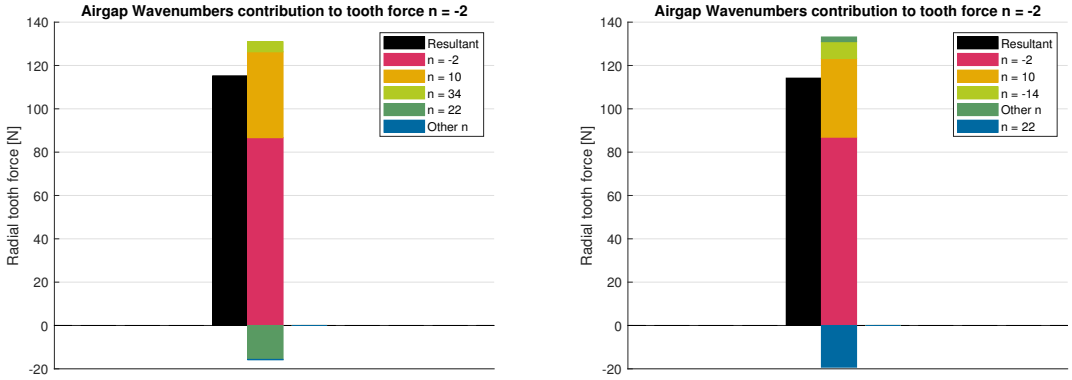

(a) MST (b) VWP-S

Figure 3.9 – Radial lumped tooth force decomposition at $2f_s$.

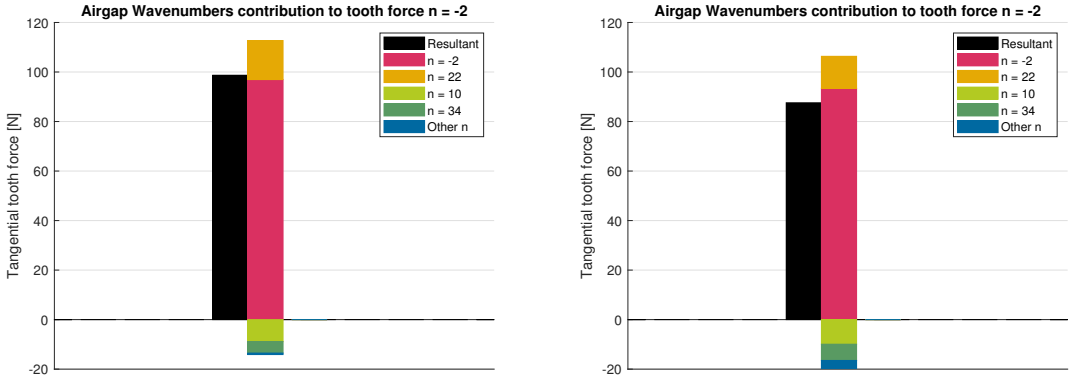

(a) MST (b) VWP-S

Figure 3.10 – Tangential lumped tooth force decomposition at $2f_s$.

The same analysis at $10f_s$ is presented in Figs. 3.11-3.12. The comparison is less favourable to the use of MST as it could lead to overestimate vibration by 10 dB (+330 %). Moreover, the contribution of the different wavenumbers is significantly different: the three mains wavenumbers are the same (-10, 14, 50) but ordered differently. Thus, the use of MST to study e-NVH reduction at $10f_s$ may not be an optimal strategy for this machine.

In conclusion, the accuracy of lumped tooth force calculation based on MST was studied. The conclusion of this work is that only an angle of integration equal to the slot pitch allows the forces per tooth to be correctly integrated. Nevertheless, differences may still exist compared to the VWP. These differences can be explained by the nature of the MST approximation which was discussed in Section 1.3.2: there is no reason for the lumped

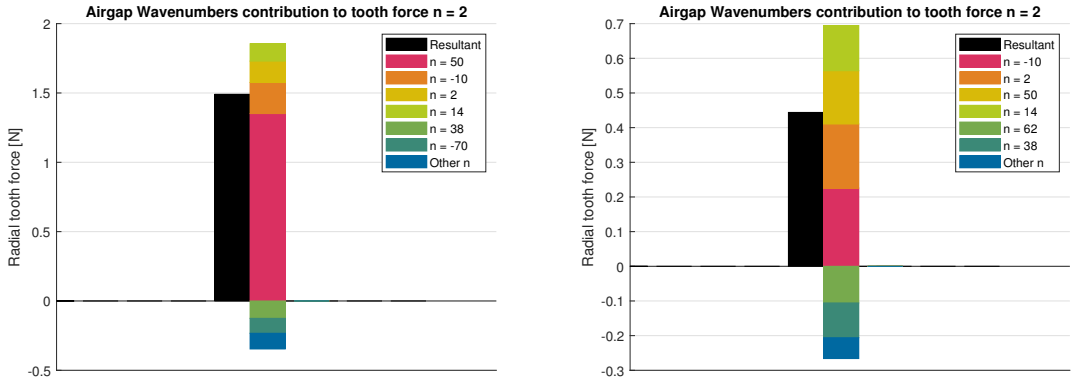

(a) MST (b) VWP-S

Figure 3.11 – Radial lumped tooth force decomposition at $10 f_s$.

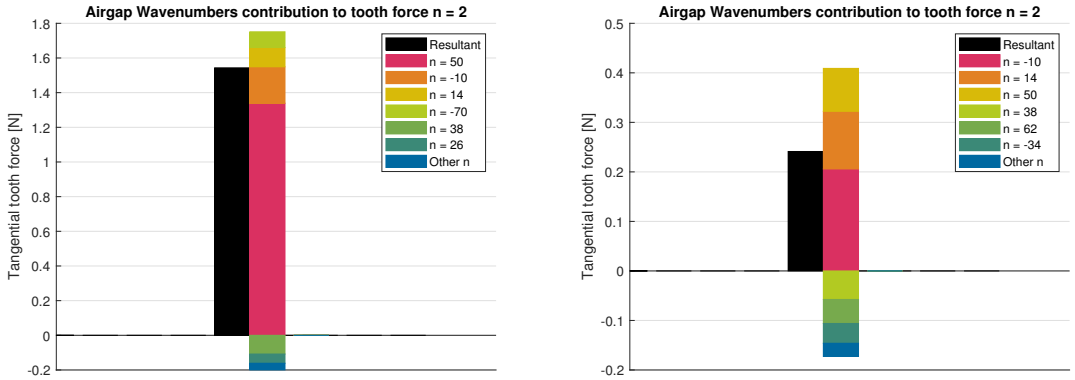

(a) MST (b) VWP-S

Figure 3.12 – Tangential lumped tooth force decomposition at $10 f_s$.

tooth force computed with MST to be accurate since the chosen integration path is not closed around each tooth.

3.3 Hybridization with Experimental Measurements

This section focuses on the methods which enable to include experimental FRF in the e-NVH simulation process. The results of this section are published in [Pile et al., 2020a, 2019; Degrendele et al., 2020a].

The FRF characterizes the response of a given structure to a given load over a whole frequency range. The transfer path between the point of application of magnetic forces (tip of stator teeth) and the vibrating surface (stator yoke outer surface) is considered to effectively characterize the vibroacoustic behaviour. FRF is then from load to acceleration. Thus the relevance of using FRF in modelling the mechanical response depends on the loading strategy. In particular, the wave-FRF [Boesing et al., 2010] and the tooth-FRF [Saito et al., 2016] are two methods used to model the response of an electrical machine to the magnetic force excitation. In both methods, lumped tooth forces are considered to load the structure.

The classical method is to perform experimental modal analysis of each part of the electrical machine, in order to find the proper combination of mechanical properties (Young modulus, Shear modulus, etc.). Then, the contact modelling between each subpart can be fitted as well, depending on the experimental modal analysis of the mounted machine. This process (illustrated in Fig. 1.25) allows to obtain an accurate simulation of the mechanical response compared to experiments. Then, the wave-FRF method as presented in Section 1.4.3 can be applied to troubleshoot the e-NVH behaviour.

The wave-FRF consists in loading all teeth at once with a spatial excitation of wavenumber n. The wave-FRF is generally performed using one lumped force vector per tooth. The wave-FRF method allows us to diagnose e-NVH sources based on the analytical analysis of the different electromagnetic sources. However, wave-FRF is hardly measurable through direct experimental measurements because in real electrical machines several wavenumbers coexist at a same frequency in almost every topology.

On the other hand, the tooth-FRF consists in loading a single tooth per simulation (or experiment) with a normalized frequency vector as explained in Section 1.4.4. The experimental tooth-FRF can be obtained by impacting a tooth with an impact hammer and measuring its external yoke vibration response with accelerometers normalized by the injected force. Hence the experimental set-up is fairly reduced as the experiments only require to have the devices to perform experimental modal analyses (hammer and accelerometers) but without the post-processing algorithms.

This section proposes to define a Tooth Wave Frequency Response Function (TWFRF) method which generates an artificial wave-FRF based on tooth-FRF measurements. The main interest of the TWFRF is to enable the import of experimental tooth response in order to numerically simulate the vibration and noise emitted by the machine during operation. Thus, it is a complementary tool to the workflow based on mechanical FE analysis. The method relies on the small angle hypothesis to simplify the interpretation.

In order to validate the method, the experimental protocol to measure tooth-FRF is presented. Then the vibration on the external yoke surface is simulated for a run-up and compared with direct measurements and FE simulations for the 12s10p machine from Section A.1.

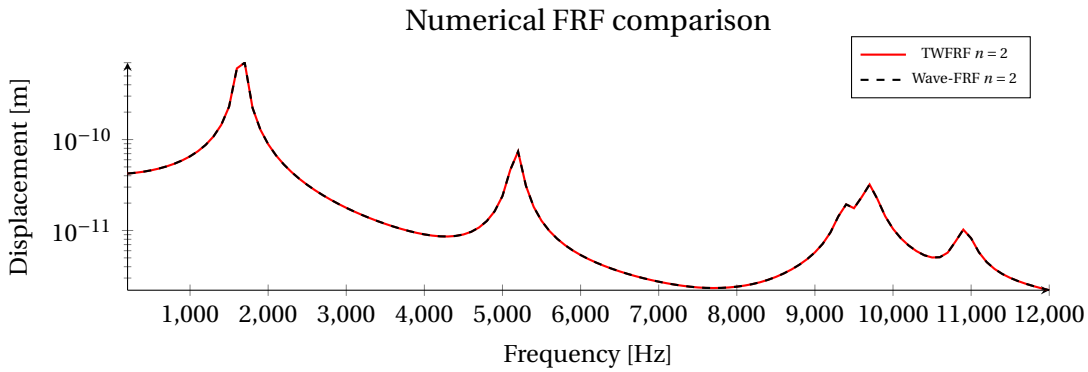

Figure 3.13 – Numerical comparison of displacement between wave-FRF method and TWFRF method.

3.3.1 Tooth Wave Frequency Response Functions

3.3.1.1 Principle

The TWFRF method consists of using the tooth-FRF results to synthesize an experimental wave-FRF. Considering the radial tooth-FRF denoted $\mathrm{TFRF}_{\mathrm{r},i,k}(\omega)$ for each tooth $i \in [1, \mathrm{Z_s}]$ and each impact point on the yoke $k \in [1, \mathrm{K_h}]$, the response to a unit excitation of wavenumber n is reconstructed a posteriori with

$$\mathrm{FRF}_{\mathrm{r},k}(n,\omega) = \sum_{i=1}^{i=\mathrm{Z_s}} \mathrm{TFRF}_{\mathrm{r},i,k}(\omega)\, \mathrm{e}^{jn\alpha_i} \tag{3.17}$$

$$\mathrm{FRF}_{\theta,k}(n,\omega) = \sum_{i=1}^{i=\mathrm{Z_s}} \mathrm{TFRF}_{\theta,i,k}(\omega)\, \mathrm{e}^{jn\alpha_i} \tag{3.18}$$

The result $\mathrm{FRF}_{r,k}(n,\omega)$ and $\mathrm{FRF}_{\theta,k}(n,\omega)$ are called TWFRF as they correspond to the displacement response at a point k on the yoke to a unit (radial or tangential) tooth force wave. Thus, any excitation wavenumber can be artificially reproduced.

By construction, it should be equivalent to the unit wave-FRF presented in Section 1.4.3 when considering numerical simulations. Thus, a validation of the principle of the method is carried out using purely numerical results with a linear mechanical FE analysis for both wave-FRF and tooth-FRF. The results are presented in Fig. 3.13: as expected there is a perfect match between the wave-FRF and the synthesized TWFRF thanks to the mechanical linearity of the simulation.

An equivalent formula can be used for the longitudinal wavenumbers, in order to take into account the non-uniform excitation (for example in skewed electrical machines). This aspect is further developed in Degrendele et al. [2020a].

3.3.1.2 Experimental Application

The main interest of the TWFRF method comes from the compatibility with experimental measurements. It is a complementary approach to the fitting of the FE model with experimental modal analysis. Indeed, the previous tooth-FRF can be measured experimentally on electrical machines. In this thesis, the tooth-FRF is measured between the tooth tip and the stator yoke. In the general case the methodology could be applied between the tooth tip and any noise radiating surface. The tooth-FRF measurements can be performed using an impact hammer on the tip of the teeth while measuring the

deflection on the yoke with an accelerometer. The results of these measurements are available online as part of the open-data benchmark project [Degrendele et al., 2020b]

Then the equivalent wave-FRF can be built using (3.17) and (3.18). However, the impact area on tooth tip is more or less accessible depending on the topology, especially for the tangential direction. As a consequence, the mechanical reciprocity principle [Holland and Fahy, 1997; Avitabile, 2001] is introduced in the methodology to solve this last issue. Assuming that the mechanical behaviour of the machine is linear, the reciprocity principle states that impacting the tooth and measuring the yoke deflection can be equivalent to impacting the yoke and measuring the tooth deflection as illustrated in Fig. 3.14. Hence, the experimental protocol is much more feasible because a small accelerometer can be placed on the tooth tip and the external surface is much more accessible for the impact hammer.

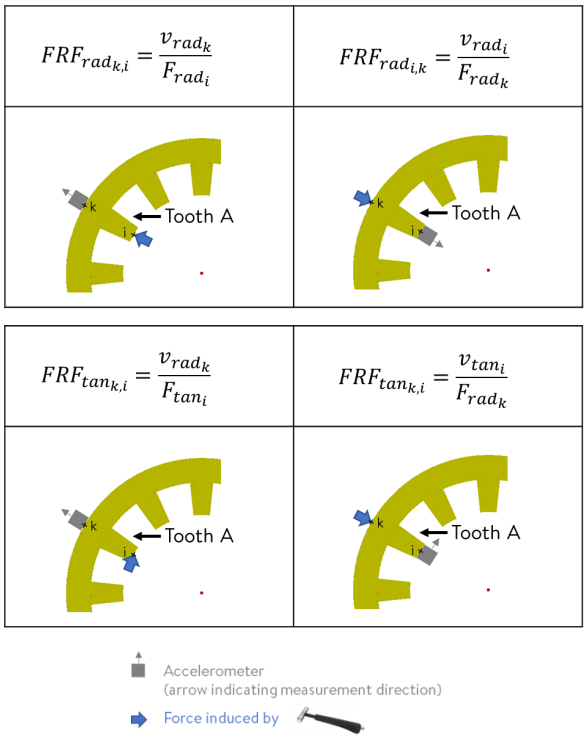

Figure 3.14 – Reciprocity principle for tooth-FRF measurements: v is the measured acceleration (or velocity), F_{rad} and F_{tan} are the imposed excitations [Degrendele et al., 2020a].

Experimental measurements are performed using 12 accelerometers glued on every tooth tip (see Fig. 3.15) in successively four different planes perpendicular to the axial direction of the machine as described in Fig. 3.16.

Both radial and tangential accelerations are monitored while successively impacting the 96 points of the external stator envelope. All measurements are carried with OROS OR38 32 channel and OR35 10 channel acquisition systems. Since axial excitations are neglected in this thesis, the response is averaged on the four planes. This is leading to 2304 different FRFs (96 impact points, 12 teeth, 2 directions) used for this study. Examples of radial stator tooth-FRF are given in Fig. 3.17: measured acceleration does not tend towards 0 due to measurements uncertainty and material limitations. This is an issue when considering low frequency, as it will artificially increase the computed displacement.

The validity of the principle is verified in Fig. 3.19: an FRF between the tip of a tooth

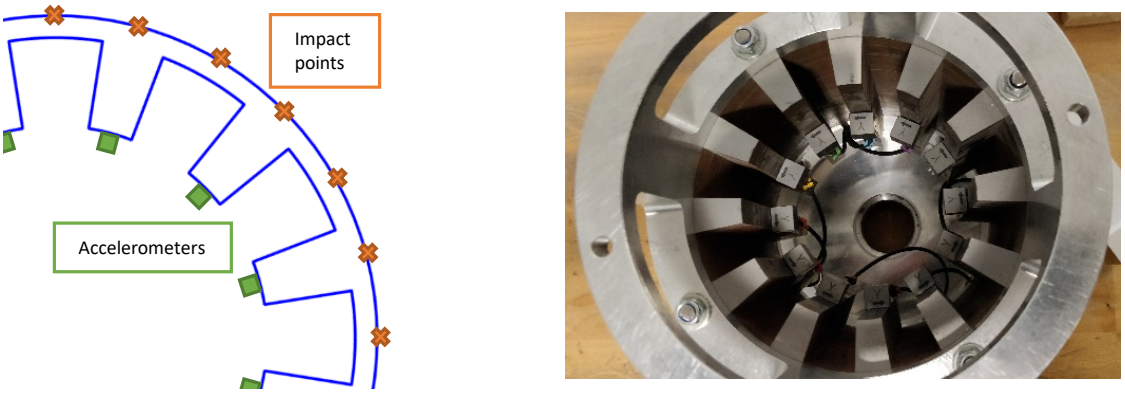

Figure 3.15 – Benchmark 12s10p SPMSM for tooth-FRF measurement: K_h = 96 impact points evenly spaced on the yoke for 12 tri-axis accelerometers (1 on each tooth tip).

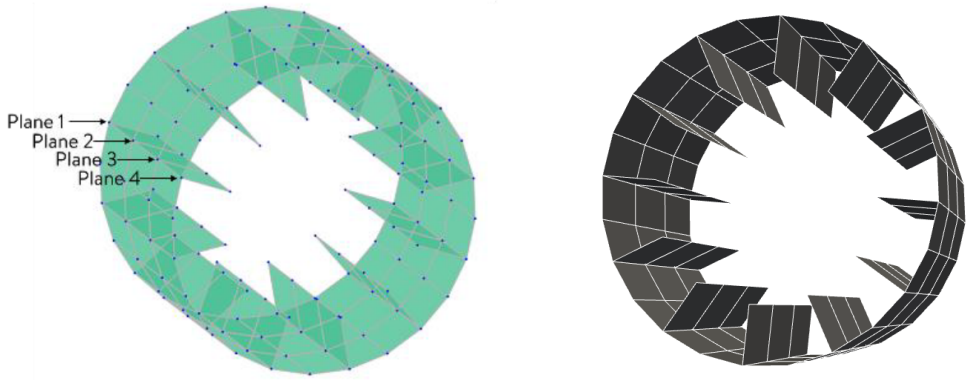

Figure 3.16 – Mesh of the FRF measurements.

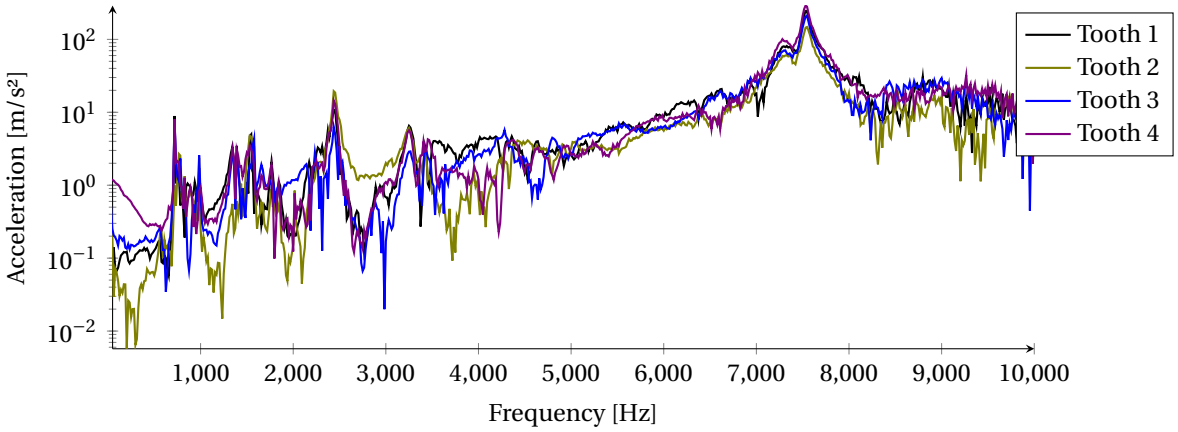

Figure 3.17 – Radial acceleration for several teeth from tooth-FRF.

and the yoke was measured in both configurations presented in Fig. 3.14 which leads to the same results below 8 kHz.

If the measured radial displacement on the tooth number i after each impact on yoke's point k is denoted $\mathrm{TFRF}_{\mathrm{r},i,k}(\omega)$, then according to the mechanical reciprocity principle:

$$\mathrm{TFRF}_{\mathrm{r},i,k}(\omega) = \mathrm{TFRF}_{\mathrm{r},k,i}(\omega) \tag{3.19}$$

Thus, tooth-FRF measurements are carried out with an accelerometer placed as in Fig. 3.15

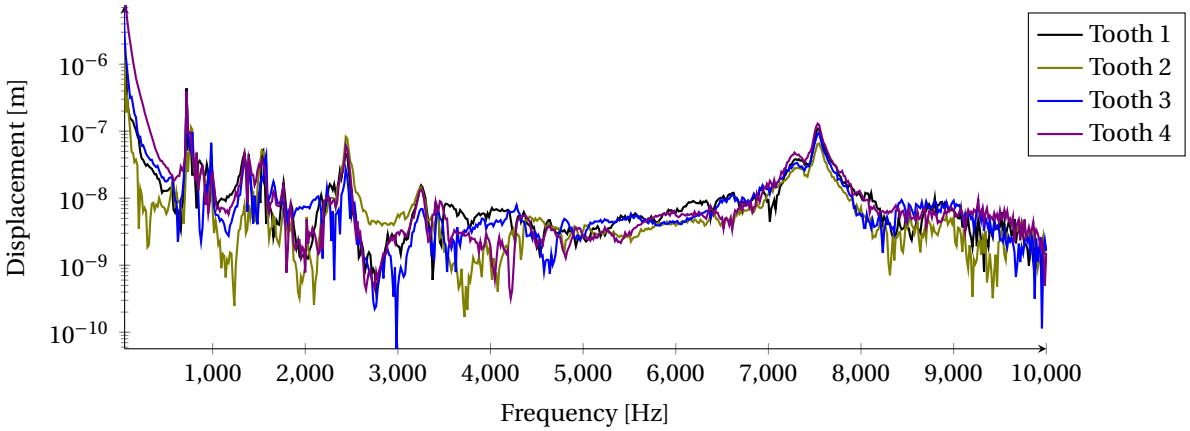

Figure 3.18 – Radial displacement for several teeth from tooth-FRF.

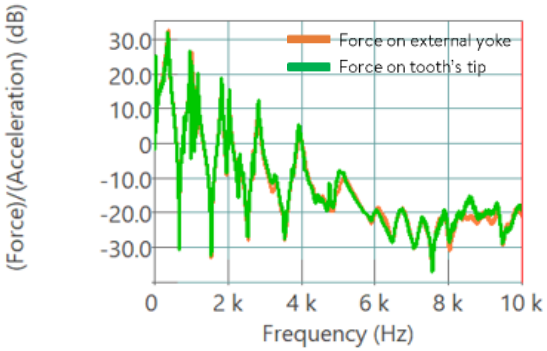

Figure 3.19 – Validation of the reciprocity principle for tooth-FRF measurements [Degrendele et al., 2020a].

to ease the use of the impact hammer. $K_h = 96$ different points evenly spaced on the outer surface of the stator are measured (24 per plane).

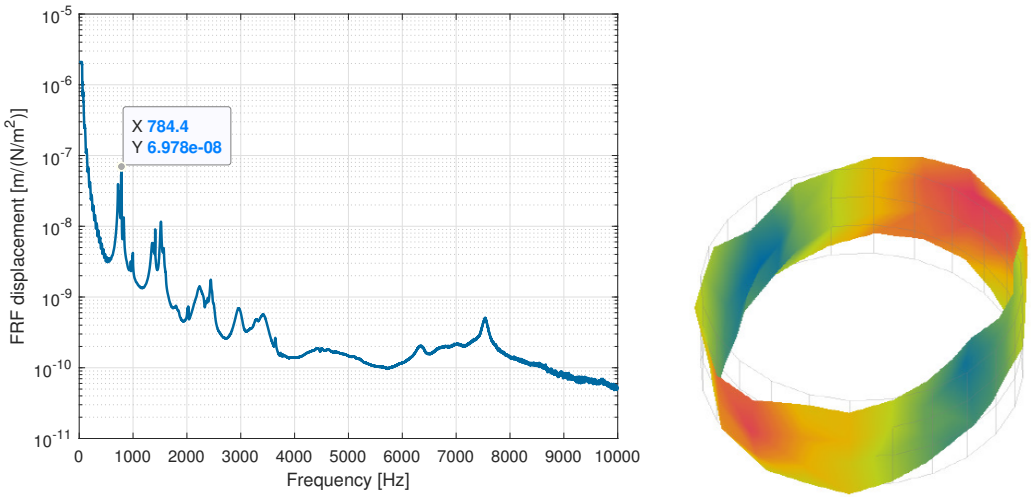

(a) RMS

(b) Deflection shape

Figure 3.20 – Displacement on the external yoke from TWFRF for wavenumber n=2 generated with MANATEE from experimental tooth-FRF.

Once these measurements are carried out, the experimental displacement $TFRF_{r,i,k}$

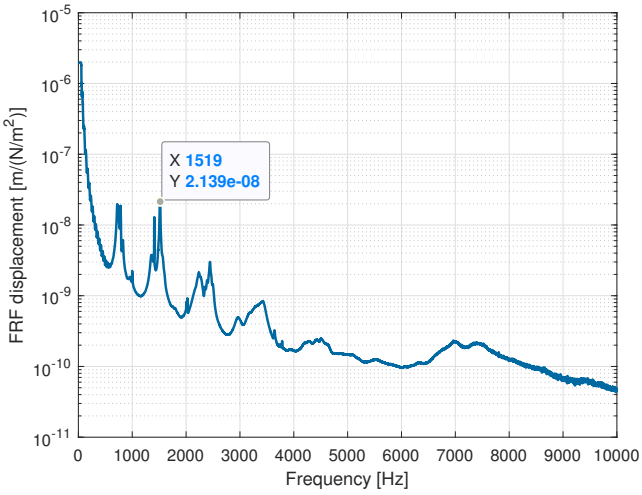

(a) RMS

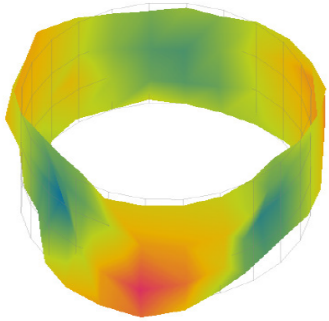

(b) Deflection shape

Figure 3.21 – Displacement on the external yoke from TWFRF for wavenumber n=3 generated with MANATEE from experimental tooth-FRF.

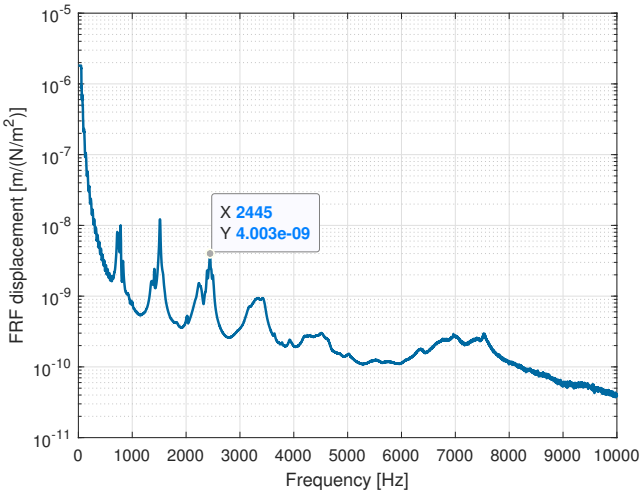

(a) RMS

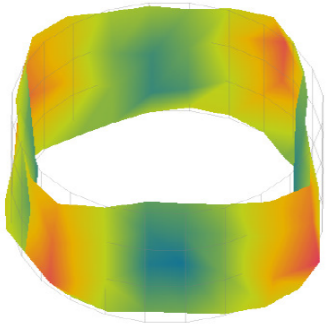

(b) Deflection shape

Figure 3.22 – Displacement on the external yoke from TWFRF for wavenumber n=4 generated with MANATEE from experimental tooth-FRF.

is obtained. Then the TWFRF can be computed using (3.17) and (3.18). It leads to the results presented in Figs. 3.20-3.24: for each wavenumber, the displacement average amplitude is plotted next to the corresponding deformation map. To ease the reading, only the RMS value is plotted:

$$\mathrm{FRF}_r(n,\omega) = \sqrt{\sum_{i=1}^{\mathrm{K_h}} |\mathrm{FRF}_{r,k}(n,\omega)^2| / \mathrm{K_h}} \tag{3.20}$$

Another way to check the validity of the TWFRF method is to compare the frequency of the peak-value for each wavenumber with experimental modal analysis. It is worth noting that the experimental modal analysis was performed with the mounted rotor.

This comparison is performed in Table 3.1: it shows a good correlation suggesting that natural frequencies are correctly captured by the tooth-FRF measurements. It

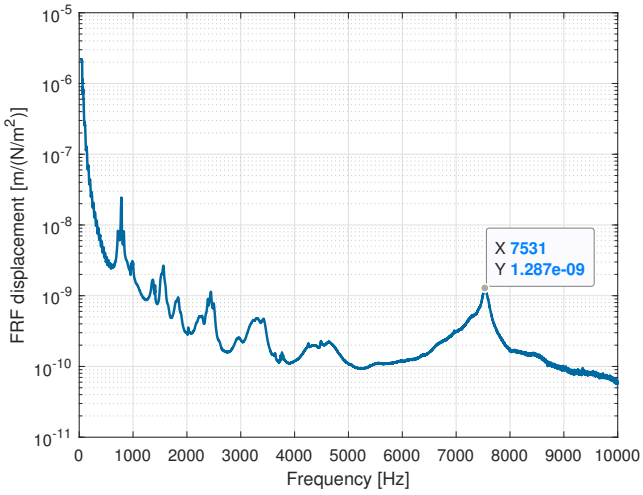

(a) RMS

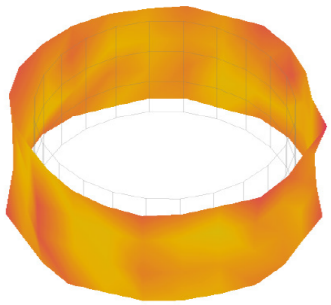

(b) Deflection shape

Figure 3.23 – Displacement on the external yoke from TWFRF for wavenumber n=0 generated with MANATEE from experimental tooth-FRF.

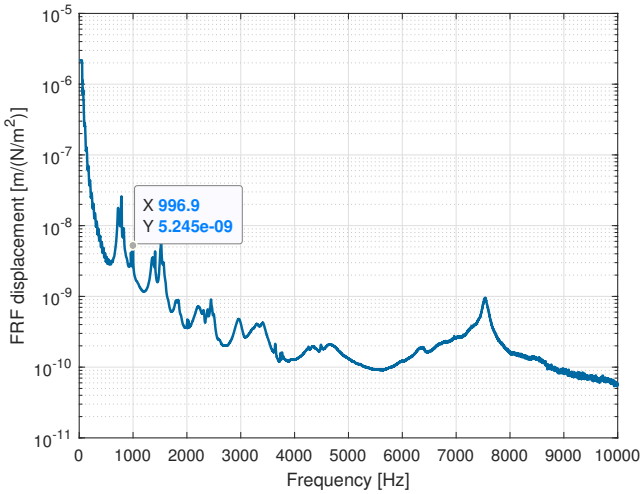

(a) RMS

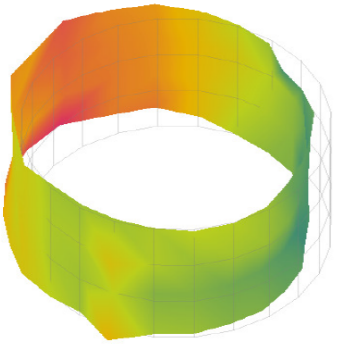

(b) Deflection shape

Figure 3.24 – Displacement on the external yoke from TWFRF for wavenumber n=1 generated with MANATEE from experimental tooth-FRF.

means that the main electromagnetic noise phenomena - such as resonances - should be correctly modelized when applying the corresponding magnetic force wave amplitude.

Table 3.1 – Comparison of experimental modes and TWFRF predicted resonance

Mode number	TWFRF	EMA (Ref)	Deviation
(0,0)	7542 [Hz]	7583 [Hz]	-1 %
(2,0)	731 [Hz]	741 [Hz]	-1 %
(1,0)	997 [Hz]	1087 [Hz]	-9 %
(3,0)	1517 [Hz]	1532 [Hz]	-1%
(4,0)	2450 [Hz]	2474 [Hz]	-1 %

Nevertheless, the discrepancy between the TWFRF and experimental analysis may be influenced by the rotor mounting. Indeed, the rotor has to be dismounted to per-

form the tooth-FRF measurements. The rotor has two ways to influence the benchmark mechanical behaviour: through the bearings, and through strong magneto-mechanical coupling as the magnets pulling force may influence the modal behaviour of the structure. Then, these influences could explain the larger deviation observed for the mode (1, 0) since it is known to be more sensitive to boundary conditions.

3.3.2 Comparison with Experiments

3.3.2.1 Run-up Acceleration from Simulation

The TWFRF is used as a mechanical input in a simulation performed with MANATEE software [EOMYS ENGINEERING, 2020] in order to check the validity of the method. The vibration can be computed on all previous K_h points based on the electromagnetic simulation. The magnetic tooth force wave $\hat{F}_r(n,\omega)$ is computed from (3.11) to be applied on the mechanical response to get the operational deflection spectrum RMS according to

$$Y(\omega) = \sqrt{\sum_n \sum_m \hat{F}_r(n,\omega)\hat{F}_r^*(m,\omega) \sum_{i=1}^{K_h} FRF_{r,k}(n,\omega)FRF_{r,k}^*(m,\omega)/K_h} \tag{3.21}$$

where $\hat{F}_r^*$ and $FRF_{r,k}^*$ are respectively the complex conjugates of $\hat{F}_r(n,\omega)$ and $FRF_{r,k}$. Considering $FRF_{r,k}(n,\omega)$ is obtained using the tooth-FRF experimental measurement and (3.17), $Y(\omega)$ is an hybrid prediction of the yoke displacement based on both mechanical measurements and magnetic force numerical simulation. This is called the TWFRF vibration synthesis. The AGSF spectrum used in this simulation is presented in Fig. 3.7.

Simulation and experimental results are presented under the form of a spectrogram in Fig. 3.25: the visible excitations correspond to harmonic content proportional to the electrical frequency f_s. In particular, $2f_s$, $4f_s$ and $10f_s$ are the main excitations. The $2f_s$ and $4f_s$ excitations are below any natural frequency in the tested speed range such that the vibration is only due to forced mechanical response. However the $10f_s$ excitation hits a natural frequency at 736 Hz and 892 RPM. It can be guessed from Table 3.1 that a resonance has occurred with mode (2,0). To a lesser extent, the (1,0) mode is excited by the $10f_s$ around 1000 Hz.

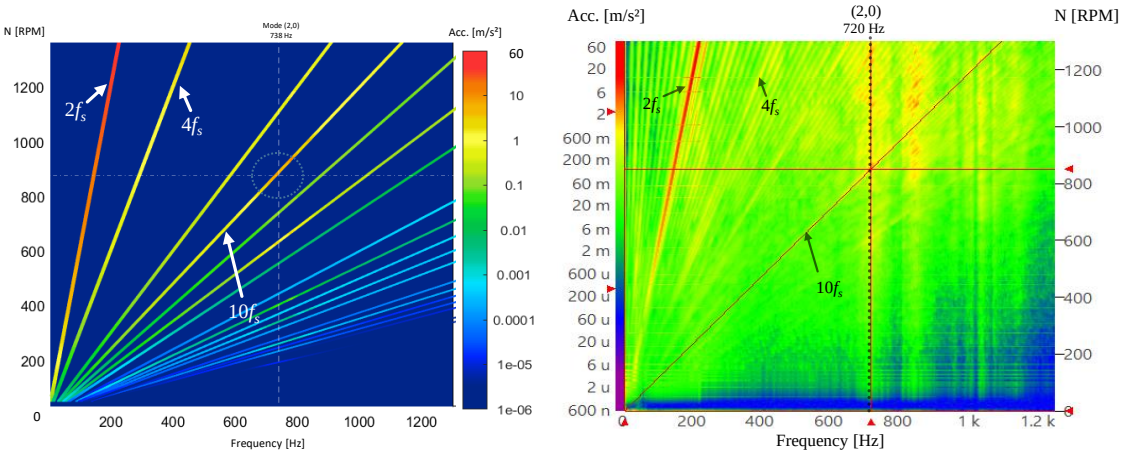

(a) Hybrid TWFRF

(b) Experimental run-up Measurements

Figure 3.25 – Spectrograms for the 12s10p prototype.

3.3.2.2 Spectrograms & Order Tracking

The goal of this section is to validate the previous predictions from the simulation based on tooth-FRF measurements. For this purpose, the experimental acceleration spectrum is measured at various rotation speeds on the benchmark using the experimental setup presented in Fig. 3.26.

Measurement results of one run-up are presented under the form of a spectrogram on the right side of Fig. 3.25 and it can be compared to the simulation on the left side. Indeed the main phenomena can be found back: the $2f_s$, $4f_s$ and $10f_s$ are again the main excitations, and the $10f_s$ excitation causes a resonance around 720 Hz at approximately 850 RPM. The excitation of the mode (1,0) is also visible around 850 Hz. However, the excitation of the mode (1,1) at 1150 Hz is not detected by the simulation since 3D excitations are not considered in this work.

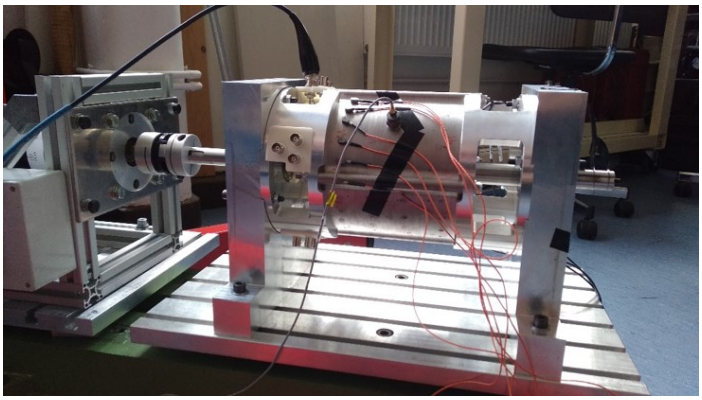

Figure 3.26 – Experimental setup for acceleration measurements during run-up on the prototype 12s10p SPMSM

In order to refine the comparison, the TWFRF-based vibration synthesis is compared to direct measurements along an order of spectrograms from Fig. 3.26 and Fig. 3.25. The results are presented in Fig. 3.27 at $10f_s$ and $2f_s$. The prediction of the $2f_s$ from TWFRF is not satisfying because of the inaccuracy of the tooth FRF measurements at low frequencies. One solution could be to (artificially) chose a cut-off frequency, such that the low frequencies are approximated by a constant curve starting at the foot of the first peak of each wave-FRF. This method allows us to obtain a better shape for the $2f_s$ order as illustrated in Annex B.6, but the obtained level completely depend on the chosen cut-off frequency. This issue should be the subject of future research work.

The result obtained for the order $10f_s$ is more interesting: both TWFRF vibration synthesis and direct run-up measurement have the same behaviour. A zoom on the order $10f_s$ is made in Fig. 3.28, and the results which would be obtained without modulation effect is added. The TWFRF simulation underestimates the vibration level. The main natural frequencies seems to have stayed

First, the main e-NVH phenomenon that is observed is the resonance with the two different (2,0) modes in Fig. 3.28 around 880 rpm. Another resonance is observed for the run-up around 1800 rpm in Fig. 3.28 with the mode (3, 0) which is excited. The last peak at 2700 rpm correspond to the mode (4,0).

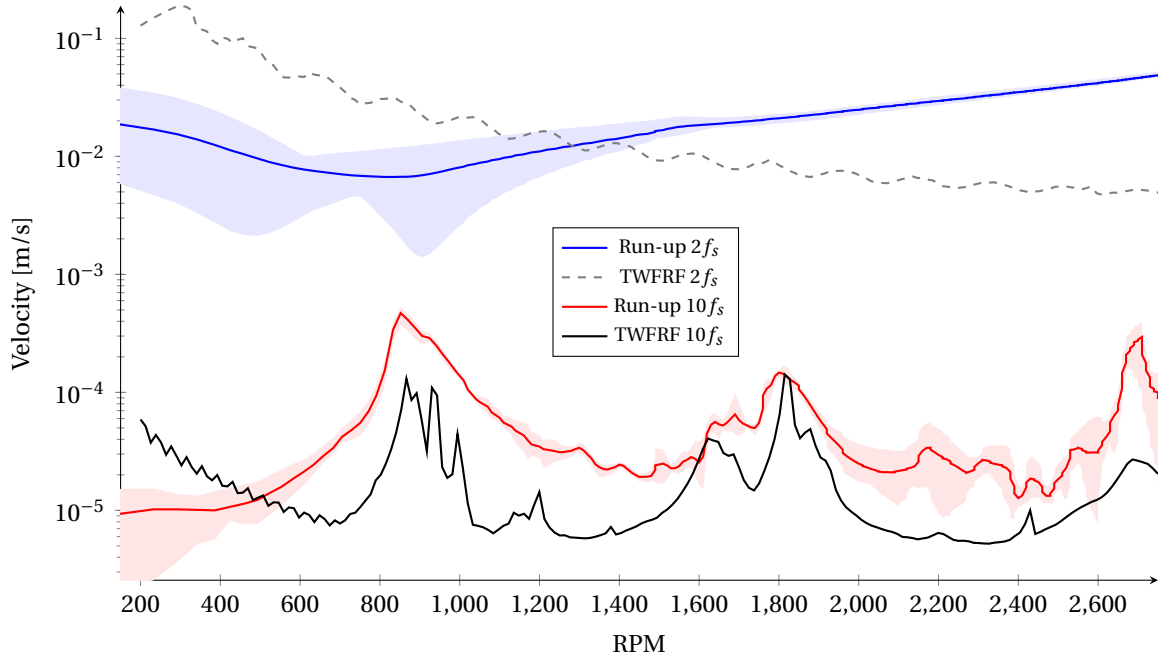

Figure 3.27 – Comparison of the order tracking between the direct measurement during a run-up and the hybrid simulations based on the TWFRF method.

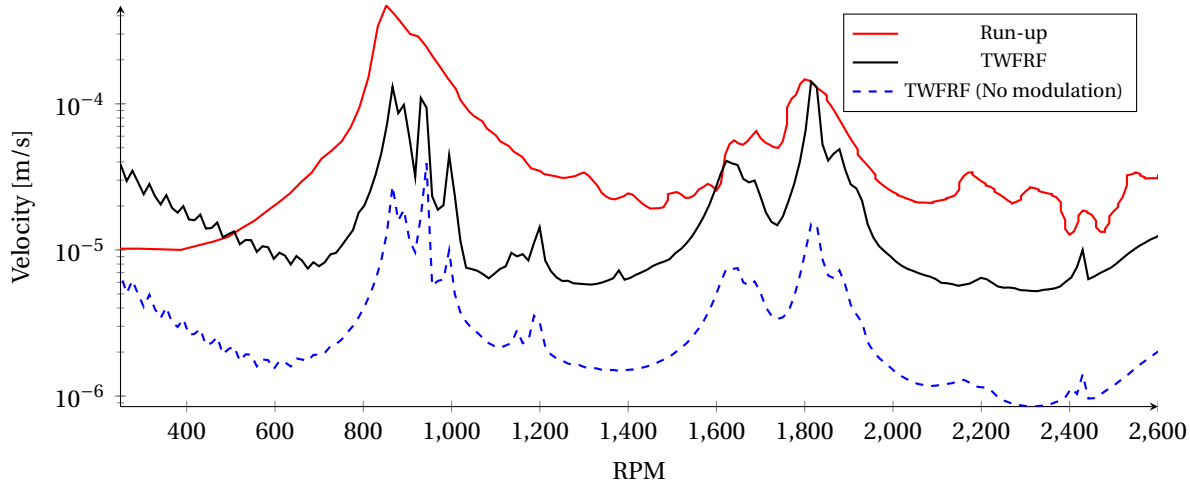

Figure 3.28 – Comparison of the order tracking at $10f_s$ between the direct measurement during a run-up and the hybrid simulations based on the TWFRF method.

3.3.3 Discussion

These vibration predictions and experiments based on tooth FRF allowed us to identify the resonance in the 12s10p machine. The main excited natural frequencies seems to have been correctly estimated from the tooth-FRF measurements, meaning the influence of temperature on natural frequencies was negligible (at least during the 20 minutes needed for the run-up measurements). However, some significant differences remained and there were many sources of experimental uncertainty such as:

— Accuracy of the tooth-FRF measurement: the FRF measurements were performed

by hand with an impact hammer, such that the excitations could have not been only radial on the external surface.

— Accuracy of accelerometers position and alignment (matching with radial and tangential direction) could have significant impact on the result.

— Mounting/Dismounting repeatability: The sheet of the lamination were held together by the ears of the stator and also by the friction between the leaves. Unfortunately, significant differences could be observed depending on the run-up, which could be attributed to the uncertainty of the mounting.

— Homogeneity of the lamination in the axial direction (related to the mounting).

— Rotor mounting effect on the bending modes and longitudinal modes.

— Eccentricities and unbalanced magnetization. Indeed, the magnetic forces are computed with ideal magnetic excitations, missing the uncertainty of magnets position and magnetization. In future research work, the air-gap magnetic flux density should be measured to adjust the magnetic force model.

— Influence of temperature on mechanical properties.

— B-H law and saturation levels: The BH law was not measured for the tested lamination.

— Driving machine influence through axis excitations.

— The last laminations has started to peel off from the rest of the stack. Although this should remain secondary, it still impacts repeatability via edge effects.

In order to reduce the uncertainties due to lamination and mounting, the stator with ears was replaced by a new version without ears at the end of the thesis (see Fig. A.2 and Fig. 3.29). The ears are removed and instead the different laminations are welded together. It improves the repeatability of the measurements by keeping more uniform properties along the stack. Hopefully, it will improve the correlation between measurements and hybrid TWFRF simulation. Unfortunately, there was not enough time to perform the same type of measurement and simulation on this new stack.

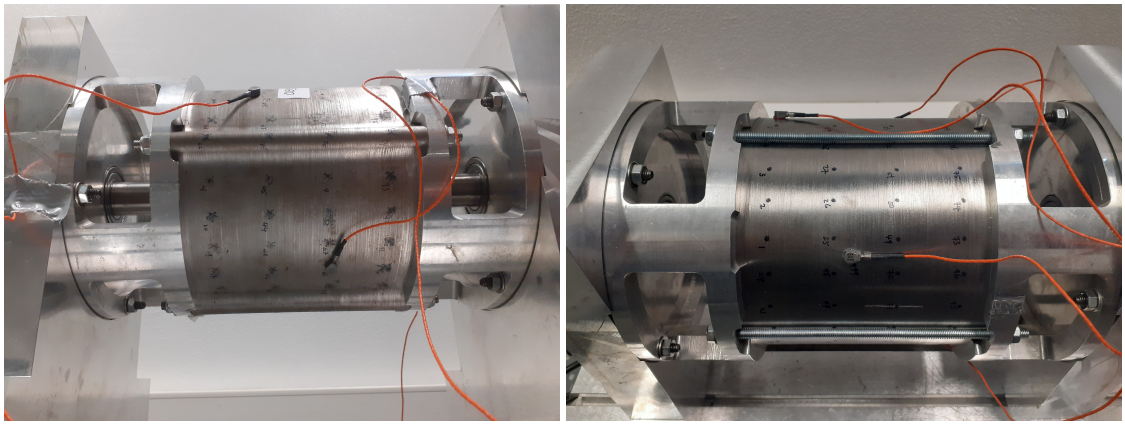

(a) Stator with ears. (b) Stator without ears.

Figure 3.29 – Different mounted versions of the stator.

Finally, uncertainties due to the lumped tooth force modelling could also explain part of the differences. Thus, the aim of the next and last section is to quantify the errors between a distributed loading and a lumped tooth force loading for the e-NVH simulation of electrical machines.

3.4 Comparison with Mesh-to-Mesh Projection

In previous Section 3.2.2, the 2D magnetic mesh was extruded as a 3D prismatic mesh in order to perform mechanical FE simulations with the VWP nodal force loading. This method can be used for stator-only mechanical study or academic applications. However, the electromagnetic mesh of the stator is unsuitable and computationally costly to integrate into a complex FE model in order to: perform the modal analysis fitting, compute e-NVH analysis, perform an optimization, etc. Thus, this section proposes to use mesh-to-mesh projection workflow introduced in Section 1.4.6 in order to load the mechanical model with distributed nodal magnetic forces.

In the whole section, the simulations and analyses are performed on the 12s10p machine described in Annex A.1 in which only magnetic surface force are considered due to very low magnetic saturation. The magnetic field is solved using 2D non-linear magnetostatic FE analysis with MANATEE-FEMM coupling [EOMYS ENGINEERING, 2020]. As expected, the main magnetic force harmonic is at twice the electrical frequency $2f_s$ as shown in Fig. 3.7 (for example $2f_s$ = 92 [Hz] at N = 550 [RPM]). This frequency is used to test the proposed approach of mesh-to-mesh projection as it is known to be responsible for vibro-acoustic issues [Devillers et al., 2018]. The Section 3.4.1 proposes to quantify the errors by comparing tooth forces before and after projection. Once the projection parameters have been judiciously chosen, the Section 3.4.2 proposes to discuss the modulation effect by comparing the vibration response between tooth forces and distributed forces computed with mesh-to-mesh projection.

3.4.1 Sensitivity Study for Tooth Force

The goal of this section is to define a good strategy for choosing the number of Gauss points used to perform mesh-to-mesh projection. It is proposed to define the accuracy of the mesh-to-mesh projection by comparing tooth forces before and after projection. The results of this section are published in [Pile et al., 2020].

The magnetic mesh shown in Fig. 3.30a has been highly refined to serve as a reference for forces calculation. The average number of tooth tip elements is N_θ^{mag} = 13. Since only magnetic surface forces are considered, it is necessary to select the adequate sub-mesh as explained in Section 1.4.6.2. Thus, the nodes at the ferromagnetic-air interface in order to build a new sub-mesh are composed of only 2 nodes lines.

In order to focus on the errors introduced by the integral approximation and the number of Gauss points, a pseudo 2D mechanical mesh composed of quadrilateral is temporarily considered, as shown in Fig. 3.30b. This mesh cannot be used to solve structural harmonic FE, but it allows us to study the mesh-to-mesh projection in a 2D space in adequacy with the magnetic problem. As with magnetic mesh, the edge of the pseudo-mechanical is selected to build a sub-mesh composed of 2 nodes lines. Then, the magnetic shape function (see Annex C.1.1) of both meshes are defined in the same mathematical space as first order polynomials.

The magnetic forces are computed according to (1.71) at every time step. Then the time Fourier transform is computed for each nodal force. Thus, the magnetic nodal forces associated with frequency $2f_s$ can be extracted as shown in Fig. 3.31.

The next step is to compute the magnetic surface force density as explained in Section 1.4.6.1. The result is presented in Fig. 3.32: it is visually smoothed compared to Fig. 3.31 as expected by the change in the nature of the result (from nodal resultant to

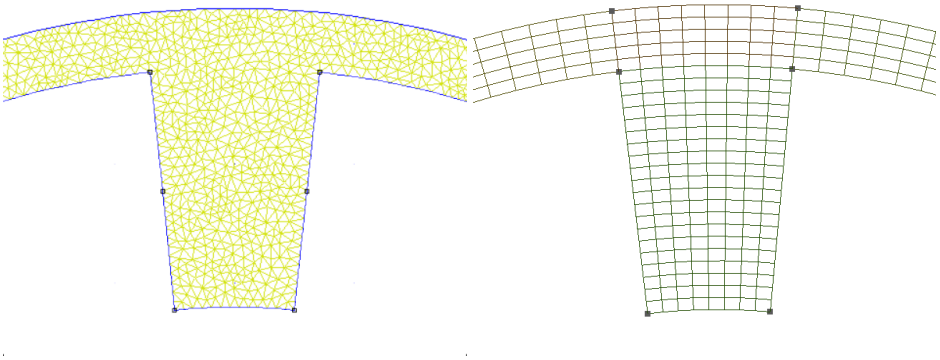

(a) 2D magnetic mesh (b) 2D mechanical mesh

Figure 3.30 – Illustration of the two types of 2D meshing on a tooth.

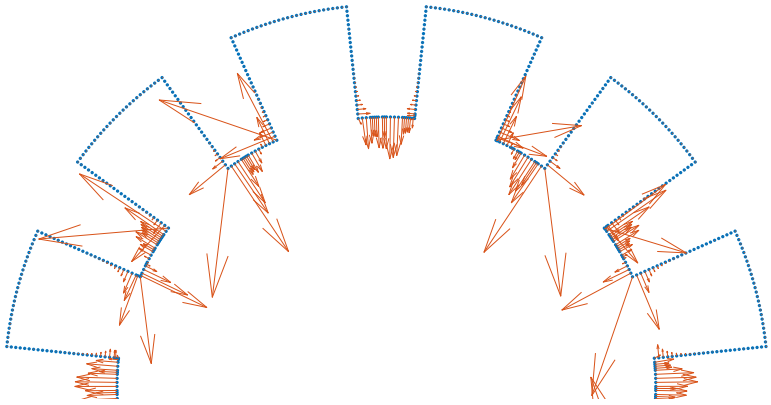

Figure 3.31 – Magnetic nodal forces calculated with the VWP at $2f_s$.

density). It is also possible to note that the dominant wavenumber $n = 10$ predicted by the AGSF in Fig. 3.7 can be observed by counting all the maxima in Fig. 3.32.

Finally the mechanical mesh is read to get the new surface elements for the considered surface force. Then (1.117) and (1.120) can be calculated before solving (1.116). An example of the results computed with the mechanical mesh from Fig. 3.30b is presented in Fig. 3.33. The final step is to compute the magnetic nodal forces on the mechanical mesh [Parent et al., 2008].

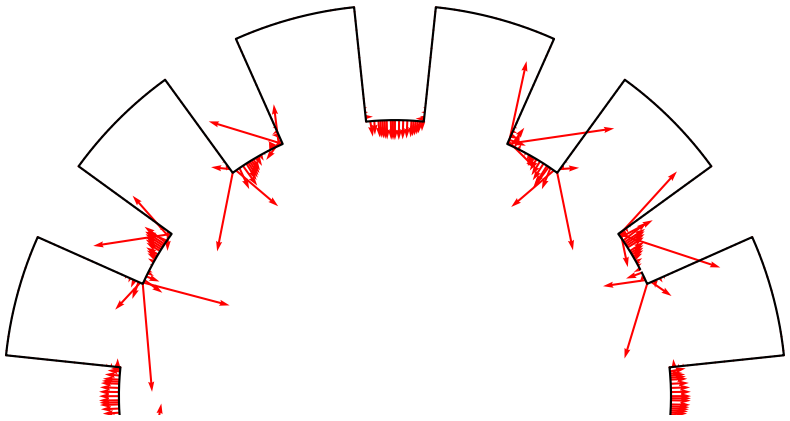

Figure 3.32 – Magnetic surface force density on the magnetic mesh at $2f_s$.

Tooth forces are defined as the sum of all nodal forces per tooth, and applied in the middle of the tooth tip as shown in Fig. 3.34. In this section, the reference is the value of

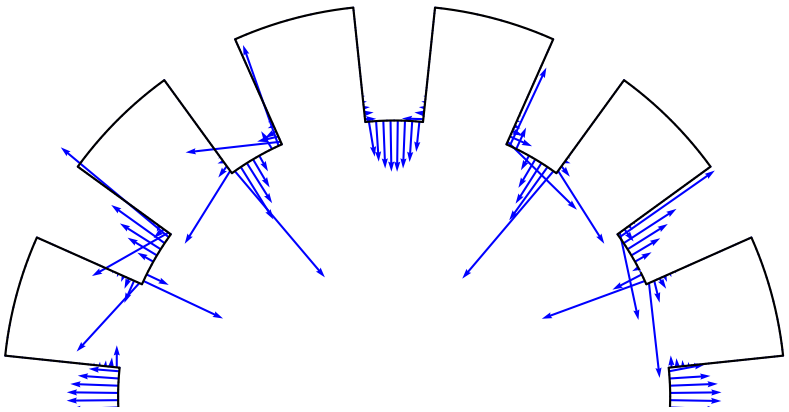

Figure 3.33 – Magnetic surface force density on the mechanical mesh at $2f_s$.

the tooth force computed on the magnetic mesh.

Indeed, tooth forces are commonly used to perform magneto-mechanical coupling [Saito et al., 2016; Fang et al., 2019] as a tool to identify the main eNVH sources. The mesh-to-mesh projection may improve the accuracy of the magneto-mechanical coupling. However, it is necessary to have at least an adequate accuracy regarding tooth forces (and torque) before using the results of mesh-to-mesh projection. Thus, this section proposes to compare tooth forces before and after performing the mesh-to-mesh projection. An example of tooth force distribution is given in Fig. 3.34.

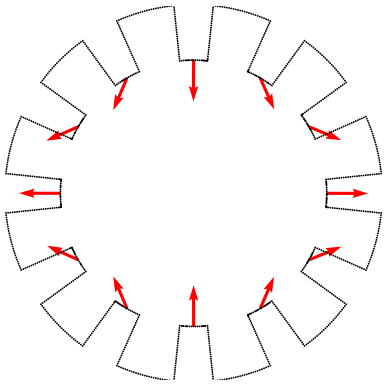

Figure 3.34 – Magnetic tooth forces on the mechanical mesh at $2f_s$

In order to simplify the parametrization of the mechanical mesh, N_θ is defined as the number of divisions on the tip of the teeth. The other parameters of the mesh are calculated from N_θ such that:

$$\begin{aligned} N_{r,\text{yoke}} &= \text{floor}\{N_\theta(R_{sy} - (R_{sbo} + H_s))/H_s + 1\} \\ N_{r,\text{teeth}} &= 2N_\theta \\ N_{\theta,slot} &= \text{floor}\{1.2N_\theta\} \end{aligned} \tag{3.22}$$

with $N_{r,\text{yoke}}$ the number of divisions in the yoke thickness, $N_{r,\text{teeth}}$ the number of divisions in the teeth height, and $N_{\theta,slot}$ the number of angular divisions in the slots. The different possible results are illustrated in Fig. 3.35.

The first value to drive the precision is the number of Gauss points used in (1.120). This study is performed with the magnetic mesh in Fig. 3.30a and several mechanical mesh defined by the mesh size ratio $R = N_\theta/N_\theta^{mag} = N_\theta/13$ between the mechanical mesh and magnetic mesh.

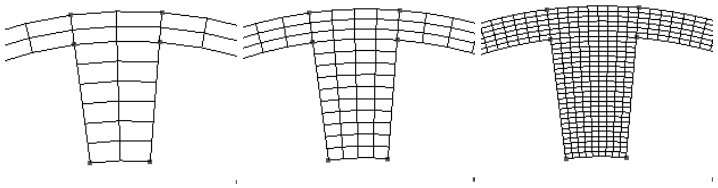

Figure 3.35 – Example of mechanical mesh with thinness ratio R = 2/13, R = 4/13, and R = 9/13 on the tooth tip.

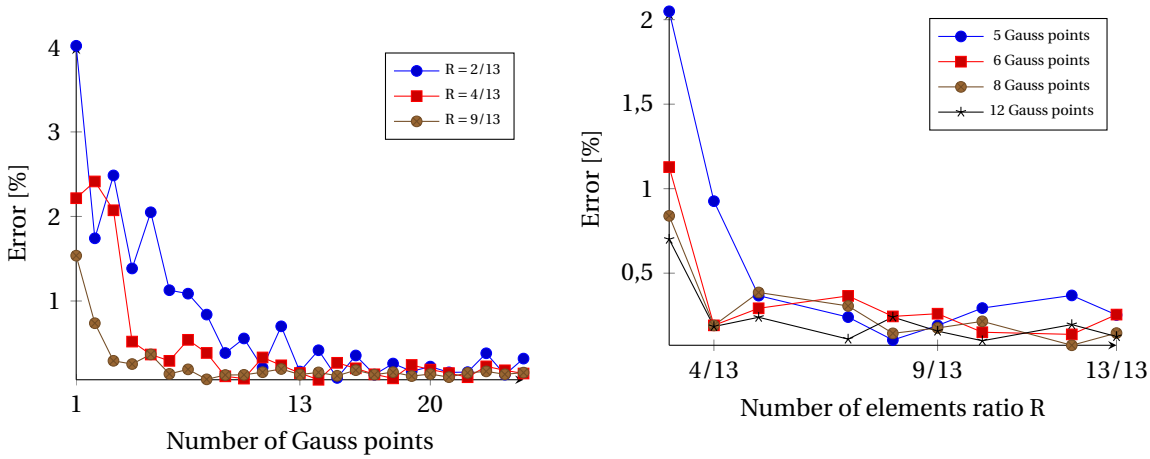

(a) Function of Gauss points number.

(b) Function of mesh size.

Figure 3.36 – Radial tooth forces relative error on the mechanical mesh compared to magnetic mesh at $2f_s$.

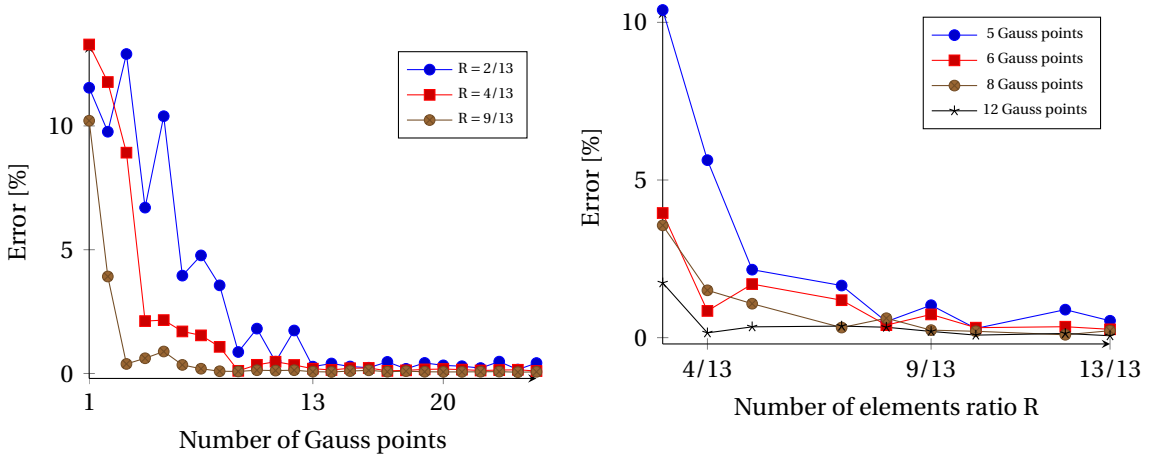

(a) Function of Gauss points number.

(b) Function of mesh size.

Figure 3.37 – Tangential tooth forces relative error on the mechanical mesh compared to magnetic mesh at $2f_s$.

The direction of the magnetic force is important to predict the resulting vibrations. In order to ease the physical interpretation, the magnetic force is generally split into radial and tangential tooth forces defined from the radial direction in the middle of each tooth tip. The results are presented in Fig. 3.36a for the radial tooth force, and in Fig. 3.37a for the tangential tooth force. The projection has a more significant impact on the direction of the magnetic force: if the error on the radial force stay below 4% for all cases, the error on tangential force reaches up to 15% when the number of Gauss points is low.

The error in the radial direction could correspond to $20\log_{10}(1.04) = 0.35$ dB in a vibro-acoustic study, while the error in the tangential direction could correspond to 1.2 dB. But with a high projection error, there is a risk of introducing new purely numerical spatial harmonics which can excite unexpected mechanical modes.

The differences between radial and tangential errors can be explained by their spatial distribution: the tangential force is concentrated very close to the corners. Then the previous Gauss quadrature must be very accurate in this area to correctly capture the strong variations in the tangential force density. The radial force is more evenly distributed on tooth tip such that these errors have less impact. In order to keep the error as small as possible, the choice of the number of Gauss points must be made according to the ratio of the mesh size. In this case, the worst mesh ratio is R = 2/13. In theory, two Gauss points are needed in each magnetic element to exactly compute the integrals since linear shape functions are considered [Stroud and Secrest, 1966]. But here 13 Gauss points per mechanical elements does not ensure an exact integration because the Gauss points of the mechanical mesh do not generally match with the Gauss points of the magnetic mesh (see Section 1.4.6.3). It can explain the slight oscillation of errors in Figs. 3.36a-3.37a: these local error peaks are due to an unfortunate placement of the Gauss points in the magnetic mesh. The same results applied to torque are presented in Annex C.4.

Nevertheless, the error can be fairly reduced by increasing the number of Gauss points [Wang et al., 2016]. The computation cost of each Gauss point is pretty low because it does not influence the size of the system (1.116) to be solved. However, it increases the computational cost of the algorithm which builds the different matrices.

The third parameter to drive the precision is the mechanical mesh size. This study is performed by adjusting the mesh size as a function of angular division, while keeping the shape functions of order 1 for both meshes.

For the tooth force, the results are presented in Fig. 3.36b for the radial direction, and in Fig. 3.37b for the tangential direction. In both cases, there is again a convergence of the error with the fineness of the mechanical mesh. However, this solution is much more expensive because not only it increases the size of the linear system (1.116) to be solved, but it also increases the computation time for solving the mechanical problem. It leads to the solving of two systems of complexity proportional to N^3 with N the number of unknowns [Krishnamoorthy and Menon, 2013].

The last step is to compare the vibration results computed with a lumped tooth force based the nodal forces from the mechanical mesh, and from the magnetic mesh. As explained in Section 3.2.2.2, the outputs of interest are the order tracking at $2f_s$ and $10f_s$. Thus, the nodal forces are filtered to keep only the distributed forces at corresponding frequencies. A resonance with the ovalization modes (2,0) is expected at $10f_s$ according to [Devillers, 2018].

The mechanical mesh is now defined in 3D as illustrated in Fig. 3.38. There is approximately a ratio of 5 elements between the magnetic mesh ($\approx$ 30 per tooth tip) and the mechanical mesh (6 per tooth tip) in this application. Then, a total of 121 gauss points (11 for each Cartesian direction) is used for mesh-to-mesh projection in accordance with the previous conclusions.

In order to simplify the analysis, only the stator lamination is considered in the following calculation, but the whole benchmark geometry was included for the numerical modal analysis (see Annex A.1). The first steps are the same as in Section 3.4.1 with the exception of the mesh-to-mesh projection which is now performed from the 2D magnetic mesh onto the 3D mechanical mesh: the 2D magnetic forces are consid-

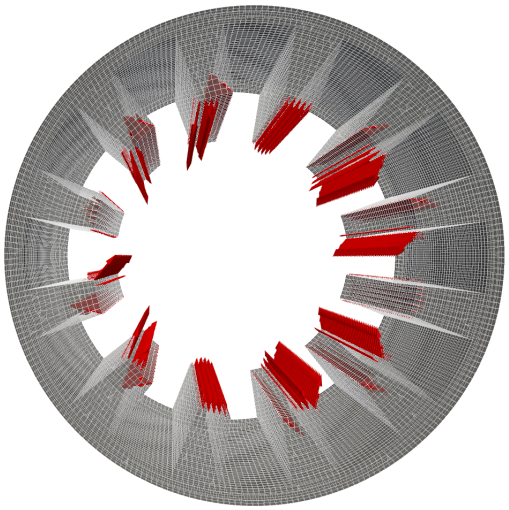

Figure 3.38 – Magnetic nodal forces at $2f_s$ for the 3D mechanical mesh.

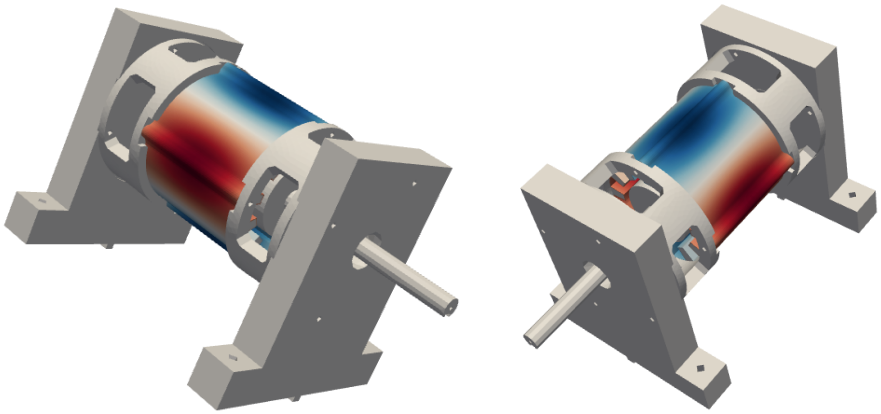

Figure 3.39 – Deflection shape (ovalization) of the stator under the magnetic force at $2f_s$.

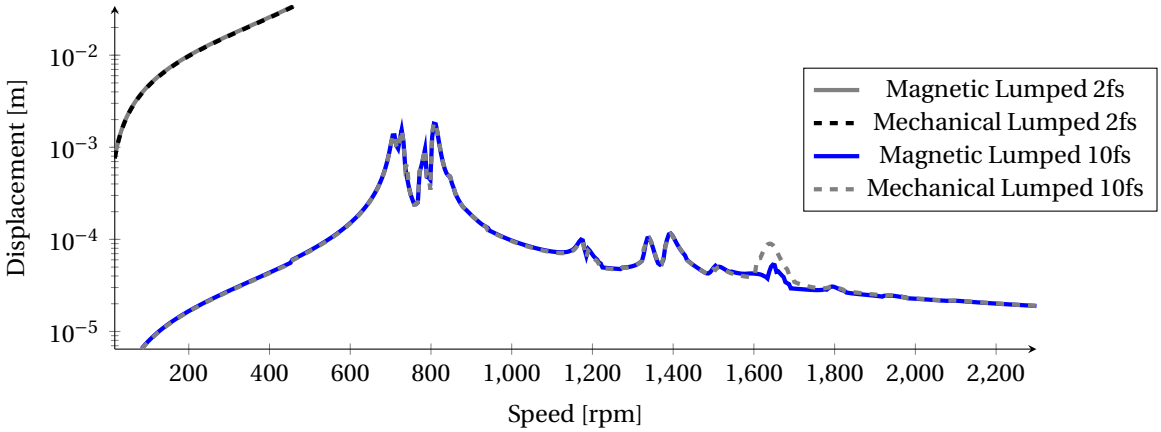

Figure 3.40 – Comparison between lumped tooth forces FRF computed on the magnetic mesh and mechanical mesh.

ered uniform in the axial direction of the machine. The nodal forces are computed on the mechanical mesh, and then the lumped tooth force is computed on the mechanical mesh (denoted Mechanical lumped). The ovalization of the stator yoke under these

forced excitations at $2f_s$ can be observed in Fig. 3.39. The final step is to compare the obtained vibration from the lumped tooth force computed on the magnetic mesh (Magnetic Lumped). The results are presented in Fig. 3.40: the response is almost the same except at 1640 Hz. This frequency corresponds to the natural frequency of the modes (3,0) (see modal analysis in annex, Table A.5). These modes are excited by the mechanical lumped force only. Then, it can be assumed that this particular excitation is coming from numerical error (small unbalanced magnetic forces) introduced by the mesh-to-mesh projection. This point can be verified by comparing the total force acting on the stator before and after mesh-to-mesh projection. The unbalanced magnetic force amplitude at $10f_s$ is 2e−5 N before mesh-to-mesh projection, and 8e−2 N after. It highlights a significant risk of exciting undesired modes by using mesh-to-mesh projection.

Now that the numerical mesh-to-mesh projection error is quantified, the difference between a distributed force model and tooth force model can be studied to conclude about the modulation effect.

3.4.2 Study of Lumped Tooth Force Model

The goal of this section is to study the accuracy of the lumped tooth force model (i.e. one load vector per tooth tip) for the e-NVH simulation. This study is motivated by the previous study of the modulation effect in Section 3.2 and the FRF tooth technique in Section 3.3: in both sections, the central hypothesis relies on the accuracy of a single load vector per tooth tip. Thus, it is proposed to compare the results obtained with lumped tooth forces with a reference simulation based on distributed nodal forces as presented in Section 3.4. At the end of this section, another loadcase is added to the comparison using a complete lumped tooth torsor (lumped tooth force and lumped tooth moment). The three different loadcases are illustrated in Fig. 3.41.

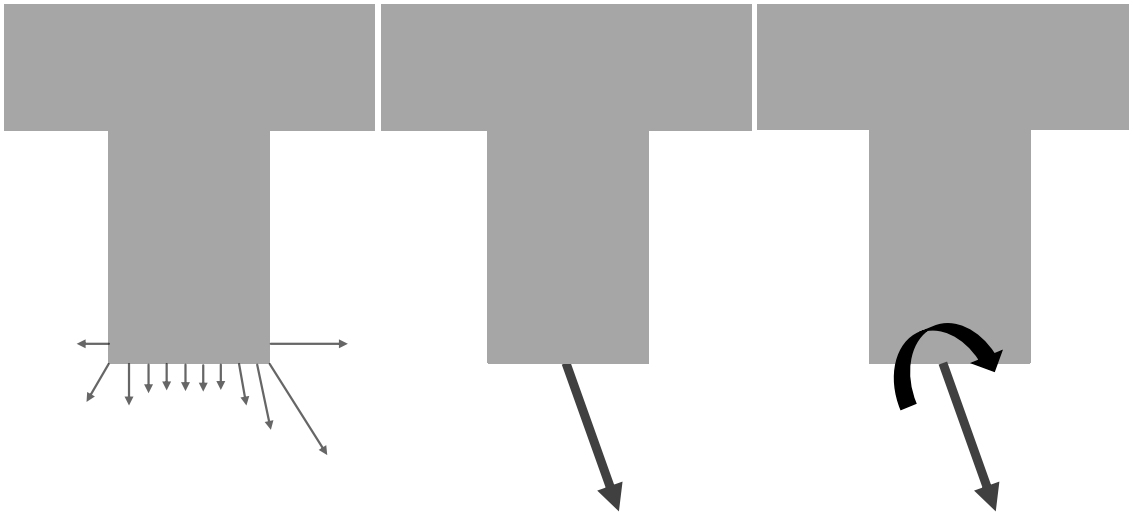

(a) Distributed forces (reference) (b) Lumped tooth force (c) Lumped tooth torsor

Figure 3.41 – Studied loadcases for vibration simulation based on Maxwell forces computed with the VWP.

The first step is to validate the numerical magneto-mechanical model based on distributed nodal forces. To this end, measurements on the actual benchmark test-bed with the mounted 12s10p prototype have been performed. Several run-ups (up to 2700 rpm) with different measurements points have been performed. Details about variability and

repeatability of these measurements are presented in Annex B.3. The comparison between numerical and experimental vibration RMS are presented in Fig. 3.42. The comparison at $2f_s$gives less than 3 dB (or -40%) of difference between the simulation and the experiment. The comparison at $10f_s$ gives approximately 6 dB error on the speed range, except at the resonance around 2000 rpm where there is an error of 16 dB. This last resonance corresponds to the mode (3,0). In our numerical model, the unbalanced magnetic forces have been neglected, explaining the differences observed with simulation. It could also explain the limited resonance on the experimental measurements at 1100 rpm: this mode has not been identified in the experimental modal analysis, but it could correspond to a bending mode of the benchmark excited by unbalanced magnetic forces.

The experimental uncertainties are the same as discussed in Section 3.3.2.2. Simulation could be further improved by performing a deep fitting of the numerical modal basis from the knowledge of the experimental modal basis (in particular, contact models).

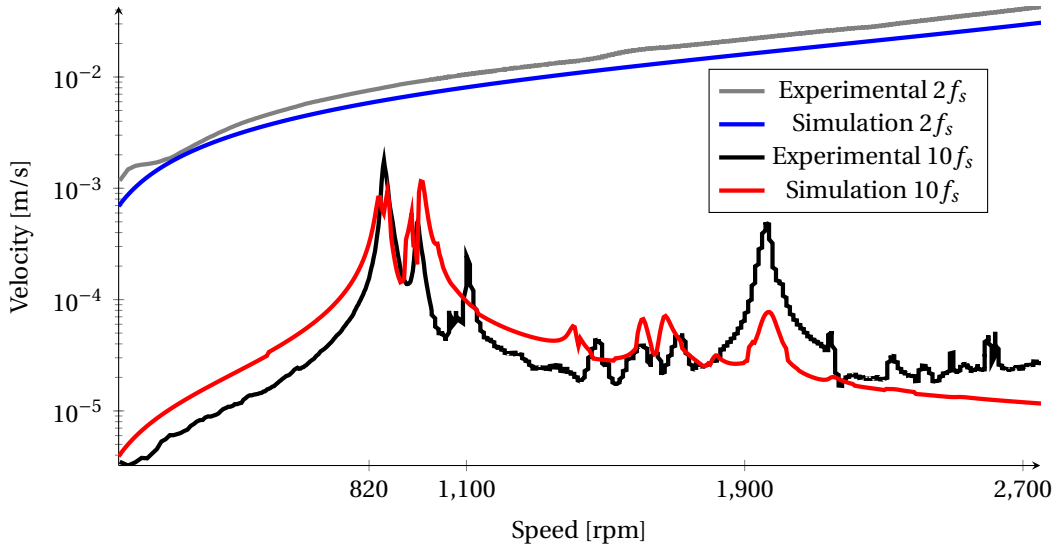

Figure 3.42 – Experimental run-up measurement compared to simulation using distributed nodal forces.

Further comparison can be done by using the modal projection factor: it can be computed as a dot product between the normalized modal basis $\mathbf{Q}_n$ corresponding to the n-th mode and the nodal force distribution:

$$\left(\mathbf{Q}_n \cdot \hat{\mathbf{F}}\right)(\omega) = \sum_i \mathbf{Q}_n^i \hat{\mathrm{F}}_s^i(\omega) \tag{3.23}$$

The values of modal participation factors (3.23) are presented in Figs. 3.43a-3.43b. In both cases, the two main excited modes are the modes n°2 and n°4 which are symmetric (2,0) ovalization modes of the yoke at natural frequencies 727 Hz and 810 Hz (see Table A.5) to be compared with the experimental natural frequencies 721 Hz and 797 Hz of the same modes (see Table B.1). Nevertheless, the numerical model seems to have additional secondary (2,0) modes (n°1 and n°3) which are not observed in experimental results of Fig. 3.42. The difference probably comes from inaccuracy for contacts in the FE model. This should be the subject of future research work. Finally, modes n°9 and n°10 correspond to (2,1) modes of the stator which are slightly excited despite the fact that the forces are constant in the axial direction of the machine.

Although some differences remain between the numerical prediction and the experimental measurement, it is assumed in the following that the numerical model based on distributed nodal forces can be used as the reference to study the differences between the magnetic loading strategies.

It can also be observed that the two harmonics $2f_s$ and $10f_s$ seem to have the same modal projection considering the respective amplitudes. This is verified in Fig. 3.44: the modal projection at $10f_s$ is multiplied by 850 which is approximately the difference with the $2f_s$ magnetic tooth force amplitude observed in Figs 3.9-3.12. This is an indication that tooth forces might be accurate: in spite of a different distribution of wavenumbers, both harmonics have a proportional modal projection.

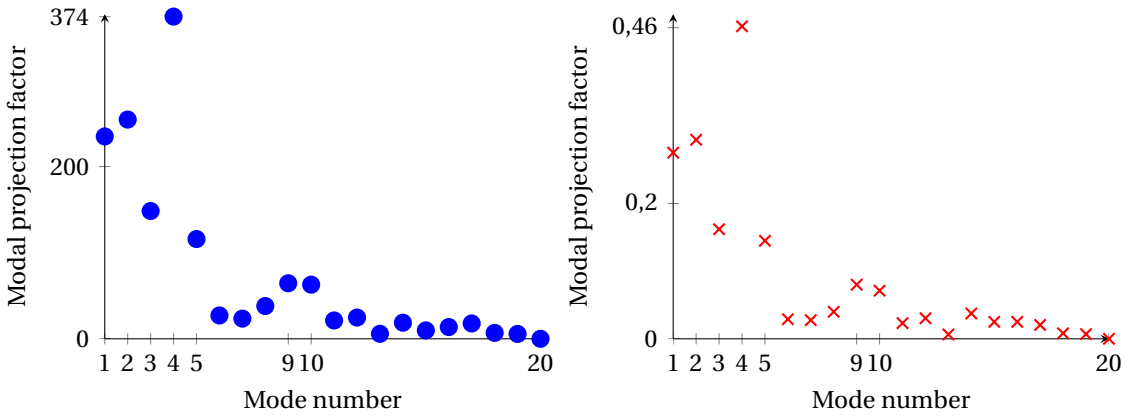

(a) $2f_s$ (b) $10f_s$

Figure 3.43 – Modal participation factor (3.23) for each eigenvector.

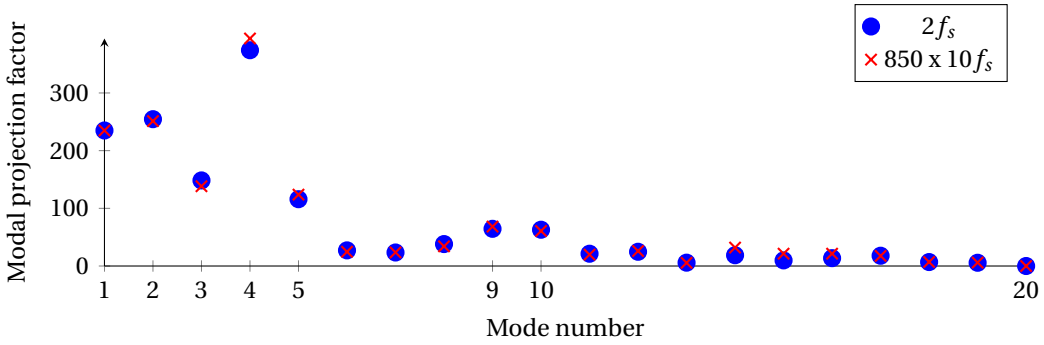

Figure 3.44 – Modal projection factor on each structural mode computed with numerical simulation: the values at $10f_s$ are amplified by a factor of 850 to ease the comparison with $2f_s$

Thus, the next step is to compare lumped tooth force loading with distributed force loading as in Fig. 3.41b. The results are presented in Fig. 3.45: the difference represents 4dB at $10f_s$ and less than 1dB at $2f_s$, and stay almost constant at every speed (or frequency). The number of considered eigenvectors has a negligible impact on the observed difference as shown in Fig. 3.46: the number of eigenvectors has been increased from $N_{eig} = 20$ to $N_{eig} = 50$. Unfortunately, the only differences are observed for the higher frequencies, and the gap remains the same.

The remaining hypothesis to explain the difference is that the tooth tip moment contributes significantly to the vibration. Indeed, the main difference between the dis-

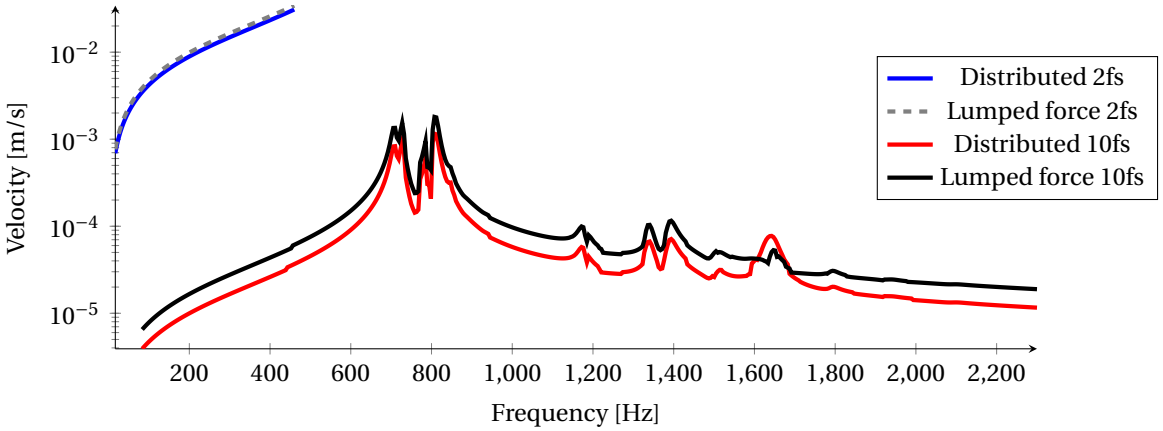

Figure 3.45 – Comparison between distributed nodal forces FRF and lumped tooth forces FRF ($N_{eig} = 20$).

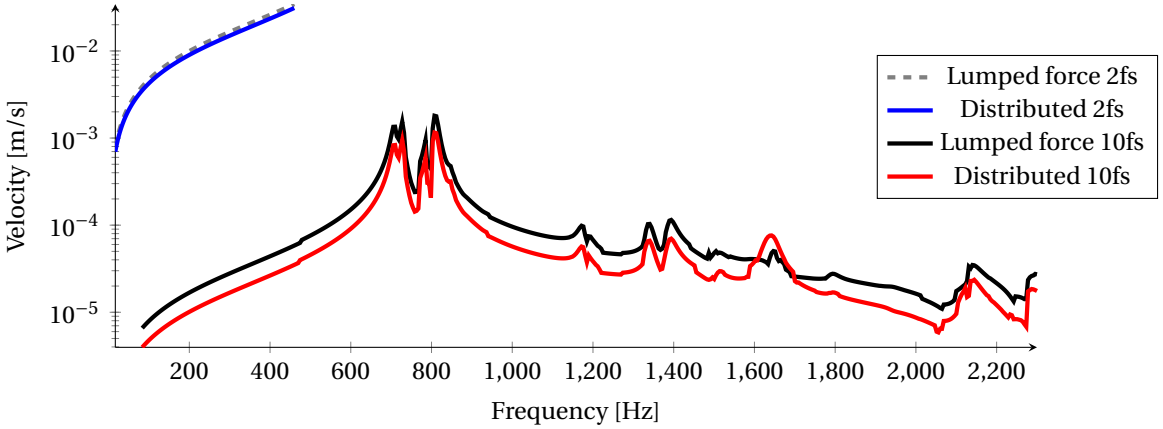

Figure 3.46 – Comparison between distributed nodal forces FRF and lumped tooth forces FRF ($N_{eig} = 50$).

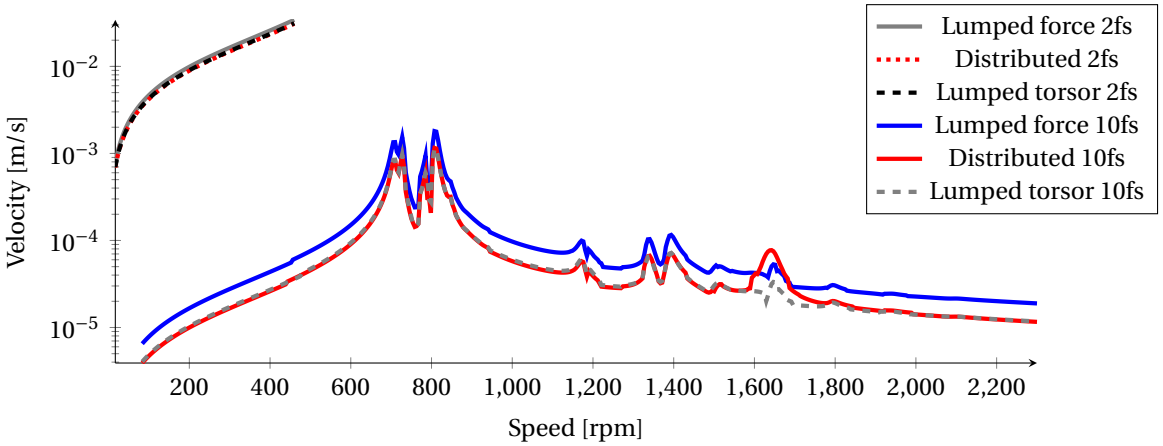

Figure 3.47 – Contribution of the tooth tip moments to the velocity.

tributed forces and the lumped tooth force is the moment between the point of application of the nodal force and the one of the lumped tooth force. In order to check the

contribution of the moment to the displacement, another type of loading "Lumped + Moment" is defined in which the moment is taken into account in the modal projection as illustrated in Fig. 3.41c. The comparison of all the different types of loading is presented in Fig. 3.47: adding the moment to the lumped tooth force loading gives back the almost same results as the reference (< 1dB) on the computed velocity. The only exception, which appears at 1650 Hz, was already discussed at the end of Section 3.4.1. Thus, the lumped tooth moment have significant contribution to the noise in this application, and can be accurately taken into account through a lumped torsor model.

3.5 Conclusion

Throughout this chapter, the different cases of application have shown that the lumped tooth force can be an accurate tool for the e-NVH troubleshooting of electrical machines. The most accurate method is to compute lumped tooth torsor (lumped force and moment) from VWP nodal forces. Nevertheless, this method is more limited to troubleshoot electrical machines since it lacks the wavenumber decomposition. This issue can be solved by using the equivalent AGSF presented in Section 2.4.2 and the lumped tooth force wavenumber decomposition as in Section 3.2.2.2. The MST can still be used at early/intermediary design stage, with an awareness of the limits of its accuracy, especially at higher electrical harmonics f_s. The conclusions of Section 3.4.2 means that the observed errors using the tooth-FRF in Section 3.3 mainly come from experimental uncertainties.

Then, whatever the chosen method to compute lumped tooth force, it is proposed that a unit-wave FRF such as presented in Section 1.4.3 of wavenumber $n + kZ_s$ can be computed from the knowledge of another unit-wave FRF:

$$\mathrm{FRF}_{n+kZ_s} = \mathrm{FRF}_n \tag{3.24}$$

This is consistent with the previous related work [Weh, 1964; Wang et al., 2020; Fang et al., 2019; Liang, 2017]. The proposed model reduces accurately the magneto-mechanical model by simulating only the essential magnetic force wavenumbers (up to $Z_s/2$) and to extrapolate the results to higher wavenumbers. This method reduces significantly the mechanical computation time for electrical machines at variable speed, especially when magnetic forces vary significantly depending on the control strategy of the machine.

However, it is possible to propose a different formula for the modulation effect in order to take into account the conclusions from Section 3.2.2. Considering the lumped tooth force integration (3.11) and (3.12), the amplitude of the tooth force corresponding to wavenumber n is computed:

$$\mathrm{F}_r(n,\omega) = \mathrm{R_s L_s}\left(\mathrm{A}_n^{rr}\hat{\mathrm{P}}_\mathrm{r}(\mathrm{R_s},n,\omega) + j\mathrm{A}_n^{rt}\hat{\mathrm{P}}_\theta(\mathrm{R_s},n,\omega)\right), \tag{3.25}$$

$$\mathrm{F}_\theta(n,\omega) = \mathrm{R_s L_s}\left(-j\mathrm{A}_n^{rt}\hat{\mathrm{P}}_\mathrm{r}(\mathrm{R_s},n,\omega) + \mathrm{A}_n^{rr}\hat{\mathrm{P}}_\theta(\mathrm{R_s},n,\omega)\right). \tag{3.26}$$

Then, the displacement corresponding to the wavenumber $(n + kZ_s) \geq Z_s/2$ with $k \in \mathbb{N}$, can be computed with the following relation in the radial direction:

$$\mathrm{Y_r}(n + kZ_s,\omega) = \hat{\mathrm{F}}_r(n + kZ_s,\omega)\mathrm{FRF}_r(n,\omega). \tag{3.27}$$

The same principle applies for tangential direction and tooth tip moments. The advantage of this model with respect to the previous works is that it takes into account wavenumbers proportional to Z_s accurately. Moreover, it enables to model the contribution of the radial AGSF wavenumbers onto the tangential tooth force and respectively the tangential AGSF onto the radial tooth force.

Summary and outlook

This thesis has mainly studied the domain of validity of the Maxwell Stress Tensor application to compute magnetic force in the context of noise and vibration in electrical machines. At first, the scientific literature was presented in Chapter 1 in order to identify the main methods used to perform the magneto-mechanical coupling. The focus was given on weak-coupling methods (i.e. neglecting the effects of displacement and mechanical stress on the magnetic problem). The interest for the Maxwell Stress Tensor method as a tool to troubleshoot vibration was highlighted: there exist analytical links between the computed force and the electromagnetic sources, so that the main issues can be identified. Nevertheless, another method based on Virtual Work Principle was identified as the most accurate method but also computationally expensive. In both cases, the use of lumped tooth force is widespread to perform magneto-mechanical coupling in e-NVH studies, and it has recently brought to light the issue of the modulation effect. In the light of the literature, it seems that the widespread use of Maxwell Stress Tensor is explained by the convenience of analysis and the empirically good results. However, the extent of its validity for calculating forces in the air-gap has been little studied.

The air-gap surface forces computed with Maxwell Stress Tensor were analytically studied in Chapter 2. The aim was to understand the dependency of these forces with the radius of computation in the air-gap. In a first part, the air-gap surface forces were studied on an analytical electromagnetic case using a virtual slotless machine. An analytical equation was found: from the knowledge of the air-gap surface forces at one radius value in the air-gap, the value at any other radius can be computed. The formula was called the air-gap surface force transfer law. In a second part, this result was generalized to any radial flux electrical machine with a cylindrical air-gap band. In a third part, numerical validations of this transfer law were performed on several electrical machine topologies by comparing the results to the magnetic forces computed with the Virtual Work Principle. It was found that the formula improves the accuracy of the air-gap surface forces computed with Maxwell Stress Tensor, but incompressible differences remain. These differences are supposed to have negligible effect on the vibration with classical magneto-mechanical coupling and troubleshooting methods. However, the last application case with a turbo-alternator simulation suggests that the combination with the modulation effect could have an audible effect.

Then, the Chapter 3 performs a numerical and experimental study of the modulation effect. In a first part, the analytical integration of lumped tooth force is reviewed in detail. The main difference between the methods is the angular opening considered for the integration: either based on the tooth tip angle or the slot pitch. A specific numerical validation case with a 36s36p electrical machine has been designed to test both methods. The method based on the slot pitch was found to be significantly more accurate but with a major limitation when considering wavenumbers proportional to the number of teeth Z_s. To overcome this issue, a new equation was proposed to compute lumped

tooth force per wavenumber. In a second part, an hybrid method using experimental mechanical characterization and numerical simulation of magnetic force is proposed. The method relies on lumped tooth forces, so the previous conclusions were applied to compute them. A comparison with experimental run-up acceleration measurements was performed. In particular, the order tracking at $10 f_s$ showed that the method allows us to identify resonance. However, some significant differences remained: there were many sources of experimental uncertainty, but there was also uncertainty due to the lumped tooth force modelling. As a consequence, the third part of the chapter proposed to compare lumped tooth force results with mesh-to-mesh projection. The magneto-mechanical model was validated by comparison with experimental measurements. It was found that the lumped tooth force model tends to amplify resonance phenomenon, but within an acceptable level (under 4dB) for noise analysis. Therefore, this last chapter validates and improves the modulation effect for e-NVH studies.

The outlooks of this thesis can be better understood by looking at the main hypotheses. First, the effect of magnetic saturation and magnetic volume forces has been neglected because the studied topologies (in particular the 12s10p) were in accordance with this assumption. It would be interesting to see the robustness of these results - in particular, the modulation effect and the lumped tooth force assumptions - in condition of high saturation and with different topologies.

In order to explore these aspects, three variants of the 12s10p machine presented in Fig. 3.48a were designed during the thesis:

— one with a slot-opening of 6 degrees (Fig.3.48b);

— one with a slot-opening of 2 degrees (Fig.3.48c);

— one with closed slots (Fig.3.48d).

The experimental testing of theses variants is the subject of work to come.

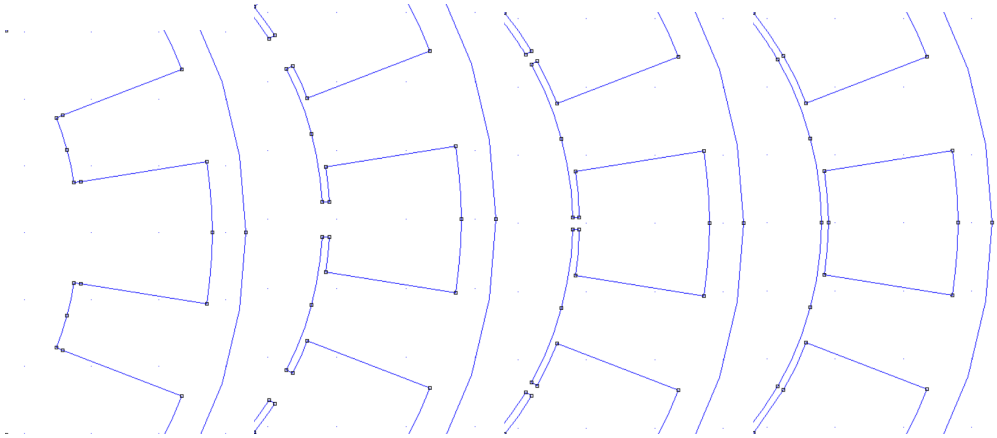

(a) Initial (b) 6° opening (c) 2° opening (d) Closed slots

Figure 3.48 – Different designs of the 12s10p stator.

Then, the issues of accuracy, repeatability and reproducibility of the tooth FRF should be studied. In particular, the effect of rotor mounting and unbalanced magnetic forces could be included in the different simulations. Moreover, these measurements could be useful to perform retro-engineering on electrical machines: from the vibration measurements and tooth FRF, the operational magnetic force could be predicted and compared to simulations. Another possibility is considered to solve the various problems encountered: the FRF measurements could be used to build an experimental analysis which

includes the tip of the teeth. Therefore, it would be possible to compute the modal projection & expansion with lumped tooth forces.

Furthermore, the mesh-to-mesh numerical workflow was performed in three steps: computing the magnetic force field from nodal forces, projection onto the target (mechanical) mesh, and computing nodal forces from force field. These last steps are necessary to compute the modal projection. Thus, it would be efficient to propose a method which performs mesh-to-mesh projection directly with nodal forces, instead of force fields.

Finally, the technique of model order reduction [Henneron and Clenet, 2014] could be used to optimize the vibro-acoustic behaviour of the machine at reduced computational cost. The electromagnetic model can be reduced, and the mechanical model as well. However, this work does not support the use of model reduction on the coupled magneto-mechanical system for e-NVH. Indeed, the previous conclusions showed that simulating the mechanical problem independently of the electromagnetic problem thanks to the unit-wave FRF method is giving accurate results. It would first be necessary to find a system where the weak-coupling and lumped tooth force assumptions are challenged. Then model order reduction on the complete magneto-mechanical system could be considered.

An essential part of the thesis was made possible by the use of MANATEE software: the different methods to solve the electromagnetic field, and to solve the mechanical simulations, were already available. Thus, a significant amount of time was dedicated to the implementation of the algorithms developed for this work in both the open-source software PYLEECAN and the commercial software MANATEE. The work in Pyleecan focused on the algorithmic architecture to store and visualise the different data. This architecture was then imported in MANATEE to implement the different projection algorithms. The above perspectives would be addressed with the support of one or the other of these software.

Bibliography

Alger, P. L. (1953). The Acoustic Behavior of Induction Motors. *Journal of the Acoustical Society of America*, 25(4). 38, 58

Alger, P. L. and Erdelyi, E. (1956). Magnetic Noise of Polyphase Induction Motors. *Journal of the Acoustical Society of America*, 28(4). 38

Allemang, R. J. (1981). Investigation of some multiple input/output frequency response function experimental modal analysis techniques. 40

Amor, A. H., Timar, P. L., and Poloujadoff, M. (1995). Induction squirrel cage machine design with minimization of electromagnetic noise. *IEEE Transactions on Energy Conversion*, 10(4):681–687. 42

Armor, A. F. and Chari, M. V. K. (1976). Heat flow in the stator core of large turbine-generators, by the method of three-dimensional finite elements (part I: Analysis by scalar potential formulation). *IEEE Transactions on Power Apparatus and Systems*, 95(5):1648–1656. 9

Avitabile, P. (2001). Experimental modal analysis. *Sound and vibration*, 35(1):20–31. 40, 103

Azeem, M., Humza, M., and Kim, B. (2019). Analytical investigation of air-gap flux density distribution of a pm vernier motor. *IJAEM*, 59(3):943–949. 30

Barré, O., Brochet, P., and Hecquet, M. (2006). Experimental validation of magnetic and electric local force formulations associated to energy principle. *IEEE Transactions on Magnetics*, 42(4):1475–1478. 35

Bathe, K.-J. (1996). Finite element procedures. isbn: 0-13-301458-4. 31

Bekemans, M. (2006). *Modélisation des machines électriques en vue du contrôle des efforts radiaux*. PhD thesis, Univ. de Louvain. 31, 63

Belahcen, A. (2004). *Magnetoelasticity, magnetic forces and magnetostriction in electrical machines*. G4 monografiaväitöskirja, Helsinki University of Technology. 16, 25

Biro, O. and Preis, K. (1989). On the use of the magnetic vector potential in the finite-element analysis of three-dimensional eddy currents. *IEEE Transactions on Magnetics*, 25(4):3145–3159. 18

Bjørk, R., Smith, A., and Bahl, C. R. (2010). Analysis of the magnetic field, force, and torque for two-dimensional Halbach cylinders. *Journal of Magnetism and Magnetic Materials*, 322(1):133–141. 62

Boesing, M. (2013). *Noise and Vibration Synthesis based on Force Response Superposition*. PhD thesis, Fakultät für Elektrotechnik und Informationstechnik der Rheinisch-Westfälischen Technischen Hochschule Aachen. 27, 30, 42, 43, 44, 45, 48

Boesing, M., Schoenen, T., Kasper, K. A., and De Doncker, R. W. (2010). Vibration Synthesis for Electrical Machines Based on Force Response Superposition. *IEEE Transactions on Magnetics*, 46(8):2986–2989. 23, 46, 47, 57, 78, 101

Boisson, J. (2014). *Modélisation analytique magnéto-acoustique des machines synchrones à commutation de flux à aimants permanents : optimisation du dimensionnement*. PhD thesis, Ecole normale supérieure de Cachan. 39

Bossavit, A. (1993). *Electromagnetisme, en vue de la modelisation*, volume 14. Springer Science & Business Media. 9, 19

Bossavit, A. (1998). How Weak is the " Weak Solution " in Finite Element Methods ? *IEEE Trans. on Magnetics*, 34(5):2429–2432. 50

Bossavit, A. (2016). Bulk forces and interface forces in assemblies of magnetized pieces of matter. *IEEE Trans. on Magn.*, 52(3):1–4. 25

Boualem, B. (1997). *Contribution à la modélisation des systèmes électrotechniques à l'aide des formulations en potentiels: application à la machine asynchrone*. PhD thesis, Lille 1. 33

Boughrara, K., Takorabet, N., Ibtiouen, R., Touhami, O., and Dubas, F. (2015). Analytical Analysis of Cage Rotor Induction Motors in Healthy, Defective, and Broken Bars Conditions. *IEEE Transactions on Magnetics*, 51(2):1–17. 20, 82

Braunisch, D., Ponick, B., and Bramerdorfer, G. (2013). Combined Analytical–Numerical Noise Calculation of Electrical Machines Considering Nonsinusoidal Mode Shapes. *IEEE Transactions on Magnetics*, 49(4):1407–1415. 58

Brezis, H. (2010). *Functional analysis, Sobolev spaces and partial differential equations*. Springer Science & Business Media. 19

Brudny, J. F. (1997). Modélisation de la denture des machines asynchrones : phénomènes de résonances. *Journal of Physics III*, 37(7):1009–1023. 21

Carpenter, C. (1960). Surface-integral methods of calculating forces on magnetized iron parts. *Proceedings of the IEE-Part C: Monographs*, 107(11):19–28. 35

Chandrupatla, T. R., Belegundu, A. D., Ramesh, T., and Ray, C. (2002). *Introduction to finite elements in engineering*, volume 10. Prentice Hall Upper Saddle River, NJ. 48

Chen, Y., Yang, Y., and Shen, Y. (2018). Influence of small teeth on vibration for dual-redundancy permanent magnet synchronous motor. *Energies*, 11(9):2462. 16

Chu, B.-T. (1959). Thermodynamics of Electrically Conducting Fluids. *Physics of Fluids*, 2(5):473. 24

Cook, R. D. et al. (2007). *Concepts and applications of finite element analysis*. John wiley & sons. 48

Coulomb, J.-l. (1983). A methodology for the determination of global electromechanical quantities from a finite element analysis and its application to the evaluation of magnetic forces, torques and stiffness. *IEEE Transactions on Magnetics*, 19(19):2514. 24, 31, 32, 33

Coulomb, J.-L. and Meunier, G. (1984). Finite element implementation of virtual work principle for magnetic or electric force and torque computation. *IEEE Transactions on Magnetics*, 20(5):1894–1896. 23, 24, 33

Curti, M., Paulides, J., and Lomonova, E. (2017). Separation of volume and surface forces and torques in a DC excited Flux Switching Machine. In *2017 Twelfth International Conference on Ecological Vehicles and Renewable Energies (EVER)*, number June, pages 1–3. IEEE. 26, 35, 50

Das, S., Chowdhury, A., Paul, S. P., Wan, Z., Islam, R., and Sozer, Y. (2019). Experimental and simulation based study of vibration prediction in fractional slot permanent magnet synchronous machines. *2019 IEEE International Electric Machines and Drives Conference (IEMDC)*, pages 1138–1143. 16

Das, S., Hasan, I., Sozer, Y., Islam, R., Ortega, A. J., and Klass, J. (2018). Noise and vibration performance in fractional slot permanent magnet synchronous machines using stator bridge. *2018 IEEE Transportation Electrification Conference and Expo (ITEC)*, pages 632–637. 16

de Medeiros, L., Reyne, G., Meunier, G., Medeiros, L. H. D., Reyne, G., and Meunier, G. (1999). About the distribution of forces in permanent magnets. *IEEE Transactions on Magnetics*, 35(3):1215–1218. 31, 32

Degrendele, K., Le Besnerais, J., Pile, R., Gning, P., , and Devillers, E. (2020a). Characterization of ev/hev nvh issues using electrical machine tooth frf. In *International Conference on Noise and Vibration Engineering, ISMA2020*. 101, 102, 103, 105

Degrendele, K., Le Besnerais, J., Pile, R., Gning, P., Devillers, E., and Wen, X. (2020b). E-nvh benchmark - tooth/wave frequency response functions (version 1.0.0) [data set]. Zenodo. http://doi.org/10.5281/zenodo.3898554. 103

Delaere, K., Sas, P., Belmans, R., and Hameyer, K. (1999). Weak coupling of magnetic and vibrational analysis using local forces. In *IEEE International Electric Machines and Drives Conference. IEMDC'99. Proceedings (Cat. No.99EX272)*, pages 514–516. 9

Despret, G., Hecquet, M., Lanfranchi, V., and Fakam, M. (2016). Skew effect on the radial pressure of induction motor. *2016 11th International Conference on Ecological Vehicles and Renewable Energies, EVER 2016*, pages 0–5. 58

Devillers, E. (2018). *Electromagnetic subdomain modeling technique for the fast prediction of radial and circumferential stress harmonics in electrical machines*. PhD thesis, Ecole Centrale de Lille. 16, 20, 46, 54, 55, 57, 59, 116, 138

Devillers, E., Hecquet, M., Cimetiere, X., Lecointe, J., Besnerais, J. L., and Lubin, T. (2018). Experimental benchmark for magnetic noise and vibrations analysis in electrical machines. In *2018 XIII International Conference on Electrical Machines (ICEM)*, pages 745–751. 112

Devillers, E., Le Besnerais, J., Lubin, T., Hecquet, M., and Lecointe, J. (2016). A review of subdomain modeling techniques in electrical machines: Performances and applications. In *2016 XXII International Conference on Electrical Machines (ICEM)*, pages 86–92. 20

Doherty, R. E. and Nickle, C. A. (1926). Synchronous machines I-an extension of blondel's two-reaction theory. *Transactions of the American Institute of Electrical Engineers*, XLV:912–947. 21

Dubas, F. and Boughrara, K. (2017). New scientific contribution on the 2-d subdomain technique in cartesian coordinates: taking into account of iron parts. *Mathematical and Computational Applications*, 22(1):17. 20

Ellison, A. J. and Moore, C. J. (1968). Acoustic noise and vibration of rotating electric machines. *Proceedings of the Institution of Electrical Engineers*, 115(11):1633–1640. 54

Ennassiri, H. (2018). *Analyse magnéto-vibroacoustique des machines synchrones discoides à commutation de flux dédiées aux véhiculex électriques hybrides*. Theses, Normandie Université. 54

Eomys Engineering (2017). Videos on electromagnetically-excited noise and vibrations. *https://eomys.com/e-nvh/article/videos-on-electromagnetically-excited-noise-and-vibrations?lang=en*. 8

EOMYS ENGINEERING (2020). MANATEE software: Magnetic acoustic noise analysis tool for electrical engineering (v1.09.01). 56, 57, 58, 79, 94, 108, 112

Fahy, F. and Gardonio, P. (2007). *Sound and Structural Vibration*. Elsevier. 53

Fakam, M., Hecquet, M., Lanfranchi, V., and Randria, A. (2015). Design and magnetic noise reduction of the surface permanent magnet synchronous machine using complex air-gap permeance. *IEEE Transactions on Magnetics*, 51(4):1–9. 16

Fang, H., Guo, J., Xu, Y., Li, D., and Qu, R. (2019). Experimental study of magnetostriction on motor vibration considering mechanical characteristics. In *2019 22nd International Conference on Electrical Machines and Systems (ICEMS)*, pages 1–4. 16

Fang, H., Li, D., Qu, R., and Yan, P. (2019). Modulation Effect of Slotted Structure on Vibration Response in Electrical Machines. *IEEE Transactions on Industrial Electronics*, 66(4):2998–3007. 16, 43, 48, 86, 88, 92, 94, 114, 123

Farrell, P. E. and Maddison, J. R. (2011). Conservative interpolation between volume meshes by local Galerkin projection. *Computer Methods in Applied Mechanics and Engineering*, 200(1-4):89–100. 52

Fiedler, J. O., Kasper, K. A., and De Doncker, R. W. (2010). Calculation of the acoustic noise spectrum of srm using modal superposition. *IEEE Transactions on Industrial Electronics*, 57(9):2939–2945. 41

Fu, W. N., Zhou, P., Lin, D., Stanton, S., and Cendes, Z. J. (2004). Magnetic force computation in permanent magnets using a local energy coordinate derivative method. *IEEE Transactions on Magnetics*, 40(2 II):683–686. 31, 32

Garvey, S. (1997). Modelling the vibrational behaviour of stator cores of electrical machines with a view to successfully predicting machine noise. In *IEE Colloquium on Modelling the Performance of Electrical Machines*, volume 1997, pages 3–3. IEE. 16, 42, 46

Gaussens, B., Hoang, E., de la Barriere, O., Saint-Michel, J., Lécrivain, M., and Gabsi, M. (2012). Analytical Approach for Air-Gap Modeling of Field-Excited Flux-Switching Machine: No-Load Operation. *IEEE Transactions on Magnetics*, 48(9):2505–2517. 21

Geuzaine, C., Meys, B., Henrotte, F., Dular, P., Legros, W., and Tilman, S. (1999). A Galerkin projection method for mixed finite elements. *IEEE Transactions on Magnetics*, 35(3):1438–1441. 49, 50

Gieras, J. F., Wang, C., and Lai, J. C. (2005). *Noise of polyphase electric motors*. CRC Press. 23, 27, 42, 58

Green, G. (1828). *An essay on the application of mathematical analysis to the theories of electricity and magnetism*. Wezäta-Melins Aktiebolag. 19, 27, 69, 72

Gysen, B. (2011). *Generalized harmonic modeling technique for 2D electromagnetic problems : applied to the design of a direct-drive active suspension system*. PhD thesis, Department of Electrical Engineering. 16

Hallal, J., Druesne, F., and Lanfranchi, V. (2013). Study of Electromagnetic Forces Computation Methods for Machine Vibration Estimation. *ISEF. International Symposium on Electromagnetic Fields*, i(SEPTEMBER):2–3. 29, 62, 90

Hartog, J. P. D. (1960). *Vibrations mécaniques*. Dunod, Paris. 38

Hasan, I., Sozer, Y., Ortega, A. P., Paul, S., and Islam, R. (2017a). Investigation of design based solutions to reduce vibration in permanent magnet synchronous machines with low order radial forces. *2017 IEEE Energy Conversion Congress and Exposition (ECCE)*, pages 5431–5437. 16

Hasan, I., Sozer, Y., Piña, A., Paul, S., Islam, R., and Klass, J. (2017b). Stator design techniques to reduce vibration in permanent magnet synchronous machines. *2017 20th International Conference on Electrical Machines and Systems (ICEMS)*, pages 1–6. 16

Helbling, H., Benabou, A., Van Gorp, A., El Youssef, M., Tounzi, A., Boughanmi, W., and Laloy, D. (2020). Effect on magnetic properties of inhomogeneous compressive stress in thickness direction of an electrical steel stack. *Journal of Magnetism and Magnetic Materials*, 500:166353. 25

Henneron, T. and Clenet, S. (2014). Model order reduction applied to the numerical study of electrical motor based on pod method taking into account rotation movement. *International Journal of Numerical Modelling: Electronic Networks, Devices and Fields*, 27(3):485–494. 127

Henrotte, F., Deliége, G., and Hameyer, K. (2004). The eggshell approach for the computation of electromagnetic forces in 2D and 3D. *COMPEL - The International Journal for Computation and Mathematics in Electrical and Electronic Engineering*, 23(4):996–1005. 23

Henrotte, F. and Hameyer, K. (2004). Computation of electromagnetic force densities: Maxwell stress tensor vs. virtual work principle. *Journal of Computational and Applied Mathematics*, 168(1-2):235–243. 23, 24, 25

Holland, K. and Fahy, F. (1997). A guide to the exploitation of vibroacoustic reciprocity in noise control technology. *ISVR Technical Report No 264*. 103

IEC61672-1 (2013). Electroacoustics - Sound level meters - Part 1: Specifications. 54

Jackson, J. D. (1999). Classical electrodynamics 3rd ed john wiley & sons. *Inc., NewYork, NY*. 19, 24

Jiles, D. (2015). *Introduction to magnetism and magnetic materials*. CRC press. 18

Jordan, H. (1950). *Electric motor silencer-formation and elimination of the noises in the electric motors*. W.Giradet-Essen. 38, 39, 58

Journeaux, A. A., Bouillault, F., and Roger, J.-Y. (2013). Multi-physics problems computation using numerically adapted meshes: application to magneto-thermo-mechanical systems. *Eur. Phys. J. Appl. Phys.*, 61(3):30001. 49, 51

Kiyoumarsi, A. and Zadeh, M. R. H. (2009). A new analytical technique for analysis of the rotor eccentricity in rotating electrical machines. *IJAEM*, 30(1-2):83–93. 30

Kotter, P. (2019). *Vibroacoustics of Electrical Drive Systems*. PhD thesis, ETH ZURICH. 35, 38, 49, 50, 52, 58

Kotter, P., Morisco, D., Boesing, M., Zirn, O., and Wegener, K. (2017). Noise-Vibration-Harshness-Modeling and Analysis of a Permanent-Magnetic Disc Rotor Axial-Flux Electric Motor. *IEEE Transactions on Magnetics*, pages 1–4. 49

Krishnamoorthy, A. and Menon, D. (2013). Matrix inversion using cholesky decomposition. In *Signal Processing: Algorithms, Architectures, Arrangements, and Applications (SPA)*, pages 70–72. IEEE. 116

Landau, L. D. and Lifshitz, E. (1975). The classical theory of fields. vol. 2. *Course of theoretical physics*. 19, 63, 69, 72

Larson, M. G. and Bengzon, F. (2010). The finite element method: theory, implementation, and practice. *Texts in Computational Science and Engineering*, 10. 19

Le Besnerais, J. (2008). *Reduction of magnetic noise in PWM supplied induction machines: low-noise design rules and multi-objective optimisation*. PhD thesis, Ecole Centrale de Lille, France. 42

Le Besnerais, J. (2016). Fast prediction of variable-speed acoustic noise due to magnetic forces in electrical machines. In *ICEM 2016*, pages 2259–2265, Lausanne. IEEE. 79

Le Besnerais, J., Lanfranchi, V., Hecquet, M., Brochet, P., and Friedrich, G. (2010). Prediction of Audible Magnetic Noise Radiated by Adjustable-Speed Drive Induction Machines. *IEEE Transactions on Industry Applications*, 46(4):1367–1373. 46, 55, 57

Le Besnerais, J., Lanfranchi, V., Hecquet, M., and Friedrich, G. (2010). Permeance computation for determination of induction motor acoustic noise. *Przeglad Elektrotechniczny*, 86(5):91–94. 30

Le Besnerais, J., Lanfranchi, V., Hecquet, M., Lemaire, G., Augis, E., and Brochet, P. (2009). Characterization and Reduction of Magnetic Noise Due to Saturation in Induction Machines. *IEEE Transactions on Magnetics*, 45(4):2003–2008. 55

Le Besnerais, J. and Souron, Q. (2016). Design of Quiet Permanent Magnet Synchronous Electrical Motors By Optimum Skew Angle. *International Congress on Sound & Vibration*, pages 1–9. 46

Lee, K.-S., DeBortoli, M., Lee, M., and Salon, S. (1991). Coupling finite elements and analytical solution in the airgap of electric machines. *IEEE Transactions on Magnetics*, 27(5):3955–3957. 73

Li, M. and Lowther, D. A. (2009). Local electromagnetic force computation in the presence of numerical field errors. *IEEE Trans. on Magn.*, 45(3):1344–1347. 28, 65, 79

Liang, W. (2017). *The investigation of electromagnetic radial force and associated vibration in permanent magnet synchronous machines*. PhD thesis, Cranfield University. 42, 45, 48, 123

Lubin, T., Mezani, S., and Rezzoug, A. (2010). Exact analytical method for magnetic field computation in the air gap of cylindrical electrical machines considering slotting effects. *IEEE Transactions on Magnetics*, 46(4):1092–1099. 10, 63, 64, 73

Lubin, T., Mezani, S., and Rezzoug, A. (2012). Two-dimensional analytical calculation of magnetic field and electromagnetic torque for surface-inset permanent-magnet motors. *IEEE Transactions on Magnetics*, 48(6):2080–2091. 20

MacNeal, R. H. (1971). A hybrid method of component mode synthesis. *Computers & Structures: Special Issue on Structural Dynamics*, 1(4):581 – 601. 41

Marinescu, M. and Marinescu, N. (1988). Numerical computation of torques in permanent magnet motors by maxwell stresses and energy method. *IEEE Transactions on Magnetics*, 24(1):463–466. 27

Meek, B., Van der Auwear, H., and De Langhe, K. (2013). *Challenges in NVH for Electric Vehicles*, pages 675–685. Springer Berlin Heidelberg, Berlin, Heidelberg. 10

Meeker, D. (2019). FEMM (Finite Element Method Magnetics) v4.2. 19, 79, 88, 94

Meessen, K. J., Paulides, J. J. H., and Lomonova, E. A. (2013). Force calculations in 3-D cylindrical structures using fourier analysis and the maxwell stress tensor. *IEEE Transactions on Magnetics*, 49(1):536–545. 24, 62

Melcher, J. R. (1981). *Continuum electromechanics*, volume 2. MIT press Cambridge, MA. 23, 24, 27

Millithaler, P. (2015). Dynamic behaviour of electric machine stators : modelling guidelines for efficient finite-element simulations and design specifications for noise reduction. 16

Mizia, J., Adamiak, K., Eastham, A., and Dawson, G. (1988). Finite element force calculation: comparison of methods for electric machines. *IEEE Transactions on Magnetics*, 24(1):447–450. 23

Mottershead, J. E., Link, M., and Friswell, M. I. (2011). The sensitivity method in finite element model updating: A tutorial. *Mechanical Systems and Signal Processing*, 25(7):2275 – 2296. 40

Muller, W. (1990). Comparison of different methods of force calculation. *IEEE Transactions on Magnetics*, 26(2):1058–1061. 35

Niemann, H., Bonnefoy, X., Braubach, M., Hecht, K., Maschke, C., Rodrigues, C., Robbel, N., et al. (2006). Noise-induced annoyance and morbidity results from the pan-european lares study. *Noise and Health*, 8(31):63. 10

Ouagued, S., Amara, Y., and Barakat, G. (2016). Comparison of hybrid analytical modelling and reluctance network modelling for pre-design purposes. *Mathematics and Computers in Simulation*, 130:3–21. 11th International Conference on Modeling and Simulation of Electric Machines, Converters and Systems. 20

Parent, G. (2008). *Mise en oeuvre d'une technique de projection de grandeurs discrètes : application aux couplages magnétothermique et magnétomécanique*. PhD thesis, Université des Sciences et Technologies de Lille, Université de Liège. 33

Parent, G., Dular, P., Ducreux, J.-P. P., and Piriou, F. (2008). Using a galerkin projection method for coupled problems. *IEEE Transactions on Magnetics*, 44(6):830–833. 35, 49, 51, 80, 113

Passchier-Vermeer, W. and Passchier, W. F. (2000). Noise exposure and public health. *Environmental health perspectives*, 108(Suppl 1):123. 10

Pellerey, P. (2012). *Étude Et Optimisation Du Comportement Vibro-Acoustique Des Machines Électriques : Application Au Domaine Automobile*. PhD thesis, Université Technologique de Compiègne. 39

Pile, R., Devillers, E., and Le Besnerais, J. (2018a). Comparison of Main Magnetic Force Computation Methods for Noise and Vibration Assessment in Electrical Machines. *IEEE Transactions on Magnetics*, 54(7):1–13. 92

Pile, R., Le Besnerais, J., Devillers, E., and Degrendele, K. (2019). e-nvh response synthesis of electric motors based on stator teeth FRF measurements. In *International Symposium on Electromagnetic Fields in Mechatronics, Electrical and Electronic Engineering (ISEF 2019), Nancy, France*. 101, 144

Pile, R., Le Besnerais, J., Devillers, E., and Degrendele, K. (2020a). e-nvh response synthesis of electric motors based on stator teeth FRF measurements. *International Journal of Applied Electromagnetics and Mechanics*. In Press. 101

Pile, R., Le Besnerais, J., Le Menach, Y., Parent, G., Henneron, T., and Lecointe, J.-P. (2020b). Étude de la projection des forces magnétiques pour le calcul des vibrations dans les machines électriques. In *Symposium de Génie Electrique (SGE), Nantes, France*. 94

Pile, R., Le Besnerais, J., Parent, G., Devillers, E., Henneron, T., Le Menach, Y., and Lecointe, J.-P. (2020c). Analytical study of air-gap surface force - application to electrical machines. *Open Physics*, 18(1):658–673. 72

Pile, R., Le Menach, Y., Le Besnerais, J., and Parent, G. (2020). Study of the combined effects of the air-gap transfer for maxwell tensor and the tooth mechanical modulation in electrical machines. *IEEE Transactions on Magnetics*, 56(1):1–4. 88

Pile, R., Parent, G., Devillers, E., Henneron, T., Le Menach, Y., Le Besnerais, J., and Lecointe, J.-p. (2018b). Application limits of the airgap maxwell tensor. In *18th Biennial IEEE Conference on Electromagnetic Field Computation (CEFC)*. 62

Pile, R., Parent, G., Le Menach, Y., Le Besnerais, J., Henneron, T., and Lecointe, J.-p. (2020). Effect of mesh-to-mesh projection on the magnetic tooth forces calculation in electrical machines. In *24th International Conference on Electrical Machines (ICEM)*. 112

Piranda, J. (2001). Analyse modale expérimentale. *Techniques de l'ingénieur: Mesures acoustiques et vibratoires*, base documentaire : TIB420DUO.(ref. article : r6180). 40

Piriou, F. and Razek, A. (1990). A model for coupled magnetic-electric circuits in electric machines with skewed slots. *IEEE Transactions on Magnetics*, 26(2):1096–1100. 16, 58

Rafinéjad, P. (1977). *Adaptation de la méthode des éléments finis à la modélisation des systèmes électromécaniques de conversion d'énergie*. PhD thesis, Institut National Polytechnique de Grenoble. 23, 31

Rasmussen, P. O., Blaabjerg, F., Pedersen, J. K., Kjaer, P. C., and Miller, T. J. (1999). Acoustic noise simulation for switched reluctance motors with audible output p. 42

Ren, Z. (1994). Comparison of Different Force Calculation Methods in 3D Finite Element Modelling. *IEEE Transactions on Magnetics*, 30(5):3471–3474. 28, 35, 65

Robinson, F. N. H. (1973). *Macroscopic electromagnetism*, volume 57. Pergamon. 24

Roivainen, J. (2009). *Unit-wave response-based modeling of electromechanical noise and vibration of electrical machines*. PhD thesis, Helsinki University of Technology. 46

Rosensweig, R. E. (1985). *Ferrohydrodynamics*. Cambridge University Press. 23, 24, 25

Roubache, L., Boughrara, K., Dubas, F., and Ibtiouen, R. (2019). Elementary subdomain technique for magnetic field calculation in rotating electrical machines with local saturation effect. *COMPEL - The international journal for computation and mathematics in electrical and electronic engineering*, 38(1):24–45. 20

Sadowski, N., Lefèvre, Y., Lajoie-Mazenc, M., and Bastos, J. P. A. (1992). Sur le calcul des forces magnétiques. *Journal de Physique III*, 2(5):859–870. 35

Saito, A., Kuroishi, M., and Nakai, H. (2016). Vibration Prediction Method of Electric Machines by using Experimental Transfer Function and Magnetostatic Finite Element Analysis. *Journal of Physics: Conference Series*, 744:012088. 23, 27, 42, 43, 47, 57, 78, 101, 114

Spargo, C. M., Mecrow, B. C., and Widmer, J. D. (2014). A seminumerical finite-element postprocessing torque ripple analysis technique for synchronous electric machines utilizing the air-gap maxwell stress tensor. *IEEE Transactions on Magnetics*, 50(5):1–9. 97

Stroud, A. H. and Secrest, D. (1966). Gaussian quadrature formulas. 51, 116

Tan-Kim, A., Lanfranchi, V., Legranger, J., Palleschi, F., and Redon, M. (2014). Influence of temperature on the vibro-acoustic behavior of claw-pole alternators. *2014 International Conference on Electrical Machines (ICEM)*, pages 1628–1634. 16

Tessarolo, A. and Olivo, M. (2016). A new method for the analytical determination of the complex relative permeance function in linear electric machines with slotted air gap. In *2016 International Symposium on Power Electronics, Electrical Drives, Automation and Motion (SPEEDAM)*, pages 1330–1335. 21

Thompson, R. A. (2015). *Galerkin Projections Between Finite Element Spaces*. PhD thesis, Virginia Tech. 19

Tiegna, H., Amara, Y., and Barakat, G. (2013). Overview of analytical models of permanent magnet electrical machines for analysis and design purposes. *Mathematics and Computers in Simulation*, 90:162–177. 10

Timar, P. L. (1989). *Noise and vibration of electrical machines*. Elsevier. 38, 58

Traxler-Samek, G., Lugand, T., and Uemori, M. (2012). Vibrational Forces in Salient Pole Synchronous Machines Considering Tooth Ripple Effects. *IEEE Transactions on Industrial Electronics*, 59(5):2258–2266. 39

Van der Giet, M. (2011). *Analysis of electromagnetic acoustic noise excitations: A contribution to low-noise design and to the auralization of electrical machines*. Shaker. 38, 41

Vandevelde, L., Gyselinck, J., De Wulf, M. A. C., and Melkebeek, J. A. A. (2004). Finite-element computation of the deformation of ferromagnetic material taking into account magnetic forces and magnetostriction. *IEEE Transactions on Magnetics*, 40(2):565–568. 25

Verez, G., Barakat, G., and Amara, Y. (2014). Influence of slots and rotor poles combinations on noise and vibrations of magnetic origins inu'-core flux-switching permanent magnet machines. *Progress In Electromagnetics Research*, 61:149–168. 16

Verez, G. and Espanet, C. (2016). Limites des modèles analytiques usuels pour le calcul des fréquences propres des machines électriques. 39

Verma, S. P. and Balan, A. (1994). Determination of radial-forces in relation to noise and vibration problems of squirrel-cage induction motors. *IEEE Trans. on En. Conv.*, 9(2):404–412. 30

Virtic, P., Pisek, P., Hadziselimovic, M., Marcic, T., and Stumberger, B. (2009). Torque analysis of an axial flux permanent magnet synchronous machine by using analytical magnetic field calculation. *IEEE Transactions on Magnetics*, 45(3):1036–1039. 10

Wang, S., Hong, J., Sun, Y., and Cao, H. (2020). Analysis of Zeroth-Mode Slot Frequency Vibration of Integer Slot Permanent-Magnet Synchronous Motors. *IEEE Transactions on Industrial Electronics*, 67(4):2954–2964. 42, 48, 92, 96, 123

Wang, S., Polac, L., and Baron, E. (2017). Phénomènes fondamentaux de l'acoustique des moteurs d'automobile. *Techniques de l'ingénieur Acoustique des transports*, base documentaire : TIB523DUO.(ref. article : br2770). fre. 7

Wang, Z. (2013). *Contribution to finite element analysis of magneto-mechanical and magneto-thermal phenomena*. PhD thesis, Lille 1. 51

Wang, Z., Henneron, T., and Hofmann, H. (2016). Space-Time Field Projection: Finite-Element Analysis Coupled Between Different Meshes and Different Time-Step Settings. *IEEE Transactions on Magnetics*, 52(3):1–4. 49, 50, 51, 52, 116

Weh, H. (1964). Zur elektromagnetischen Schwingungsanregung bei Asynchronmaschinen. 42, 43, 47, 88, 92, 123

Weilharter, B., Biro, O., Rainer, S., and Stermecki, A. (2011). Computation of rotating force waves in skewed induction machines using multi-slice models. *IEEE transactions on magnetics*, 47(5):1046–1049. 16

Yang, S. J. (1981). *Low noise electrical motors*. Oxford University Press, Oxford. 53, 54

Zarko, D., Ban, D., and Lipo, T. A. (2006). Analytical calculation of magnetic field distribution in the slotted air gap of a surface permanent-magnet motor using complex relative air-gap permeance. *IEEE Transactions on Magnetics*, 42(7):1828–1837. 20, 21

Zelazo, R. E. and Melcher, J. R. (1969). Dynamics and stability of ferrofluids: Surface interactions. *Journal of Fluid Mechanics*, 39(1):1–24. 24

Appendices

Appendix A

Electrical Machines Description

A.1 12s10p Polar Teeth

This section contains electromagnetic and mechanical parameter about the initial 12s10p electrical machines used in this thesis. This prototype was designed during a previous thesis Devillers [2018].

A.1.1 Electromagnetic Parameters

The stator and rotor data are presented in Table A.1, and the geometry is shown in Fig. A.1. The spectrum of the AGSF is presented in Fig. 3.7.

Table A.1 – 12s10p SPMSM parameters of the existing experimental prototype

Parameter	Symbol	Value
Number of poles	p	10
Number of stator teeth	Z_s	12
Air gap width	g	2.5 [mm]
Rotation speed	N	550 [RPM]
Electrical frequency	f_s	46 [Hz]
Stator lamination		M400-50A
Stator bore radius	R_s	48 [mm]
Stator yoke height	H_y	5 [mm]
Stator tooth length	H_t	20 [mm]
Stator outer radius	R_y	73 [mm]
Stator stack length	L_s	140 [mm]
Stator slot width	W_s	18 [deg]
Tooth opening	β	12 [deg]
Permanent magnet (polar)		NdFeB (N42)
Remanent induction (20°C)	B_r	1.28 [T]
Relative permeability	μ_{rm}	1.05
Magnet width	W_{mag}	34.65 [°]
Magnet top radius	R_{mag}	45 [mm]
Magnet height	H_{mag}	5 [mm]
Magnet length	L_{mag}	2 × 70 [mm]
Rotor lamination		C22 (XC18)
Rotor bore radius	R_r	40 [mm]
Rotor shaft radius	R_{ry}	20 [mm]
Rotor length	L_{st2}	140 [mm]

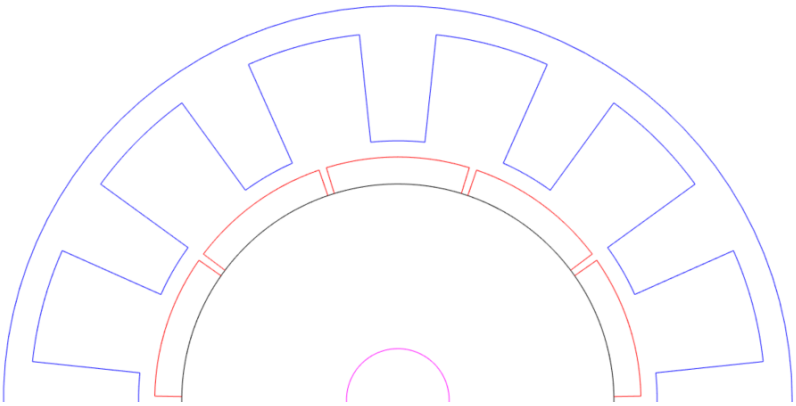

Figure A.1 – Sketch of the 12s10p stator and rotor geometry.

A.1.2 Mechanical Parameters

The lamination material properties used in the simulation is described in Table A.2. The rings (green in Fig. A.3) and the endshields (blue in) are made of an aluminium alloy which properties are presented in Table A.3. Finally, the other part of the model are assumed to be made of the steel material presented in Table A.4.

Table A.2 – Orthotropic Lamination Material Properties

Parameter	Symbol	**Value**
Young Modulus	E_x	210 GPa
	E_y	210 GPa
	E_z	21 GPa
Poisson coefficient	μ_{xy}	0.3
	μ_{yz}	0.1
	μ_{zx}	0.01
Shear Modulus	G_{xy}	80.77 GPa
	G_{yz}	32.19 GPa
	G_{zx}	32.19 GPa
Mass density	ρ	7650 kg/m^3

Table A.3 – Isotropic Aluminium Material Properties

Parameter	Symbol	**Value**
Young Modulus	E	60 GPa
Poisson coefficient	μ	0.1
Mass density	ρ	2700 kg/m^3

Table A.4 – Isotropic Steel Material Properties

Parameter	Symbol	**Value**
Young Modulus	E	200
Poisson coefficient	μ	0.3
Mass density	ρ	7850 kg/m^3

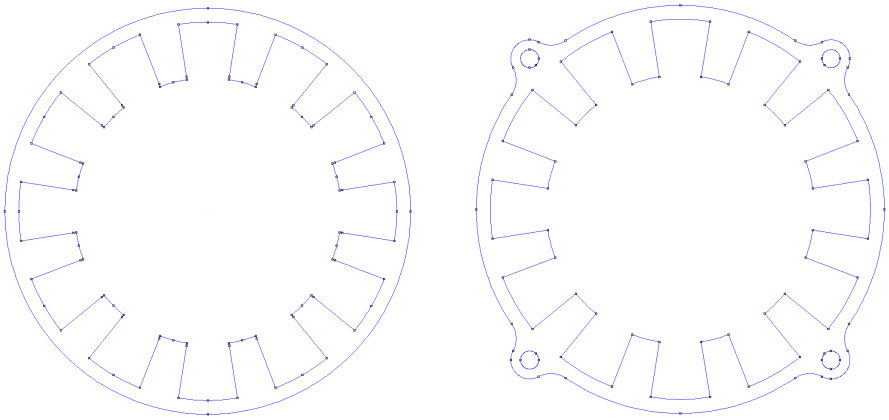

(a) Stator without mounting ears. (b) Stator with mountings ears.

Figure A.2 – Schematics of the different versions of the stator.

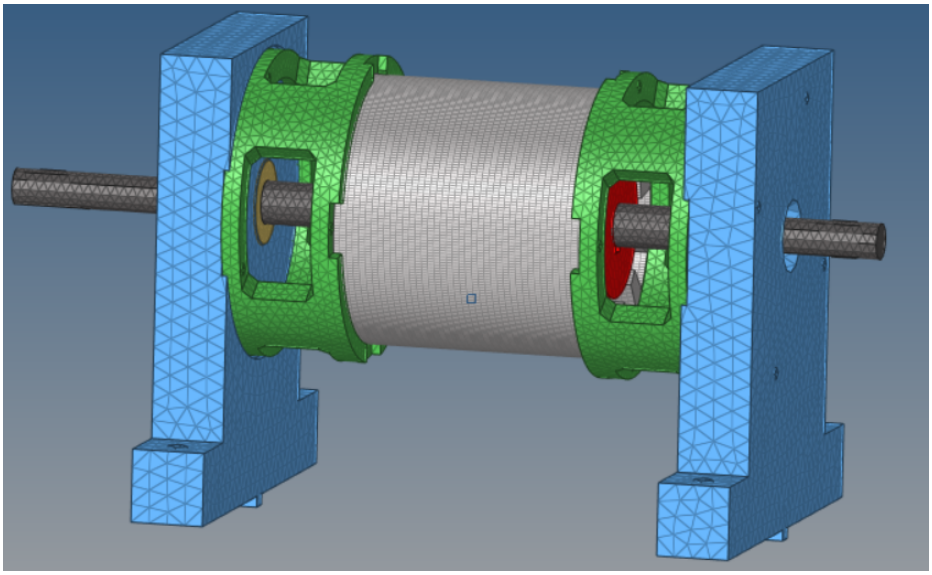

Figure A.3 – Numerical mechanical model (HyperMesh-Optistruct).

Table A.5 – Numerical Modal Analysis (damping equal to 0.2%) on the yoke of the mounted benchmark with the 12s10p machine (A.1) without ears. Only significant stator modes are reported.

Mode Number	Mode identification	Natural Frequency [Hz]
1	(2,0)	708
2	(2,0)	727
3	(2,0)	787
4	(2,0)	810
5	(2,0)	844
8	(2,1)	1175
9	(2,1)	1338
10	(2,1)	1388
15	(3,0)	1637
16	(3,0)	1645
24	(3,1)	2577
25	(3,1)	2606
26	(4,0)	2626
27	(4,0)	2635

A.2 36s36p

This section contains electromagnetic and mechanical parameter about a 36s36p electrical machine designed in this thesis to perform numerical study of the modulation effect. The 36 permanent magnets are regularly placed without gaps. There are neither windings nor currents in the stator slots.

A.2.1 Electromagnetic Parameters

Table A.6 – 36s36p SPMSM parameters used for no-load simulation.

Paramètre	**Symbole**	**Valeur**
Number of poles	p	36
Number of stator teeth	Z_s	36
Airgap width	g	1.5 [mm]
Rotation speed	N	1188 [RPM]
Electrical frequency	f_s	356.4 [Hz]
Stator lamination		M400-50A
Bore radius	R_s	132.5 [mm]
Yoke width	H_y	35 [mm]
Tooth height	H_t	32.5 [mm]
External yoke	R_y	200 [mm]
Lamination length	L_s	350 [mm]
Slot opening	W_s	5.19 [deg]
Tooth opening	β	4.81 [deg]
Permanent magnet (polar)		
Remanent induction (20°C)	B_r	1 [T]
Relative permeability	μ_{rm}	1.05
Magnet width	W_{mag}	0.0223 [rad]
Top radius	R_{mag}	131 [mm]
Bottom radius	R_{mag}	128 [mm]
Height	H_{mag}	3 [mm]
Rotor lamination		M400-50A
Bore radius	R_r	128 [mm]
Internal radius	R_{ry}	90 [mm]
Lamination length	L_r	350 [mm]

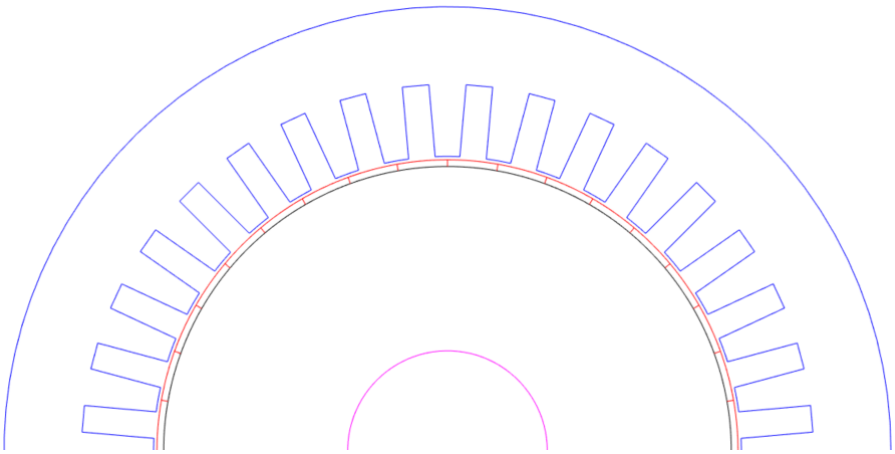

Figure A.4 – Sketch of the 36s36p stator and rotor geometry.

A.2.2 Mechanical Parameters

In the mechanical FE simulation, the stator is considered to be purely composed of the isotropic steel material described in Table A.4.

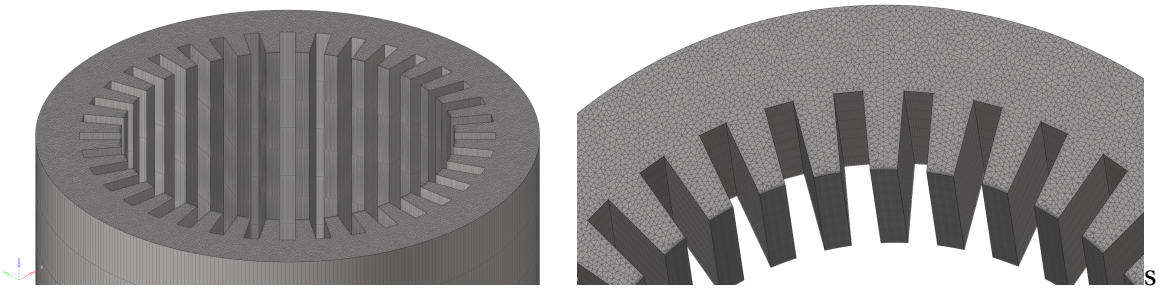

Figure A.5 – Mechanical mesh constructed by extruding the triangular magnetic mesh into prisms on 8 layers.

A.3 12s8p

Table A.7 – 12s8p SPMSM parameters of the existing experimental prototype

Parameter	Symbol	Value
Number of poles	p	8
Number of stator teeth	Z_s	12
Air gap width	g	2.5 [mm]
Rotation speed	N	1500 [RPM]
Electrical frequency	f_s	200 [Hz]
Stator lamination		M400-50A
Stator bore radius	R_s	42.5 [mm]
Stator yoke height	H_y	5.76 [mm]
Stator tooth length	H_t	20 [mm]
Stator outer radius	R_y	73 [mm]
Stator stack length	L_s	140 [mm]
Stator slot width	W_s	18 [deg]
Tooth opening	β	12 [deg]
Permanent magnet (polar)		NdFeB (N42)
Remanent induction (20°C)	B_r	1.28 [T]
Relative permeability	μ_{rm}	1.05
Magnet width	W_{mag}	43.32 [°]
Magnet top radius	R_{mag}	45 [mm]
Magnet height	H_{mag}	5 [mm]
Magnet length	L_{mag}	2×70 [mm]
Rotor lamination		C22 (XC18)
Rotor bore radius	R_r	40 [mm]
Rotor shaft radius	R_{ry}	20 [mm]
Rotor length	L_{st2}	140 [mm]

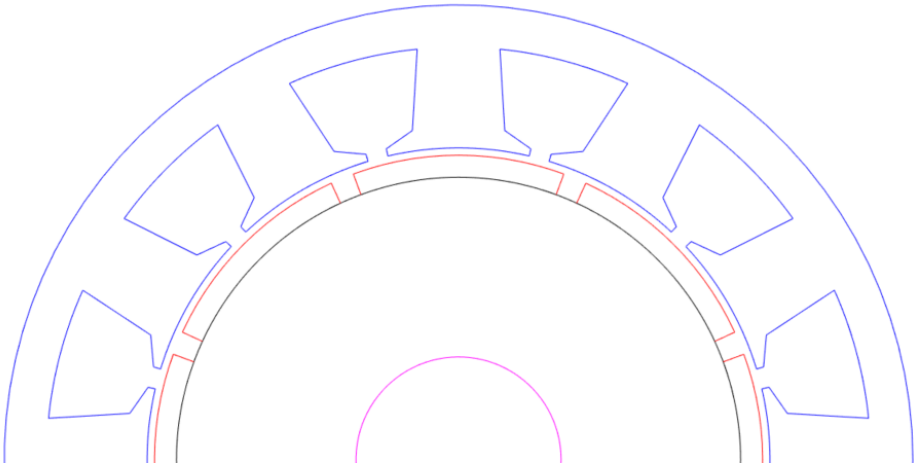

Figure A.6 – Sketch of the 12s8p stator and rotor geometry.

A.4 Turbo-alternator

Table A.8 – Turbo-alternator parameters

Parameter	Symbol	Value
Number of poles	p	4
Number of stator teeth	Z_s	48
Ferromagnetic Relative permeability	μ	1000
Air gap length	g	100 [mm]
Machine length	L	1000 [mm]
Middle air-gap radius	R_{ag}	800 [mm]
Stator bore radius	R_s	850 [mm]
Stator yoke height	H_y	350 [mm]
Stator tooth length	H_t	200 [mm]
Stator outer radius	R_y	1400 [mm]
Stator slot width	W_s	50 [mm]
Stator current amplitude	A, B, C	$1e4$ [A]
Rotor bore radius	R_r	750 [mm]
Rotor current amplitude	I	1600 [A]

Appendix B

Experimental Supplementary Material

B.1 Experimental Modal Analysis

Table B.1 – Experimental Modal Analysis on the yoke of the mounted benchmark with the 12s10p machine (A.1) without ears.

Mode identification	Natural Frequency [Hz]	Damping [%]
(2,0)	721	0.23
(2,0)	797	0.19
(2,1)	1474	0.65
(3,0)	1630	0.21
(3,0)	1639	0.31
(2,1)	1689	0.28
(3,1)	2602	0.4
(3,1)	2628	0.34
(4,0)	2659	0.25
(4,0)	2668	0.24
(5,0)	3644	0.18
(5,0)	3668	0.2
(4,1)	3930	0.45
(6,0)	4213	0.14

B.2 FRF Tooth

This section presents the results obtained with the first set of tooth-FRF which was measured during this thesis and presented in [Pile et al., 2019]. The protocol is almost the same as presented in Section 3.3.1.2, except that the radial response was measured for only one tooth and extrapolated to all the other teeth with a phase shift:

$$\mathrm{TFRF}_{\mathrm{r},i+1,k}(\omega) = \mathrm{TFRF}_{\mathrm{r},i,k}(\omega)\mathrm{e}^{j2\pi/Z_s}. \tag{B.1}$$

Then, the simulation process is exactly the same, and leads to the TWFRF presented in Figs. B.1-B.5. A cut-off frequency was chosen for each wavenumber in order to remove low frequency singularity due to measurements, such that each wave-FRF starts with a constant line. Finally, the order tracking can be perform to extract the amplitude at $10\,f_s$ and $2\,f_s$ and compared to corresponding measured run-up.

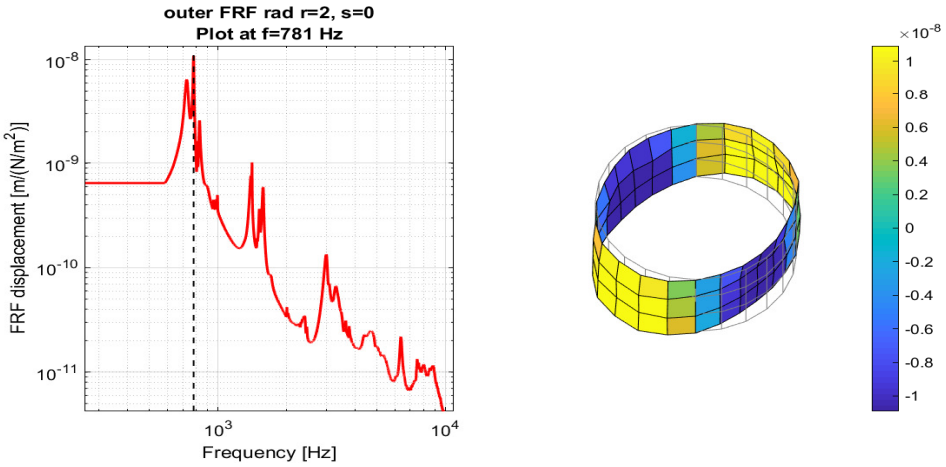

Figure B.1 – Displacement from TWFRF for wavenumber r=2 generated with MANATEE from experimental data.

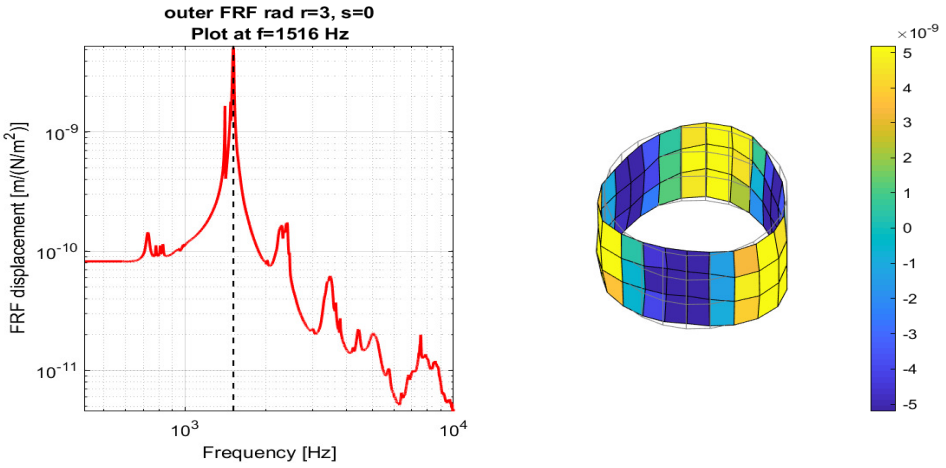

Figure B.2 – Displacement from TWFRF for wavenumber r=3 generated with MANATEE from experimental data.

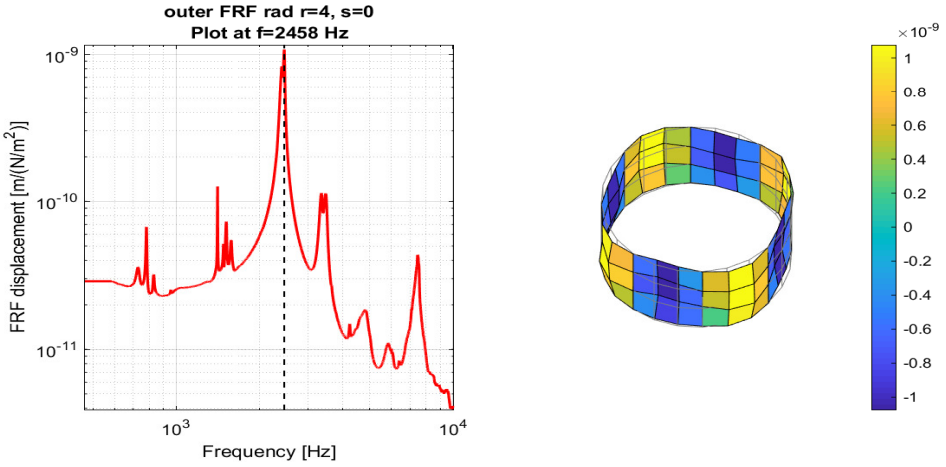

Figure B.3 – Displacement from TWFRF for wavenumber r=4 generated with MANATEE from experimental data.

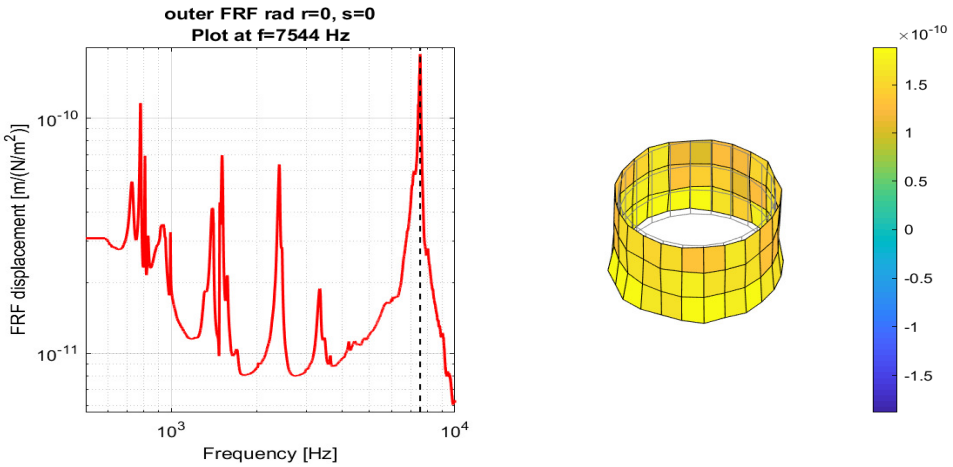

Figure B.4 – Displacement from TWFRF for wavenumber r=0 generated with MANATEE from experimental data.

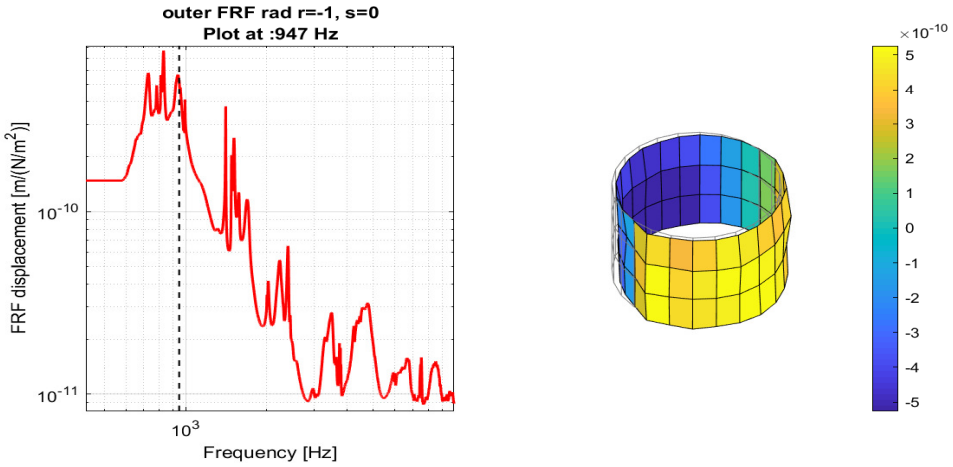

Figure B.5 – Displacement from TWFRF for wavenumber r=1 generated with MANATEE from experimental data.

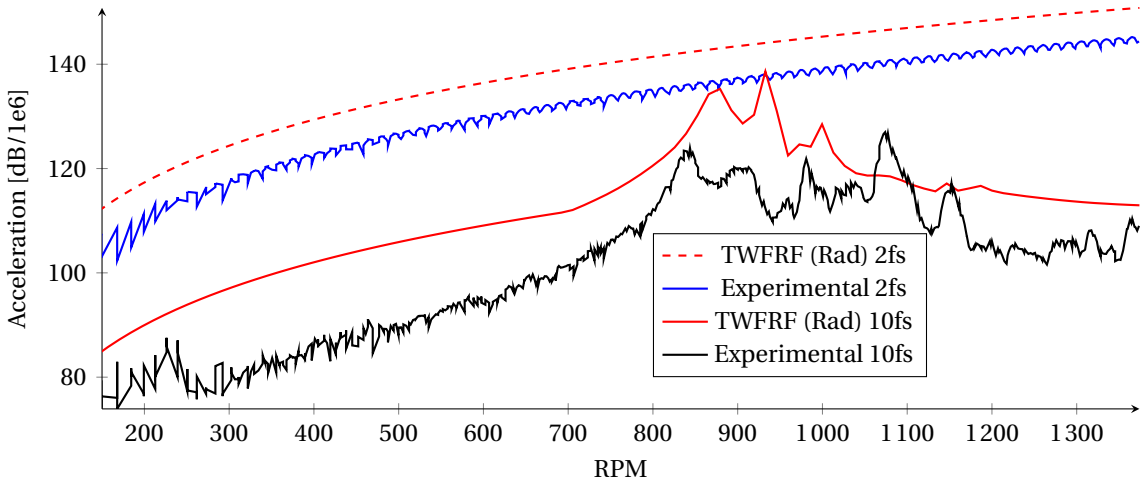

Figure B.6 – Comparison of the order tracking at $2f_s$ between the direct measurement of the acceleration during a run-up and the synthesized acceleration based on the TWFRF method.

B.3 Measurements Repeatability

The goal of this section is to provide the data which concern the repeatability of the run-up measurements performed on the 12s10p prototype. The 5 accelerometers were placed on the centre of the yoke, and distributed around the circumference. A voltage ramp was applied to control the drive machine from 0 to 2760 RPM. The rotation speed was measured by a laser tachometer. Figs. B.7-B.8 show the values from one accelerometer for 3 different run-up at $2f_s$ and $10f_s$. Figs. B.9-B.10 show the values from the accelerometers at $2f_s$ and $10f_s$.

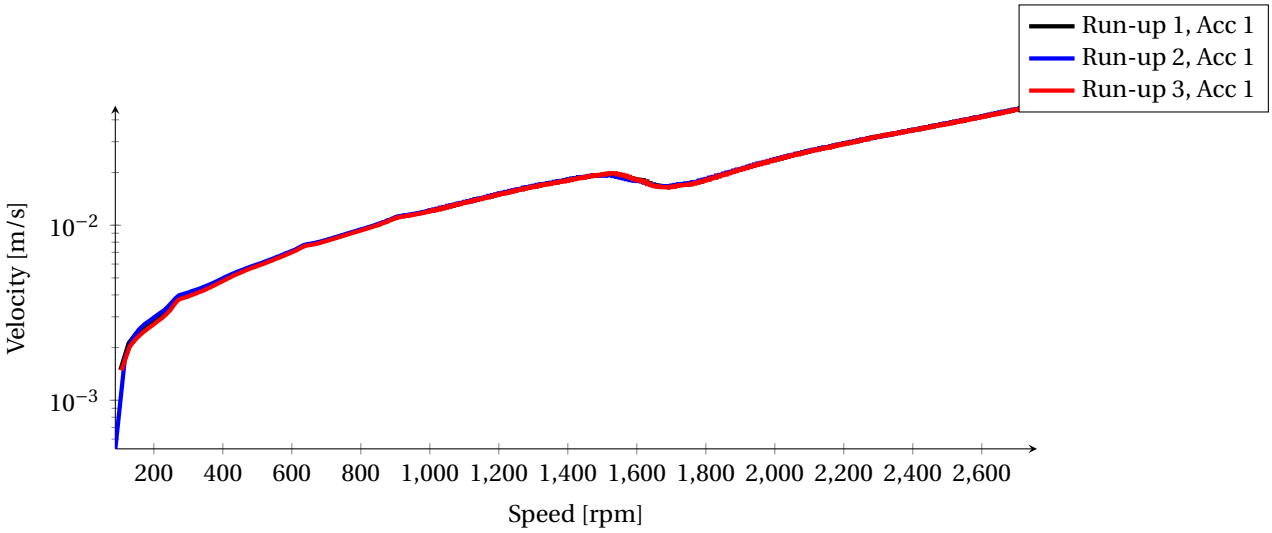

Figure B.7 – One accelerometer measurement for 3 different run-up at $2f_s$.

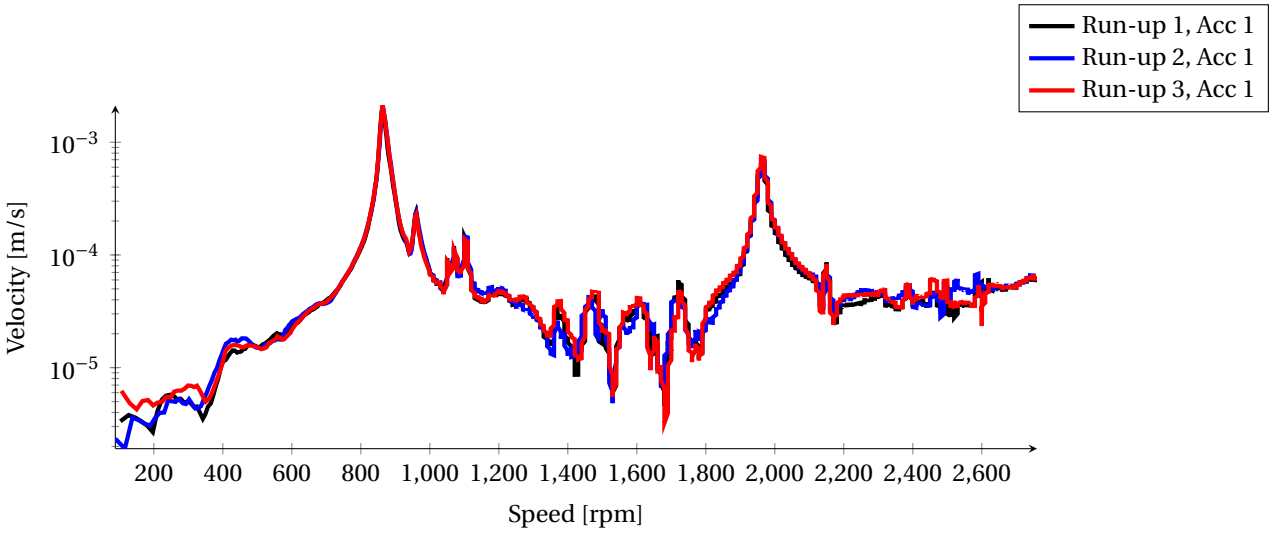

Figure B.8 – One accelerometer measurement for 3 different run-up at $10f_s$.

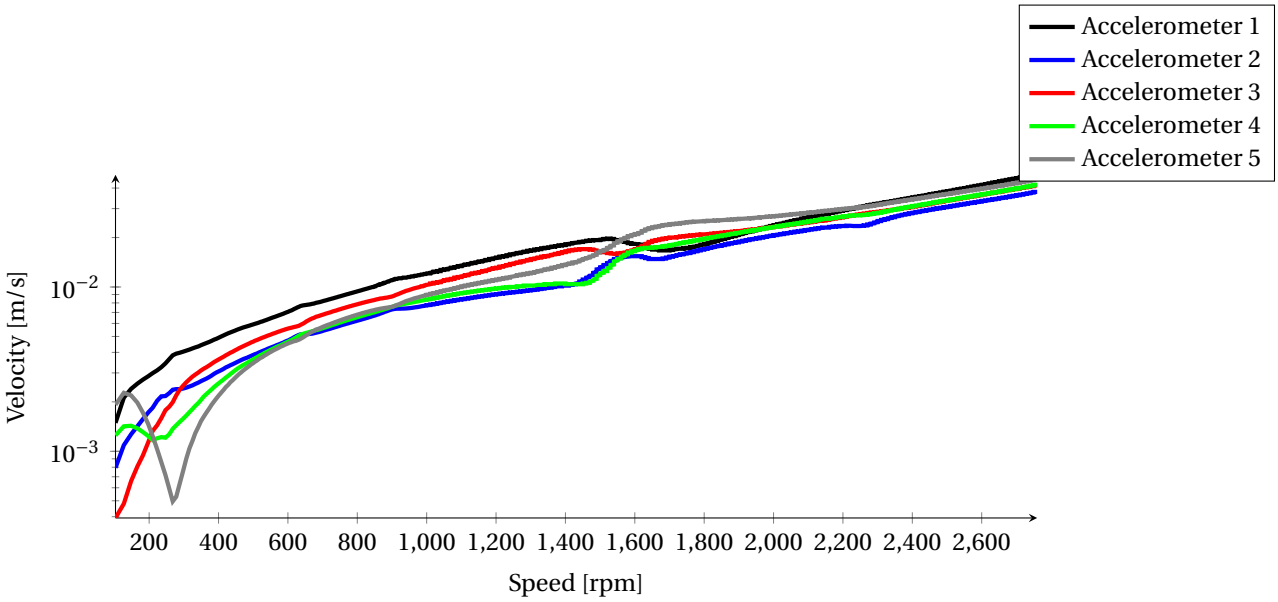

Figure B.9 – Different accelerometers measurements for one run-up at $2f_s$.

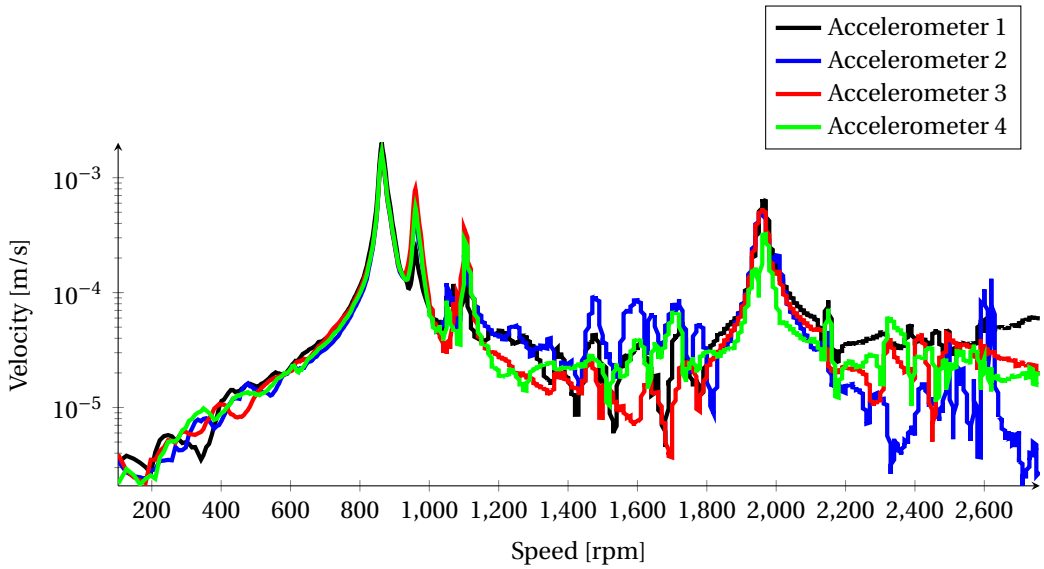

Figure B.10 – Different accelerometers measurements for one run-up at $10f_s$.

Appendix C

Mathematical Supplementary Material

C.1 Shape Functions

C.1.1 Segment

Let be a two nodes reference segment defined by the coordinates $(0,0)$, $(0,1)$. The

nodal shape functions are:

$$\begin{aligned} \phi_1(x) &= 1-x \\ \phi_2(x) &= x \end{aligned} \tag{C.1}$$

C.1.2 Triangle

Let be a three nodes reference triangle defined by the coordinates $(0,0)$, $(1,0)$ and $(0,1)$. The nodal shape functions are:

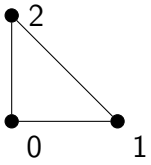

$$\begin{aligned} \phi_1(x,y) &= 1-x-y \\ \phi_2(x,y) &= x \\ \phi_3(x,y) &= y \end{aligned} \tag{C.2}$$

Then the gradient of the shape functions is:

$$\nabla\phi = \begin{pmatrix} -1 & -1 \\ 1 & 0 \\ 0 & 1 \end{pmatrix} \tag{C.3}$$

C.1.3 Quadrilateral

Let be a four nodes reference quadrilateral defined by the coordinates $(0,0)$, $(1,0)$, $(0,1)$, $(1,1)$.

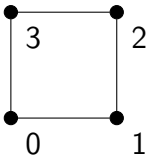

The nodal shape functions are:

$$\begin{aligned}\phi_1(x,y) &= (1-x)(1-y)/4\\ \phi_2(x,y) &= (1+x)(1-y)/4\\ \phi_3(x,y) &= (1+x)(1+y)/4\\ \phi_4(x,y) &= (1-x)(1+y)/4\end{aligned} \tag{C.4}$$

C.2 Example of Jacobian Derivative Calculation

This section proposes an example to calculate the previous derivatives (1.69) and (1.70) towards $s = y$ direction for the node 1 of a 3-nodes triangle element with linear shape functions (see Annex C.1.2). The calculation of the Jacobian leads to:

$$\mathbb{J} = \begin{pmatrix} x_2 - x_1 & y_2 - y_1 \\ x_3 - x_1 & y_3 - y_1 \end{pmatrix} \tag{C.5}$$

Next step is the virtual displacement matrix:

$$\frac{\partial \mathrm{S}}{\partial y}^{1} = \begin{pmatrix} 0 & 1 \\ 0 & 0 \\ 0 & 0 \end{pmatrix} \tag{C.6}$$

which allows to compute the contribution of the first node to (1.69):

$$\frac{\partial \mathrm{J}}{\partial y}^{(1)} = \begin{pmatrix} 0 & 0 & 0 \\ 0 & 0 & 0 \end{pmatrix} \begin{pmatrix} x_1 & y_1 \\ x_2 & y_2 \\ x_3 & y_3 \end{pmatrix} + \begin{pmatrix} -1 & 1 & 0 \\ -1 & 0 & 1 \end{pmatrix} \begin{pmatrix} 0 & 1 \\ 0 & 0 \\ 0 & 0 \end{pmatrix} = \begin{pmatrix} 0 & -1 \\ 0 & -1 \end{pmatrix} \tag{C.7}$$

For the determinant derivative, first the Jacobian inverse can be calculated:

$$\mathbb{J}^{-1} = \frac{1}{|\mathrm{J}|} \begin{pmatrix} y_3 - y_1 & y_1 - y_2 \\ x_1 - x_3 & x_2 - x_1 \end{pmatrix} \tag{C.8}$$

then

$$\frac{\partial |\mathrm{J}|}{\partial y}^{(1)} = \mathrm{Tr}\left(\frac{1}{|\mathrm{J}|} \begin{pmatrix} y_3 - y_1 & y_1 - y_2 \\ x_1 - x_3 & x_2 - x_1 \end{pmatrix} \begin{pmatrix} 0 & -1 \\ 0 & -1 \end{pmatrix} \right) |\mathrm{J}| = x_3 - x_2 \tag{C.9}$$

C.3 Calculation of Tooth Tip Moment per Wavenumber

Introducing the lever arm vector

$$\mathbf{O_i M} = \mathrm{R_{sbo}}(\cos\alpha - \cos\alpha_i)\mathbf{u_x} + \mathrm{R_{sbo}}(\sin\alpha - \sin\alpha_i)\mathbf{u_y}, \tag{C.10}$$

then the contribution of radial and tangential AGSF to the tooth tip bending moment can be calculated according to:

$$\mathrm{M_{r},}_i(n,\omega) = \mathrm{R_{sbo}L_s}\int_{\alpha_i-\gamma/2}^{\alpha_i+\gamma/2} \mathbf{O_i M} \otimes \hat{\mathrm{P}}_\mathrm{r}(\mathrm{R_{ag}}, n, \omega)\mathbf{e}_\mathrm{r}(\theta)\exp^{n\theta}\mathrm{d}\theta \cdot \mathbf{u_z} \tag{C.11}$$

$$\mathrm{M_{\theta},}_i(n,\omega) = \mathrm{R_{sbo}L_s}\int_{\alpha_i-\gamma/2}^{\alpha_i+\gamma/2} \mathbf{O_i M} \otimes \hat{\mathrm{P}}_\theta(\mathrm{R_{ag}}, n, \omega)\mathbf{e}_\theta(\theta)\exp^{n\theta}\mathrm{d}\theta \cdot \mathbf{u_z} \tag{C.12}$$

All calculations done, it leads to the following result:

$$\mathrm{M_{r},}_i(n,\omega) = \mathrm{R_{sbo}^2 L_s}\hat{\mathrm{P}}_\mathrm{r}(\mathrm{R_{ag}}, n, \omega)\, j\mathrm{A}_n^{rt}\exp^{n\alpha_i}, \tag{C.13}$$

$$\mathrm{M_{\theta},}_i(n,\omega) = \mathrm{R_{sbo}^2 L_s}\hat{\mathrm{P}}_\theta(\mathrm{R_{ag}}, n, \omega)\mathrm{A}_n^{m}\exp^{n\alpha_i}, \tag{C.14}$$

with $\mathrm{A}_n^{\mathrm{rt}}$ from (3.6), and if $|n| \neq 1$ and $n \neq 0$:

$$\mathrm{A}_n^{\mathrm{m}} = -2\frac{\left(n^2\left(\cos\left(\frac{\gamma}{2}\right)-1\right)\right)\sin\left(n\frac{\gamma}{2}\right) - n\sin\left(\frac{\gamma}{2}\right)\cos\left(n\frac{\gamma}{2}\right)}{n\left(n^2-1\right)}, \tag{C.15}$$

else if $|n| = 1$:

$$\mathrm{A}_1^{\mathrm{m}} = -n\frac{1}{2}\left(\gamma - 4\sin\left(\frac{\gamma}{2}\right) + \sin(\gamma)\right), \tag{C.16}$$

and if $n = 0$:

$$\mathrm{A}_0^{\mathrm{m}} = -\frac{1}{2}\left(\gamma - 2\sin\left(\frac{\gamma}{2}\right)\right). \tag{C.17}$$

C.4 Mesh-to-mesh Projection and Torque

This annex presents the results of Section 3.4.1 applied to the computation of torque in Fig. C.1. The errors for torque are much lower than lumped tooth force. Thus, torque is an unsuitable criterion for judging the accuracy of the mesh-to-mesh projection.

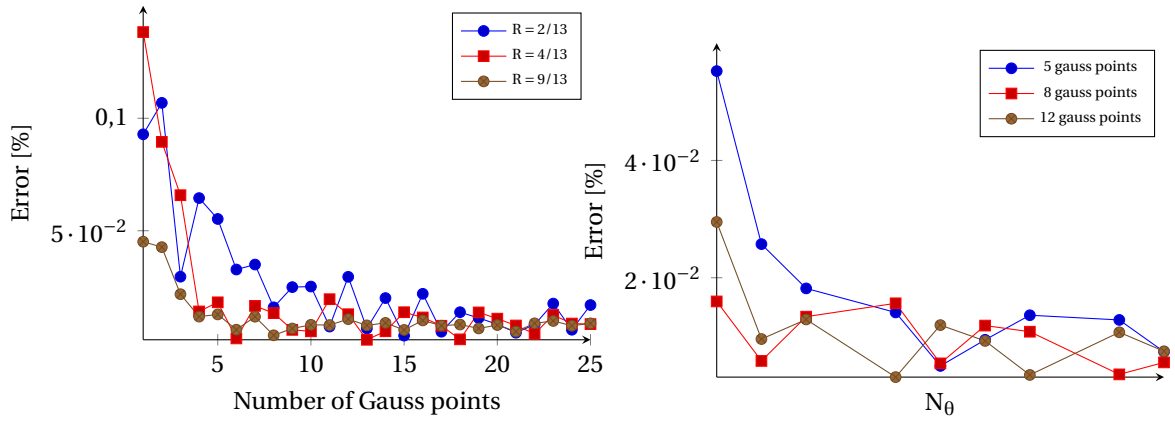

(a) Function of Gauss points number.

(b) Function of mesh size.

Figure C.1 – Relative error for torque on the mechanical mesh compared to magnetic mesh.

C.5 Definition of 2D Polar Referential

The 2D polar coordinate system is defined for electrical machines in the Fig. C.2. $\mathbf{e}_r$ is called the radial vector and $\mathbf{e}_\theta$ is called the tangential vector. In 2D, the notion of "tangential" is commonly used to describe the direction that would be called circumferential in a 3D cylindrical reference. This misuse of language is also used in this thesis.

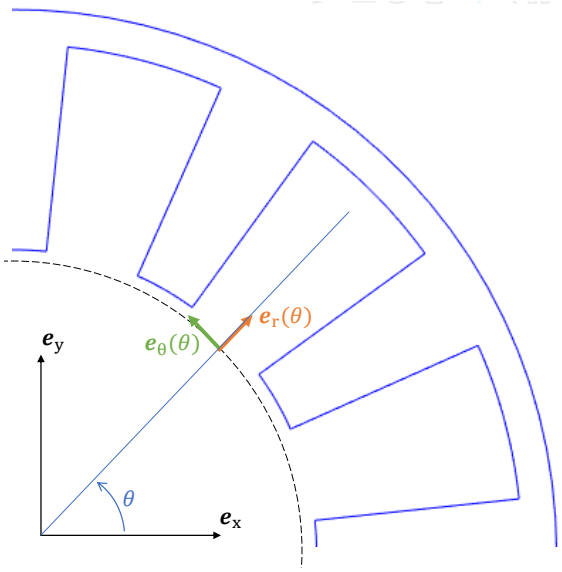

Figure C.2 – Definition of polar referential for electrical machines.

Appendix D

List of acronyms

AGSF Air-Gap Surface Force. 27–30, 34–37, 41–48, 55, 58, 59, 62, 65–71, 73–82, 86, 88–90, 92–98, 108, 113, 123, 138, 151

e-NVH Electromagnetic Noise, Vibrations and Harshness. 7–11, 14–17, 19, 21–23, 32, 35, 36, 38, 44, 46, 49, 55–59, 62, 79, 80, 90, 92, 98, 99, 101, 111, 112, 118, 123, 125–127

FE Finite-Element. 17, 19, 20, 22, 28, 31, 32, 34, 38, 40, 41, 44, 46, 48, 49, 57, 65, 79, 94, 96, 101, 102, 112, 119, 141

FRF Frequency Response Function. 37, 38, 40, 41, 46, 47, 57, 59, 96, 101–110, 117, 121, 123, 126, 127, 144

MST Maxwell Stress Tensor. 23–25, 27, 28, 30, 31, 34, 35, 62, 65, 90, 94, 97–100, 123, 125

PMSM Permanent Magnet Synchronous Machine. 55–59

RMS Root Mean Square. 54, 105–108, 119

SCIM Squirrel Cage Induction Machine. 55, 56, 81, 82, 86

SPMSM Surface Permanent Magnet Synchronous Machine. 16, 81, 86, 94, 104, 138, 141, 142

SRM Switched Reluctance Machine. 55, 56

SynRM Synchro-Reluctant Machine. 55, 56

TWFRF Tooth Wave Frequency Response Function. 101, 102, 105–111, 144–146

VWP Virtual Work Principle. 23, 24, 31–36, 48, 49, 79, 80, 94–97, 99, 100, 112, 118, 123, 125

WRSM Wound Rotor Synchronous Machine. 55, 56

Appendix E

List of main symbols

A Magnetic potential vector. 18

$B_{\mathbf{r}}$ Radial magnetic flux density. 24

B_θ Tangential magnetic flux density. 24

B Magnetic flux density vector. 17

$F_{\mathbf{r}}$ Radial magnetic lumped tooth force. 42

F_θ Tangential magnetic lumped tooth force. 42

$f_{\mathbf{s}}$ Stator current electric frequency or synchronous frequency. 56

H Magnetic field vector. 17

j Imaginary number. 30

$L_{\mathbf{s}}$ Stator axial length. 42

μ Magnetic permeability. 18, 24

n Wavenumber (angular harmonic). 30

ω Pulsation (time harmonic). 30, 37

p Number of poles. 8, 56

$P_{\mathbf{r}}$ Radial magnetic air-gap surface force. 29

$\hat{P}_{\mathbf{r}}$ Fourier transform of P_r. 30

P_θ Tangential magnetic air-gap surface force. 29

$\hat{P}_\theta$ Fourier transform of P_θ. 30

$R_{\mathbf{ag}}$ Airgap middle radius. 30

$R_{\mathbf{r}}$ Rotor bore radius. 29

$R_{\mathbf{s}}$ Stator bore radius. 29

θ Angular position. 8

Z_s Number of stator slots. 42, 56, 123

Abstract

Abstract The presence of electromagnetic force harmonics in electrical machines is generally a source of acoustic noise and vibration (e-NVH). This phenomenon must be considered at early design stage to comply with acoustic and vibration standards, particularly in the automotive sector. The eNVH level is obtained from multi-physical simulations based on electromagnetic, mechanical and acoustic models. This industrial PhD thesis takes part in the internal research program of EOMYS ENGINEERING. This company develops and commercializes Manatee software, dedicated to the e-NVH simulation of electrical machines. In this modeling context, this thesis focuses on numerical methods for the calculation of electromagnetic forces as well as magneto-mechanical weak coupling. The validity of the air-gap forces based on Maxwell Stress Tensor (MST) method, as well as the mechanical modulation effect have been studied. In particular, this work focuses on the validity of one load vector per tooth tip to achieve the magneto-mechanical coupling. A test bench based on a Permanent Magnet Synchronous Machine (SPMSM) with 12 slots and 10 poles was characterized in order to compare different models for eNVH simulations. This PhD work contains several contributions. The first result proposes an analytical equation to improve air-gap force accuracy. The second result discusses how to reduce accurately the magneto-mechanical model by using normalized simulation and modulation effect. The third result deals with a complementary experimental protocol to mechanical finite element analysis. The interest of the method is demonstrated in a hybrid magneto-mechanical simulation. The last result highlights the contribution of the tooth tip bending moments to magnetic vibrations.

Keywords Electrical machines, Electromagnetic noise, Machines vibrations, Magnetic Force, Maxwell Stress, Virtual Work Principle, Magneto-mechanical coupling.

Résumé La présence d'harmoniques de force électromagnétique dans les machines électriques est généralement une source de bruit et de vibrations acoustiques (B&V). Ce phénomène doit être pris en compte dès le début de la conception afin de respecter les normes acoustiques et vibratoires, notamment dans le secteur automobile. Le niveau de B&V est obtenu à partir de simulations multi-physiques basées sur des modèles électromagnétiques, mécaniques et acoustiques. Cette thèse CIFRE s'inscrit dans le cadre du programme de recherche interne d'EOMYS ENGINEERING. Cette entreprise développe et commercialise le logiciel Manatee, dédié à la simulation électromagnetique et vibroacoustique de machines électriques. Dans ce contexte de modélisation, cette thèse porte sur les méthodes numériques de calcul des forces électromagnétiques ainsi que sur le couplage faible magnéto-mécanique. La validité de la force surfacique d'entrefer calculée par la méthode du tenseur de Maxwell, ainsi que l'effet de modulation mécanique ont été étudiés. En particulier, ce travail se concentre sur la validité d'une résultante par tête de dent pour réaliser le couplage magnéto-mécanique numérique. Un banc d'essai basé sur une machine synchrone à aimant permanent (MSAPS) à 12 encoches et 10 pôles a été caractérisé afin de comparer différents modèles pour les simulations B&V. Ce travail de doctorat contient plusieurs contributions. Le premier résultat propose une équation analytique pour améliorer la précision de la force surfacique d'entrefer. Le second résultat traite de la manière de réduire avec précision le modèle magnéto-mécanique en utilisant une simulation normalisée et l'effet de modulation. Le troisième résultat porte sur un protocole expérimental complémentaire à l'analyse mécanique par éléments finis: l'intérêt de la méthode est démontré dans une simulation magnéto-mécanique hybride. Le dernier résultat met en évidence la contribution aux vibrations magnétiques des moments de torsion en tête de dent.

Mots-clefs Machines électriques, Bruit d'origine électromagnétique, Vibrations des machines, Forces électromagnétiques, Forces de Maxwell, Principe des travaux virtuels, Couplage magnéto-mécanique.